NONLINEAR NUMERICAL METHODS TO ANALYZE GROUND FLOW AND SOIL-PILE INTERACTION IN LIQUEFIABLE SOIL

XIAOWEI TANG

SEPTEMBER 2004

NONLINEAR NUMERICAL METHODS TO ANALYZE GROUND FLOW AND SOIL-PILE INTERACTION IN LIQUEFIABLE SOIL

XIAOWEI TANG

SEPTEMBER 2004

KYOTO UNIVERSITY

Nonlinear Numerical Methods to Analyze Ground Flow and Soil-Pile Interaction in Liquefiable Soil

(液状化地盤の流動と杭-地盤の相互作用を解析するための非線形数値解析法)

DISSERTATION

for the Degree of

DOCTOR OF ENGINEERING

Submitted to

the Graduate School of Engineering

of

KYOTO UNIVERSITY

Abstract

This research is focused on the numerical analysis method of liquefiable soil. The aim is to improve the approximate quality of nonlinear numerical simulation of liquefaction process with large deformation. Two main parts are included in the thesis: three-dimensional FE-FD analysis of liquefiable soil considering large deformation with the cyclic elasto-plastic constitutive model and the fluidal elasto-plastic constitutive model; *h*-adaptive FE analysis of liquefiable soil. The new methods are suitable to solve the problems of the seismic analysis of soil structures and soil-pile interaction in liquefiable soil with large deformation.

In the first objective, the cyclic elasto-plastic model and the fluidal elasto-plastic model are adopted as the constitutive models of liquefiable soil in FE-FD coupled method. The material nonlinearity of saturated sand is simulated effectively with these constitutive models. Updated Lagrangian formulation, which belongs to finite deformation theory, has also been applied to three-dimensional FE-FD coupled method to deal with the geometrical nonlinearity of liquefiable soil due to large deformation. The efficiencies of this three-dimensional analysis considering large deformation are demonstrated with two simple examples of the compression of saturated sand and the flow of Newton viscous fluid. The further tests were also conducted with two practical examples of the seismic analysis of embankment and the dynamic analysis of soil-pile interaction system. The development of this method in three-dimensional analysis is a new try and shows special worth to practical engineering.

In the second objective, adaptive technique is applied to non-linear FE analysis of saturated soil considering large deformation including liquefaction phenomenon. We used fission procedure belong to the *h*-refinement indicated by the error estimator which is a posteriori error estimate procedure depending on L_2-norm of strain and superconvergent patch recovery method. The adaptive FE method is developed not only in two-dimensional analysis but in three-dimensional analysis. The convergence of this error estimates method to the mesh quality and the effectiveness of *h*-adaptive mesh

refinement are demonstrated with two- and three- dimensional simple examples. The adaptive FE method was also used in two- and three- dimensional practical analysis of embankment and soil-pile interaction, the efficiency was tested in detail. The application of adaptivity to nonlinear analysis of saturated soil including liquefaction process, especially in three-dimension, is a valuable attempt in the developments of adaptive techniques. The special treatment of slave nodes in the joint sides or side surfaces is proposed in the fission procedure of soil-pile interaction analysis. It is a new progress of adaptive techniques and helpful to increase the accuracy of the soil elements surrounding the pile.

Keywords: *liquefaction, flow of liquefied ground, seismic analysis, saturated soil, soil-pile interaction, the cyclic elasto-plastic constitutive equation, the fluidal elasto-plastic constitutive equation, large deformation, updated Lagrangian formulation, error estimate, adaptive mesh refinement*

TABLE OF CONTENTS

List of Figures

List of Tables

Chapter 1

Statement of Research

1.1 Research Background

Soil structures such as river dikes, high way embankments and earth dams have been frequently damaged during past major earthquakes. This damage was often mainly caused by liquefaction of the embankment and foundation soils. In most cases, unacceptable, large, permanent deformation occurred due to liquefaction of the supporting loose cohesionless foundation soil, resulting in cracking, settlement, lateral spreading, and slumping. Sevier liquefaction of embankment and river dike foundations was reported during the 1960 Alaskan earthquake, the 1964 Niigata earthquake, the 1983 Nipponkai-Chubu earthquake, among many others. During the 1995 Hyogoken-Nanbu earthquake, nearly 1200 small earth embankments suffered some level of damage.

The damages caused by liquefaction also occurred in the structures constructed on the piles in liquefied soil due to the failure of the piles. Depending on the occurrence of

liquefaction, the pile foundation may undergo substantial shaking, while the soil is in a fully liquefied state and soil stiffness is at a minimum. During this shaking phase, the pile is prone to suffering severe cracking or even fracture. Liquefaction leads also to substantial increases in pile cap displacement comparing to the non-liquefied case. After liquefaction, if the residual strength of the soil becomes less than static shear stresses developed by gravity force of ground sloping or movement of river dike, significant lateral spreading or downslope displacements may occur. The moving soil can exert damaging pressures against the piles, leading to their failure. Such failures were prevalent during the 1964 Niigata, Japan earthquake and the 1995 Hyogoken-Nanbu earthquake.

Loose cohesionless sands and silts below the water table develop high pore water pressures and liquefy during strong earthquake shaking. The high pore water pressures may lead to a significant degradation of soil strength and stiffness. This phenomenon is referred to liquefaction. Although the liquefaction process has been understood since the 1964 Niigata earthquake, the seismic design of soil structures and pile foundations in these liquefiable soils poses very difficult problems in analysis and design. Undoubtedly, such earthquake liquefaction hazard necessitates further development not only experimental investigation but numerical modeling of the phenomenon.

In computational analysis, saturated soil is described as a kind of porous media. The Biot's two-phase mixture theory leads to the application of some effective nonlinear finite element method through the derivation of the governing equations expressed u-p formulation, for example, a finite element and finite difference (FE-FD) coupled scheme (Akai and Tamura, 1978). It was used to analyze liquefaction with an infinitesimal strain condition. This method can reduce the total degrees of freedom of the coupled equations. It avoids shear locking under the undrained condition and involves less computational effort than the generalized finite element method.

In nonlinear analysis of saturated soil, an appropriate constitutive model is also important. Many effective constitutive models were developed in recent few decades. The cyclic elasto-plastic model (Oka, 1992) is one of most effective ones. It has been proposed as a numerical method to simulate the liquefaction of saturated soils based on the non-linear kinematic hardening rule. The fluidal elasto-plastic model (Sato and Moon, 2001) has been developed recently based on mechanical and numerical modeling

of seismic liquefaction and the ground flow phenomenon in saturated loose sandy soil in order to unify the phase transformations from solid to liquid as well as liquid to solid of saturated loose sand. It combines the cyclic elasto-plastic behavior of sand and the Newtonian viscous fluid characteristics of liquefied sand by defining the phase transformation-controlling function. This constitutive equation can express the entire process of liquefaction from the initial to post-liquefaction state. The advantage of the later one can solve liquefaction problems by combining the concepts of solid mechanics and fluid mechanics, but the first model is only based on solid mechanics. It is evident that, the treatment based on fluid mechanics is more appropriate to the flow problems of liquefied soil than solid mechanics.

Because the deformation caused by liquefaction is usually very large, finite deformation theory was introduced to finite element method. The further developments of FE-FD coupled scheme is also achieved in two-dimensional analysis with updated Lagrangian formulation (Sato and Di, 2001; Sato and Moon, 2002). In engineering design, a two-dimensional analysis is often used because three-dimensional finite element analysis is time consuming to conduct. This simplification often however raised a question whether the two-dimensional simplification is reasonable or not in practical cases. For this reason, we develop three-dimensional FE-FD coupled scheme with updated Lagrangian formulation. The applications of the two constitutive models introduced above to the three-dimensional FE-FD method with updated Lagrangian formulation are one of the major topics of this thesis.

On the other hand, as a type of numerical approximation method, errors are inevitable in analysis results obtained by the finite element method. The finite element method solution does not always guarantee the desired accuracy, sometimes causing serious analysis problems, especially in the analysis considering large deformation. The error mentioned here is the error caused by discretization in a FEM process. In a practical problem of liquefied soil flow caused by earthquake, the deformation of the soil is not uniform and unable to predict at where the large deformation is developed. In the elements with large deformation large numerical error is developed. Evidently, reducing the size of the elements uniformly during discretization minimizes error, but the number of nodes and elements are increased at the same time. That means a heavy burden of calculation. In fact, the region with small deformation does not need finer

mesh. It is better to use a fine mesh in the region with large error and a normal or coarse mesh in the low error region.

A method called the adaptive technique or adaptive mesh refinement has been developed and used to reduce the discretization error. It has been used successfully in many fields including solid and fluid mechanics, for linear and nonlinear problems. , to solve static and transient behavior of two-dimensional continua; however, extensions to three-dimensional, dynamic applications are in their infancy. It is a big challenge to apply adaptive mesh refinement to seismic analysis of liquefaction.

1.2 Research Objectives

The first objective of this research is to simulate the soil flow caused by liquefaction considering the material and geometrical nonlinearities of liquefiable soil. At same time, improving the accuracy of finite element by mesh refinement is another objective of this research. The effort of this research is focused on the development of three-dimensional FE-FD method considering large deformation and the application of adaptive mesh refinement to dynamic analysis of liquefiable soil.

For the first objective, the cyclic elasto-plastic model and the fluidal elasto-plastic model have been adopted as the constitutive models of liquefiable soil in FE-FD coupled method. The material nonlinearity of saturated sand is simulated effectively with these constitutive models. Updated Lagrangian formulation, which belongs to finite deformation theory, has also been applied to three-dimensional FE-FD coupled method to deal with the geometrical nonlinearity of liquefiable soil due to large deformation. The efficiencies of this three-dimensional analysis considering large deformation are demonstrated with two simple examples of the consolidation and the flow of saturated sand. The further tests were also conducted with two practical examples of the seismic analysis of embankment and the dynamic analysis of soil-pile interaction system.

For the second objective, adaptive technique was applied to non-linear FE analysis of saturated soil considering large deformation including liquefaction phenomenon. We

used fission procedure belong to the *h*-refinement indicated by the error estimator which is a posteriori error estimate procedure depending on L_2-norm of strain and superconvergent patch recovery method. The adaptive FE method is developed from two-dimensional analysis to three-dimensional analysis. The convergence of this error estimates method to the mesh quality and the effectiveness of *h*-adaptive mesh refinement are demonstrated with two- and three- dimensional simple examples. The adaptive FE method was also used in two- and three- dimensional practical analysis of embankment and soil-pile interaction, the efficiency was tested in detail.

1.3 Outline of Contents

In general, this thesis includes two main topics, three-dimensional FE-FD analysis of liquefiable soil considering large deformation and adaptive FE analysis of liquefiable soil. The first topic is presented from chapters 2 to 4 and the second topic is presented in chapters 5 and 6. Chapter 7 reviews the foregoing chapters and summarizes the principle results obtained. The content in each chapter is introduced dividually in the following.

Chapter 2 presents the application of the cyclic elasto-plastic constitutive model of saturated soil to liquefaction analysisand the development of three-dimensional FE-FD coupled method using updated Lagrangian formulation to analyze large deformation caused by liquefaction. Principle of updated Lagrangian method for porous media is also introduced. The governing equations for FE-FD method are derived in detail. Two simple effective examples are calculated to demonstrate this method.

Chapter 3 presents the principle of fluidal elasto-plastic model of saturated soil, and the derivation of the three-dimensional FE-FD equations with updated Lagrangian method and the constitutive equation of the fluidal elasto-plastic model. The method is demonstrated by a simple example, the flow simulation of liquefied soil in three-dimensional space using the Newtonian viscous fluid constitutive equation in updated Lagrangian formulation. The adaptability of this method in dynamic analysis of saturated soil is tested.

Chapter 4 introduces two practical examples of seismic analysis of embankment constructed on liquefiable soil and soil-pile interaction analysis in three-dimension. Two constitutive model of saturated soil, the cyclic elasto-plastic model and the fluidal elasto-plastic model are adopted in the examples. The efficiency of this method is demonstrated with comparison of the results calculated with updated Lagrangian formulation and with infinitesimal deformation assumption.

Chapter 5 presents the application of adaptive mesh refinement to seismic analysis of liquefiable soil. A posteriori error estimate procedure depending on L_2-norm of strain and superconvergent patch recovery method is introduced first and the convergence of this error estimator in two- and three-dimensional problem is studied with two examples of partial compress of saturated soil. The *h*-refinement algorithm including fission process in soil elements and the technique to deal with the soil elements beside concrete elements of piles is also presented. The efficiency of this method for liquefiable soil analysis is shown in the two- and three-dimensional simple examples.

In chapter 6, the posteriori error estimates based on superconvergent patch recovery smoothing technique and the *h*-adaptive mesh refinement are applied to four practical examples of seismic analysis with finite deformation theory. These examples include two- and three-dimensional, the seismic analysis of embankment constructed on liquefiable soil and the soil-pile interaction analysis. The efficiency of the h-adaptive FE method is tested further by these practical examples.

Chapter 2

3-D Analysis of Liquefaction Process Using Updated Lagrangian Method

2.1 Introduction

As a main reason of damage to structures during strong earthquakes, liquefaction has been studied intensively after Niigata earthquake (1964). Liquefaction is a phenomenon of loosely deposited saturated sandy soil which occurs during strong earthquakes. Pore water pressure of saturated sandy soil is raised to a high level by earthquake vibration of the ground if the pore water cannot dissipate quickly. Development of pore water pressure leads to loss of stiffness of saturated soil due to the decrease of effective stress and causes liquefaction finally. Usually, large deformation of ground happens with flow of liquefied soil.

In the early researches, two-phase mixture theory (Biot, 1941, 1956, 1962) was developed for saturated soil. Displacement of solid phase and the relative displacement of pore liquid to solid were used as state variables based on the Darcy's law. In 1970's,

generalized form of finite element solution were developed using displacement of solid and pressure of pore water as variables (Zienkiewicz et al, 1980 and 1984; Prevost, 1980 and 1982). A finite element and finite difference (FE-FD) coupled method was proposed (Akai and Tamura, 1978) and extended to liquefaction analysis of saturated soil (Oka et al, 1994) with infinitesimal strain assumption. In this method, the equilibrium equation for saturated soil is discretized in the space domain by the finite element method, and terms of pore pressure in the continuity equation are discretized in the space domain by the finite difference method. This method reduces the total degrees of freedom of the coupled equations and the final matrix form of governing equations is symmetric. In recent years, nonlinear material behavior of soil and geometrical nonlinearity due to large strain have been introduced to soil analysis (Zienkiewicz et al, 1990 and 1996). In a new research (Di and Sato, 2003 and 2003), updated Lagrangian method was applied to FE-FD coupled method according to finite deformation theory to deal with large deformation of saturated soil caused by liquefaction. It has been achieved in two dimensional analysis of liquefaction. In this research, the author extend FE-FD coupled method using updated Lagrangian method to three dimensional analysis of liquefaction in order to solve practical engineering problems.

In the numerical nonlinear analysis of saturated soil, the constitutive model of saturated soil is also an important problem. During the last 50 years, many constitutive models of soil have been developed with context of plasticity and visco-plasticity. Among these models, a great deal of attention has been paid to constitutive models which predict the cyclic behavior of saturated sand. This is because of the many occurrences of disastrous damages to the sandy soil caused by liquefaction.

An effective cyclic elasto-plastic constitutive model based on the non-linear kinematic hardening rule has been proposed (Oka, 1992) as a numerical method to simulate the liquefaction of saturated soils. In addition, non-linear expression of the stress-dilatancy characteristic relation and the cumulative strain-dependent characteristic of the plastic shear model have been taken into account in this constitutive relationship (Oka, 1999). The model performs well for describing soil behavior under dynamic loading and has been used for such numerical simulations of liquefaction problems as the shaking table test of deposits, the behavior of seabed deposits under wave action, and seismic analysis of embankments. This constitutive model of saturated

soil is adopted in this research.

In this chapter, Section 2.2 introduces the cyclic elasto-plastic model of saturated soil. Section 2.3 presents the development of three-dimensional FE-FD coupled method using updated Lagrangian formulation. Principle of updated Lagrangian method for porous media is introduced. The governing equations for FE-FD method are derived in detail. Section 2.4 gives two simple effective examples to demonstrate this method. Section 2.5 summarizes the chapter briefly.

2.2 Elasto-Plastic Model of saturated Soil

A cyclic elasto-plastic model is proposed by Oka based on modified flow rule and the nonlinear kinematic hardening rule. A new stress-dilatancy relationship and cumulative strain-dependent characteristics of the plastic shear modulus have been mainly incorporated into the proposed model. The improvements of this constitutive model for saturated sandy soil are:

(1) Taking account of the stress state of the rotational main stress by using stress parameter and relative stress ratio;

(2) Considering hardening rule and non-linear kinematic hardening rule, the hardening parameter should be initialized in stress rotating during cyclic loading;

(3) Introduced boundary surface and over consolidated boundary surface, the decrease of dilatancy with over-consolidating can be expressed.

(4) The relation between stress and dilatancy can be modified by generalized flow rule.

(5) The behavior of sand to 10% shear strain can be simulated by shear parameter depends on plastic strain.

The basic assumptions adopted in development of this model are introduced as follows:

(1) Infinitesimal-strain theory.

(2) Elasto-plastic theory.

(3) Generalized flow rule.

(4) Overconsolidation boundary surface.

(5) Non-linear kinematic hardening rule.

As a constitutive model to describe the material nonlinearity of saturated sandy soil, some nonlinear characters of saturated sandy soil are taken into account.

(1) By use of generalized flow rule, the stress-dilatancy characteristic relations are modified. Introducing a non-linear expression for the coefficient of dilatancy D_0, it becomes possible to describe the behavior of the stress path better than by the original modal. The liquefaction strength curve from the modified modal is similar to that from the experimental results.

(2) The cumulative plastic-strain dependence of the plastic shear modulus is taken into account to reproduce the continuous increase in shear strain during cyclic mobility for loose sand. Using a non-linear function which provides a decrease in the shear modulus, the development of shear strain and the reduction of the mean effective stress after cyclic mobility are consistent with the experimental results.

(3) The fading memory characteristic of the initial anisotropy was incorporated to describe well anisotropic consolidation. Introducing the fading memory characteristic into ζ, it became possible to describe the behavior of both anisotropically and isotropically consolidated sands with the same material parameters.

In the constitutive equation of this cyclic elaso-plastic model, the relation between stress and strain is expressed in a increment form as:

$$d\sigma'_{ij} = D^{ep}_{ijkl} d\varepsilon_{kl} \tag{2.2.1}$$

where D^{ep}_{ijkl} is a instantaneous elasto-plastic stiffness matrix of this model.

The derivation of the main equations of this model is introduced as follows.

Yield function

The yield of soil includes consolidation yield and shear yield. In the analysis of liquefaction, yield is induced by decrease of mean effective stress of saturated soil. For this reason, shear yield is considered in here. The yield function for changes in the stress ratio is expressed as:

$$f = \overline{\eta}(\chi) - k = [(\eta_{ij} - \chi_{ij})(\eta_{ij} - \chi_{ij})]^{1/2} - k \tag{2.2.2}$$

where k is a numerical parameter which controls the size of the elastic region;

$\overline{\eta}(\chi)$ is relative stress ratio;

χ_{ij} is kinematic hardening parameter;

$\eta(\chi)_{ij}$ is stress ratio tensor and defined as $\eta_{ij} = s_{ij} / \sigma'_m$;

s_{ij} is deviatoric stress tensor and defined as $s_{ij} = \sigma'_{ij} - \sigma'_m \delta_{ij}$;

σ'_{ij} is effective stress tensor;

σ'_m Is mean effective stress.

Hardening Rule

The evolution equation for the hardening parameter is defined according to nonlinear kinematic hardening rule as:

$$d\chi_{ij} = B(Ade^P_{ij} - \chi_{ij} d\gamma^P) \tag{2.2.3}$$

where A, B are material hardening parameters. And can be expressed by the stress ratio at failure M_f, and the initial plastic shear modulus normalized to the mean effective stress G^P.

de^P_{ij} is the current plastic deviatoric strain, defined as

$$e^P_{ij} = \varepsilon^P_{ij} - \frac{1}{3}\varepsilon^P_{ij}\delta_{ij} \tag{2.2.4}$$

where ε^P_{ij} is plastic strain tensor.

$d\gamma^P$ is second invariant of plastic deviatoric strain increment de^P_{ij}, and defined as

$$d\gamma^P = (de^P_{ij} de^P_{ij})^{1/2} \tag{2.2.5}$$

In Eq.(2.2.3), the second term of right hand is the nonlinear term that depends on the magnitude of the increment of plastic shear strain. If it is neglected, Prager's linear kinematic hardening rule is derived from Eq.(2.2.3):

$$d\chi_{ij} = BA\, de^p_{ij} \tag{2.2.6}$$

Assuming in the undrained simple shear condition ($\sigma'_{12} \neq 0, e^p_{12} \neq 0$, and the values of other stress and strain are zero), Eq.(2.2.3) is integrated explicitly, the hardening rule is derived in an exponential function as

$$\chi_{12} = \frac{A}{\sqrt{2}}\left\{1 - \exp(-\sqrt{2}\, Be^p_{12})\right\} \tag{2.2.7}$$

If e^p_{12} becomes maximum, we get

$$\chi_{12}\big|_{e^p_{12}\to\infty} = \frac{A}{2} \tag{2.2.8}$$

And if e^p_{12} become minimum, the gradient of χ_{12} is rewritten as

$$\left.\frac{\chi_{12}}{e^p_{12}}\right|_{e^p_{12}\to 0} = AB \tag{2.2.9}$$

On the other hand, if with the assumption of simple shear condition, the hardening rule is derived in an hyperbolic function as

$$\eta_{12} = \frac{M_f G^p e_{12}^p}{M_f + \sqrt{2} G^p e_{12}^p} \tag{2.2.10}$$

If e_{12}^p becomes maximum, we get

$$\eta_{12}\big|_{e_{12}^p \to \infty} = \frac{M_f}{\sqrt{2}} \tag{2.2.11}$$

And if e_{12}^p become minimum, the gradient of η_{12} is rewritten as

$$\left.\frac{\eta_{12}}{e_{12}^p}\right|_{e_{12}^p \to 0} = G^p \tag{2.2.12}$$

Comparing Eq.(2.2.8) with Eq.(2.2.11) and Eq.(2.2.9) with Eq.(2.2.12), we get the relations between the hardening parameters A and B with the stress ratio at failure M_f, and the initial plastic shear modulus normalized to the mean effective stress G^P.

The relation of Prager's linear hardening rule Eq.(2.2.6), Eq.(2.2.7) and Eq.(2.2.10) in the simple shear strain condition are given in **Fig.2.1**. In this figure, A=2.0, B=250 and M_f=2.0, G^P=500.

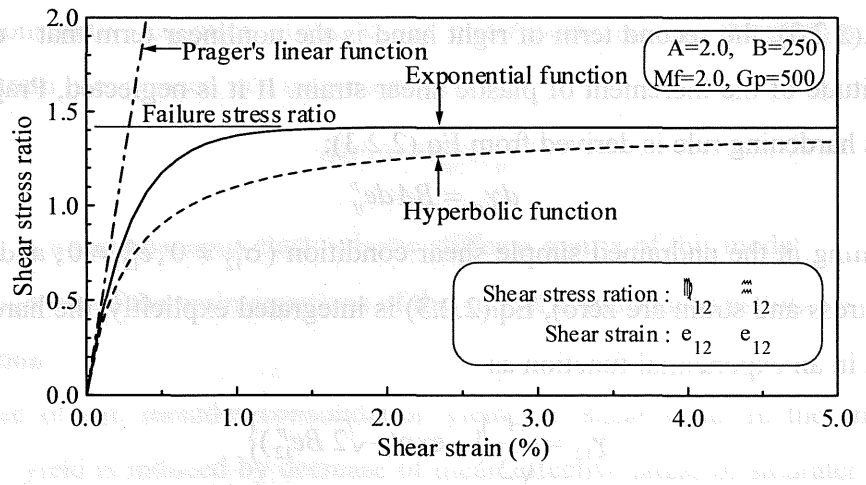

Fig.2.1 Hardening Function

To simulate the liquefaction behavior of saturated sand, the mean effective stress of sand should be made to 0 under the cyclic load. That means a reduction of shear parameter. A method for reducing shear parameter B is introduced as follows.

The method for reducing shear parameter B

The plastic shear stiffness depends on strain. It can simulate the increment of shear strain after the stress path across the phase changing line. This method is used to reducing the deviatoric plastic strain when stress path arrives the phase changing line.

$$B = \frac{B_0}{1+\gamma_{ap}^{P}/\gamma_r^{P}} \tag{2.2.13}$$

where B_0 is the initial value of B.

γ_{DA}^{p} is the value of γ^{P} after arriving phase changing line.

γ^{P} is plastic reference strain.

In the same way, elastic constants (Lame constant $\tilde{\lambda}$, $\tilde{\mu}$) are reduced as

$$\tilde{\lambda} = \frac{\tilde{\lambda}_0}{1+\gamma_{DA}^{p}/\gamma_r^{e}} \tag{2.2.14}$$

$$\tilde{\mu} = \frac{\tilde{\mu}_0}{1+\gamma_{DA}^{p}/\gamma_r^{e}} \tag{2.2.15}$$

This method is adapted to the complex states of stress in earthquake, and the numerical analysis results with it are stable.

Overconsolidation boundary surface

The overconsolidation boundary surface f_b=0 is defined as

$$f_b = \overline{\eta}_{(0)} + M_m \ln(\sigma'_m/\sigma'_{mb}) = 0 \tag{2.2.16}$$

where, Mm is the value of the stress ratio when the volume compression strain is maximum during shear deformation; $\overline{\eta}_{(0)}$ is the relative stress ratio after consolidation, it is defined as

$$\overline{\eta}_{(0)} = \{(\eta_{ij}-\eta_{ij(0)})(\eta_{ij}-\eta_{ij(0)})\}^{1/2} \tag{2.2.17}$$

where $\eta_{ij(0)}$ denotes the value of η_{ij} at the end of consolidation, and defined as

$$\eta_{ij(0)} = (s_{ij}/\sigma'_m)_{(0)} \tag{2.2.18}$$

The condition f_b<0 means that the stress state stays in an overconsolidation region, while $f_b \geq 0$ means that the stress state stays in a normally consolidated region. Herein, σ'_{mb} in Eq.(2.2.16) is denoted as

$$\sigma'_{mb} = \sigma'_{mbi}\exp\left(\frac{1+e}{\lambda-k}v^{p}\right) \tag{2.2.19}$$

where σ'_{mbi} is the initial value of σ'_{mb} and is equal to the value of $\sigma'_{m(0)}$, that is, the

mean effective stress at the end of consolidation. e is the initial void ratio, λ and κ are the compression index and the swelling index, respectively, and v^P is the volumetric plastic strain. Furthermore, σ'_{mc}, which is the effective mean stress at the intersection of the overconsolidated boundary surface and the σ'_m axis, is defined as

$$\sigma'_{mc} = \sigma'_{mbi} exp\left(\frac{\eta_{(0)}}{M_m}\right) \tag{2.2.20}$$

Plastic potential function

Based on the relationship between the stress ratio and the increment of plastic strain, the plastic potential function is denoted as

$$g = [(\eta_{ij} - \chi_{ij})(\eta_{ij} - \chi_{ij})]^{1/2} + \tilde{M} ln(\frac{\sigma'_m}{\sigma'_{ma}}) = 0 \tag{2.2.21}$$

where σ '$_{ma}$ is a constant; $\tilde{M}$ is a variable depending on the stress state, it controls the direction of the plastic strain increment. It is defined by

$$\tilde{M} = \begin{cases} M_m & f_b \geq 0 \\ -\dfrac{\eta}{\ln(\sigma'_m / \sigma'_{mc})} & f_b < 0 \end{cases} \tag{2.2.22}$$

where η is stress ratio, $\eta = (\eta_{ij}\eta_{ij})^{1/2} = \dfrac{\sqrt{2J_2}}{\sigma'_m}$, and J_2 is second invariant of deviatoric stress. $\tilde{M}$ controls the direction of the plastic strain increment. When the stress state is inside the overconsolidated region, $\tilde{M}$ takes a value that is less than that of M_m.

The plastic potential function and the overconsolidation boundary surface are shown in **Fig.2.2**.

Flow rule

The floe rule is given as

$$d\varepsilon_{ij}^P = H_{ijkl} \frac{\partial g}{\partial \sigma'_{kl}} \tag{2.2.23}$$

where, H_{ijkl} is a fourth-rank isotropic tensor:

$$H_{ijkl} = a\delta_{ij}\delta_{kl} + b(\delta_{ik}\delta_{jl} + \delta_{il}\delta_{jk}) \tag{2.2.24}$$

where a and b are the parameters depending on the states of stress and strain. From Eq.(2.2.23) and Eq.(2.2.24), deviatoric strain increment tensor de_{ij}^P and plastic column strain increment dv^P are obtained as

$$de_{ij}^{P} = 2b\frac{\partial g}{\partial s_{ij}} \tag{2.2.25}$$

$$dv^{P} = d\varepsilon_{kk}^{P} = (3a+2b)\frac{\partial g}{\partial \sigma'_{m}} \tag{2.2.26}$$

$$\frac{\partial g}{\partial \sigma'_{ij}} = \frac{\eta_{ij}-\chi_{ij}}{\eta(\chi)\sigma'_{m}} + \{\tilde{M} - \frac{\eta_{mn}(\eta_{mn}-\chi_{mn})}{\overline{\eta}(\chi)}\}\frac{\delta_{ij}}{3\sigma'_{m}} \tag{2.2.27}$$

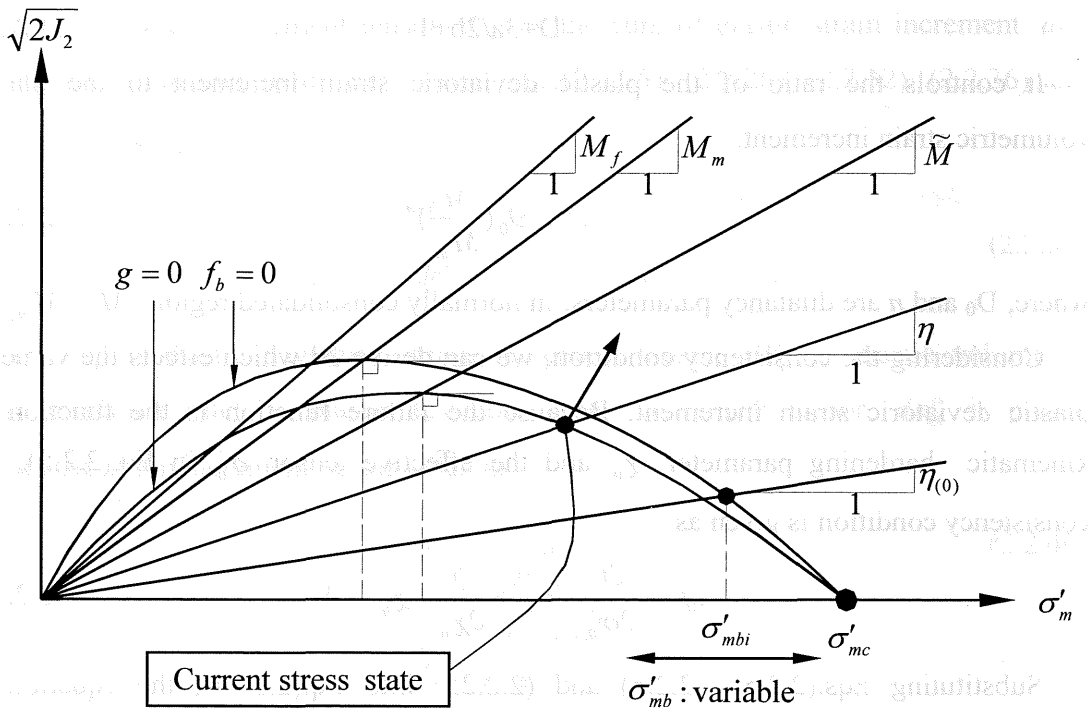

Fig.2.2 Plastic potential function and overconsolidation boundary surface

From Eqs.(2.2.5), (2.2.25) and (2.2.27), we can get the second invariant of plastic deviatoric strain as:

$$d\gamma^{P} = 2b\frac{1}{\sigma'_{m}} \tag{2.2.28}$$

From Eqs.(2.2.26) and (2.2.27), we can get the plastic volumetric strain increment:

$$dv^{P} = (3a+2b)(\tilde{M} - \tilde{\eta}(\chi))\frac{1}{\sigma'_{m}} \tag{2.2.29}$$

where, $\tilde{\eta}(\chi)$ is defined as

$$\tilde{\eta}(\chi) = \frac{\eta_{mn}(\eta_{mn} - \chi_{mn})}{\overline{\eta}(\chi)} \tag{2.2.30}$$

From Eqs.(2.2.28) and (2.2.29), the relation between stress and dilatancy is obtained:

$$\frac{dv^P}{d\gamma^P} = D(\tilde{M} - \tilde{\eta}(\chi)) \tag{2.2.31}$$

where, D is so-called coefficient of dilatancy and defined by

$$D=3a/2b+1 \tag{2.2.32}$$

It controls the ratio of the plastic deviatoric strain increment to the plastic volumetric strain increment.

$$D = D_0(\frac{\tilde{M}}{M_m})^n \tag{2.2.33}$$

where, D_0 and n are dilatancy parameters. In normally consolidated region $\tilde{M} = M_m$

Considering the consistency condition, we can derive 2d which effects the value of plastic deviatoric strain increment. Because the failure function is the function of kinematic hardening parameter χ_{ij} and the effective tensor σ'_{ij} in Eq.(2.2.2), the consistency condition is given as

$$df = \frac{\partial f}{\partial \sigma'_{ij}} d\sigma'_{ij} + \frac{\partial f}{\partial \chi_{ij}} d\chi_{ij} = 0 \tag{2.2.34}$$

Substituting Eqs.(2.2.5), (2.2.6) and (2.2.25) into Eq.(2.2.34), the equation to evaluate 2b is obtained

$$2b = \frac{\frac{\partial f}{\partial \sigma'_{ij}} d\sigma'_{ij}}{B\frac{\partial f}{\partial \chi_{mn}}\{\chi_{mn}(\frac{\partial g}{\partial s_{kl}}\frac{\partial g}{\partial s_{kl}})^{1/2} - A\frac{\partial g}{\partial s_{mn}}\}} = h\frac{\partial f}{\partial \sigma'_{ij}} d\sigma'_{ij} \tag{2.2.35}$$

where h is hardening coefficient

Elastic strain increment.

The elastic deviatoric strain increment tensor is given as

$$de^e_{ij} = \frac{1}{2\tilde{\mu}} ds_{ij} \tag{2.2.36}$$

where elastic shear coefficient $\tilde{\mu}$ is calculated by Eq.(2.2.15). $\tilde{\mu}_0$ in Eq.(2.2.15) is assumed to be proportional to the mean effective stress.

$$\tilde{\mu}_0 = \frac{G_0}{\sigma'_{m0}}\sigma'_m \tag{2.2.37}$$

where G_0 is initial elastic shear coefficient, is initial mean effective stress. The elastic volumetric strain increment is calculated by

$$dv^e = d\varepsilon^e_{kk} = \frac{\kappa}{(1+e)\sigma'_m}d\sigma'_m = \frac{1}{K}d\sigma'_m \tag{2.2.38}$$

where κ is swelling index., K is volumetric elastic coefficient.

The total strain increment tensor $d\varepsilon_{ij}$ is the sum of elastic strain increment $d\varepsilon^e_{ij}$ and plastic strain increment $d\varepsilon^p_{ij}$. From Eqs.(2.2.25), (2.2.26), (2.2.32), (2.2.36) and (2.2.39), we can get:

$$\begin{aligned} d\varepsilon_{ij} &= d\varepsilon^e_{ij} + d\varepsilon^p_{ij} \\ &= de^e_{ij} + \frac{1}{3}\delta_{ij}d\varepsilon^e_{kk} + de^p_{ij} + \frac{1}{3}\delta_{ij}d\varepsilon^p_{kk} \end{aligned} \tag{2.2.39}$$

where, de^e_{ij} is elastic deviatoric strain increment tensor, $d\varepsilon^e_{kk}$ is elastic volumetric strain increment, de^p_{ij} is plastic deviatoric strain increment tensor, $d\varepsilon^p_{kk}$ is plastic volumetric strain increment tensor given as

$$de^e_{ij} = \frac{1}{2\tilde{\mu}}ds_{ij} \tag{2.2.40}$$

$$d\varepsilon^e_{kk} = \frac{k}{1+e_0}\frac{d\sigma'_m}{\sigma'_m} \tag{2.2.41}$$

$$de^p_{ij} = 2b\frac{\partial g}{\partial s_{ij}} = 2b\frac{\eta_{ij} - \chi_{ij}}{\overline{\eta}_{(\chi)}}\frac{1}{\sigma'_m} \tag{2.2.42}$$

$$d\varepsilon^p_{kk} = (3a+2b)\frac{\partial g}{\partial \sigma'_m} = (3a+2b)\frac{1}{\sigma'_m}\left\{\tilde{M} - \frac{\eta_{mn}(\eta_{mn} - \chi_{mn})}{\overline{\eta}_{(\chi)}}\right\} \tag{2.2.43}$$

The parameters of soil used in the equation are: void ratio e, compression index λ, dilatancy index κ,initial elastic shear coefficient G_0, failure stress ratio M_f, phase transformation ratio M_m, the initial value of kinematic hardening parameter B_0, the lowest value of kinematic parameter B_l, material parameter C_f for the control of decrease in kinematic hardening parameter B, dilatancy parameter D_0 and n, reference parameters γ^p_r and γ^e_r.Control parameter of anisotropy C_d. The initial stress state and the stress state of pre-consolidation are also needed in this equation. All parameters introduced above are test values. But usually, it is not easy to get the values of the

parameters from B_0 to C_d in test. In this case, these parameters are fitted by the comparison between the simulation curves and test curves.

Stress increment and strain increment relation

First, using elastic matrix, the relation of elastic strain increment and elastic stress increment is given as

$$d\sigma'_{ij} = D^e_{ijkl} d\varepsilon^e_{kl} = \tilde{\lambda} d\varepsilon^e_{kk}\delta_{ij} + 2\tilde{\mu} d\varepsilon^e_{ij} = (\tilde{\lambda} + \frac{2}{3}\tilde{\mu}) d\varepsilon^e_{kk}\delta_{ij} + 2\tilde{\mu} de^e_{ij} \tag{2.2.44}$$

where $\tilde{\lambda}$ is calculated by Eq.(2.2.14). $\tilde{\lambda}_0$ in Eq.(2.2.14) is calculated by

$$\tilde{\lambda}_0 = K - \frac{2}{3}\tilde{\mu}_0 = \frac{1+e}{\kappa}\sigma'_m - \frac{2}{3}\tilde{\mu}_0 \tag{2.2.45}$$

From Eqs.(2.2.25), (2.2.26) and (2.2.32), the plastic strain increment is calculated by

$$d\varepsilon^P_{ij} = 2b\frac{\partial g}{\partial s_{ij}} + D \cdot 2b\frac{\partial g}{\partial \sigma'_m}\frac{\delta_{ij}}{3} \tag{2.2.46}$$

The derivative of plastic potential function respected to stress is given as

$$\frac{\partial g'}{\partial \sigma'_{ij}} = \frac{\partial g}{\partial s_{ij}} + D\frac{\partial g}{\partial \sigma'_m}\frac{\delta_{ij}}{3} \tag{2.2.47}$$

From Eqs.(2.2.45) and (2.2.46), the plastic strain increment is expressed using the scalar hardening coefficient as

$$d\varepsilon = 2b\frac{\partial g'}{\partial \sigma'_{ij}} \tag{2.2.48}$$

From Eqs.(2.2.35) and (2.2.38), we can get:

$$2b = h\frac{\partial f}{\partial \sigma'_{ij}} D^e_{ijkl} d\varepsilon^e_{kl} \tag{2.2.49}$$

Substituting Eq.(2.2.39) into Eq.(2.2.49), we can get:

$$2b = h\frac{\partial f}{\partial \sigma'_{ij}} D^e_{ijkl} (d\varepsilon_{kl} - D\varepsilon^P_{kl}) \tag{2.2.50}$$

Substituting Eq.(2.2.48) into Eq.(2.2.50), we can get:

$$2b = h\frac{\partial f}{\partial \sigma'_{ij}} D^e_{ijkl} (d\varepsilon_{kl} - 2b\frac{\partial g}{\partial \sigma'_{kl}})$$

$$= \frac{\dfrac{\partial f}{\partial \sigma'_{ij}} D^e_{ijkl} d\varepsilon_{kl}}{\dfrac{1}{h} + \dfrac{\partial f}{\partial \sigma'_{mn}} D^e_{mnpq} \dfrac{\partial g'}{\partial \sigma'_{pq}}} \tag{2.2.51}$$

Substituting Eqs.(2.2.39) and (2.2.48) into Eq.(2.2.44), we can get stress increment and strain increment relation as

$$d\sigma'_{ij} = D^e_{ijkl}(d\varepsilon_{kl} - 2b\frac{\partial g'}{\partial \sigma'_{kl}}) \tag{2.2.52}$$

Substituting Eq.(2.2.52) into Eq.(2.2.51), the stress increment and strain increment relation is obtained as

$$d\sigma'_{ij} = D^{ep}_{ijkl} d\varepsilon_{kl}$$

$$= (D^e_{ijkl} - \frac{D^e_{ijmn} \dfrac{\partial g'}{\partial \sigma'_{mn}} \dfrac{\partial f}{\partial \sigma'_{pq}} D^e_{pqkl}}{\dfrac{1}{h} + \dfrac{\partial f}{\partial \sigma'_{mn}} D^e_{mnpq} \dfrac{\partial g'}{\partial \sigma'_{pq}}}) d\varepsilon_{kl} \tag{2.2.53}$$

where, D^{ep}_{ijkl} is elastic-plastic matrix. The elastic matrix is given as

$$[D^e] = \begin{bmatrix} \tilde{\lambda}+2\tilde{\mu} & \tilde{\lambda} & \tilde{\lambda} & 0 & 0 & 0 \\ \tilde{\lambda} & \tilde{\lambda}+2\tilde{\mu} & \tilde{\lambda} & 0 & 0 & 0 \\ \tilde{\lambda} & \tilde{\lambda} & \tilde{\lambda}+2\tilde{\mu} & 0 & 0 & 0 \\ 0 & 0 & 0 & 2\tilde{\mu} & 0 & 0 \\ 0 & 0 & 0 & 0 & 2\tilde{\mu} & 0 \\ 0 & 0 & 0 & 0 & 0 & 2\tilde{\mu} \end{bmatrix} \tag{2.2.54}$$

The derivative of failure function respected to stress is derived from Eq.(2.2.1) as

$$\frac{\partial f}{\partial \sigma'_{ij}} = \frac{\partial f}{\partial s_{ij}} + \frac{\partial f}{\partial \sigma'_{ij}} \frac{\delta_{ij}}{3} = \frac{\eta_{ij} - \chi_{ij}}{\bar{\eta}(\chi)\sigma'_m} - \frac{(\eta_{kl} - \chi_{kl})\eta_{kl}}{\bar{\eta}(\chi)} \frac{\delta_{ij}}{3\sigma'_m} \tag{2.2.55}$$

The derivative of plastic potential function respected to stress derived from Eqs.(2.2.27) and (2.2.47) as

$$\frac{\partial g'}{\partial \sigma'_{ij}} = \frac{\partial g}{\partial s_{ij}} + D\frac{\partial g}{\partial \sigma'_m} \frac{\delta_{ij}}{3} = \frac{\eta_{ij} - \chi_{ij}}{\bar{\eta}(\chi)\sigma'_m} + D(\tilde{M} - \frac{(\eta_{kl} - \chi_{kl})\eta_{kl}}{\bar{\eta}(\chi)}) \frac{\delta ij}{3\sigma'_m} \tag{2.2.56}$$

The reciprocal of the hardening coefficient is given as

$$\frac{1}{h} = B\frac{\partial f}{\partial \chi_{ij}} \{\chi_{ij} (\frac{\partial g}{\partial s_{kl}} \frac{\partial g}{\partial s_{kl}})^{1/2} - A\frac{\partial g}{\partial s_{ij}}\} \tag{2.2.57}$$

2.3 Updated Lagrangian Formulation Applied to 3-D FE-FD Analysis of Porous Media of Which the Constitutive Equation Defined by Elasto-Plastic Model

A FE-FD coupled method (Oka et al, 1991 and 1994) has been proposed for liquefaction analysis of saturated soils. In the space domain, the equilibrium equation for fluid-saturated soil is discretized by the finite element method, and terms associated with excess pore pressure in the continuity equation are discretized by the finite difference method. This method can reduce the total degrees of freedom of the coupled equations and avoid shear locking under the undrained condition. The method is extended in two dimensional problem based on the updated Lagrangian method (Sato and Di, 2003 and 2004) to deal with the large deformation due to liquefaction caused by large earthquake. Resulting equations of the coupled system are solved incrementally with the time step Δt. In this section, the principle of this method are introduced and the derivation of the three dimensional equations of this method are derived with updated Lagrangian formulation. The left superscripts of a quantity here indicate the configuration at which this quantity occurs.

2.3.1 Conception of Updated Lagrangian Method for Porous Media

First, the principle of updated Lagrangian method and the definition of the important variables used here are introduced as follows.

Consider large displacements of a porous deformable soil body composed of a skeleton with a fluid flowing through its pore space. A fixed rectangular frame with a Cartesian coordinate system describes the motion from the reference configuration at some time, t, to the current configuration at time $t + dt$. As shown in **Fig.2.3**, the porous body occupies a region in space, ${}^{t}V$, bounded by a surface, ${}^{t}A$, at time t, and a material point position of the soil skeleton is represented by X_i. At some later time, $t + dt$, the porous body will have moved to the region. ${}^{t+dt}V$ bounded by the surface ${}^{t+dt}A$ at time $t + dt$. x_i corresponds to the position of skeleton particle X_i in the current

configuration after deformation,

$$x_i = X_i + u_i \tag{2.3.1}$$

The quantity u_i represents displacement of the skeleton measured relative to the position of the body at time t. The soil skeleton deformation gradient is

$$\mathbf{F} = \frac{\partial x_i}{\partial X_j} \tag{2.3.2}$$

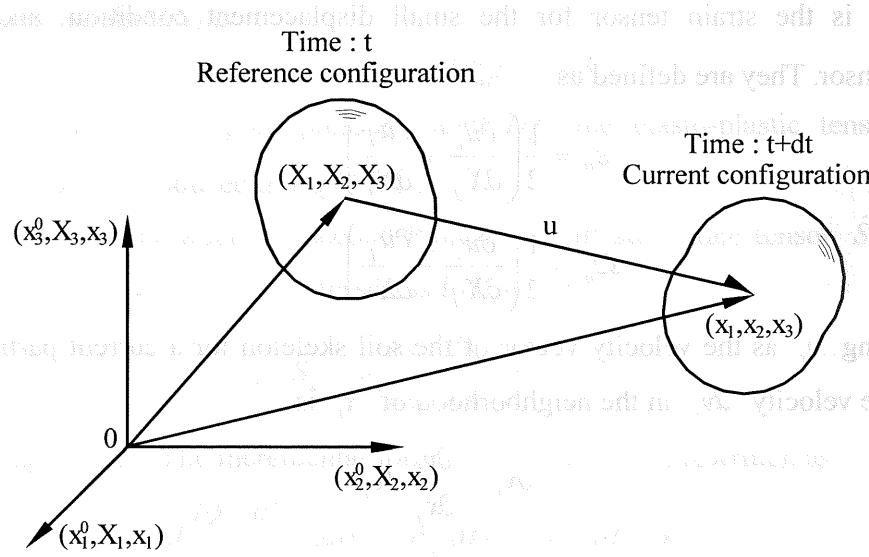

Fig.2.3 Motion and configuration of soil

Vector $d\mathbf{X}$ at point $\mathbf{X}$ in the reference configuration and $d\mathbf{x}$ at point $\mathbf{x}$ in the current configuration are related by

$$d\mathbf{x} = \mathbf{F}d\mathbf{X} \tag{2.3.3}$$

From this equation, the volume change between the reference and current configurations is

$$d^{t+dt}V = det\,\mathbf{F}\,d^tV = Jd^tV \tag{2.3.4}$$

where J is the Jacobian determination of the deformation gradient tensor.

The Lagrangian stain tensor, $\mathbf{E}$, is expressed by

$$E_{ij} = \frac{1}{2}\left(\frac{\partial u_i}{\partial X_j} + \frac{\partial u_j}{\partial X_i} + \frac{\partial u_k}{\partial X_i}\frac{\partial u_k}{\partial X_j}\right) = \varepsilon_{ij} + \eta_{ij} \tag{2.3.5}$$

where the small subscript after a comma denotes the partial derivative with respect to the reference coordinate X_i; ε_{ij} is the linear part of strain; η_{ij} the nonlinear part and

defined by $\eta_{ij} = \frac{1}{2}\frac{\partial u_k}{\partial X_i}\frac{\partial u_k}{\partial X_j}$.

The displacement gradient tensor $\frac{\partial u_i}{\partial X_j}$ is decomposed into the sum of the symmetrical part ε_{ij}, and skew-symmetric part Ω_{ij};

$$\frac{\partial u_i}{\partial X_j} = \frac{1}{2}\left(\frac{\partial u_i}{\partial X_j} + \frac{\partial u_j}{\partial X_i}\right) + \frac{1}{2}\left(\frac{\partial u_i}{\partial X_j} - \frac{\partial u_j}{\partial X_i}\right) = \varepsilon_{ij} + \Omega_{ij} \tag{2.3.6}$$

where ε_{ij} is the strain tensor for the small displacement condition, and Ω_{ij} the rotation tensor. They are defined as

$$\varepsilon_{ij} = \frac{1}{2}\left(\frac{\partial u_i}{\partial X_j} + \frac{\partial u_j}{\partial X_i}\right) \tag{2.3.7}$$

$$\Omega_{ij} = \frac{1}{2}\left(\frac{\partial u_i}{\partial X_j} - \frac{\partial u_j}{\partial X_i}\right) \tag{2.3.8}$$

Defining v_i as the velocity vector of the soil skeleton for a current particle at x_i, the relative velocity dv_i in the neighborhood of x_i is

$$dv_i = \frac{\partial v_i}{\partial x_j} dx_j \tag{2.3.9}$$

where $\frac{\partial v_i}{\partial x_j}$ is the velocity gradient expressed as the sum of the symmetric rate of the deformation tensor l_{ij} plus the antisymmetric spin tensor ω_{ij};

$$\frac{\partial v_i}{\partial x_j} = \frac{1}{2}\left(\frac{\partial v_i}{\partial x_j} + \frac{\partial v_j}{\partial x_i}\right) + \frac{1}{2}\left(\frac{\partial v_i}{\partial x_j} + \frac{\partial v_j}{\partial x_i}\right) = l_{ij} + \omega_{ij} \tag{2.3.10}$$

2.3.2 Constitutive equation

In this research, the effective cyclic elasto-plastic constitutive model is used to describe the non-linear behavior of saturated soils. The rate of deformation tensor is suitable for the application to a constitutive law because it vanishes when the body exhibits a rigid-body motion. Thus, the stress rate used for a constitutive law must be invariant with respect to the rigid-body rotation. The material derivative $d\sigma_{ij}/dt$ does not in general satisfy the invariance by a rigid-body rotation. To extend this model to a large deformation problem, for the constitutive relations it is necessary to use an

invariant stress rate with respect to rigid-body rotation. The Jaumann effective stress rate, an objective measure of the stress rate, was adopted for the present formulation;

$$\dot{\sigma}'^{J}_{ij} = \dot{\sigma}'_{ij} - \sigma'_{ik}\omega_{jk} - \sigma'_{kj}\omega_{ik} \tag{2.3.11}$$

where σ'_{ij} is the effective Cauchy stress, and $\dot{\sigma}'_{ij}$ the effective Cauchy stress rate. Another expression in the incremental form is given as

$$d\sigma'^{J}_{ij} = d\sigma'_{ij} - \sigma'_{ik}\Omega_{jk} - \sigma'_{kj}\Omega_{ik} \tag{2.3.12}$$

The linear relationship between the objective stress and deformation rates (i.e., the effective stress-strain law) is

$$\dot{\sigma}^{J}_{ij} = \dot{\sigma}'^{J}_{ij} - \dot{p}\delta_{ij} = D^{ep}_{ijkl}l_{kl} - \dot{p}\delta_{ij} \tag{2.3.13}$$

where $\dot{p}$ is the rate of pore pressure, and D^{ep}_{ijkl} the elasto-plastic tensor of the constitutive model introduced in Eq.(2.2.1).

The relationship between the second Piola-kirchhoff stress rate tensor $\dot{S}_{ij}$ and the Causy stress rate tensor $\dot{\sigma}_{ij}$ is expressed as follows.

$$\dot{S}_{ij} = J\frac{\partial X_i}{\partial x_k}\frac{\partial X_j}{\partial x_l}\dot{\sigma}_{kl} \tag{2.3.14}$$

Using Eq.(2.3.12), The incremental form of this equation is rewritten as

$$dS_{ij} = J\frac{\partial X_i}{\partial x_k}\frac{\partial X_j}{\partial x_l}\left(d\sigma^{J}_{ij} + \sigma_{kl}d\Omega_{lm} + \sigma_{ml}d\Omega_{kl}\right)\dot{\sigma}_{kl} \tag{2.3.15}$$

Generally, large deformation cannot be expressed linearly in terms of displacements, because the elastic and plastic parts of the deformation rate are not summable. If each time step of updated Lagrangian analysis is small enough, the total Lagrangian strain rate $\dot{E}_{ij}$ can be decomposed into the elastic component, $\dot{E}^{e}_{ij}$, and the plastic component, $\dot{E}^{p}_{ij}$.

$$\dot{E}_{ij} = \dot{E}^{e}_{ij} + \dot{E}^{p}_{ij} \tag{2.3.16}$$

2.3.3 Equilibrium Equation

Motion of the soil skeleton based on the Lagrangian description, and motion of fluid based on the pseudo-displacement ω_i relative to the skeleton of soil were described. The average seepage velocity $\dot{\omega}_i$ is given by

$$\dot{\omega}_i = n\left(v^{f}_{i} - v^{s}_{i}\right) \tag{2.3.17}$$

where v^{s}_{i} is the velocity of the soil skeleton and v^{f}_{i} the velocity of the fluid phase.

The average acceleration of the fluid phase is expressed by

$$\dot{v}_i^f = \dot{v}_i^s + \frac{1}{n}\left(\frac{\partial \dot{w}_i}{\partial t} + \dot{w}_k \dot{w}_{i,k}\right) \tag{2.3.18}$$

The local equilibrium equation of motion for the total saturated porous media is

$$\frac{\partial \sigma_{ji}}{\partial x_j} + \rho b_i - (1-n)\rho^s \dot{v}_i^s - n\rho^f \dot{v}_i^f = 0 \tag{2.3.19}$$

Substituting Eq.(2.3.18), Eq.(2.3.19) is rewritten as

$$\frac{\partial \sigma_{ji}}{\partial x_j} + \rho b_i - \rho \ddot{u}_i - \rho^f \left(\frac{\partial \dot{w}_i}{\partial t} + \dot{w}_k \dot{w}_{i,k}\right) = 0 \tag{2.3.20}$$

where σ_{ij} is the Cauchy total stress in the combined solid and fluid mixture, and b_i the body force acceleration.

For the pore fluid, the equation of motion is

$$-\frac{\partial (np)}{\partial x_i} + n\rho^f b_i + R_i - n\rho^f \dot{v}_i^f = 0 \tag{2.3.21}$$

where p is the pore pressure (taken as positive when compressive), and R_i the viscous drag force acting on the fluid phase by the soil skeleton, which according to Darcy's law can be written as

$$R_i = -n\frac{\gamma^f}{k_{ij}}\dot{w}_j \tag{2.3.22}$$

where k_{ij} is the Darcy permeability coefficient. In isotropic condition, k_{ij} is a constant k, Darcy's law is rewritten as

$$R_i = -n\frac{\gamma^f}{k}\dot{w}_i \tag{2.3.23}$$

where γ^f is the unit weight of the fluid.

Substituting Eqs.(2.3.18) and (2.3.23) into Eq.(2.3.21) gives

$$\frac{\partial (np)}{\partial x_i} - n\rho^f b_i + n\gamma^f k_{ij}^{-1}\dot{w}_i + \rho^f \left(n\ddot{u}_i + (\frac{\partial \dot{w}_i}{\partial t} + \dot{w}_k \frac{\partial \dot{w}_i}{\partial x_k})\right) = 0 \tag{2.3.24}$$

We assume that the acceleration relative of the fluid phase to the soil skeleton can be neglected. The u-p approximation (Zienkiewicz et al., 1982 and 1984) is valid for low frequency problem of dynamic analysis. The equations of motion for the total mixture given by Eq.(2.3.20) can be simplified to

$$\frac{\partial \sigma_{ij}}{\partial x_j} + \rho b_i - \rho \ddot{u}_i = 0 \tag{2.3.25}$$

and the pore fluid motion equation (2.3.24) is rewritten as

$$\frac{\partial(np)}{\partial x_i} - n\rho^f b_i + n\gamma^f k^{-1}\dot{w}_i + n\rho^f \ddot{u}_i = 0 \tag{2.3.26}$$

Defining the excess pore pressure p_E, by

$$\frac{\partial(np - np_E)}{\partial x_i} = n\rho^f b_i, \tag{2.3.27}$$

Eq.(2.3.26) becomes

$$\frac{\partial(np_E)}{\partial x_i} + n\gamma^f k^{-1}\dot{w}_i + n\rho^f \ddot{u}_i = 0 \tag{2.3.28}$$

From Eq.(2.3.28), we obtain

$$\dot{w}_i = -\frac{k}{\gamma^f}\left(\frac{1}{n}\frac{\partial(np_E)}{\partial x_i} + \rho^f \ddot{u}_i\right) \tag{2.3.29}$$

2.3.4 Continuity Equation

Consider any arbitrary deformed volume V, the total mass m^s of its soil particles, and the total mass m^f of its fluid given of densities by the volume integrals;

$$m^s = \int_V (1-n)\rho^s dv \tag{2.3.30}$$

$$m^f = \int_V n\rho^f dv \tag{2.3.31}$$

According to the law of mass conservation, the material time derivatives of these masses are zero. For the soil skeleton, the derivative is

$$\dot{m}^s = \int_V \left(\frac{\partial\left(\rho^s(1-n)\right)}{\partial t} + \frac{\partial\left(\rho^s(1-n)v_i^s\right)}{\partial x_i}\right)dv = 0 \tag{2.3.32}$$

With the localization

$$\frac{\partial\left(\rho^s(1-n)\right)}{\partial t} + \frac{\partial\left(\rho^s(1-n)v_i^s\right)}{\partial x_i} = 0 \tag{2.3.33}$$

Similarly, for the fluid it is

$$\dot{m}^f = \int_V \left(\frac{\partial\left(n\rho^f\right)}{\partial t} + \frac{\partial\left(n\rho^f v_i^f\right)}{\partial x_i}\right)dv = 0 \tag{2.3.34}$$

With the localization

$$\frac{\partial\left(n\rho^f\right)}{\partial t}+\frac{\partial\left(n\rho^f v_i^f\right)}{\partial x_i}=0 \tag{2.3.35}$$

After manipulation (Oka, et al., 1994), Eqs.(2.3.33) and (2.3.35) give

$$\frac{\partial \dot{w}_i}{\partial x_i}+\frac{\partial v_i^s}{\partial x_i}+n\frac{\dot{\rho}^f}{\rho^f}+(1-n)\frac{\dot{\rho}^s}{\rho^s}=0 \tag{2.3.36}$$

which can be rewritten as

$$\frac{\partial \dot{w}_i}{\partial x_i}+l_{ii}+n\frac{\dot{\rho}^f}{\rho^f}+(1-n)\frac{\dot{\rho}^s}{\rho^s}=0 \tag{2.3.37}$$

where l_{ij} is the symmetric rate of the deformation tensor. ρ^s is constant and $\dot{\rho}^s$ is zero since skeletons in soils are assumed to be incompressible., $\dot{\rho}^f$ is the material derivative of the fluid phase density related to the material derivative $\dot{p}_E$ of the excess pore pressure by

$$\dot{\rho}^f=\frac{\dot{p}_E}{K^f}\rho^f \tag{2.3.38}$$

where K^f is the bulk modulus of the fluid phase.

Substituting Eq.(2.3.38) in Eq.(2.3.37), gives

$$\frac{\partial \dot{w}_i}{\partial x_i}+l_{ii}+\frac{n}{K^f}\dot{P}_E=0 \tag{2.3.39}$$

From Eq.(2.3.29), the sum of the partial derivatives of $\dot{w}_i$ with respect to the coordinate x_i is

$$\frac{\partial \dot{w}_i}{\partial x_i}=-\frac{k}{g}\left(\dot{l}_{ii}+\frac{1}{\rho^f}\left(\frac{\partial^2 p_E}{\partial^2 x_i}\right)_i\right) \tag{2.3.40}$$

$$-\frac{k}{g}\left(\frac{1}{n\rho^f}\frac{\partial p_E}{\partial x_i}-\frac{1}{\left(\rho^f\right)^2}\frac{\partial p_E}{\partial x_i}\frac{\partial \rho^f}{\partial x_i}+\frac{p_E}{n\rho^f}\left(\frac{\partial^2 n}{\partial^2 x_i}\right)-\frac{p_E}{n\left(\rho^f\right)^2}\frac{\partial n}{\partial x_i}\frac{\partial \rho^f}{\partial x_i}-\frac{p_E}{n^2\rho^f}\frac{\partial n}{\partial x_i}\frac{\partial n}{\partial x_i}\right)$$

Form Eq.(2.3.38),

$$\frac{\partial p_E}{\partial x_i}=K^f\frac{\partial\left(\ln\rho^f\right)}{\partial x_i} \tag{2.3.41}$$

Substituting it in Eq.(2.3.40) gives

$$\frac{\partial \dot{w}_i}{\partial x_i} = -\frac{k}{g}\left(\dot{l}_{ii} + \frac{1}{\rho^f}\left(\frac{\partial^2 p_E}{\partial^2 x_i}\right)_i\right) \tag{2.3.42}$$

$$-\frac{k}{g\rho^f}\left(\left(K^f - p_E\right)\frac{\partial(\ln n)}{\partial x_i}\frac{\partial(\ln \rho^f)}{\partial x_i} - K^f\left(\frac{\partial(\ln \rho^f)}{\partial x_i}\right)^2 + p_E\left(\frac{\partial^2(\ln n)}{\partial x_i}\right)_i\right)$$

where g is the acceleration caused by gravity.

If the gradients of ln(n) and $\ln(\rho^f)$ are so small that their quadratic terms in the above expressions can be ignored, then

$$\frac{\partial \dot{w}_i}{\partial x_i} = -\frac{k}{g}\left(\dot{l}_{ii} + \frac{1}{\rho^f}\left(\frac{\partial^2 p_E}{\partial^2 x_i}\right)_i + \frac{p_E}{\rho^f}\left(\frac{\partial^2(\ln n)}{\partial x_i^2}\right)_i\right) \tag{2.3.44}$$

The distribution of porosity is assumed to be smooth enough in the soils, therefore satisfying

$$\left(\frac{\partial^2(\ln n)}{\partial x_i^2}\right)_i = 0 \tag{2.3.45}$$

Then Eq.(2.3.44) is expressed by

$$\frac{\partial \dot{w}_i}{\partial x_i} = -\frac{k}{g}\left(\dot{l}_{ii} + \frac{1}{\rho^f}\left(\frac{\partial^2 p_E}{\partial^2 x_i}\right)_i\right) \tag{2.3.46}$$

Finally, substituting Eq.(2.3.46) in Eq.(2.3.39), the final form of the continuity equation is

$$\frac{k}{g}\dot{l}_{ii} - l_{ii} + \frac{k}{\gamma^f}\left(\frac{\partial^2 p_E}{\partial^2 x_i}\right)_i - \frac{n}{K^f}\dot{p}_E = 0 \tag{2.3.47}$$

Clearly, Eqs.(2.3.25) and (2.3.47) together with the constitutive law define a coupled set of equations for saturated soils, in which u_i and p_E are the only unknown variables.

2.3.5 The u-p Equations in Spatial Discrete Form

The equilibrium equation is satisfied at the end of each time step, $t + \Delta t$. In the updated Lagrangian method, the relevant quantities, such as stress and strain, are correlated with the reference configuration at time t, and the weak formulation of Eq.(2.3.25) is obtained

$$\int_v \rho \ddot{u}_i \delta v_i d^t V + \int_v \left(\int^{t+\Delta t} \dot{S}_{ij} dt \right) \delta \dot{E}_{ij} d^t V + \int_v {}^t\sigma_{ij} \delta \dot{E}_{ij} d^t V = {}^{t+\Delta t}\mathbf{F} \tag{2.3.48}$$

where ${}^t\sigma_{ij}$ is the Cauchy stress tensor at time t, and ${}^{t+\Delta t}\mathbf{F}$ the external virtual work done by the applied body forces and tractions. Let ${}^{t+\Delta t}b_i$ be the force acceleration per unit volume and ${}^{t+\Delta t}t_i$ the traction, then ${}^{t+\Delta t}\mathbf{F}$ is

$${}^{t+\Delta t}\mathbf{F} = \int_{+\Delta t_A} {}^{t+\Delta t}t_i \delta v_i d^{t+\Delta t} A + \int_{+\Delta t_V} \rho^{t+\Delta t} b_i \delta v_i d^{t+\Delta t} V \tag{2.3.49}$$

Using Eqs.(2.3.13)-(2.3.15), the second Piola-Kirchhoff stress rate can be approximated in the following form.

$$\dot{S}_{ij} = (D_{ijkl} + \psi_{ijkl}) \dot{E}_{kl} + \dot{p}\delta_{ij} \tag{2.3.50}$$

where is the 4th-order tensor (Chen and Mizuno, 1990) given as

$$\psi = \begin{bmatrix} -\sigma_{11} & \sigma_{11} & \sigma_{11} & -\sigma_{12} & 0 & -\sigma_{13} \\ \sigma_{22} & -\sigma_{22} & \sigma_{22} & -\sigma_{12} & -\sigma_{23} & 0 \\ \sigma_{33} & \sigma_{33} & -\sigma_{33} & 0 & -\sigma_{23} & -\sigma_{13} \\ 0 & 0 & \bar{\sigma}_{12} & -\frac{1}{2}(\sigma_{11}+\sigma_{22}) & -\frac{1}{2}\sigma_{13} & -\frac{1}{2}\sigma_{23} \\ \sigma_{23} & 0 & 0 & -\frac{1}{2}\sigma_{13} & -\frac{1}{2}(\sigma_{22}+\sigma_{33}) & -\frac{1}{2}\sigma_{12} \\ 0 & \sigma_{13} & 0 & -\frac{1}{2}\sigma_{23} & -\frac{1}{2}\sigma_{12} & -\frac{1}{2}(\sigma_{11}+\sigma_{33}) \end{bmatrix} \tag{2.3.51}$$

By use of the standard finite element approach procedure, the displacement and velocity fields within an element are explained in terms of its nodal values;

$$\delta \mathbf{u} = \mathbf{N} \delta \mathbf{u}_\mathbf{N} \tag{2.3.52}$$

where $\mathbf{N}$ is the displacement shape function, and $\mathbf{u}_\mathbf{N}$ is the respective displacement at the nodes.

The incremental strain rates are

$$\delta \dot{\varepsilon} = \mathbf{B}_\mathbf{L} \delta \mathbf{v}_\mathbf{N} \tag{2.3.53}$$

$$\delta \dot{\eta} = \mathbf{B}_\mathbf{NL} \delta \mathbf{v}_\mathbf{N} \tag{2.3.54}$$

In the FEM-FDM method used, pore water pressure $\mathbf{p}_\mathbf{E}$ is defined at element's center of gravity, but is expressed as the value of a certain node of the element.

Substituting Eqs.(2.3.52)-(2.3.54) in Eq. (2.3.48), the weak form od equilibrium equation is derived as

$$\mathbf{M}\ddot{\mathbf{u}}_\mathbf{N} + (\mathbf{K}_\mathbf{L} + \mathbf{K}_\mathbf{NL}) \Delta \mathbf{u}_\mathbf{N} + \mathbf{Q}\mathbf{p}_\mathbf{E} = \mathbf{T} \tag{2.3.55}$$

where the mass matrix $\mathbf{M} = \int_V \rho \mathbf{N}^{\mathrm{T}} \mathbf{N} d^t V$;

$$\mathbf{K}_{\mathrm{L}} = \int_V \mathbf{B}_{\mathrm{L}}^{\mathrm{T}} (\mathbf{D} + \psi) \mathbf{B}_{\mathrm{L}} d^t V ;$$

$$\mathbf{K}_{\mathrm{NL}} = \int_V \mathbf{B}_{\mathrm{NL}}^{\mathrm{T}} \mathbf{A} \mathbf{B}_{\mathrm{NL}} d^t V ;$$

$$\mathbf{Q} = -\int_V \mathbf{B}_{\mathrm{V}}^{\mathrm{T}} d^t V$$

$$\mathbf{T} = {}^{t+\Delta t}\mathbf{F} - \int_V \mathbf{B}_{\mathrm{L}}^{\mathrm{T}} {}^{t}\sigma' d^t V$$

where ${}^{t}\sigma'$ is the effective stress vector at time t, and

$$\mathbf{B}_{\mathrm{NL}} = \begin{bmatrix}
N_{1,1} & 0 & 0 & N_{2,1} & 0 & 0 & \cdots & N_{8,1} & 0 & 0 \\
0 & N_{1,2} & 0 & 0 & N_{2,2} & 0 & \cdots & 0 & N_{8,2} & 0 \\
0 & 0 & N_{1,3} & 0 & 0 & N_{2,3} & \cdots & 0 & 0 & N_{8,3} \\
N_{1,2} & N_{1,1} & 0 & N_{2,2} & N_{2,1} & 0 & \cdots & N_{8,2} & N_{8,1} & 0 \\
0 & N_{1,3} & N_{1,2} & 0 & N_{2,3} & N_{2,2} & \cdots & 0 & N_{8,3} & N_{8,2} \\
N_{1,3} & 0 & N_{1,1} & N_{2,3} & 0 & N_{2,1} & \cdots & N_{8,3} & 0 & N_{8,1} \\
\frac{1}{2}N_{1,2} & -\frac{1}{2}N_{1,1} & 0 & \frac{1}{2}N_{2,2} & -\frac{1}{2}N_{2,1} & 0 & \cdots & \frac{1}{2}N_{8,2} & -\frac{1}{2}N_{8,1} & 0 \\
0 & \frac{1}{2}N_{1,3} & -\frac{1}{2}N_{1,2} & 0 & \frac{1}{2}N_{2,3} & -\frac{1}{2}N_{2,2} & \cdots & 0 & \frac{1}{2}N_{8,3} & -\frac{1}{2}N_{8,2} \\
-\frac{1}{2}N_{1,3} & 0 & \frac{1}{2}N_{1,1} & -\frac{1}{2}N_{2,3} & 0 & \frac{1}{2}N_{2,1} & \cdots & -\frac{1}{2}N_{8,3} & 0 & \frac{1}{2}N_{8,1}
\end{bmatrix} \tag{2.3.56}$$

$$\mathbf{A} = \begin{bmatrix}
\sigma_{11} & 0 & 0 & \frac{1}{2}\sigma_{12} & 0 & \frac{1}{2}\sigma_{13} & \sigma_{12} & 0 & -\sigma_{13} \\
 & \sigma_{22} & 0 & \frac{1}{2}\sigma_{21} & \frac{1}{2}\sigma_{23} & 0 & -\sigma_{21} & \sigma_{23} & 0 \\
 & & \sigma_{33} & 0 & \frac{1}{2}\sigma_{32} & \frac{1}{2}\sigma_{31} & 0 & -\sigma_{32} & \sigma_{31} \\
 & & & \frac{1}{2}s_{12} & \frac{1}{4}\sigma_{13} & \frac{1}{4}\sigma_{23} & \frac{1}{2}\tau_{21} & \frac{1}{2}\sigma_{13} & -\frac{1}{2}\sigma_{23} \\
 & & & & \frac{1}{2}s_{13} & \frac{1}{4}\sigma_{32} & -\frac{1}{2}\sigma_{13} & \frac{1}{2}\tau_{32} & \frac{1}{2}\sigma_{21} \\
 & & & & & \frac{1}{2}s_{13} & \frac{1}{2}\sigma_{32} & -\frac{1}{2}\sigma_{12} & \frac{1}{2}\tau_{13} \\
 & & & & & & 2s_{12} & -\sigma_{13} & -\sigma_{23} \\
 & & \textit{Symmtric} & & & & & 2s_{23} & -\sigma_{21} \\
 & & & & & & & & 2s_{31}
\end{bmatrix} \tag{2.3.57}$$

$$s_{ij} = \tfrac{1}{2}(\sigma_{ii} + \sigma_{jj})$$
$$\tau_{ij} = \tfrac{1}{2}(\sigma_{ii} - \sigma_{jj})$$

$$\mathbf{B}_{\mathrm{V}} = \{N_{1,1} \quad N_{1,2} \quad N_{1,3} \quad N_{2,1} \quad N_{2,2} \quad N_{2,3} \quad \cdots \quad N_{8,1} \quad N_{8,2} \quad N_{8,3}\} \tag{2.3.58}$$

Integrating Eq.(2.3.47) for element volume gives

$$\int_V \rho^f \dot{l}_{ii} d^t V - \int_V \frac{\gamma^f}{k} l_{ii} d^t V + \int_V \left(\frac{\partial^2 (p_E)}{\partial x_i^2} \right)_i d^t V - \int_V \frac{n\gamma^f}{kK_f} \dot{p}_E d^t V = 0 \qquad (2.3.59)$$

Substituting Eq.(2.3.43) in Eq.(2.3.46), gives

$$\rho^f \mathbf{Q}^{\mathrm{T}} \ddot{\mathbf{u}}_{\mathrm{N}} - \frac{\gamma^f}{k} \mathbf{Q}^{\mathrm{T}} \dot{\mathbf{u}}_{\mathrm{N}} - \int_V \left(\frac{\partial^2 (p_E)}{\partial x_i^2} \right)_i d^t V + \int_V \frac{n\gamma^f}{kK_f} \dot{p}_E d^t V \qquad (2.3.60)$$

By use of the FE-FE coupled method (Oka et al, 1991 and 1994), the derivative in the third term on left side of Eq.(2.3.59) can be replaced by a difference expression in terms of pore pressure values at the gravity centers of the element and neighboring elements (see **Fig.2.4**). In other words, the terms associated with excess pore pressure in Eq.(2.3.60) are discretized by the finite difference method in the space domain in a grid pattern that is name as the mesh for the finite element method. Using the Gauss theorem, the third term on the left side of Eq.(2.3.60) is expressed as

$$\int_V \nabla^2 p_E d^t V = \oint_A \frac{\partial p_E}{\partial x_i} n_i d^t A \qquad (2.3.61)$$

where ${}^tA$ is surface of the element and n_i the normal direction vector of ${}^tA$.

The value of partial derivative $\partial p_E / \partial x_i$ on the common boundary of two elements is approximated by a difference expression in terms of excess pore pressure values at the gravity centers of the element and adjacent elements. It is calculated by

$$\oint_A \frac{\partial p_E}{\partial x_i} n_i d^t A \approx p_E \sum_{i=1}^{6} \left(\mathbf{n}_\mathbf{i}^{\mathbf{A}} \cdot \mathbf{n}_\mathbf{i}^{\mathbf{E}} \right) A_i + \sum_{i=1}^{6} p_{Ei} \left(\mathbf{n}_\mathbf{i}^{\mathbf{A}} \cdot \mathbf{n}_\mathbf{i}^{\mathbf{Ei}} \right) A_i \qquad (2.3.62)$$

where p_E is the excess pore pressure value at the gravity centers of the element; p_{Ei} that of adjacent element; A_i area of joint surface between the element and its adjacent element i; $\mathbf{n}_\mathbf{i}^{\mathbf{A}}$ the normal direction vector of A_i; $\mathbf{n}_\mathbf{i}^{\mathbf{E}}$ the norm direction vector of dissipation from the element to its adjacent element i; $\mathbf{n}_\mathbf{i}^{\mathbf{Ei}}$ the norm direction vector of dissipation from its adjacent element i to the element as shown in **Fig.2.4**.

Using Eqs.(2.3.61) and (2.3.62), Eq.(2.3.59) then is rewritten as

$$\rho^f \mathbf{Q}^{\mathrm{T}} \ddot{\mathbf{u}}_{\mathrm{N}} - \frac{\gamma^f}{k} \mathbf{Q}^{\mathrm{T}} \dot{\mathbf{u}}_{\mathrm{N}} - \mathbf{H}\mathbf{p}_{\mathbf{E}} + \mathbf{L}\dot{\mathbf{p}}_{\mathbf{E}} = 0 \qquad (2.3.63)$$

where $\mathbf{Hp_E}$ is calculated by Eq.(2.3.62) and $\mathbf{L}\dot{\mathbf{p}}_{\mathbf{E}} = \int_V \frac{n\gamma^f}{kK_f} \dot{p}_E d^t V$. This is the weak form of continuity equation.

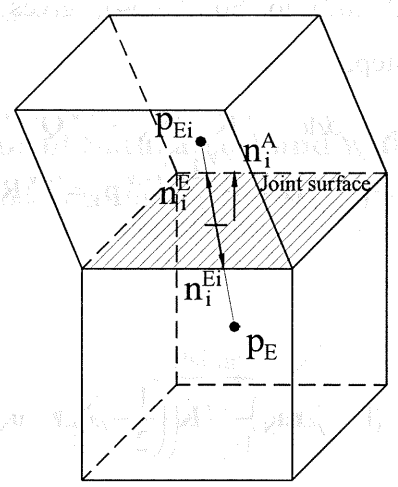

Fig.2.4 Dissipation pore water between elements

2.3.6 Discrete Equations in Time Domain with Newmark-β Method

Adding the Rayleigh damping, the complete FE-FD coupled method equations at time $t+\Delta t$ are given as

$$\begin{cases} {}^{t+\Delta t}\mathbf{M}\,{}^{t+\Delta t}\ddot{\mathbf{u}}_N + {}^{t+\Delta t}\mathbf{C}\,{}^{t+\Delta t}\dot{\mathbf{u}}_N + {}^{t+\Delta t}(\mathbf{K}_L + \mathbf{K}_{NL})\Delta\mathbf{u}_N + {}^{t+\Delta t}\mathbf{Q}\,{}^{t+\Delta t}\mathbf{p}_E = {}^{t+\Delta t}\mathbf{T} \\ \rho^f\,{}^{t+\Delta t}\mathbf{Q}^T\,{}^{t+\Delta t}\ddot{\mathbf{u}}_N - \dfrac{\gamma^f}{k}\,{}^{t+\Delta t}\mathbf{Q}^T\,{}^{t+\Delta t}\dot{\mathbf{u}}_N - {}^{t+\Delta t}\mathbf{H}\,{}^{t+\Delta t}\mathbf{p}_E + {}^{t+\Delta t}\mathbf{L}\,{}^{t+\Delta t}\dot{\mathbf{p}}_E = 0 \end{cases} \tag{2.3.64}$$

The Newmark method is used for the time domain integration, and the variables and their derivatives at time $t+\Delta t$ are expressed as functions of their values at time t (Zienkiewicz et al., 1990 and 1995);

$$\begin{aligned} {}^{t+\Delta t}\dot{\mathbf{u}}_N &= {}^{t}\dot{\mathbf{u}}_N + \Delta t\,{}^{t}\ddot{\mathbf{u}}_N + \gamma\Delta t\Delta\ddot{\mathbf{u}}_N \\ &= {}^{t}\dot{\mathbf{u}}_N + \Delta t(1-\gamma)\,{}^{t}\ddot{\mathbf{u}}_N + \gamma\Delta t\,{}^{t+\Delta t}\ddot{\mathbf{u}}_N \end{aligned} \tag{2.3.65}$$

$$\begin{aligned} \Delta\mathbf{u}_N &= {}^{t+\Delta t}\mathbf{u}_N - {}^{t}\mathbf{u}_N = \Delta t\,{}^{t}\dot{\mathbf{u}}_N + \frac{1}{2}\Delta t^2\,{}^{t}\ddot{\mathbf{u}}_N + \beta\Delta t^2\Delta\ddot{\mathbf{u}}_N \\ &= \Delta t\,{}^{t}\dot{\mathbf{u}}_N + \left(\frac{1}{2}-\beta\right)\Delta t^2\,{}^{t}\ddot{\mathbf{u}}_N + \beta\Delta t^2\,{}^{t+\Delta t}\ddot{\mathbf{u}}_N \end{aligned} \tag{2.3.66}$$

where γ and β are the parameters of this method.

Using difference in time domain, the velocity of pore water pressure is calculated by

$${}^{t+\Delta t}\dot{\mathbf{p}}_E = \frac{{}^{t+\Delta t}\mathbf{p}_E - {}^{t}\mathbf{p}_E}{\Delta t} \tag{2.3.67}$$

Substituting Eqs. (2.3.65)-(2.3.67) to Eq.(2.3.64), gives the discretized system of equations valid in each time step;

$$\begin{cases} {}^{t+\Delta t}\mathbf{M}\,{}^{t+\Delta t}\ddot{\mathbf{u}}_{\mathrm{N}} + \gamma\Delta t\,{}^{t+\Delta t}\mathbf{C}\,{}^{t+\Delta t}\ddot{\mathbf{u}}_{\mathrm{N}} + \beta\Delta t^{2}\,{}^{t+\Delta t}\mathbf{K}\,{}^{t+\Delta t}\ddot{\mathbf{u}}_{\mathrm{N}} + {}^{t+\Delta t}\mathbf{Q}\,{}^{t+\Delta t}\mathbf{p}_{\mathrm{E}} = {}^{t+\Delta t}\mathbf{R}_{\mathrm{u}} \\ {}^{t+\Delta t}\mathbf{Q}^{\mathrm{T}}\left(\rho^{f} - \frac{\gamma^{f}}{k}\gamma\Delta t\right){}^{t+\Delta t}\ddot{\mathbf{u}}_{\mathrm{N}} - \left({}^{t+\Delta t}\mathbf{H} + \frac{{}^{t+\Delta t}\mathbf{L}}{\Delta t}\right){}^{t+\Delta t}\mathbf{p}_{\mathrm{E}} = {}^{t+\Delta t}\mathbf{R}_{\mathrm{p}} \end{cases} \tag{2.3.68}$$

where

$${}^{t+\Delta t}\mathbf{R}_{\mathrm{u}} = {}^{t+\Delta t}\mathbf{T} - {}^{t+\Delta t}\mathbf{C}\left({}^{t}\dot{\mathbf{u}}_{\mathrm{N}} + (1-\gamma)\Delta t\,{}^{t}\ddot{\mathbf{u}}_{\mathrm{N}}\right) - {}^{t+\Delta t}\mathbf{K}\left(\left(\frac{1}{2}-\beta\right)\Delta t^{2}\,{}^{t}\ddot{\mathbf{u}}_{\mathrm{N}} + \Delta t\,{}^{t}\dot{\mathbf{u}}_{\mathrm{N}}\right)$$

$${}^{t+\Delta t}\mathbf{R}_{\mathrm{p}} = \frac{\gamma^{f}}{k}{}^{t+\Delta t}\mathbf{Q}^{\mathrm{T}}\left({}^{t}\dot{\mathbf{u}}_{\mathrm{N}} + (1-\gamma)\Delta t\,{}^{t}\ddot{\mathbf{u}}_{\mathrm{N}}\right) + \frac{{}^{t+\Delta t}\mathbf{L}}{\Delta t}{}^{t}\mathbf{p}_{\mathrm{E}}$$

$$\mathbf{K}=\mathbf{K}_{\mathrm{L}}+\mathbf{K}_{\mathrm{NL}}$$

Eq.(2.3.69) gives the final form of the above equation;

$$\begin{bmatrix} {}^{t+\Delta t}\mathbf{M} + \gamma\Delta t\,{}^{t+\Delta t}\mathbf{C} + \beta\Delta t^{2}\,{}^{t+\Delta t}\left(\mathbf{K}_{\mathrm{L}} + \mathbf{K}_{\mathrm{NL}}\right) & {}^{t+\Delta t}\mathbf{Q} \\ \alpha'\,{}^{t+\Delta t}\mathbf{Q}^{\mathrm{T}} & -\left({}^{t+\Delta t}\mathbf{H} + \frac{{}^{t+\Delta t}\mathbf{L}}{\Delta t}\right) \end{bmatrix} \begin{Bmatrix} {}^{t+\Delta t}\ddot{\mathbf{u}}_{\mathrm{N}} \\ {}^{t+\Delta t}\mathbf{p}_{\mathrm{E}} \end{Bmatrix} =$$

$$\begin{Bmatrix} {}^{t+\Delta t}\mathbf{T} - {}^{t+\Delta t}\mathbf{C}\left({}^{t}\dot{\mathbf{u}}_{\mathrm{N}} + (1-\gamma)\Delta t\,{}^{t}\ddot{\mathbf{u}}_{\mathrm{N}}\right) - {}^{t+\Delta t}\mathbf{K}\left(\left(\frac{1}{2}-\beta\right)\Delta t^{2}\,{}^{t}\ddot{\mathbf{u}}_{\mathrm{N}} + \Delta t\,{}^{t}\dot{\mathbf{u}}_{\mathrm{N}}\right) \\ \frac{\gamma^{f}}{k}{}^{t+\Delta t}\mathbf{Q}^{\mathrm{T}}\left({}^{t}\dot{\mathbf{u}}_{\mathrm{N}} + (1-\gamma)\Delta t\,{}^{t}\ddot{\mathbf{u}}_{\mathrm{N}}\right) + \frac{{}^{t+\Delta t}\mathbf{L}}{\Delta t}{}^{t}\mathbf{p} \end{Bmatrix} \tag{2.3.69}$$

where $\alpha' = \frac{\gamma^{f}}{g} - \frac{\gamma^{f}}{k}\gamma\Delta t$.

2.4 Demonstration of the Method

The cyclic elasto-plastic model and FE-FD coupled method for saturated sandy soil extended to three-dimensional analysis using updated Lagrangian method were introduced above. In this section, the effectiveness of this method is demonstrated with two simple classical examples. The advantage of three-dimensional analysis with finite

deformation theory is discussed.

2.4.1 Dynamic Behavior of Saturated Sand with a single element

First, a single element model of saturated soil (shown in **Fig.2.5**) is used to simulate

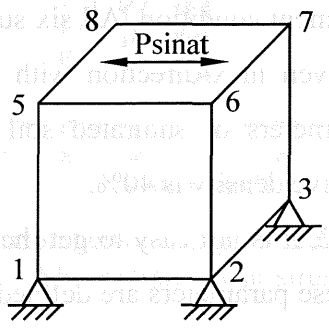

Fig.2.5 Dynamic simulation of single element

Table 2.1 Parameters of Ensyunada sand with Dr about 40%

parameter	value
Initial void ratio $\mathbf{e_0}$	0.992
Compression index λ	0.025
Swelling index κ	0.0025
Normalized initial shear modulus $\mathbf{G_0}/\sigma'_{\mathbf{m0}}$	1000
Phase transformation stress ratio $\mathbf{M_m}$	0.710
Failure stress ratio $\mathbf{M_f}$	0.960
Coefficient for hardening equation $\mathbf{B_0}$	6000
Coefficient for hardening equation $\mathbf{B_1}$	30
Coefficient for hardening equation $\mathbf{C_f}$	0
Coefficient of dilatancy $\mathbf{D_0}$	1.00
Coefficient of dilatancy **n**	3
Reference strain for plastic $\gamma^{\mathbf{P}}_{\mathbf{ref}}$	0.001
Referencr strain for elastic $\gamma^{\mathbf{P}}_{\mathbf{ref}}$	0.060
The second viscous coefficient λ'	0

the dynamic behavior of saturated soil with FE-FD coupled method considering large deformation. As a classical example used in many researches, it is effective to test both nonlinear models of saturated soil and analysis method. With this example, the three-dimensional FE-FD coupled method with finite deformation theory is demonstrated in dealing with liquefaction of saturated soil induced by strong vibration.

It is a one-meter cubic element, bottom nodes 1-4 are fixed, upper nodes 5-8 are constrained with same displacement condition. All six surfaces of the cubic element are undrained. The vibration is given in x-direction with a cyclic sin acceleration with amplitude 9.81m/s^2. The parameters of saturated soil are given as **Table.2.1**, it is Ensyunada sand which the relative density is 40%.

As introduced in section 2.2, it is not easy to get the values of the parameters from B_0 to C_d in test. In this case, these parameters are defined by trial and error to be able to fit several experimental data the simulations as shown in **Figs.2.6-2.9**.

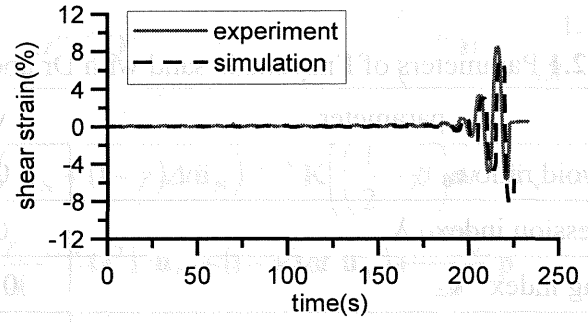

Fig.2.6 Comparison between experiment and simulation (Shear strain)

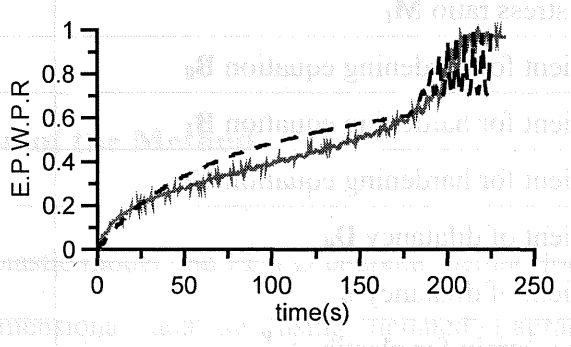

Fig.2.7 Comparison between experiment and simulation (Pore water pressure ratio)

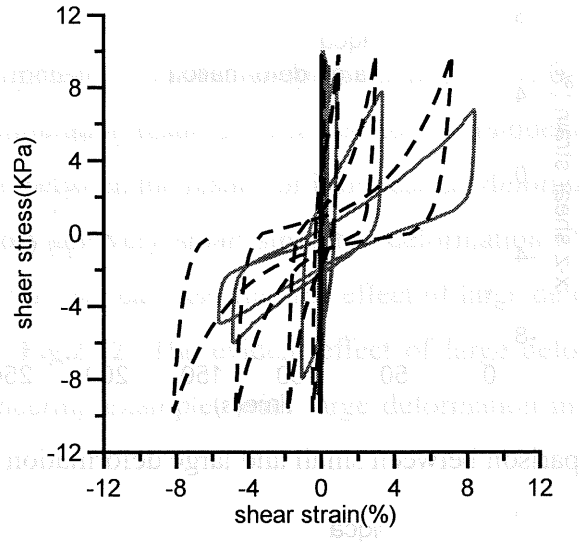

Fig.2.8 Comparison between experiment and simulation (Shear strain-shear stress)

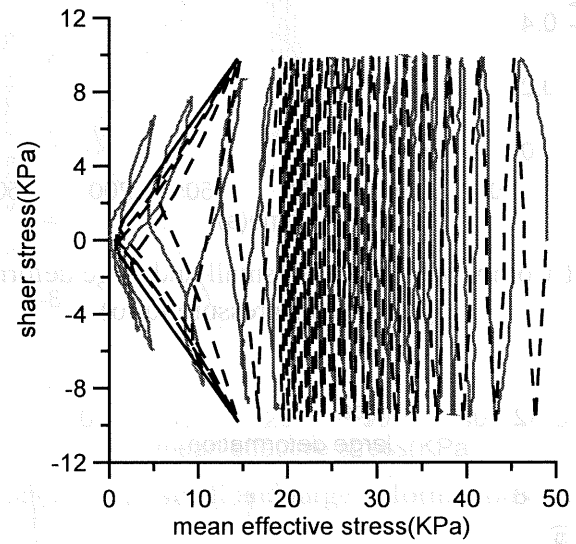

Fig.2.9 Comparison between experiment and simulation (Effective stress paths)

The simulation results of the single element under strong vibration with three dimensional FE-FD coupled method using updated Lagrangian formulation are given in **Figs.2.10-2.13**. The results without considering large deformation are also given as comparisons.

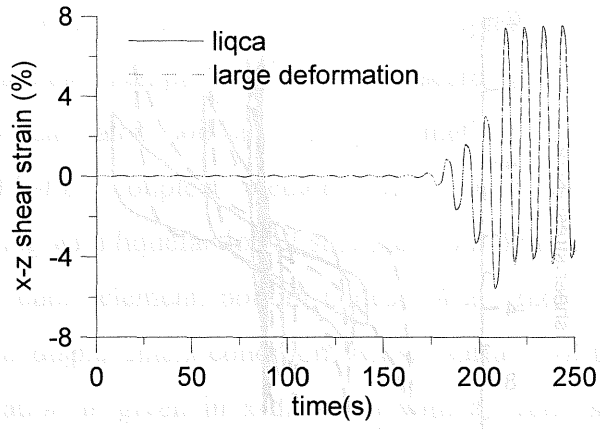

Fig.2.10 Comparison between small and large deformation (Shear shtrain)

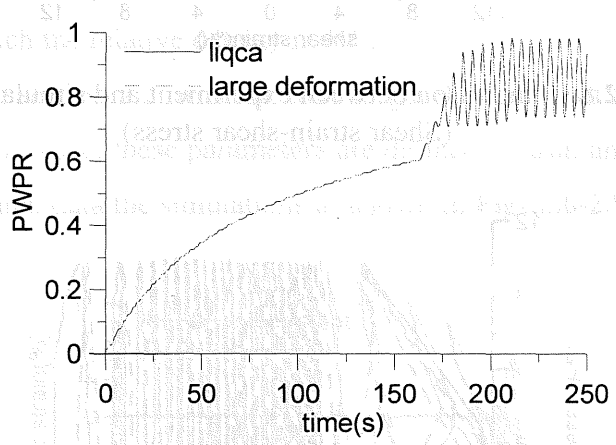

Fig.2.11 Comparison between small and large deformation (Pore water pressure ratio)

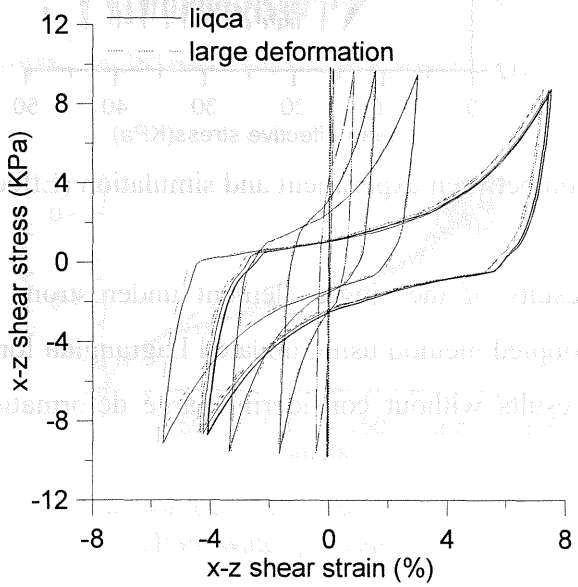

Fig.2.12 Comparison between small and large deformation (Shear strain-shear stress)

Obviously, three-dimensional FE-FD coupled method based on updated Lagrangian method gives a good simulation result of saturated soil in a liquefaction process. In this example, the difference between the results of infinitesimal deformation assumption and finite deformation theory are very small since the deformation of this example is not large enough. Even as this, we can also find the effect of large deformation in the shear strain result shown as **Fig.2.12**. The evident effect of large deformation is shown in Chapter 4, some engineering examples with large deformation in liquefactions due to strong earthquakes.

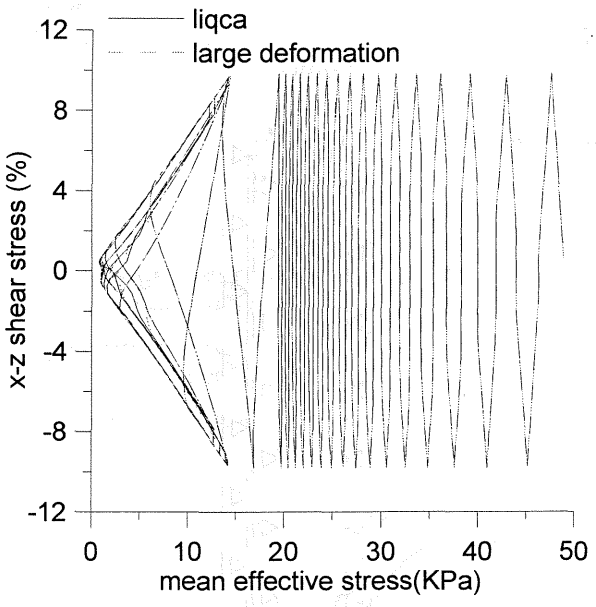

Fig.2.13 Comparison between small and large deformation (Effective stress paths)

2.4.2 Consolidation of Saturated Soil

The second problem is one-dimensional finite elastic consolidation which was used in some researches (Babuska, 1971; Chen and Mizuno, 1990; Huang et al, 2001; Di and Sato, 2004). It is adopted here to test FE-FD coupled method with updated Lagrangian formulation. The saturated soil with ten meters depth is compressed by a uniformly distributed load at the top surface of the ground. The load is increased linearly up to T during 2 second.

Considering a soil column with the foursquare section, a model with ten cubic elements is created as shown in **Fig.2.14**. The sides of the cubic are one meter long. The drainage is allowed only through the top surface. The boundary conditions imposed are that all element nodes are constrained horizontally, nodes at the bottom are fixed in the vertical direction, and the lateral boundary of the soil column is impermeable. The following material parameters make up the soil column: the elastic modulus of the ground $E = 1\text{Gpa}$, the Poisson ratio $\nu = 0.0$, the initial soil porosity $n = 0.3$, and the specific permeability $k = 0.001 m/s$; moreover, the pore fluid is assumed as incompressible. Pressure at the top surface is assumed to be atmospheric. Four load levels of T equal to 0.2GPa, 0.4GPa, 0.6GPa and 0.8GPa are considered.

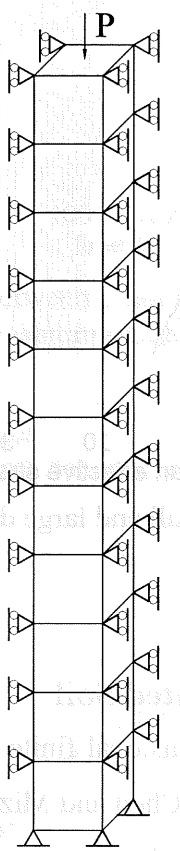

Fig.2.14 One dimensional compression model

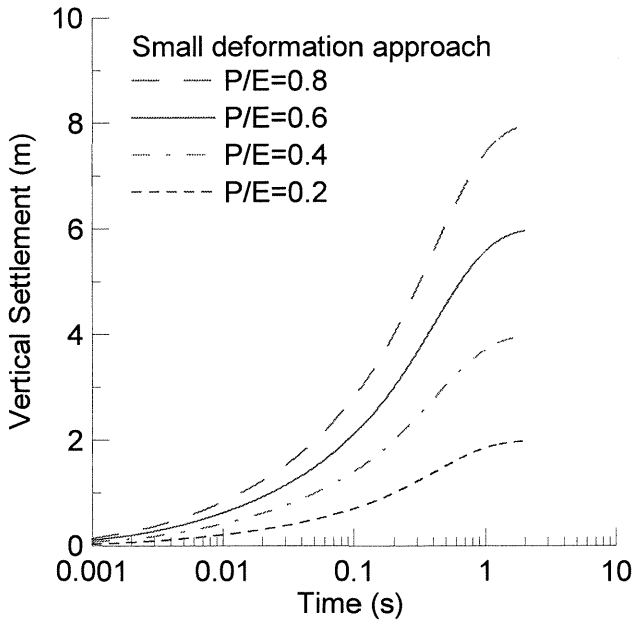

Fig.2.15 Settlement versus normalized time for small deformation approach

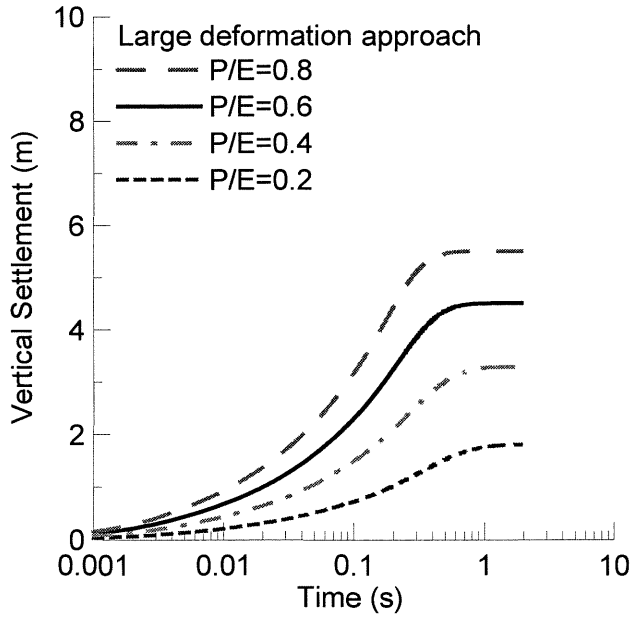

Fig.2.16 Settlement versus normalized time for large deformation approach

The settlements of small deformation approach and large deformation approach at ground surface vs. the normalized time t is shown in **Figs.15** and **16** respectively. The types of curves represent different load levels. It is easy to find that, the larger the applied load, the more clear the difference between the numerical results of the two

approaches.

The theoretical relationships between the applied loads T and final vertical settlements W, as well as the computed results from the developed program, are shown in **Fig.2.17**. The thin dashed line represents the results of small strain analysis, the solid one the theoretical solution for large deformation, the black dotted line large deformation computational result.

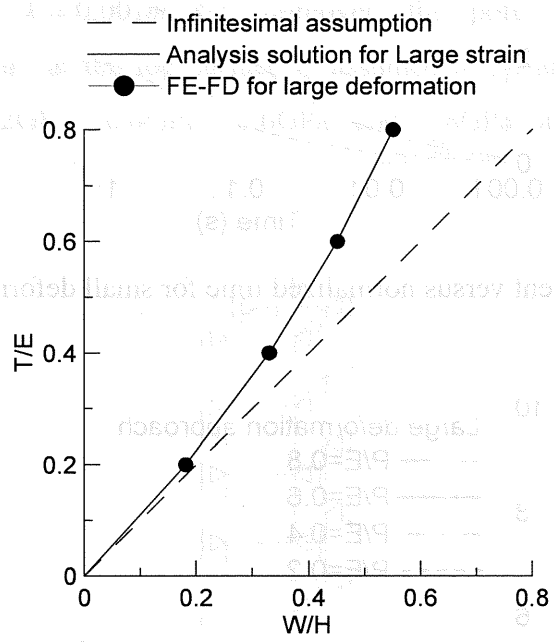

Fig.2.17 Final settlement versus the applied load level

2.5 Conclusion

In this chapter, the author introduced the development of three-dimensional FE-FD coupled method with a cyclic elasto-plastic model of saturated soil and updated Lagrangian formulation. The cyclic elasto-plastic model is adopted to deal with material nonlinearity of saturated soil. Updated Lagrangian formulation is applied to three-dimensional FE-FD coupled method to deal with geometrical nonlinearity. The coefficient of porosity is updated according to the deformation of the soil skeleton and the coefficient of permeability is updated concerning with the void ratio in every time

increment with updated Lagrangian formulation.

This three dimensional liquefaction analysis considering large deformation is demonstrated by two simple examples. The adaptation of this method to elasto-plastic analysis of saturated soil is tested by single element simulation example. It is found that this method describe the elasto-plastic behavior of saturated soil very well. One dimensional finite strain consolidation example is analyzed to test the updated Lagrangian formulation applied to three-dimensional FE-FD coupled method. The good agreement is found between numerical and analytical solutions.

References

[1] Tang X and Sato T. Dynamic Analysis of Saturated Porous Medium by 3D FE-FD Coupled Method Considering Large Deformation, Proceedings of KAIST-KU Joint Seminar on Earthquake Engineering (2002), 83-88.

[2] Tang X, Zhang F and Sato T. 3-D Numerical Analysis on Soil -Pile Interaction of Liquefied Ground Considering Large Deformation, The 57th Conference of JSCE (2002).

[3] Di Y, Sato T. Liquefaction analysis of saturated soils taking into account variation in porosity and permeability with large deformation, Computers and Geotechnics, 30(2003), 623-635.

[4] Di Y, Sato T. A practical numerical method for large strain liquefaction analysis of saturated soils, Soil Dynamics and Earthquake engineering, 24(2004), 251-260.

[5] Biot MA. General theory of three dimensional consolidation, J. Appl. Phys., 12(1941),155-164.

[6] Biot MA. Theory of propagation of elastic waves in a fluid saturated porous solid, J. Acust. Soc. Am., 28(1956), 168-191.

[7] Biot MA. Generalized theory of acoustic propagation in porous dissipation media, Theory of propagation of elastic waves in a fluid saturated porous solid, J. Acust. Soc. Am., 34(1962), 1254-1268.

[8] Zienkiewicz OC, Chang CT, Bettess P. Drained, undrained, consolidating and dynamic behavior assumptions in soil, Limits of validity, Geotechnique, 30(1980), 385-395.

[9] Zienkiewicz OC and Shiomi T. Static and dynamic behavior of saturated porous medium:

the generalized Biot formulation and its numerical solution, Int. J. Numer. Analytic. Mech. Geomech., 8(1984), 71-96.

[10] Zienkiewicz OC. Coupled problems and their numerical solution, in: R.W. Lewis, P. Bettess and E. Hinton, Eds., Numerical Method in Coupled Systems, John Wiley & Sons, New York, 1984, 35-58.

[11] Prevost JH. Mechanics of continuous porous media, Int. J. Eng. Sci., 18(1980), 787-800

[12] J.H. Prevost. nonlinear transient phenomena in saturated porous media, Comp. Meth. Appl. Eng., 20(1982), 3-18.

[13] Zienkiewicz OC. Basic formulation of static and dynamic behavior of soil and other porous media, in: J. B. Martins, Ed., Numerical Method in Geomechanics, D. Reidel, Norwell, MA, 1982,39-57.

[14] Meroi EA, Schrefler BA and Zienkiewicz OC. Large strain static and dynamic semisaturated soil behavior, Int. J. Numer. Analytic. Meth. Geomech., 19(1995), 81-106

[15] Zienkiewicz OC, Chan AHC, Pastor M, Paul DK and Shiomi T. Static and dynamic behavior of soils: a ratinal approach to quantitative solutions. I: Fully saturated problems. In:Proc. Roy. Soc. Lond., A429(1990), 285-309.

[16] Zienkiewicz OC, Chan AHC, Pastor M, Paul DK and Shiomi T. Static and dynamic behavior of soils: a ratinal approach to quantitative solutions. II: Semi-saturated problems. In:Proc. Roy. Soc. Lond., A429(1990), 311-321.

[17] Zienkiewicz OC, Huang M, Wu J, Wu S. A new algorithm for coupled soil-pore fluid problem, Shock and Vibration, 1(1993), 3-13.

[18] Zienkiewicz OC, Wu J. Incompressibility without tears — how to avoid restrictions of mixed formulation, Int. J. Numer. Methods Eng., 32(1991), 1189-1203.

[19] Huang M, Wu S, Zienkiewicz OC. Incompressible or nearly compressible soil dynamic behavior — a new staggered algorithm to circumvent restrictions of mixed formulation, Soil Dynamic and Earthquake Engineering, 21(2001), 169-179.

[20] Babuska I. Error bounds for finite element methods, Num. Math., 16(1971), 322-333.

[21] Babuska I. The finite element method with Lagrange multipliers, Num. Math., 20(1973), 179-192.

[22] Taylor RL, Simo JC, Zienkiewicz OC, Chan AHC. The patch test — a condition for assessing FEM convergence, Int. J. Numer. Methods Eng. 22(1986), 39-62.

[23] Zienkiewicz OC, Qu S, Taylor RL, Nakazawa S. The patch test for mixed formulation, Int.

J. Numer. Methods Eng. 23(1986), 1873-1883.

[24] Pastor M, Li T, Liu X, Zienkiewicz OC, Quecedo M. A fractional step algorithm allowing equal order of interpolation for coupled analysis of saturated soil problems, Mech. Cohes.-Frict. Mater. 5(2000), 511-534.

[25] Oka F, Yashima A, Shibata T, Kato M, Uzuoka R. FEM-FDM coupled liquefaction analysis of a porous soil using an elastic-plastic model, Applied Scientific Research, 52(1994), 209-245.

[26] Shibata T, Sato T, Uzuoka R, Oka F, Yashima A, Kato M. FEM-FDM coupled liquefaction analysis of a fluid-saturated ground, in: G. Beer, J.R. Booker, J.P. Carter, Eds., Computer Methods and Advances in Geomechanics, Balkema, Rotterdam, 1991, 869-874.

[27] Oka F, Kodaka T, Koizumi T, Sunami S. Liquefaction analysis of quay wall structur based on large deformation theory, in: 13th KKNN Symposium on Civil Engineering, Taipei, 2000,pp285-290.

[28] Oka F, Yashima A, Tateishi A, Taguchi Y, Yamashita S. A cyclic elastic-plastic constitutive model for sand considering a plastic-strain dependence of the shear modulus, Geotechnique, 49(1999), 661-680.

[29] Oka F, Yashima A, Kato A and Sekiguchi K. A constitutive model for sand based on the non-linear kinematic hardening rule and its application, in: Proc. 10th World Conference on Earthquake Engineering, (Barcelona, 1992), 2529-2534.

[30] Oka F. A cyclic elasto-viscoplastic constitutive model for clay based on the non-linear equations for the hardening rule, in: Proc. 4th Int. Symp. Numer. Models Geomech., (Swansea, 1992), 105-114.

[31] Matsuo O, Shimazu T, Uzuoka R, Mihara M, Nishi K. Numerical analysis of seismic behavior of embankments founded on liquefiable soils, Soils and Foundations, 40(2000), 21-39.

[32] Zienkiewicz OC, Bettess P. Soils and other saturated media under transient, dynamic conditions, in: G.N. Pande, O.C. Zienkiewicz, Eds., Soil Mechanics Transient and Cyclic Loads, John Wiley & Sons, New York, 1982,pp1-16.

[33] Lubarda VA, Lee EH. A correct definition of elastic and plastic deformation and its computational significance, J. Appl. Mech., 48(1981), 35-40.

[34] Lee EH. Some comments on elastic-plastic analysis, Int. J. Solids Struct., 17(1981), 859-872.

[35] Gadala MS, Dokainish MA, Oravas GA. Formulation methods of geometric and material nonlinearity problems, Int. J. Numer. Methods Eng., 20(1984), 887-914.

[36] Chen WF, Mizuno E. Nonlinear Analysis in Soil Mechanics, Elsevier Science Publishers B. V., 1990.

[37] Akira Tateishi, Makito Nago, Akinori Koike. Seismic deformation analysis of a caisson type quay wall using input seismic motion for aseismic design, in: Proc. Of Aseimic Design of Soils and Structures from Earthquakes(Level 2), JGS Kansai Chapter, Osaka, 1998,81-88(in Japanese).

[38] Moon Y, Sato T, Uzuoka R. A study of pre-and post-liquefaction processes for a caisson type quay wall using earthquake motion design, in: Proc. Of Aseisimic Design of Soils Structures from Earthquakes(Level 2), JGS Kansai Chapter, Osaka, 1998, 319-324(in Japanese).

[39] Kawasumi H (Editor-in-chief). General report on the Niigata Earthquake of 1964, Tokyo Electrical Engineering College Press, Tokyo, 1968.

[40] Committee on Earthquake Engineering, Japan Society of Civil Engineers,The 1995 Hyogoken-Nanbu Earquake: Investugation into Damage to Civil Engineering Structures, Japan Society of Civil Engineers,Tokyo, 1996.

Chapter 3

3D Analysis of Liquefaction and Flow Process of Ground Using Updated Lagrangian Method

3.1 Introduction

In the process of liquefaction the states of soil are generally classified in three parts: the solid state before the onset of liquefaction, the fluid state after liquefaction, and the recovered solid state owing to dissipation of the excess pore water pressure and dilatancy caused by development of large shear strain. Analysis methods proposed so far solve the phase transfer with those three phases independently using proper constitutive models suitable to express different states, but it should be continuous processes that represent change from the solid to fluid state or from the fluid to solid state. Therefore, the total processes of the combined liquefaction-ground flow phenomenon should be treated as a series of processes of phase transformation between the solid and fluid states.

To deal with liquefaction and ground flow phenomenon, many constitutive models

have been developed for saturated or unsaturated soil based on such established solid mechanisms as the cyclic elasto-plastic model, elasto-plastic sub-loading surface model, densification model. These methods focus mainly on the stress-strain response of pre-liquefaction. The ground flow phenomenon that generates a large deformation is not considered.

A fluidal elasto-plastic model (Sato and Moon, 2001) has been developed recently based on mechanical and numerical modeling of seismic liquefaction and the ground flow phenomenon in saturated loose sandy soil in order to unify these phase transformations of saturated loose sand. It combines the cyclic elasto-plastic behavior of sand and the Newtonian viscous fluid characteristics of liquefied sand by defining the phase transformation-controlling function. This constitutive equation provides a unified constitutive equation to characterise the entire process of liquefaction from the initial to post-liquefaction state. It is well known that phase transformation between the solid and fluid states is irregularly distributed over time and in the space domain. It is impossible to simulate liquefaction and subsequent ground flow under complicated in-site field conditions by methods to deal with every states of liquefiable soil separately. But the fluidal elasto-plastic model can solve this kind of problems. With a phase controlling function, this model adapts to solid state or fluid state freely.

The fluidal elasto-plastic model has been used in liquefaction and ground flow analysis through a FE-FD coupled method. Updated Lagrangian formulation has also been applied to two-dimension FE-FD coupled method with the fluidal elasto-plastic model (Moon, 2002). The aim of this chapter is to extend this nonlinear numerical method to three-dimensional numerical analysis considering large deformation.

In this chapter, section 3.2 introduces the development of fluidal elasto-plastic model of saturated soil, the constitutive equation of this model is given using the cyclic elasto-plastic model and Newtonian viscous fluid constitutive equation; Section 3.3 presents the derivation of the three dimensional FE-FD equations with updated Lagangian method and the constitutive equation of fluidal elasto-plastic model; Section 3.4 demonstrates this new method with a simple examples, the flow simulation of liquefied soil using three dimensional Newtonian viscous fluid constitutive equation and the scheme of updated Lagrangian formulation.

3.2 Fluidal Elasto-Plastic Model of saturated Soil

According to solid mechanics, the relationship between the total stress and effective stress of a mixture using the component of pore water pressure is

$$\sigma_{ij} = \sigma'_{ij} + p\delta_{ij} \tag{3.2.1}$$

where σ_{ij}, σ'_{ij}, p are the total stress tensor, effective stress tensor, and pore water pressure, and δ_{ij} is the Kronecker delta.

When the solid skeleton of a mixture is assumed to be an elasto-plastic body, the effective stress, σ'_{ij}, in Eq.(3.2.1) becomes the stress, σ^{ep}_{ij}, of the elasto-plastic body. And Eq.(3.2.1) becomes

$$\sigma_{ij} = \sigma^{ep}_{ij} + p\delta_{ij} \tag{3.2.2}$$

In contrast, the total stress of the viscous fluid in fluid mechanics generally is described as

$$\sigma_{ij} = \sigma^{vf}_{ij} + p\delta_{ij} \tag{3.2.3}$$

where σ^{vf}_{ij} is the viscous resistance stress tensor in the viscous fluid.

A comparison of Eqs.(3.2.2) and (3.2.3) shows that the component in which the pore water pressure is subtracted from the total stress tensor expresses the effective stress tensor in Eq.(3.2.2) and the viscous stress tensor in Eq.(3.2.3). This means that the viscous stress tensor in fluid mechanics coincides with the effective stress tensor concerned with the stiffness of a soil skeleton of a mixture.

Combining these two relationships, we propose a simple constitutive equation for loose saturated sand that expresses the phase transformation between the solid and fluid states during the liquefaction and ground flow processes. The newly proposed constitutive equation is called the fluidal elasto-plastic constitutive equation and defined as Eq.(3.2.4), and a schematic view of the constitutive equation is shown in **Fig.3.1**.

$$\sigma_{ij} = (1-\alpha)\,\sigma^{ep}_{ij} + \alpha\,\sigma^{vf}_{ij} + p\delta_{ij} \tag{3.2.4}$$

where α is the phase transformation-controlling function. The stress σ^{ep}_{ij} is evaluated by the cyclic elasto-plastic constitutive equation. The relationship is written as follows

by means of the incremental formulation

$$d\sigma_{ij}^{ep} = D_{ijkl}^{ep}\, d\varepsilon_{kl} \tag{3.2.5}$$

where D_{ijkl}^{ep} is the fourth-order isotropic tensor concerned with the stress-strain relationship for the elasto-plastic constitutive equation, and $d\varepsilon_{kl}$ is the strain tensor increment. The stress and strain in Eq.(3.2.5) are expressed by incremental formulation in order to describe the nonlinear property of the material.

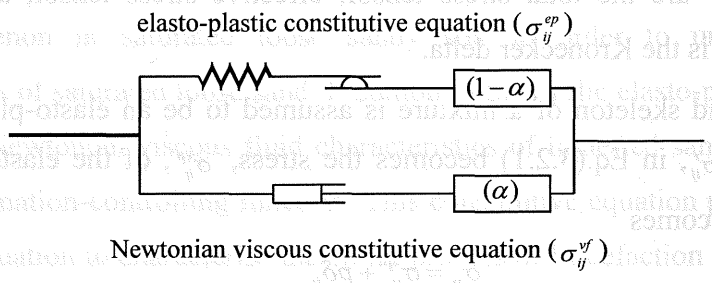

Fig.3.1 Concept of the fluid-elasto-plastic constitutive equation

The stress, σ_{ij}^{vf}, is evaluated by a Newtonian viscous fluid constitutive equation as

$$\sigma_{ij}^{vf} = D_{ijkl}^{vf}\, \dot{\varepsilon}_{kl} = 2\mu'\dot{\varepsilon}_{ij} + \lambda'\dot{\varepsilon}_{kk}\delta_{ij} \tag{3.2.6}$$

where D_{ijkl}^{vf} is the fourth-order isotropic tensor concerned with the stress-strain rate relationship for the Newtonian viscous fluid, $\dot{\varepsilon}_{kl}$ is the strain rate tensor, and μ', λ' are the viscous and the second viscous coefficients.

In some investigation (Yasuda et al., 1994), the stress-strain relationships of sand after liquefaction was conducting torsional shear tests. In torsional shear tests, the cyclic loading was applied to the specimens in undrained conditions. The cyclic loading was terminated when the excess pore water pressure ratio, or FL, reached a prescribed value. Then, a monotonic loading was applied during undrained condition. Liquefaction occurred when the number of cycles during the cyclic loading exceeded 20, and the severity of liquefaction increased with the number of cycles. The severity of liquefaction was indicated by the factor of safety against liquefaction called the FL.

The stress-strain relationships and the pore water pressure-strain relationships during the monotonic loading under the various FL conditions are shown in **Fig.3.2**. From this result, recovery of stiffness is related to increase of effective stress due to the dilatancy.

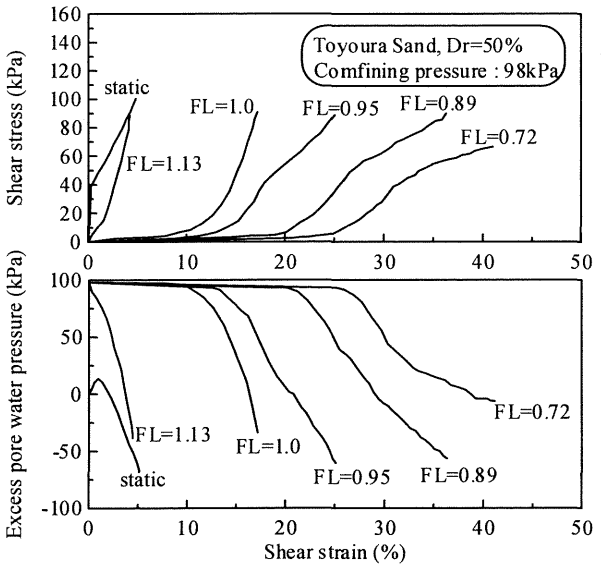

Fig.3.2 Results of the torsional shear test

In this viewpoint, the following researchers (Sato and Moon, 2001) assumed that phase transformation function is as a function of the effective stress through the whole progress of the occurrence of liquefaction, the flow phenomenon and the recovery of stiffness. Then the phase transformation function α is expressed by a function of the relative effective stress ratio (R.E.S.R.) throughout the process of liquefaction, ground flow and recovery of stiffness. The phase transformation function is expressed by

$$\alpha = 1.0 + \tanh(a \cdot (1 - \sigma'_m / \sigma'_{m0}) - b) \tag{3.2.7}$$

where σ'_m, σ'_{m0} are current and initial mean effective stresses, $1 - \sigma'_m / \sigma'_{m0}$ is the relative effective stress ratio (R.E.S.R.) and a, b are parameters.

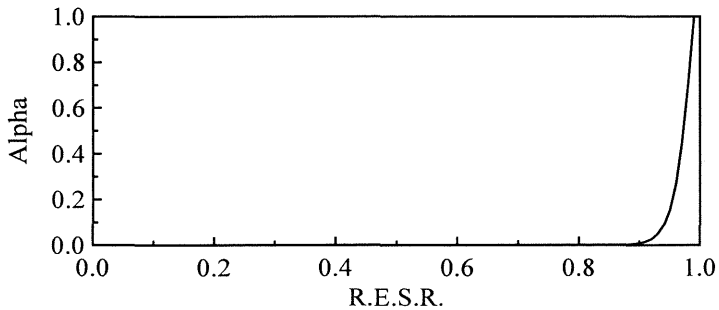

Fig.3.3 Relationship between α and R.E.S.R.

This relationship between α and R.E.S.R. is shown in **Fig.3.3**. When R.E.S.R. is

more than 0.9, the value of α rapidly increases, and when the value reaches 1.0, α becomes 1.0 reversibly. α then rapidly decreases with recovery of the mean effective stress caused by seepage and dilatancy. Actuation of the fluid behavior modeled by a Newtonian viscous fluid is limited to a region in which the mean effective stress is very small. The shape of α is controlled by the values of 'a' and 'b' in Eq.(3.2.7).

3.3 Updated Lagrangian Formulation Applied to 3-D FE-FD Analysis of Porous Media of Which Constitutive Equation Defined by Fluidal Elasto-Plastic Model

A FE-FD coupled method with fluidal elasto-plastic model considering large deformation has been achieved in two-dimensional analysis (Moon, 2002). The governing equations were also derived with updated Lagrangian method. In this research, Fe-FD coupled method with fluidal elasto-plastic model and updated Lagrangian formulation is extended to three-dimensional analysis. This section presents the derivation of the governing equations for three-dimensional FE-FD coupled method. Because that fluidal elasto-plastic model is a combination of the cyclic elasto-plastic model and Newtonian viscous fluid theory, and the equations of the cyclic elasto-plastic model are introduced in Chapter.2, the parts of derivation without concerning with fluidal elasto-plastic model are not rewritten here.

The derivative form of equilibrium equation and continuity equation for fluidal elasto-plastic model according to Biot's two-phase mixture theory are same with those of cyclic elasto-plastic model since the stress used in the equations are not divided into the stresses from the cyclic elasto-plastic model and Newtonian viscous fluid. The constitutive equation in derivative form of fluidal elasto-plastic model is introduced in section 3.2. The introduction of governing equations is started from weak form.

3.3.1 The u-p Equations in Spatial Discrete Form

According to the concept of fluidal elasto-plastic model, the stress includes two parts from the elasto-plastic model and Newtonian viscous fluidal theory. The second

Piola-Kirchhoff stress tensor is also includes two parts and given as

$$ {}^{t+\Delta t}S_{ij} = {}^{t+\Delta t}S_{ij}^{ep} + {}^{t+\Delta t}S_{ij}^{vf} + {}^{t+\Delta t}p\delta_{ij} \tag{3.3.1} $$

where ${}^{t+\Delta t}S_{ij}^{ep}$ is the part given by the cyclic elasto-plastic model; ${}^{t+\Delta t}S_{ij}^{vf}$ the part given by Newtonian viscous fluidal constitutive model.

Substitute Eq.(3.3.1) into Eq.(2.3.48), the weak form of equilibrium equation of fluidal elasto-plastic model is obtained as

$$ \int_{{}^tV} \rho \ddot{u}_i \, \delta v_i \, d^tV + \int_{{}^tV} {}^{t+\Delta t}S_{ij}^{ep}{}_{|t+\Delta t} \delta E_{ij}^{t+\Delta t} d^tV + \int_{{}^tV} {}^{t+\Delta t}S_{ij}^{vf} \delta E_{ij} d^tV + \int_{{}^tV} {}^{t+\Delta t} p\delta E_{ii} d^tV = {}^{t+\Delta t}F \tag{3.3.2} $$

where ${}^{t+\Delta t}\mathbf{F}$ is given as Eq.(2.3.49).

According to updated Lagrangian formulation, the part of stress from the cyclic elasto-plastic model is calculate by

$$ {}^{t+\Delta t}S_{ij}^{ep} = {}^{t}S_{ij}^{ep} + dS_{ij}^{ep} \tag{3.3.3} $$

Using Eq.(2.3.14), Eq.(3.3.3) is rewritten as

$$ {}^{t+\Delta t}S_{ij}^{ep} = {}^{t}\sigma_{ij}^{ep} + dS_{ij}^{ep} \tag{3.3.4} $$

The relation between the stress and strain velocity in the Newtonian viscous fluidal constitutive equation is linear. Assuming that the time increment is small enough in every calculation step, the part of stress from Newtonian viscous fluidal constitutive model ${}^{t+\Delta t}S_{ij}^{vf}$ is approximated as

$$ {}^{t+\Delta t}S_{ij}^{vf} \approx {}^{t}S_{ij}^{vf} = {}^{t}\sigma_{ij}^{vf} \tag{3.3.5} $$

Substituting Eqs.(3.3.4) and (3.3.5) into Eq.(3.3.3) obtains

$$ \begin{aligned} &\int_{{}^tV} \rho \ddot{u}_i \, \delta v_i \, d^tV + \int_{{}^tV} {}^{t}\sigma_{ij}^{ep} \delta(dE_{ij}) d^tV + \int_{{}^tV} {}^{t+\Delta t} dS_{ij}^{ep} \delta(dE_{ij}) d^tV + \\ &\int_{{}^tV} {}^{t}\sigma_{ij}^{vf} \delta(dE_{ij}) d^tV + \int_{{}^tV} {}^{t+\Delta t} p\delta(dE_{ii}) d^tV = {}^{t+\Delta t}\mathbf{F} \end{aligned} \tag{3.3.6} $$

Using the relation from the assumption of infinitesimal displacement shown as follows

$$ \int_{{}^tV} dS_{ij}^{ep} \delta(dE_{ij}) d^tV \approx \int_{{}^tV} dS_{ij}^{ep} \delta(d\varepsilon_{ij}) d^tV \tag{3.3.7} $$

$$ \int_{{}^tV} {}^{t+\Delta t} p\delta(dE_{ii}) d^tV_{|t} \approx \int_{{}^tV} {}^{t+\Delta t} p\delta(d\varepsilon_{ii}^s) d^tV \tag{3.3.8} $$

Eq.(3.3.6) is rewritten as

$$\begin{aligned}&\int_{{}^tV}\rho\ddot{u}_i\,\delta v_i\,d^tV+\int_{{}^tV}{}^t\sigma_{ij}^{ep}\delta(dE_{ij})d^tV+\int_{{}^tV}{}^{t+\Delta t}dS_{ij}^{ep}\delta(d\varepsilon_{ij})d^tV+\\&\int_{{}^tV}{}^t\sigma_{ij}^{vf}\delta(dE_{ij})d^tV+\int_{{}^tV}{}^{t+\Delta t}p\delta(d\varepsilon_{ii})d^tV={}^{t+\Delta t}\mathbf{F}\end{aligned}\tag{3.3.9}$$

where dE_{ij} is Lagrangian strain tensor defined as

$$\begin{aligned}dE_{ij}&=\frac{1}{2}\left(du_{i,j}+du_{j,i}+du_{k,i}du_{k,j}\right)\\&=d\varepsilon_{ij}+d\eta_{ij}\end{aligned}\tag{3.3.10}$$

$$d\varepsilon_{ij}=\frac{1}{2}\left(du_{i,j}+du_{j,i}\right)\tag{3.3.11}$$

$$d\eta_{ij}=\frac{1}{2}\left(du_{k,i}du_{k,j}\right)\tag{3.3.12}$$

The further derivation gives

$$\delta(dE_{ij})=\delta(\dot{\varepsilon}_{ij})+\delta(\dot{\eta}_{ij})\tag{3.3.13}$$

$$\delta(d\dot{\varepsilon}_{ij})=\frac{1}{2}\left\{\delta v_{i,j}+\delta v_{j,i}\right\}\tag{3.3.14}$$

$$\delta\dot{\eta}_{ij}=\frac{1}{2}\left\{\delta v_{k,i}v_{k,j}+v_{k,i}\delta v_{j,i}\right\}\tag{3.3.15}$$

From Eq.(2.3.50), the part of the second Piola-Kirchhoff stress tensor increment from the cyclic elasto-plastic model is calculated by

$$\dot{S}_{ij}^{ep}=\{(1-\alpha)D_{ijkl}^{ep}+\psi_{ijkl}\}\dot{E}_{kl}\tag{3.3.16}$$

Substituting Eqs.(3.3.13)-(3.3.16) and Eqs.(2.3.52)-(2.3.54) into Eq.(3.3.9), the discretezation of equilibrium in spatial domain is obtained as

$$\mathbf{M}\ddot{\mathbf{u}}_{\mathbf{N}}+\left(\mathbf{K}_{\mathbf{L}}+\mathbf{K}_{\mathbf{NL}}+\mathbf{K}_{\mathbf{CNL}}\right)\Delta\mathbf{u}_{\mathbf{N}}+\mathbf{C}^{\mathbf{vf}}\dot{\mathbf{u}}_{\mathbf{N}}+\mathbf{Q}\mathbf{p}_{\mathbf{E}}=\mathbf{T}\tag{3.3.17}$$

where the mass matrix $\mathbf{M}=\int_V\rho\mathbf{N}^{\mathrm{T}}\mathbf{N}d^tV$;

$$\mathbf{K}_{\mathbf{L}}=\int_{{}^tV}\mathbf{B}_{\mathbf{L}}^{\mathrm{T}}\left((1-\alpha)\mathbf{D}^{\mathbf{ep}}+\psi\right)\mathbf{B}_{\mathbf{L}}d^tV;$$

$$\mathbf{K}_{\mathbf{NL}}=\int_{{}^tV}\mathbf{B}_{\mathbf{NL}}^{\mathrm{T}}\mathbf{A}^{\mathbf{EP}}\mathbf{B}_{\mathbf{NL}}d^tV;$$

$$\mathbf{K}_{\mathbf{CNL}}=\int_{{}^tV}\mathbf{B}_{\mathbf{NL}}^{\mathrm{T}}\mathbf{A}^{\mathbf{vf}}\mathbf{B}_{\mathbf{NL}}d^tV;$$

$$\mathbf{C}^{\mathbf{vf}}=\int_{{}^tV}\alpha\mathbf{B}_{\mathbf{L}}^{\mathrm{T}}\mathbf{D}^{\mathbf{vf}}\mathbf{B}_{\mathbf{L}}d^tV$$

$$\mathbf{Q}=-\int_V\mathbf{B}_{\mathbf{V}}^{\mathrm{T}}d^tV$$

$$\mathbf{T}={}^{t+\Delta t}\mathbf{F}-\int_V \mathbf{B}_{\mathrm{L}}^{\mathrm{T}}\,{}^{t}\sigma' d^{t}V$$

where $\mathbf{B}_{\mathrm{NL}}$, $\mathbf{B}_{\mathrm{L}}$ and ψ are referred to Eqs.(2.3.58), (2.3.56) and (2.3.51) respectively; and

$$\mathbf{A}^{\mathbf{ep}}=\begin{bmatrix}
\sigma_{11}^{ep} & 0 & 0 & \frac{1}{2}\sigma_{12}^{ep} & 0 & \frac{1}{2}\sigma_{13}^{ep} & \sigma_{12\,12}^{ep} & 0 & -\sigma_{13}^{ep} \\
 & \sigma_{22}^{ep} & 0 & \frac{1}{2}\sigma_{21}^{ep} & \frac{1}{2}\sigma_{23}^{ep} & 0 & -\sigma_{21}^{ep} & \sigma_{23}^{ep} & 0 \\
 & & \sigma_{33}^{ep} & 0 & \frac{1}{2}\sigma_{32}^{ep} & \frac{1}{2}\sigma_{31}^{ep} & 0 & -\sigma_{32}^{ep} & \sigma_{31}^{ep} \\
 & & & \frac{1}{2}s_{12}^{ep} & \frac{1}{4}\sigma_{13}^{ep} & \frac{1}{4}\sigma_{23}^{ep} & \frac{1}{2}\tau_{21}^{ep} & \frac{1}{2}\sigma_{13}^{ep} & -\frac{1}{2}\sigma_{23}^{ep} \\
 & & & & \frac{1}{2}s_{13}^{ep} & \frac{1}{4}\sigma_{32}^{ep} & -\frac{1}{2}\sigma_{13}^{ep} & \frac{1}{2}\tau_{32}^{ep} & \frac{1}{2}\sigma_{21}^{ep} \\
 & & & & & \frac{1}{2}s_{13}^{ep} & \frac{1}{2}\sigma_{32}^{ep} & -\frac{1}{2}\sigma_{12}^{ep} & \frac{1}{2}\tau_{13}^{ep} \\
 & & & & & & 2s_{12}^{ep} & -\sigma_{13}^{ep} & -\sigma_{23}^{ep} \\
 & & & \textit{Symmtric} & & & & 2s_{23}^{ep} & -\sigma_{21}^{ep} \\
 & & & & & & & & 2s_{31}^{ep}
\end{bmatrix} \tag{3.3.18}$$

$$s_{ij}^{ep}=\frac{1}{2}\left(\sigma_{ii}^{ep}+\sigma_{jj}^{ep}\right)$$
$$\tau_{ij}^{ep}=\frac{1}{2}\left(\sigma_{ii}^{ep}-\sigma_{jj}^{ep}\right)$$

$$\mathbf{A}^{\mathbf{vf}}=\begin{bmatrix}
\sigma_{11}^{vf} & 0 & 0 & \frac{1}{2}\sigma_{12}^{vf} & 0 & \frac{1}{2}\sigma_{13}^{vf} & \sigma_{12\,12}^{vf} & 0 & -\sigma_{13}^{vf} \\
 & \sigma_{22}^{vf} & 0 & \frac{1}{2}\sigma_{21}^{vf} & \frac{1}{2}\sigma_{23}^{vf} & 0 & -\sigma_{21}^{vf} & \sigma_{23}^{vf} & 0 \\
 & & \sigma_{33}^{vf} & 0 & \frac{1}{2}\sigma_{32}^{vf} & \frac{1}{2}\sigma_{31}^{vf} & 0 & -\sigma_{32}^{vf} & \sigma_{31}^{vf} \\
 & & & \frac{1}{2}s_{12}^{vf} & \frac{1}{4}\sigma_{13}^{vf} & \frac{1}{4}\sigma_{23}^{vf} & \frac{1}{2}\tau_{21}^{vf} & \frac{1}{2}\sigma_{13}^{vf} & -\frac{1}{2}\sigma_{23}^{vf} \\
 & & & & \frac{1}{2}s_{13}^{vf} & \frac{1}{4}\sigma_{32}^{vf} & -\frac{1}{2}\sigma_{13}^{vf} & \frac{1}{2}\tau_{32}^{vf} & \frac{1}{2}\sigma_{21}^{vf} \\
 & & & & & \frac{1}{2}s_{13}^{vf} & \frac{1}{2}\sigma_{32}^{vf} & -\frac{1}{2}\sigma_{12}^{vf} & \frac{1}{2}\tau_{13}^{vf} \\
 & & & & & & 2s_{12}^{vf} & -\sigma_{13}^{vf} & -\sigma_{23}^{vf} \\
 & & & \textit{Symmtric} & & & & 2s_{23}^{ep} & -\sigma_{21}^{vf} \\
 & & & & & & & & 2s_{31}^{vf}
\end{bmatrix} \tag{3.3.19}$$

$$s_{ij}^{vf}=\frac{1}{2}\left(\sigma_{ii}^{vf}+\sigma_{jj}^{vf}\right)$$
$$\tau_{ij}^{vf}=\frac{1}{2}\left(\sigma_{ii}^{vf}-\sigma_{jj}^{vf}\right)$$

The discretization of continuity equation in spatial domain is same with Eq.(2.3.63), and rewritten here

$$\rho^{f}\mathbf{Q}^{\mathrm{T}}\ddot{\mathbf{u}}_{\mathrm{N}}-\frac{\gamma^{f}}{k}\mathbf{Q}^{\mathrm{T}}\dot{\mathbf{u}}_{\mathrm{N}}-\mathbf{H}\mathbf{p}_{\mathrm{E}}+\mathbf{L}\dot{\mathbf{p}}_{\mathrm{E}}=0 \qquad \text{rewritten(2.3.63)}$$

3.3.2 Discrete Equations in Time Domain with Newmark-β Method

Adding the Rayleigh damping, the complete FE-FD coupled method equations at time $t+\Delta t$ are given as

$$\begin{cases} {}^{t+\Delta t}\mathbf{M}\,{}^{t+\Delta t}\ddot{\mathbf{u}}_N + {}^{t+\Delta t}(\mathbf{C}^{ep}+\alpha\mathbf{C}^{vf})\,{}^{t+\Delta t}\dot{\mathbf{u}}_N + {}^{t+\Delta t}(\mathbf{K}_L+\mathbf{K}_{NL}+\mathbf{K}_{CNL})\Delta\mathbf{u}_N + {}^{t+\Delta t}\mathbf{Q}\,{}^{t+\Delta t}\mathbf{p}_E = {}^{t+\Delta t}\mathbf{T} \\ \rho^f\,{}^{t+\Delta t}\mathbf{Q}^T\,{}^{t+\Delta t}\ddot{\mathbf{u}}_N - \dfrac{\gamma^f}{k}\,{}^{t+\Delta t}\mathbf{Q}^T\,{}^{t+\Delta t}\dot{\mathbf{u}}_N - {}^{t+\Delta t}\mathbf{H}\,{}^{t+\Delta t}\mathbf{p}_E + {}^{t+\Delta t}\mathbf{L}\,{}^{t+\Delta t}\dot{\mathbf{p}}_E = 0 \end{cases}$$

(3.3.20)

The Newmark method is used for the time domain integration, and the variables and their derivatives at time $t+\Delta t$ are expressed as functions of their values at time t (Zienkiewicz et al., 1990 and 1995) as Eqs(2.3.65)-(2.3.67).

Substituting Eqs. (2.3.65)-(2.3.67) in Eq.(3.3.20), gives the discretized system of equations valid in each time step;

$$\begin{cases} {}^{t+\Delta t}\mathbf{M}\,{}^{t+\Delta t}\ddot{\mathbf{u}}_N + \gamma\Delta t\,{}^{t+\Delta t}\mathbf{C}\,{}^{t+\Delta t}\ddot{\mathbf{u}}_N + \beta\Delta t^2\,{}^{t+\Delta t}\mathbf{K}\,{}^{t+\Delta t}\ddot{\mathbf{u}}_N + {}^{t+\Delta t}\mathbf{Q}\,{}^{t+\Delta t}\mathbf{p}_E = {}^{t+\Delta t}\mathbf{R}_u \\ {}^{t+\Delta t}\mathbf{Q}^T\left(\rho^f - \dfrac{\gamma^f}{k}\gamma\Delta t\right){}^{t+\Delta t}\ddot{\mathbf{u}}_N - \left({}^{t+\Delta t}\mathbf{H} + \dfrac{{}^{t+\Delta t}\mathbf{L}}{\Delta t}\right){}^{t+\Delta t}\mathbf{p}_E = {}^{t+\Delta t}\mathbf{R}_p \end{cases} \tag{3.3.21}$$

where

$${}^{t+\Delta t}\mathbf{R}_u = {}^{t+\Delta t}\mathbf{T} - {}^{t+\Delta t}\mathbf{C}\left({}^{t}\dot{\mathbf{u}}_N + (1-\gamma)\Delta t\,{}^{t}\ddot{\mathbf{u}}_N\right) - {}^{t+\Delta t}\mathbf{K}\left(\left(\frac{1}{2}-\beta\right)\Delta t^2\,{}^{t}\ddot{\mathbf{u}}_N + \Delta t\,{}^{t}\dot{\mathbf{u}}_N\right)$$

$${}^{t+\Delta t}\mathbf{R}_p = \frac{\gamma^f}{k}\,{}^{t+\Delta t}\mathbf{Q}^T\left({}^{t}\dot{\mathbf{u}}_N + (1-\gamma)\Delta t\,{}^{t}\ddot{\mathbf{u}}_N\right) + \frac{{}^{t+\Delta t}\mathbf{L}}{\Delta t}\,{}^{t}\mathbf{p}_E$$

$$\mathbf{K}=\mathbf{K}_L+\mathbf{K}_{NL}+\mathbf{K}_{CNL}$$

$$\mathbf{C}=\mathbf{C}^{ep}+\mathbf{C}^{vf}$$

Eq.(3.3.22) gives the final form of governing equation;

$$\begin{bmatrix} {}^{t+\Delta t}\mathbf{M} + \gamma\Delta t\,{}^{t+\Delta t}\left(\mathbf{C}^{ep}+\mathbf{C}^{vf}\right) + \beta\Delta t^2\,{}^{t+\Delta t}\left(\mathbf{K}_L+\mathbf{K}_{NL}+\mathbf{K}_{CNL}\right) & {}^{t+\Delta t}\mathbf{Q} \\ \alpha'\,{}^{t+\Delta t}\mathbf{Q}^T & -\left({}^{t+\Delta t}\mathbf{H} + \dfrac{{}^{t+\Delta t}\mathbf{L}}{\Delta t}\right) \end{bmatrix} \begin{Bmatrix} {}^{t+\Delta t}\ddot{\mathbf{u}}_N \\ {}^{t+\Delta t}\mathbf{p}_E \end{Bmatrix} =$$

$$\begin{Bmatrix} {}^{t+\Delta t}\mathbf{T} - {}^{t+\Delta t}\left(\mathbf{C}^{ep}+\mathbf{C}^{vf}\right)\left({}^{t}\dot{\mathbf{u}}_N + (1-\gamma)\Delta t\,{}^{t}\ddot{\mathbf{u}}_N\right) - {}^{t+\Delta t}\left(\mathbf{K}_L+\mathbf{K}_{NL}+\mathbf{K}_{CNL}\right)\left(\left(\frac{1}{2}-\beta\right)\Delta t^2\,{}^{t}\ddot{\mathbf{u}}_N + \Delta t\,{}^{t}\dot{\mathbf{u}}_N\right) \\ \dfrac{\gamma^f}{k}\,{}^{t+\Delta t}\mathbf{Q}^T\left({}^{t}\dot{\mathbf{u}}_N + (1-\gamma)\Delta t\,{}^{t}\ddot{\mathbf{u}}_N\right) + \dfrac{{}^{t+\Delta t}\mathbf{L}}{\Delta t}\,{}^{t}\mathbf{p} \end{Bmatrix} \tag{3.3.22}$$

where $\alpha' = \dfrac{\gamma^f}{g} - \dfrac{\gamma^f}{k}\gamma\Delta t$.

3.4 Demonstration of the Method

After the introducing the concept of fluidal elasto-plastic model and the governing equations FE-FD coupled method for saturated soil extended to three-dimensional analysis using updated Lagragian method and fluidal elasto-plastic model, the efficiency of this method is test with simple example in this section. Considering that the effectiveness of three dimensional FE-FD coupled method with updated Lagrangian method and the cyclic elasto-plastic model has been demonstrated in section 2.4, the task here is to test the three dimensional analysis using updated Lagrangian method and Newtonian viscous fluid model. The example is the simulation of a shaking table test with Newtonian viscous fluid model considering large deformation.

The lateral spreading experiment of liquefied sand in the inclined soil container on the shaking table was done (Hamada et al., 1994). In this experiment, the shaking was stopped after the model ground was liquefied, then the soil container was gradually inclined. Then the liquefied soil flew driven by gravity. The main feature of this experiment was that the lateral spreading occurred without excitation.

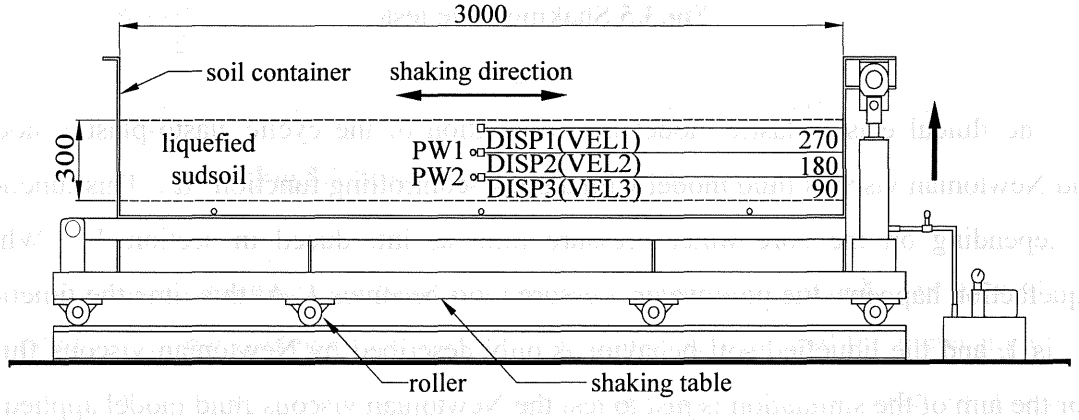

Fig.3.4 Test over view

The general view of the experiment is shown in **Figs.3.4** and **3.5**. The foundation ground was Enshunada sand (Dr=40%) whose parameters are same with the parameters in section 2.4.1 shown as **Table.2.1**. The model ground was set to be the homogeneous

loose condition using the boiling method in which the model ground was stired by rapidly pouring water from the bottom of the soil container. The measurements of displacements and velocities were carried out in the center of the soil with three different depths, d_1=0.03m, d_2=0.12m, d_3=0.21m.

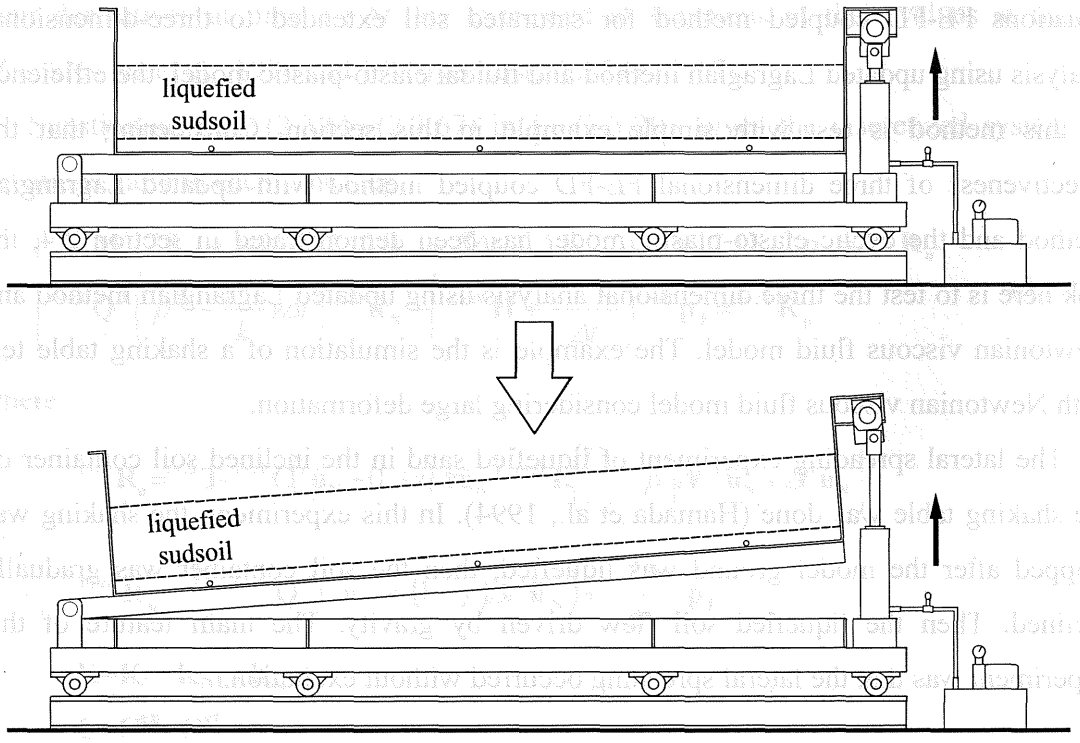

Fig.3.5 Shaking table test

The fluidal elasto-plastic model is combination of the cyclic elasto-plastic model and Newtonian viscous fluid model with a phase-controlling function α. This function is depending on the pore water pressure ratio as introduced in section 3.2. When liquefaction happens, the pore water pressure ratio becomes 1. At this time the function α is 1, and the liquefied soil behavior is only described by Newtonian viscous fluid. For the aim of the simulation is just to test the Newtonian viscous fluid model applied to three dimensional FE-FD coupled method with updated Lagrangian formulation, the simulation starts from inclining the soil container by neglecting of the shaking part. In this case, the input acceleration history is only representative gravitational force of shown in **Fig.3.6**.

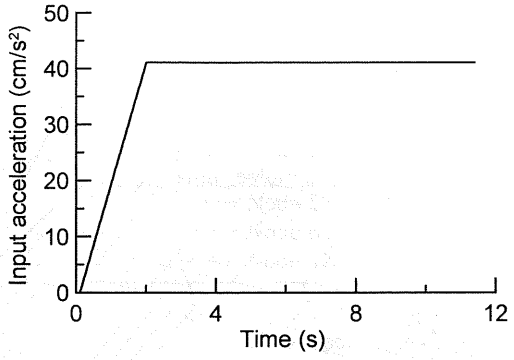

Fig.3.6 Input acceleration history

As a comparison, the result of another simulation of this experiment (Uzuoka, 2000) with Eulerian analysis method is used here. The simulation result of velocities with three different depths using Eulerian method is given in **Fig.3.7**. It is found that the horizontal flow velocities of liquefied soil increases in the beginning and reaches a peak value. After that time, the velocities of flow slow down gradually until return to 0.

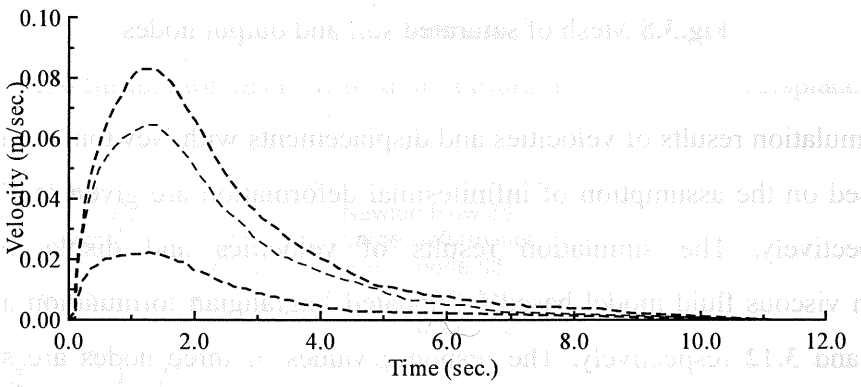

Fig.3.7 Simulation result with Eulerian method

The mesh of simulation used in this section is shown as **Fig.3.8**. The size of the saturated soil in the container is 3 meters long, 2 meters wide and 0.3 meter high. For constraint of boundary condition, the bottom nodes are fixed, the nodes on the four vertical surfaces are free to move on the surfaces and upper nodes are free to move in three directions. Drainage is allowed only on the top surface of the mesh. The inclination happens gradually during the first two seconds. The angle of inclination of the soil container is 4.2%. About the viscous parameters of Enshunada sand used here, the viscous coefficient μ' is set to 0.3, the second viscous coefficient λ' is set to 0.

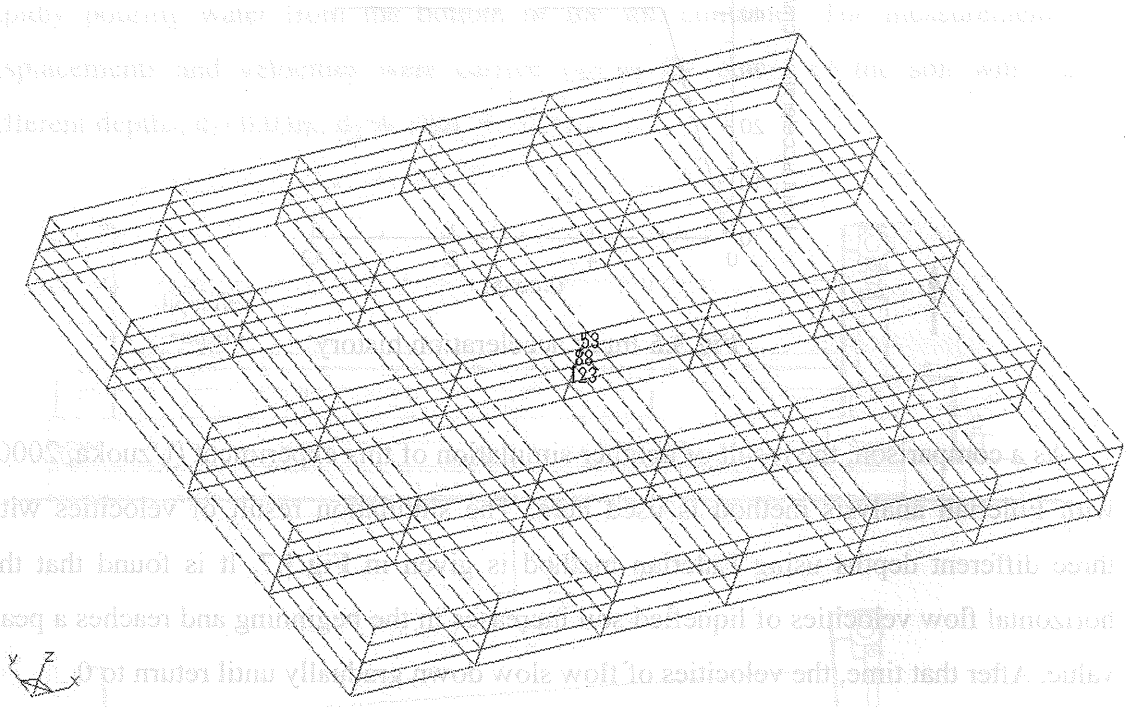

Fig.3.8 Mesh of saturated soil and output nodes

The simulation results of velocities and displacements with Newtonian viscous fluid model based on the assumption of infinitesimal deformation are given in **Figs.3.9** and **3.10** respectively. The simulation results of velocities and displacements with Newtonian viscous fluid model based on updated Lagrangian formulation are given in **Figs.3.11** and **3.12** respectively. The response values of three nodes are shown. The positions of three nodes are shown in **Fig.3.8**. As shown in **Fig.3.11**, using updated Lagrangian formulation, the flow velocities of liquefied soil increases in the first two seconds and reaches the peak value when inclining stops. Then the velocities decrease gradually and return to 0 finally. In **Fig.3.12**, the displacements of soil increase quickly at first and slow down gradually after the first two seconds. At last flow stops and the displacements reach a stable value. Rather well agreement is obtained in changing trend of velocities between the results of simulation with updated Lagrangian method and the analysis results with Enlerian method.

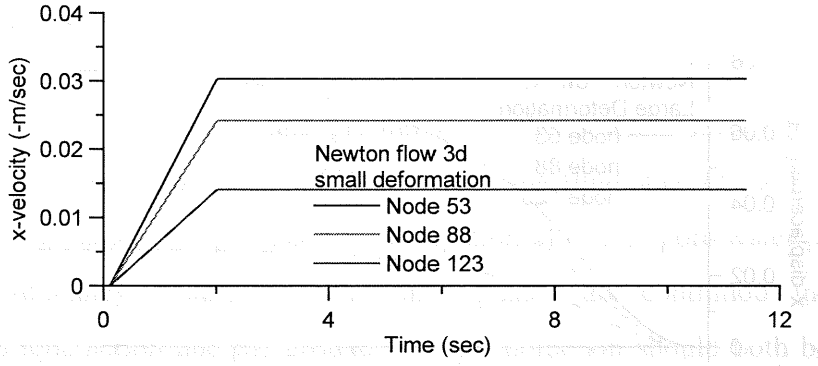

Fig.3.9 Simulation result with small deformation approach (velocity)

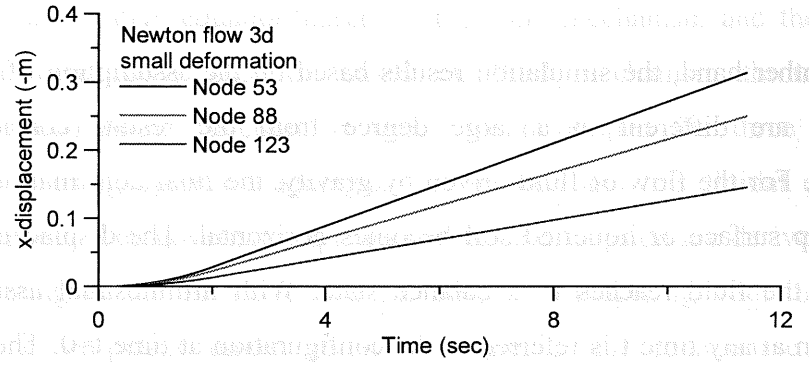

Fig.3.10 Simulation result with small deformation approach (displacement)

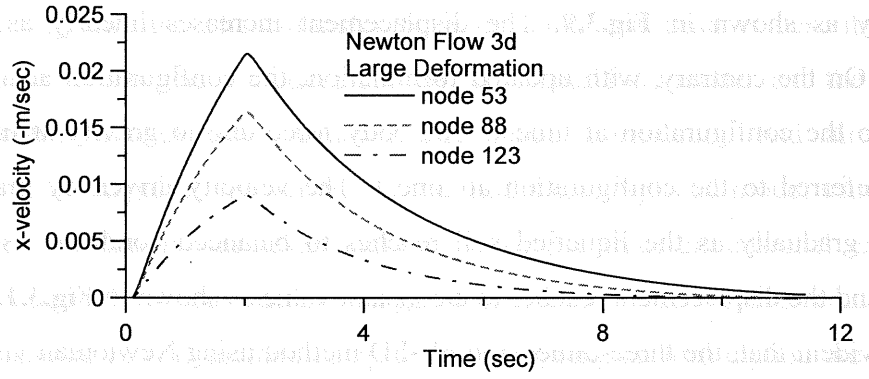

Fig.3.11 Simulation result with large deformation approach (velocity)

It is evident that there are differences between the maximum values of these two methods. Some factors cause the differences. One is the difference load acting method. In Eulerian analysis, the load is acted by adding horizontal initial gravity force. In the three dimensional simulation using Newtonian viscous fluid model and updated Lagrangian formulation, the load is acted by input acceleration history.

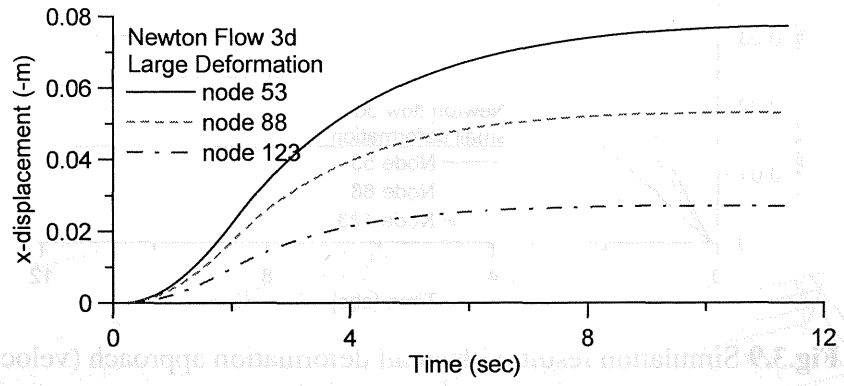

Fig.3.12 Simulation result with large deformation approach (displacement)

On the other hand, the simulation results based on the assumption of infinitesimal deformation are different in a large degree from the results considering large deformation. For the flow of fluid driven by gravity, the final deformation is obtained when the top surface of liquefied soil becomes horizontal. The displacement of fluid stops when the fluid reaches to a balance state. With infinitesimal assumption, the configuration at any time t is referred to the configuration at time t=0. The body force, gravity, is also referred to that at time t=0 without the effect of deformation. For this reason, the velocity keeps a constant value after reaching the maximum velocity caused by gravity as shown in **Fig.3.9**. The displacement increases linearly as shown in **Fig.3.10**. On the contrary, with updated formulation, the configuration at time t+dt is referred to the configuration at time t. The body force due to gravity at time t=dt is updated referred to the configuration at time t. The velocity driven by gravity force decreases gradually as the liquefied soil reaches to balanced condition as shown in **Fig.3.11** and the displacement reaches to a constant value as shown in **Fig.3.12**.

It is evident that, the three-dimension FE-FD method using Newtonian viscous fluid model and updated Lagrangian method is adaptive to analyze liquefied soil. Comparing the demonstration of three-dimension FE-FD method with the cyclic elasto-plastic model and updated Lagrangian method, it is concluded that the FE-FD method using fluidal elasto-plastic model and updated Lagrangian method is effective to analyze liquefaction and following flow phenomena.

3.5 Conclusion

The process of liquefaction and ground flow phenomenon is divided into three phases: the solid state before onset of liquefaction, the fluid state of the liquefied soil, and the recovered solid state produced by dissipation of excess pore water pressure and recovery of dilatancy. Changes in the three phases are continuous not separate phenomena. Liquefaction and the ground flow phenomenon should both be treated as solid and fluid behaviors. The fluidal elasto-plastic constitutive equation, with which to simulate the dynamic response of saturated loose sand by combining a cyclic elasto-plastic constitutive equation based on the solid mechanism and the Newtonian viscous fluid constitutive equation based on fluid mechanism through a phase transformation-controlling function, is used. We developed the three dimensional FE-FD method using updated Lagrangian formulation and this fluidal elasto-plastic constitutive model. The governing equations in three-dimension are derived to be used for implementing to the FE-FD numerical scheme. Comparing with the governing equations of elasto-plastic model given in chapter 2, the constitutive equation of Newton viscous fluid is introduced to the governing equations of three-dimensional FE-FD method using updated Lagrangian formulation here.

Considering that the phase-transfer between solid and fluid is described by the combination of elasto-plastic model and Newton viscous fluid model, and the efficiency of elasto-plastic model using updated Lagrangian formulation had already been demonstrated in chapter 2, the validity of the fluidal elasto-plastic model using updated Lagrangian formulation was tested only by a simple three-dimensional example of Newton viscous flow considering large deformation. The results calculated by three-dimensional FE-FD method using updated Lagrangian formulation are compared with the results of FE-FD method with infinitesimal assumption. It is evident that this method is adaptive to analyze liquefied soil and the results are more reasonable than the later one. The results are also compared with that obtained by Eulerian method. Rather well agreement is obtained in time changing trend of velocities between the results of simulation using updated Lagrangian method and that obtained by Enlerian method. The simulation result of liquefaction with this method is much closer to a real liquefaction process, especially in the flow of liquefied soil.

References

[1] Sato T, Moon Y, Uzuoka R. Unified analysis of liquefaction and the ground ploe phenomenon by the fluidal elasto-plastic constitutive equation International Journal for Numerical and Analytical Methods in Geomechanics, October 2002. (under examination)

[2] Sato T, Moon Y, Uzuoka R. Unified Interpretation on Pre and Post Liquefaction Process of Ground Workshop on large deformation of liquefied soil, Cornell University, USA, August 2000.

[3] Shibata T, Oka F, Ozawa Y. Characteristics of ground deformation due to liquefaction. Soils and Foundations, Special Issue on Geotechnical Aspects of the January 17 1995 Hyogoken-Nambu Earthquake 1996; 1:65-79.

[4] Tokimatsu K, Mizuno H, Kakurai M. Building damage associated with geotechnical problems. Soils and Foundations, Special Issue on Geotechnical Aspects of the January 17 1995 Hyogoken-Nambu Earthquake 1996; 1:219-234.

[5] Tokimatsu K, Asaka Y. Effects of liquefaction-induced ground displacements on pile performance in the 1995 Hyogoken-Nambu earthquake. Soils and Foundations, Special Issue on Geotechnical Aspects of the January 17 1995 Hyogoken-Nambu Earthquake 1998; 2:81-98.

[6] Hamada M, Sato H, Kawakami T. A consideration of the mechanism for liquefaction-related large ground displacement. Proceedings from the Fifth U.S-Japan Workshop on Earthquake Resistant Design of Lifeline Facilities and Countermeasures Against Soil Liquefaction, Technical Report NCEER-94-0026 1994; 217-232.

[7] Yasuda S, Ishihara K, Harada K, Shinkawa N. Effect of Soil Improvement on ground Subsidence due to Liquefaction. Soils and Foundations, Special Issue on Geotechnical Aspects of the January 17 1995 Hyogoken-Nambu Earthquake 1996; 1:99-108.

[8] Inagaki H, Iai S, Sugano T, Yamazaki H, Inatomi T. Performance of caisson type quay walls at Kobe port. Soils and Foundations, Special Issue on Geotechnical Aspects of the January 17 1995 Hyogoken-Nambu Earthquake 1996; 1:119-136.

[9] Kamon M, Wako T, Isemura K, Sawa K, Mimura M, Tateyama K, Kobayashi S. Geotechnical disasters on the waterfront. Soils and Foundations, Special Issue on Geotechnical Aspects of the January 17 1995 Hyogoken-Nambu Earthquake 1996; 1:137-147.

[10] Ishihara K, Yasuda S, Nagase H. Soil characteristics and ground damage. Soils and Foundations, Special Issue on Geotechnical Aspects of the January 17 1995 Hyogoken-Nambu Earthquake 1996; 1:109-118.

[11] Hamada M, Yasuda S, Isoyama R, Emoto K. Observation of permanent ground displacements induced by soil liquefaction. Proceedings of the society of civil engineers 1986; 376/ III-6:211-220 (in Japanese) .

[12] Hamada M, Wakanatsu K. A study on ground displacement caused by soil liquefaction. Journal of geotechnical engineering, Japan society of civil engineers 1998; 596(III.43):189-208 (in Japanese) .

[13] Ishihara K. Liquefaction and flow failure during earthquakes. Geotechnique 1993; 43/3:351-415.

[14] Yoshida N. The mechanism of a ground flow accompanying liquefaction. Symposium about the ground flow and permanent displacement of the foundation and the ground structure in case of an earthquake, The Japanese Geotechnical Society 1998; 109:53-70.

[15] Yasuda S, Yoshida N, Masuda T, Nagase H, Mine K, Kiku H. Stress-strain relationships of liquefied sands. Proceedings of IS-TOKYO'95 / The first international conference on Earthquake Geotechnical Engineering 1995; 2:811-816.

[16] Oka F, Yashima A, Tateishi A., Taguchi Y, Yamashita S. A cyclic elasto-plastic constitutive model for sand considering a plastic-strain dependence of the shear modulus." Geotechnique 1999; 49(5):661-680.

[17] Hashiguchi K, Chen Z -P. Elastoplastic constitutive equation of soils with the subloading surface and the rotational hardening. International journal for numerical and analytical methods in geomechanics 1998; 22(3):197-227.

[18] Zienkiewicz OC, Shiomi T. Dynamic behavior of saturated porous media; The generalized Biot formulation and its numerical solution. International journal for numerical and analytical methods in geomechanics 1984; 8(1):71-96.

[19] Yasuda S, Yoshida N, Adachi K, Kiku H, Gose S, Masuda T. A simplified practical method for evaluating liquefaction-induced flow. Journal of geotechnical engineering, Japan society

of civil engineers 1999; 638(III.49):71-89 (in Japanese).

[20] Shamoto Y, Zhang J M, Tokimatus K. New charts for predicting large residual post-liquefaction ground deformation. Soil Dynamics and Earthquake Engineering 1998; 17:427-438.

[21] Aydan Ö. The dynamic shear response of an infinitely long visco-elastic layer under gravitational loading. Soil Dynamics and Earthquake Engineering 1994; 13:181-186.

[22] Tamate S, Towhata I. Numerical simulation of ground flow caused by seismic liquefaction. Soil Dynamics and Earthquake Engineering 1999; 18:473-485.

[23] Uzuoka R, Yashima A, Kawakami T, Konrad J -M. Fluid dynamics based prediction of liquefaction induced lateral spreading. Computers and Geotechnics 1998; 22(3/4):243-282.

[24] Tatsuoka F, Yasuda S, Iwasakai T, Tokida K. Normalized Dynamic Undrained Strength of Sand Subjected to Cyclic and Random Loading. Soils and Foundations 1980; 20(3):1-16.

[25] Towhata I, Vargas-Monge W, Orense R P, Yao M. Shaking table tests on subgrade reaction of pipe embedded in sandy liquefied subsoil. Soil Dynamics and Earthquake Engineering 1999; 18:347-361.

[26] Biot MA. Mechanics of deformation and acoustic propagation in porous media. Journal of Applied Physics 1962; 33(4):1482-1498.

[27] Oka F, Yashima A, Shibada T, Kato M, Uzuoka R. FEM-FDM coupled liquefaction analysis of a porous soil using an elasto-plastic model. Applied Scientific Research 1994; 52:209-245.

[28] Akai K, Tamura T. Numerical analysis of multi-dimensional consolidation accompanied with elasto-plastic constitutive equation. Proceedings of the society of civil engineers 1978; 269(III):95-104.

[29] Hamada M, Shimamura K, Yanase K, Nakamura M, Tanaka A. A study for the flow characteristic of the liquefied soil. The second symposium on Enhancement of Earthquake Performance of Infrastructures Based on Investigation Into Fracturing Process 2000; 261-266 (in Japanese).

Chapter 4

3-D Dynamic Nonlinear Analysis of Embankment and Soil-Pile Interaction Considering Large Deformation

4.1 Introduction

Soil structures such as river dikes, high way embankments and earth dams have been frequently damaged during past major earthquakes. This damage was often mainly due to liquefaction of the embankment and foundation soils. The large displacement of the liquefied soil during the earthquake also caused damage to pile foundation severely. Liquefaction of soil shows strong nonlinearity which leads to large deformation. The effective constitutive model of liquefiable soil and the numerical methods dealing with large deformation are needed in the analysis of liquefaction.

In this chapter, two numerical examples of seismic analysis of embankment constructed on liquefiable soil and soil-pile interaction analysis are presented. Two constitutive model of saturated soil, the effective cyclic elasto-plastic model and the

fluidal elasto-plastic model are adopted in the examples to describe the material nonlinearity of the liquefiable soil. Three-dimensional nonlinear finite element method using updated Lagrangian formulation introduced in chapters 2 and 3 is used in order to deal with the large deformation due to liquefaction. The efficiency of this method is also demonstrated in this chapter.

4.2 Simulation of Earthquake Response of Embankment

4.2.1 Analysis Condition

As shown in **Fig. 4.1**, an embankment is constructed on saturated sand with 16m deep which is shaken by an earthquake acceleration time history in x-direction. The size is given in the figure.

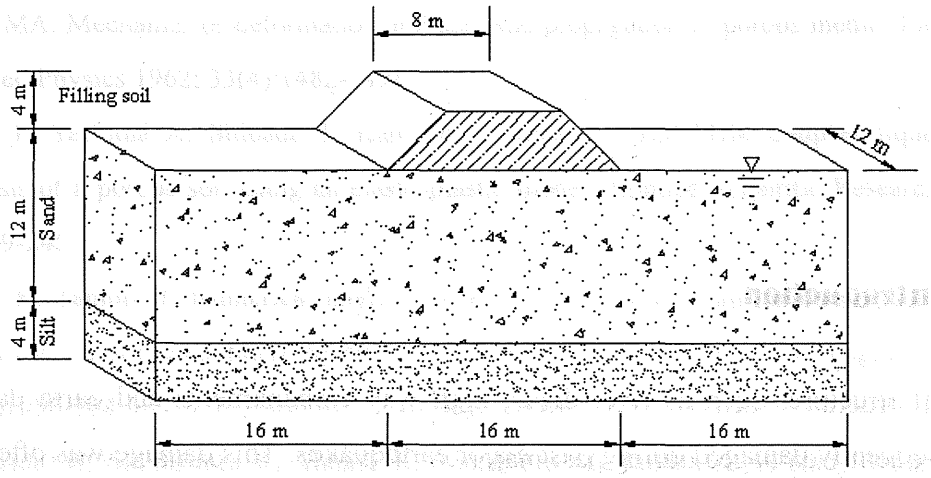

Fig. 4.1 Embankment example of 3-D analysis considering large deformation

The embankment is a kind of filling soil without pore water. The foundation soil includes two saturated soil layers, the upper one is a kind of saturated sand classified as As1 and the bottom layer is saturated silt classified as Ac1. Sand is easy to liquefy but silt is not liquefied. They are the real soil layers in Oki, Miyagi-ken, Japan. The parameters of these soils are given in **Table 4.1**.

Table 4.1 Soil parameters of embankment example

Material parameter	Sand	Silt	Filling soil
Density ρ(t/m^3)	1.700	1.700	1.900
Coefficient of permeability **k**(m/s)	1.0E-03	1.0E-06	1.0E-03
Initial void ratio e_0	0.900	2.000	0.900
Compression index λ	0.02	0.200	0.020
Swelling index κ	0.002	0.020	0.002
Initial shear modulus ratio G_0/σ_{m0}	570.2	514.2	907.0
Over consolidation ratio **OCR**	1.3	-	-
Phase transformation stress ratio M_m	1.158	1.336	1.158
Failure stress ratio M_f	1.013	1.169	1.013
Hardening parameter B_0	4500	1756	2700
Hardening parameter B_1	225	77	135
Hardening parameter C_f	-	1500	1500
Plastic reference strain γ^P	0.070	-	-
Elastic reference strain γ^E	0.008	-	-
Dilatancy parameter D_0	0.850	-	-
Dilatancy parameter **n**	0.450	-	-

The finite element mesh with 1134 elements is shown in **Fig. 4.2**. The displacement of bottom boundary are fixed. The nodes on the side boundary surfaces are allowed to slide on the surfaces. Drainage is allowed only on the top boundary surface of the mesh. The initial stresses of elements are calculated with gravity.

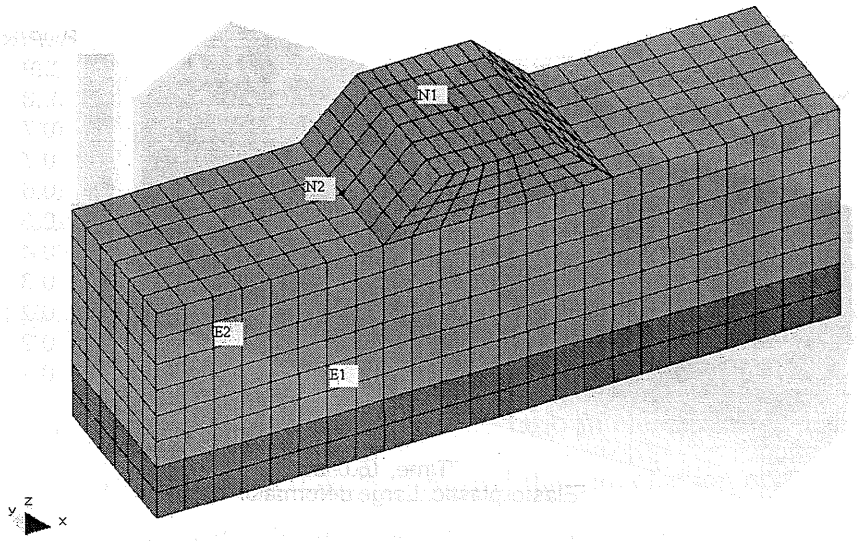

Fig. 4.2 Mesh of embankment example

The input earthquake acceleration history is shown in **Fig. 4.3**. It is recorded during the Miyagi-ken-Oki earthquake on May 26, 2003. The maximum value of the acceleration is 443 gal.

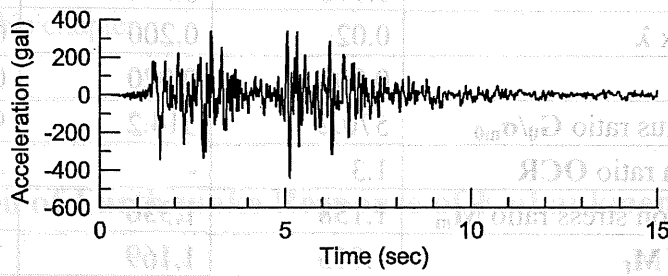

Fig. 4.3 Input acceleration history of embankment example

The effective cyclic elasto-plastic model (Oka, 1992) and the fluidal elasto-plastic model (Sato, 2000) are used as the constitutive model of saturated sand in the analysis.

4.2.2 Result of Analysis Using Elasto-Plastic Constitutive Model

First, the analysis result using elasto-plastic model is introduced. In **Figs. 4.4.** (a) and (b), the final meshes with excess pore water pressure ratio contours are given. They are the results obtained using updated Lagrangian formulation and infinitesimal deformation assumption. We can find not so much difference between the distributions of EPWPR.

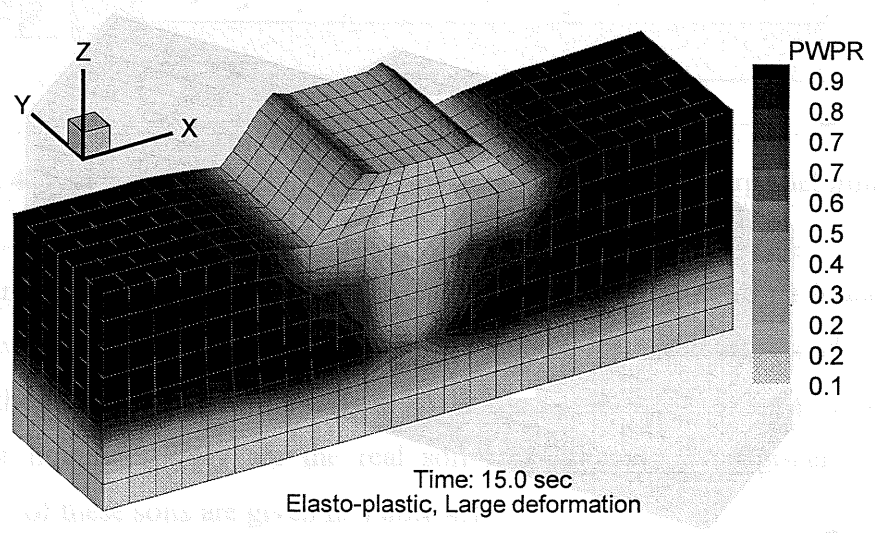

Fig. 4.4.(a) Deformed meshes and EPWPR contours with EP model (t=15.0 sec)

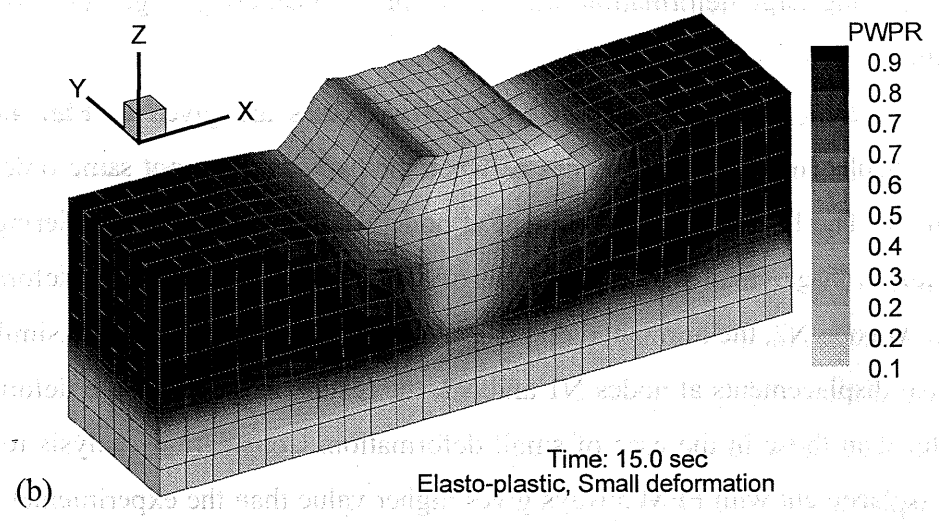

Fig. 4.4.(b) Deformed meshes and EPWPR contours with EP model (t=15.0 sec)

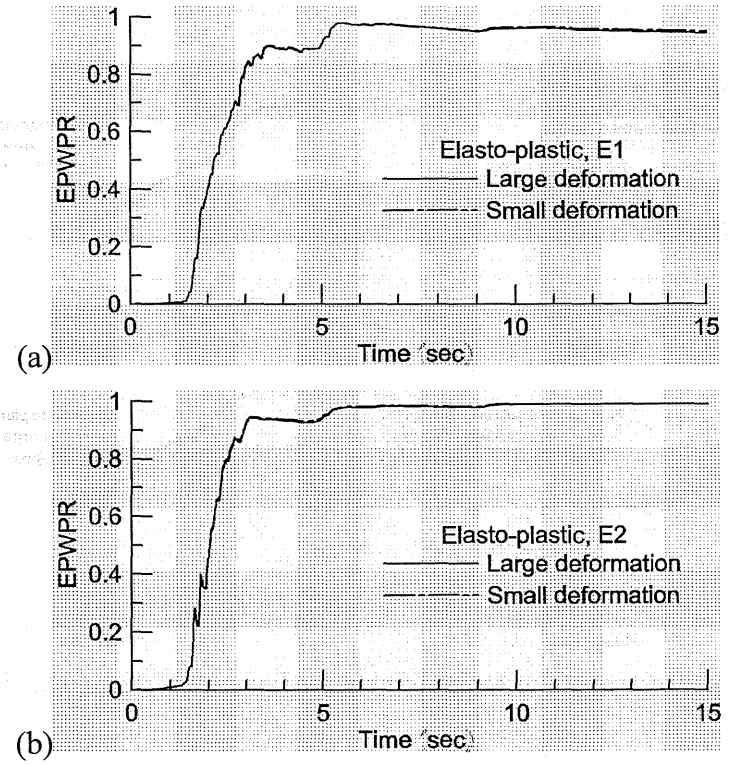

Fig. 4.5 EPWPR of embankment analysis with elasto-plastic model

The responses of excess pore water pressure ratio in elements E1 and E2 are given in **Figs. 4.5.** (a) and (b) respectively. We can find that liquefaction occurs at time t=3.0 second. The values of EPWPR do not reach 1.0 indicates that the degree of the liquefaction is not high. In this two elements, the difference of EPWPR between the

result considering large deformation and that without considering large deformation is very small.

The displacements at node N1 and N2 in two cases are given in **Fig. 4.6**. For horizontal displacement, the differences between the two cases are not same order from node to node. The horizontal displacement at node N1 in the case of considering large deformation is larger than that in the case of without considering large deformation evidently. At node N2, the horizontal displacements of the two cases are very similar.
For vertical displacements at nodes N1 and N2, the results in case of large deformation are smaller than those in the case of small deformation. Considering analysis result of vertical displacement with FEM always gives higher value than the experimental results reported in some references, the results in the case of considering large deformation , which give smaller vertical displacement, are more reasonable and accurate.

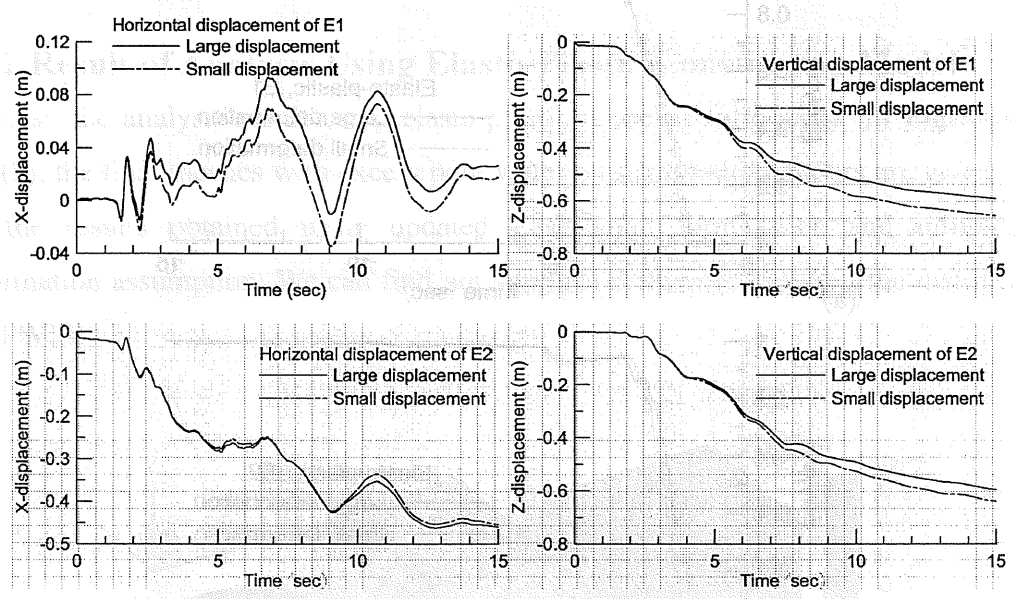

Fig. 4.6 Displacements of embankment analysis with elasto-plastic model

4.2.3 Result of Analysis Using Fluidal Elasto-Plastic Constitutive Model

This example is also analyzed using fluidal elasto-plastic model. The final mesh deformations with the contours of phase-transfer function α are given in **Fig. 4.7**. We can find the region treated as Newton viscous fluid or the region in phase transfer. This

will affect the dynamic behavior of the example model. We also can find the difference of the two cases, considering large deformation and without considering larger deformation, in the contours.

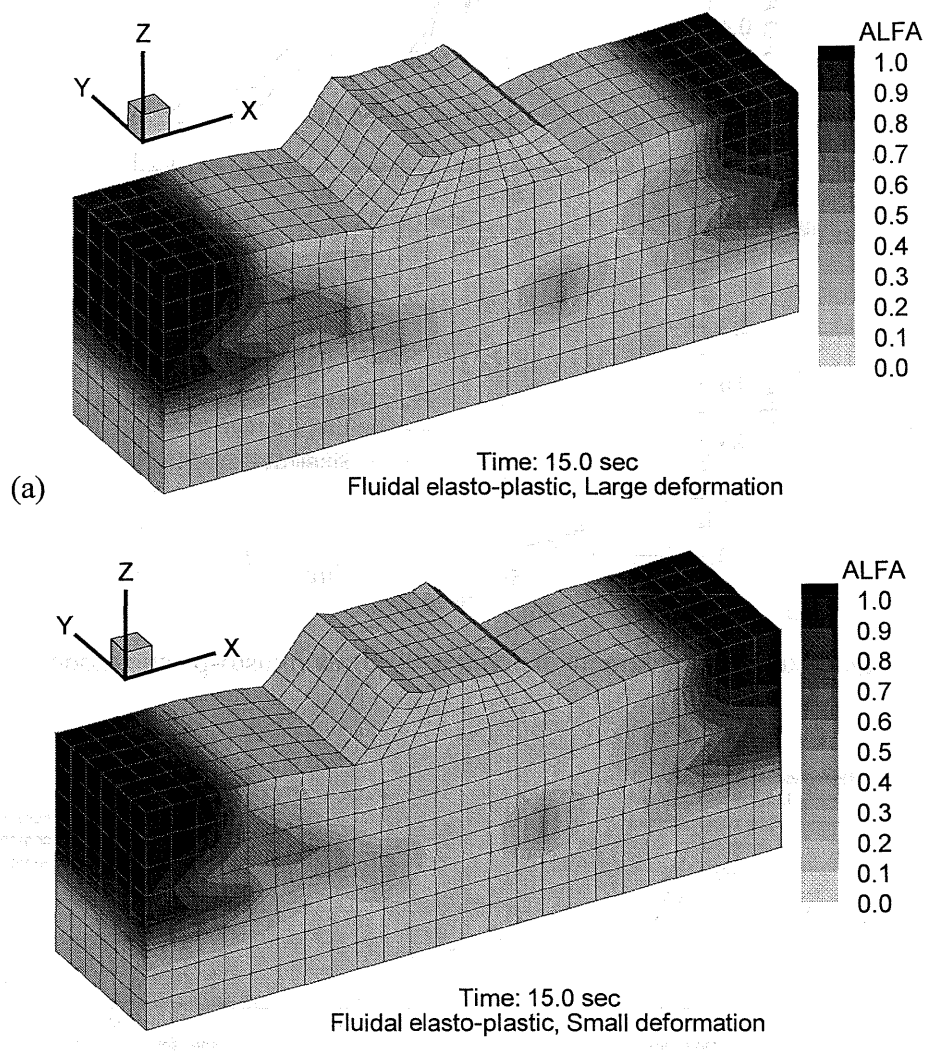

Fig. 4.7 Deformed meshes and α contours with FEP model (t=15.0 sec)

The responses of α in elements E1 and E2 are given in **Fig. 4.8**. Element E1 is in phase transfer condition after time t=5.0 second, but have not reach the liquefied soil to the pure Newton fluid condition. In element E2, the liquefied soil is treated as Newton viscous fluid at time t=10 second. We also can find the final status of phase from the α contours in **Fig. 4.7**. In element E2, the liquefied soil behave like Newton viscous fluid in the case of considering large deformation a little bit later time than in the case of

without considering large deformation.

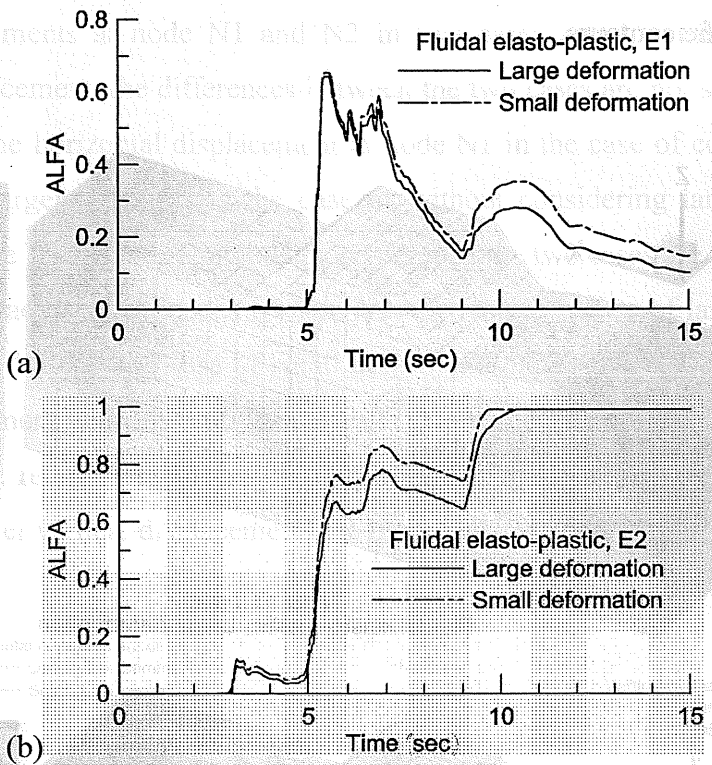

Fig. 4.8 α of embankment analysis with fluidal elasto-plastic model

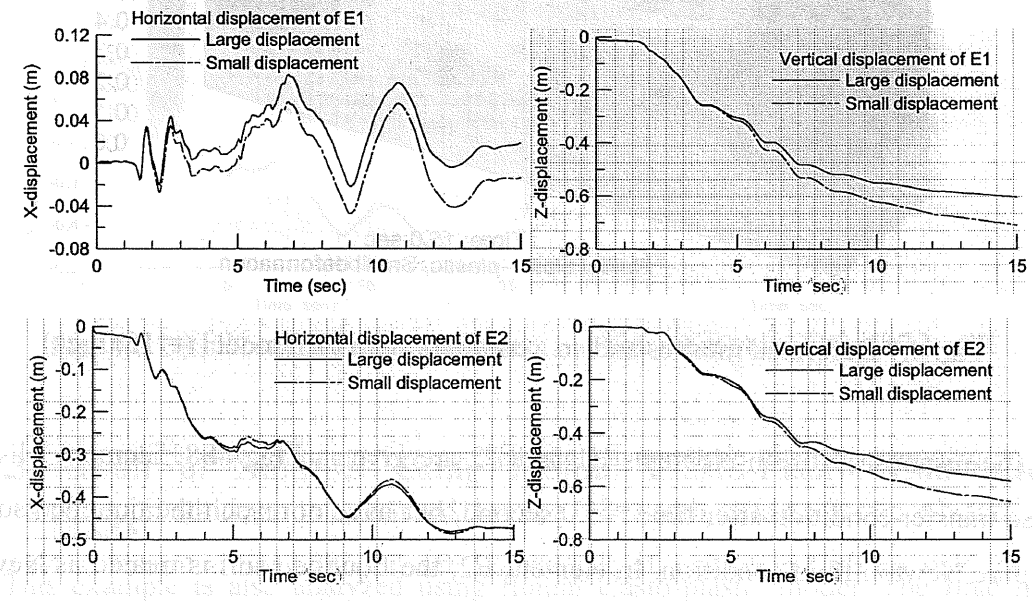

Fig. 4.9 Displacements of embankment analyzed with fluidal elasto-plastic model

The displacements at nodes N1 and N2 are given in **Fig. 4.9**. The differences

between the case of considering large deformation and the case of without considering large deformation are similar to the results calculated using elasto-plastic model. In fluidal elasto-plastic case, the differences of the displacements between the two cases are larger than that calculated using elasto-plastic model. The reason is that the fluidal elasto-plastic model gives larger displacement than the elasto-plastic model.

In general, 3-D FE analysis with updated Lagrangian formulation is applied effectively to the seismic analysis of embankment to deal with the large deformation of ground flow due to liquefaction.

4.3 Simulation of Soil-Pile Interaction

4.3.1 Analysis Condition

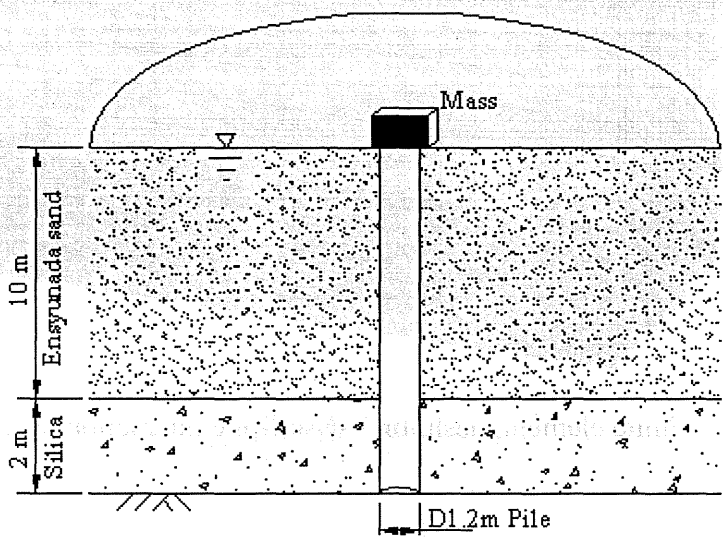

Fig. 4.10 3-D soil-pile interaction example

A concrete pile is derived in 12m-deep saturated sand and a 400kN mass is added on top of pile as the dead load from super structure as shown in **Fig. 4.10**. There are two kind of saturated sand, the upper one is saturated Edosaki sand 1 (Dr=40%) and the bottom one is the saturated silica. Edosaki sand 1 deforms in a large degree when liquefaction occurs, but the silica does not. The parameters of these saturated sands are

given in **Table 6.1**. The selected area of the soil is 42m long, and the diameter of the pile is 1.2m. The pile is resting in the center. The Yang's modulus of the pile is E=2.45E7 kN/m^2.

The effective cyclic elasto-plastic model developed by Oka and the fluidal elasto-plastic model developed by Sato are used as the constitutive model of saturated sand in this analysis. These two constitutive models of saturated sand are introduced in detail in chapters 2 and 3. The pile is described with an elastic solid column model.

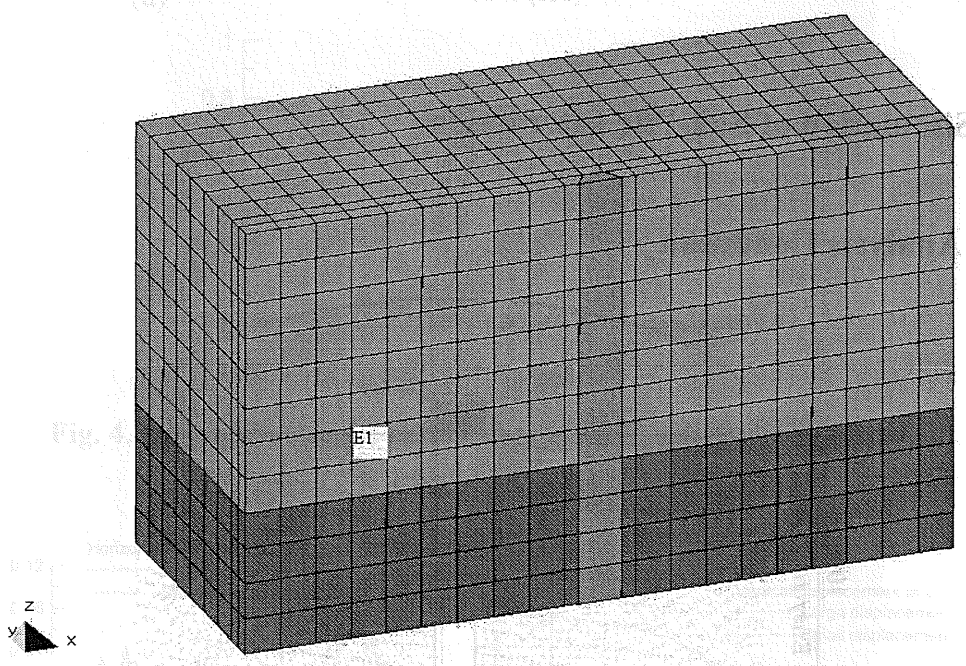

Fig. 4.11 Finite element mesh for 3-D soil-pile interaction example

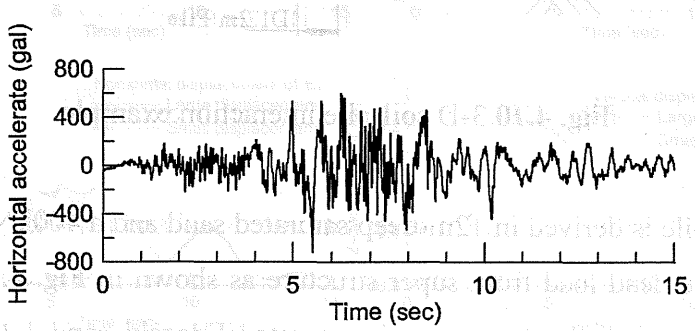

Fig. 4.12 Input acceleration history

The finite element mesh with 2268 elements is shown in **Fig. 4.11**. The fixed

boundary condition is given for the bottom nodes. The nodes on four side boundary surfaces are allowed to slide on the boundary surfaces. Drainage is only allowed on the top surface of the mesh.

The input acceleration history is shown in **Fig. 4.12** which is recorded during Hyogoken-Nanbu earthquake. The maximum value of the input acceleration is 722 cm/sec^2.

4.3.2 Result of Analysis Using Elasto-Plastic Constitutive Model

At first, the effective cyclic elasto-plastic model is used in the seismic analysis of this soil-pile interaction system. Updated Lagrangian formulation is adopted in the finite element governing equation to deal with the large deformation of liquefied sand.

The final deformed mesh of soil-pile interaction system analyzed with infinitesimal deformation assumption and updated Lagrangian formulation are shown in **Fig. 4.13.** (a) and (b) respectively. The contours of the excess pore water pressure ratio are also shown in the figures. We can find the EPWPR values of almost all elements are larger than 0.8 and the soil is in liquefied condition.

Because of the peak and trough distribution of the input acceleration are not uniform, liquefied soil has residual deformation in x-direction. The pile also declines acted by the deformation of liquefied soil and the inertia of the mass on the pile head.

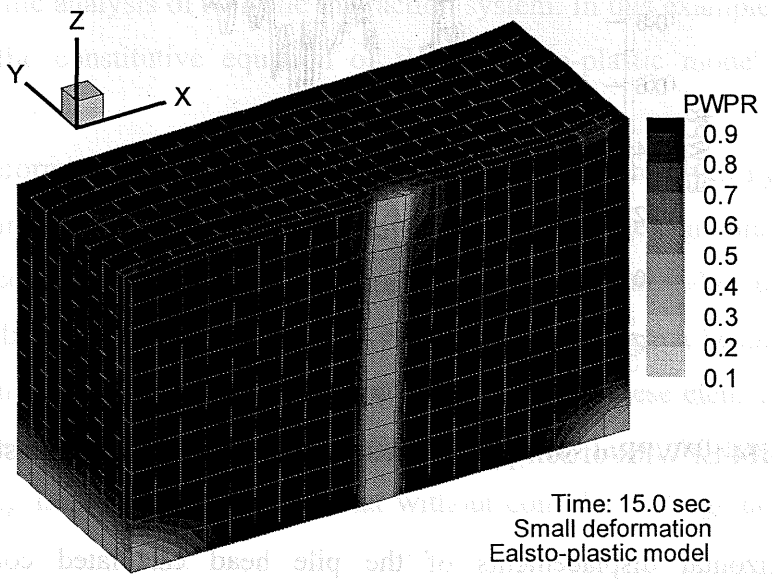

Fig. 4.13.(b) Final deformed meshes and EPWPR contours with EP model

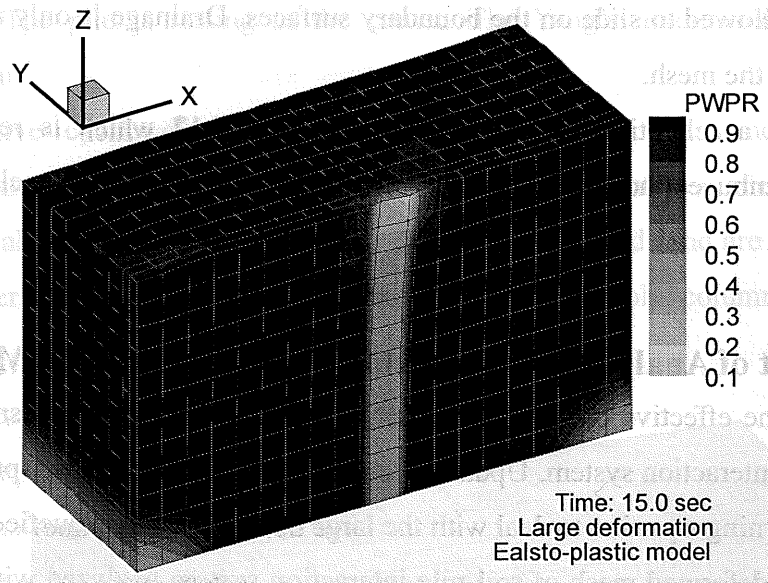

Fig. 4.13.(b) Final deformed meshes and EPWPR contours with EP model

The excess pore water pressure ratio response of the soil element E1 is shown in **Fig.4.14**. We can find that liquefaction of this element starts at time t=11.0-12.0 seconds.

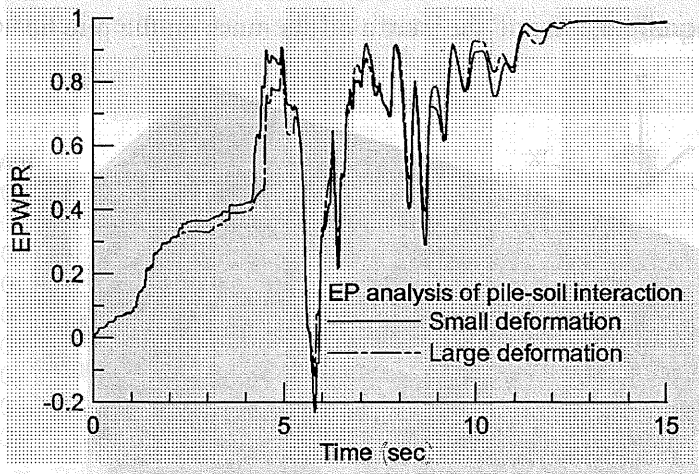

Fig. 4.14 EPWPR of soil-pile interaction analysis with elasto-plastic model

The horizontal displacements of the pile head calculated considering large deformation and without considering large deformation are shown in **Fig. 4.15**. Before the time t=11.0 second, the largest displacement is about 0.2m. At this time t=11.0

second, soil is liquefied according to **Fig. 4.14**. From this time, the displacements increase rapidly and reach to 0.5-0.57 m in a short time. The horizontal displacement value of pile head calculated with finite deformation theory is lower than that calculated with infinitesimal assumption.

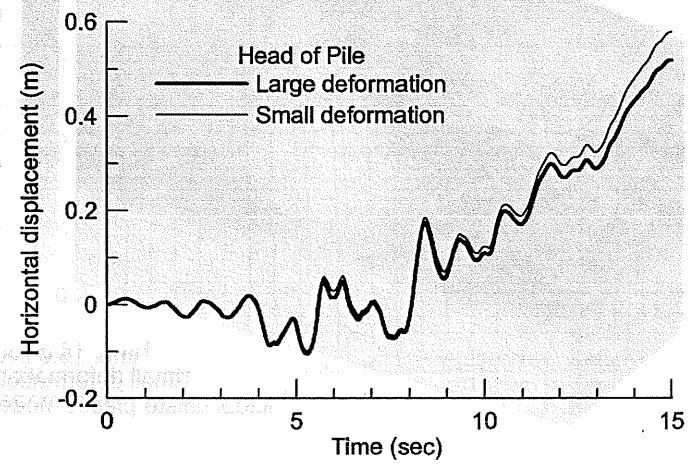

Fig. 4.15 Displacements of pile head with fluidal elasto-plastic model

4.3.3 Result of Analysis Using Fluidal Elasto-Plastic Constitutive Model

The fluidal elasto-plastic model is also used as the constitutive model of saturated sand in the seismic analysis of soil-pile interaction system. In this example, the viscous parameters in the constitutive equation of fluidal elasto-plastic model are $\lambda' = 0$, $\mu' = 0.3kPa$.

The final deformed meshes of soil-pile interaction system are given **Figs. 4.16.** (a) and (b). As an important index of fluidal elasto-plastic model, the contours of the phase transformation-controlling function, α, are shown in the figures. We can find that regions of liquefied soil behaves as Newton viscous fluid at where α becomes 1.0. The large part of soil is in phase transfer regions. The α value of these elements are larger than 0 and less than 1. Because the deformations are not very large, the difference of the mesh considering large deformation and that without considering large deformation is not evident.

The α time history of element E1 are given in **Fig. 4.17**. We can find that element E1 is described by elasto-plastic model in the beginning. The phase transfer happens at time

t=11.0 second and soil turns to Newton viscous fluid at time 12.0 second with α =1.0.

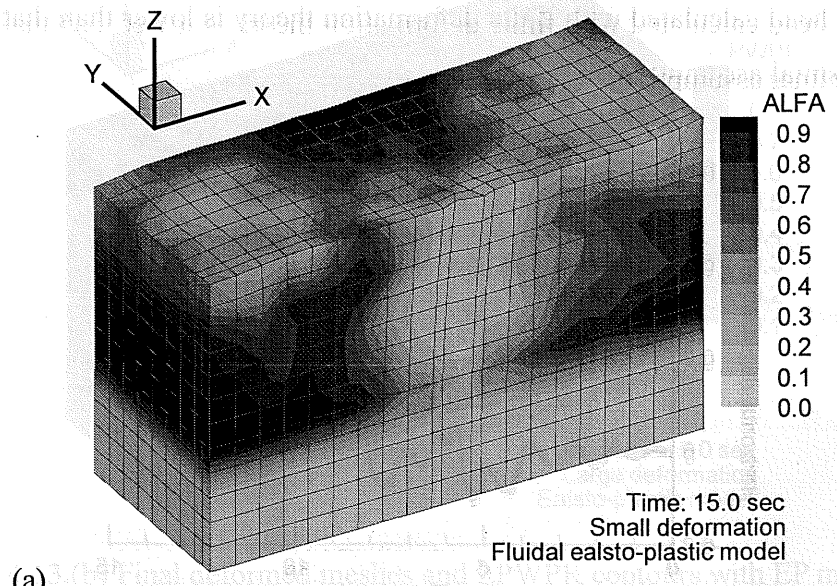

(a)

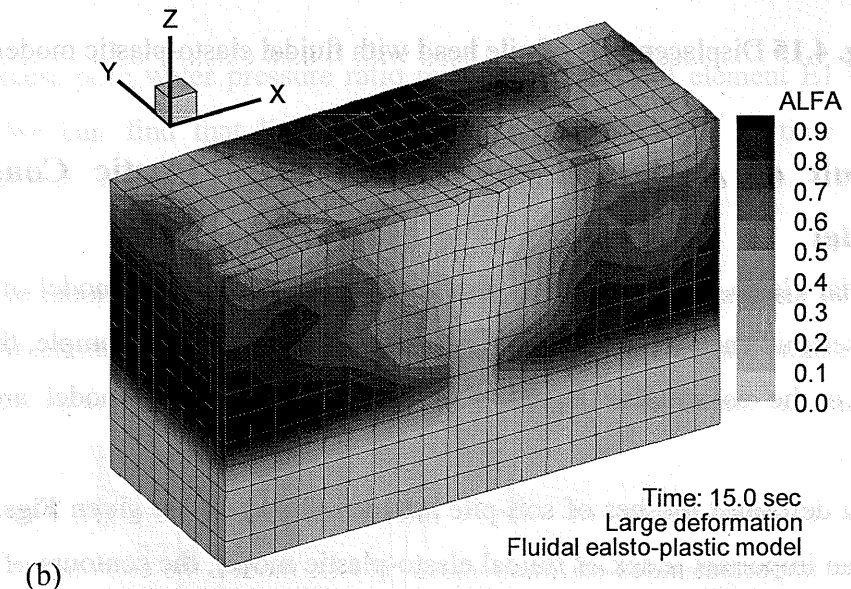

(b)

Fig. 4.16 Final deformed meshes and α contours with FEP model

The horizontal displacements of the pile head calculated with fluidal elasto-plastic constitutive model considering large deformation and without considering large deformation are given in **Fig. 4.18**. Before the time t=11.0 second, the largest displacement is about 0.2m as same as **Fig. 4.15**. At time t=11.0 second, soil is liquefied in a large degree and the phase transfer starts in large parts of the mesh as shown in **Fig. 4.15**. From that time, the displacements increase rapidly and reach to a value larger than

0.6 m. The horizontal displacement value of pile head calculated with finite deformation theory is lower than that calculated with infinitesimal assumption, as shown in **Fig. 4.18**.

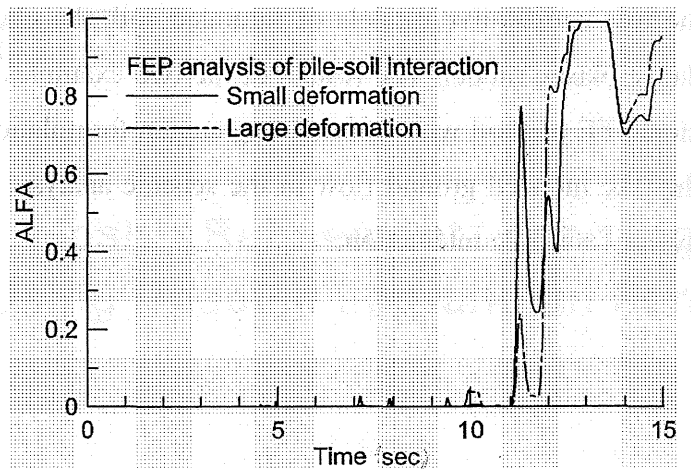

Fig. 4.17α of soil-pile interaction analysis with fluidal elasto-plastic model

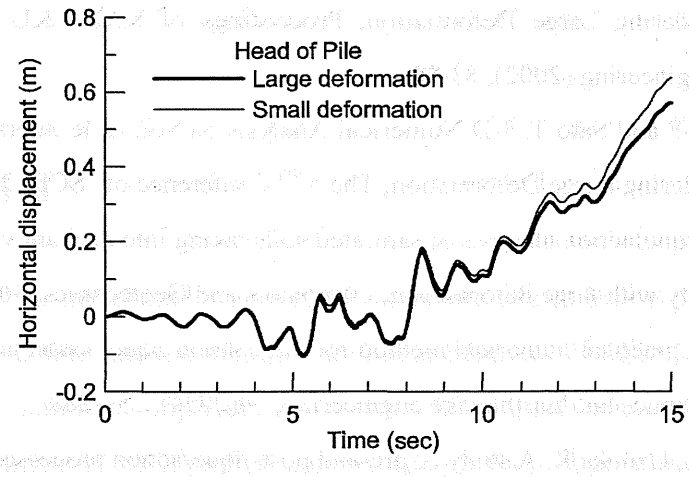

Fig. 4.18 Displacements of pile head with fluidal elasto-plastic model

4.4 Conclusion

In this chapter, two numerical examples are analyzed with two constitutive models of saturated soil and three-dimensional FE method using updated Lagrangian

formulation. The two constitutive models are used to describe the material nonlinearity of liquefiable soil and the FE method using updated Lagrangian formulation is used to deal with the geometric nonlinearity of liquefied soil with large deformation.

Three-dimensional FE method with updated Lagrangian formulation is adapted successfully to the two constitutive models of saturated soil, the elasto-plastic model and the fluidal elastic plastic model. The results of the two examples demonstrate that this three-dimensional FE method with updated Lagrangian formulation can effectively simulate the earthquake induced ground flow in the seismic analysis of soil structures and dynamic analysis of soil-pile interaction.

References

[1] Tang X and Sato T. Dynamic Analysis of Saturated Porous Medium by 3D FE-FD Coupled Method Considering Large Deformation, Proceedings of KAIST-KU Joint Seminar on Earthquake Engineering (2002), 83-88.

[2] Tang X, Zhang F and Sato T. 3-D Numerical Analysis on Soil -Pile Interaction of Liquefied Ground Considering Large Deformation, The 57th Conference of JSCE (2002).

[3] Di Y, Sato T. Liquefaction analysis of saturated soils taking into account variation in porosity and permeability with large deformation, Computers and Geotechnics, 30(2003), 623-635.

[4] Di Y, Sato T. A practical numerical method for large strain liquefaction analysis of saturated soils, Soil Dynamics and Earthquake engineering, 24(2004), 251-260.

[5] Moon Y, Sato T, Uzuoka R. A study of pre-and post-liquefaction processes for a caisson type quay wall using earthquake motion design, in: Proc. Of Aseisimic Design of Soils Structures from Earthquakes(Level 2), JGS Kansai Chapter, Osaka, 1998, 319-324(in Japanese).

[6] Sato T, Moon Y, Uzuoka R. Unified analysis of liquefaction and the ground ploe phenomenon by the fluidal elasto-plastic constitutive equation International Journal for Numerical and Analytical Methods in Geomechanics, October 2002. (under examination)

[7] Sato T, Moon Y, Uzuoka R. Unified Interpretation on Pre and Post Liquefaction Process of Ground Workshop on large deformation of liquefied soil, Cornell University, USA, August 2000.

Chapter 5

Adaptive Mesh Refinement for Liquefaction Analysis Using Updated Lagrangian Formulation

5.1 Introduction

As introduced in the chapters above, the effective cyclic elasto-plastic constitutive models was used to simulate the material nonlinear behavior of liquefiable soil. Updated Lagrangian formulation is implemented in FE-FD coupled scheme to deal with the geometrical non-linearity of liquefied soil. Although these algorithms are effective in simulating the nonlinear behavior of liquefied soil, some problems also should be noted. As a type of numerical approximation method, errors are inevitable in analysis results obtained by the finite element method. The finite element method solution does not always guarantee the desired accuracy, sometimes causing serious analysis problems. For example, in liquefaction analysis of saturated soil considering large deformation, when a coarse mesh is used to save time, error causes severe distortion of the elements and sometimes calculation stops unexpectedly. To maintain the accuracy of FEM during

the numerical analysis is a major concern to obtain stable computational results especially for the case of material nonlinearity and large deformation being involved.

The error treated in this chapter is that caused by discretization process in a FE method. Evidently, reducing the size of the elements uniformly during discretization minimizes error, but the number of nodes and elements are increased at the same time. That means a heavy burden of calculation. Our objective was to use a fine mesh in the area of large error and a normal or coarse mesh in the low error region. A method called the adaptive technique or adaptive mesh refinement has been developed successfully in many fields including solid and fluid mechanics, for linear and nonlinear problems, in order to solve static and transient behavior of 2 and 3 dimensional continua. The aim of this research is to apply the adaptive mesh refinement technique to the liquefaction analysis of soil considering large deformation.

An adaptive FE method, in which approximation is refined successively to reach a predetermined standard of accuracy, is essential for the effective use of finite element codes in practical analyses. The procedure, which refines the mesh of the finite elements according to an error indicator, has two parts: error estimate and mesh refinement. A main feature of this method is that it involves local, rather than global, refinement. In the error estimation, error is defined as the difference between the approximate and exact solutions of certain variables, such as displacement, stress, and strain. Generally, it is estimated by means of the energy norm or L_2 norm. Mesh refinement includes *h*-, *p*-, *hp*-, and *r*-refinement. *H*-refinement is the simple reduction of subdivision size, including remeshing and fission.

Here, *h*-adaptive mesh refinement method is applied to liquefaction analysis of saturated soil with updated Lagrangian formulation. The effective cyclic elasto-plastic model[1)-3)] based on Biot's two-phase mixture theory and the kinematic hardening rule was adopted as constitutive model of saturated soil. The u-p formulation was used for the governing equations that describe the coupled problem in terms of soil skeleton displacement and excess pore water pressure. The updated Lagrangian method was used in the formulation to account for large deformation. The dynamic equations were solved by the Newmark-β method. Linear four-node quadrilateral elements and linear 8-node hexahedral elements are used in the discretization of two-dimensional and three dimensional problems respectively. To estimate the error of saturated soil, a posteriori

error estimate procedure (Zienkiewicz and Zhu, 1992), which is carried out after the calculation of the incremental step. Error is evaluated by the L_2-norm of stress or strain. This error estimator depends on smoothing recovery techniques. Because it is impossible to obtain the exact value, the rather accurate variables is evaluated by a superconvergent patch recovery smoothing procedure (Zienkiewicz and Zhu, 1992) in order to make a comparison with the approximate solution. The calculation is very simple and easy to use in programming, and the result is reliable. A fission procedure[18)-20)] belonging to *h*-refinement was adopted for mesh refinement. After the calculation of one step, elements which exceed a given acceptable error limit are fissioned and the next step processed. One parent element is fissioned into 4 children elements for two-dimensional problem and eight children elements for three -dimensional problem. The flow chart of this procedure is given in **Fig.5.1**.

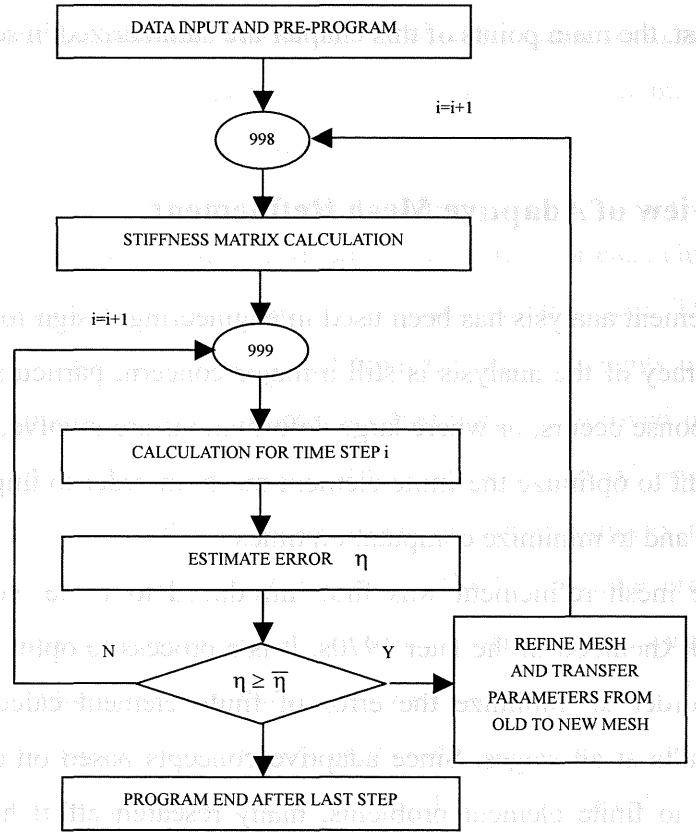

Fig.5.1 A posteriori error estimate and *h*-adaptive mesh refinement
($\bar{\eta}$ is the desired limit of relative error)

The application of this procedure to the coupled FE-FD method using the effective cyclic elasto-plastic model and updated Lagrangian method is studied in two-dimensional problem as well as in three-dimensional problem. This procedure is also modified in order to apply to the soil-pile dynamic analysis.

In this chapter, section 5.2 introduces the concept of adaptive mesh refinement and the selection of error estimator and mesh refinement algorithm. Section 5.3 presents the mehod to estimate error, a posteriori error estimate procedure depending on L_2-norm of stress or strain and superconvergent patch recovery method. The convergence of this error estimator in two-dimensional problem and three-dimensional problem is studied in section 5.4 with two examples of locally loaded on the surface of saturated soil. Section 5.5 introduces *h*-refinement algorithm including in fission process in soil elements and the technique to deal with the soil elements beside concrete elements of piles. In section 5.6, some simple examples are analysed to demonstrate applicability of the h-adaptive mesh refinement method. The efficiency of this method for liquefiable soil analysis is shown. At last, the main points of this chapter are summarized in section 5.7.

5.2 Overview of Adaptive Mesh Refinement

Finite element analysis has been used in engineering design for more than 30 years, but the accuracy of the analysis is still a major concern, particularly where non-linear material response occurs, or where large deformations are involved. For such cases, it is also important to optimize the finite element mesh, in order to improve the accuracy of computation and to minimize computation times.

Adaptive mesh refinement was first introduced to finite element calculation by Babuska and Rheinbolt in the later 1970s. It is a process to optimize the mesh of finite element in order to minimize the error of finite element calculation depending on previous results at all stages. Since adaptive concepts based on error estimators were first applied to finite element problems, many research effort has been dedicated to develop more efficient error estimators and mesh refinement algorithms. For the applications of adaptive mesh refinement to nonlinear problems, three-dimensional

problems and dynamic problems, especially to seismic analysis, researches have not been matured yet. In this study, adaptive mesh refinement is applied to seismic nonlinear analysis of saturated soil including liquefaction process, in both two-dimensional and three-dimensional problems.

There are three sources of numerical errors in the solution of nonlinear problems with the finite element method, namely:

1) Errors due to the finite element mesh discretization;
2) Errors due to the step sizes of the incremental analysis;
3) Errors due to the iterative solution of the nonlinear system of equations.

In this work, however, only errors arising from the mesh discretization are considered.

All adaptive mesh refinement procedures in finite element analysis include three stages:

1) Obtain a solution with any existing mesh and estimate the error;
2) Predict the error distribution in whole mesh and select elements to be refined;
3) Implement refinement techniques to refine the selected elements and transfer parameters from old mesh to new mesh.

Error estimate is the first and most important procedure of adaptive FE analysis. It gives an indication of the next step, mesh refinement. The error for each element, which is due to spatial discretization in the FEM, is calculated in this step. The elements, which need to be refined, can be distinguished from the other elements by comparing the errors with an acceptable limit. FEM accuracy therefore is improved in addition to saving degrees of freedom. There are two distinct types of general error estimates, recovery-based and residual-based one. Some effective error estimates method have been developed in the last decade: (a) Zienkiewicz-Zhu[12,14] simple error estimates criterion; (b) Belytschko-Tabbara[21] strain-projection criterion; (c) Diaz-Kikuchi-Taylor[27] interpolation criterion; (d) Zienkiewicz-Zhu[26,28,29] a posteriori error estimate procedure depending on superconvergent patch recovery. In the research of adaptive FE analysis of saturated soil conducted by Hu and Randolph[20], a posteriori error estimate procedure based on strain-projection criterion using L_2-projection of strain and superconvergent patch recovery was found worked well in evaluating the error to solve nonlinear soil response.

The main advantage of a posteriori error estimate procedure over other types of estimators is the simplicity of its implementation and its cost effectiveness. This is due to the fact that in practical finite element computations some smoothing procedures is always employed in the post-processing stage of the computing process to recover the derivatives of the finite element solution in order to achieve more acceptable approximations. Using such recovery derivatives, this error estimator can be calculated at a fraction of the total cost of the computation. In this research, a posteriori error estimate procedure based on L_2-projection of strain is adopted in adaptive FE analysis of liquefiable soil.

Considering that the error estimator adopted here is depending on recovery techniques, the selection of recovery scheme is also an important factor which affects the accuracy of error estimates. The recovery procedures developed so far can be classified as local (i.e., element-level), patch-based, and global procedure. The simple averaging of nodal stresses from adjacent elements is an example of the simplest patch-based stress recovery. Early attempts to employ global least-squares procedures to obtain continuous stress fields were not widely adopted. Instead, local element-level least-squares approaches appeared to be more attractive because of their intrinsic computational efficiency. However, the local schemes do not recover a continuous stress field, and a subsequent nodal averaging is generally used to achieve the stress continuity along element interfaces. With the recognition that certain interior stresses exhibit superconvergent properties, there evolved a class of local procedures involving 'projection' of these stresses to the element boundary, although other local procedures were also proposed.

Recent developments in recovery procedures have largely been motivated by the superconvergent patch recovery procedure developed by Zienkiewicz and Zhu[26,28,29]. Various modifications of the approach have been proposed subsequently. These procedures generally attempt to recover from the superconvergent value points to a value field with superconvergent properties. The latest formulation by Boroomand and Zienkiewicz[13] explored yet another polynomial patch-based procedure which uses nodal equilibrium rather than superconvergent values. In general, patch procedures are used to recover the values at nodes. If a node belongs to multiple patches, an averaging procedure must be used. The continuous value field is then defined in an ad hoc manner

by the nodal values and the finite element displacement interpolation functions. Superconvergent patch recovery procedure is applied to a posteriori error estimates in this research, and gives a recovered strain field of soil elements effectively.

If improvement of accuracy is taken as the target of the adaptive mesh refinement procedure and the error estimation gives a correct indication, then mesh refinement is the only way to the target. Various procedures exist for the refinement of finite element solution. There are four kinds of mesh refinement methods:

(1) *h*-refinement; reduce the size, *h*, of the elements in high error regions;

(2) *p*-refinement: increase the order, *p*, of the polynomial shape function in high error regions;

(3) *hp*-refinement: simultaneous application of both the *h*- and *p*-refinements;

(4) *r*-refinement: relocate the nodes.

Here, an *h*-adaptive technique is used in which the adaptive process is executed by element error measures in order to allocate elements for generating a mesh with the smallest number of elements and, at the same time, to obtain the required accuracy. The *h*-adaptive technique involves two methods: mesh regeneration and simple mesh refinement, a fission scheme.

Mesh regeneration is a means to regenerate a new mesh in the global mesh as indicated by the mesh density obtained in the error estimation process. Data transfer is needed also to move the elements and nodal variables from the old mesh to the new mesh. This of course can be expensive, especially in three dimensions where mesh generation is difficult for certain types of elements, and it also presents a problem of transferring data from one mesh to another.

The fission scheme refines the mesh by fissioning those elements with large error into smaller, equal-sized elements then transferring the variables of the nodes and elements from the old mesh to the new mesh by an interpolation procedure. Such a process is cumbersome as many hanging points are created where an element with mid-side nodes is joined to a linear element. On such occasions it is necessary to provide local constraints at the hanging points and the calculations become more involved. It is a direct refinement procedure used widely.

A comparison of these two schemes clearly shows that the latter involves less computation than the former. Data transfer in the latter scheme is local whereas in the

former it is global. Taking into account the thousands of time increment steps in the dynamic analysis, the fission scheme saves computation and improves accuracy. In this research, the fission procedure is applied to linear quadrilateral elements in two-dimensional adaptive FE analysis and to linear hexahedra elements in three-dimensional adaptive FE analysis.

5.3 Error Estimation Procedure

In this section, a posteriori error estimate procedure that depends on evaluating the L_2-norm of variables error and superconvergent patch recovery procedure, applied in this research, is introduced in detail. The formulations are derived for linear quadrilateral elements and linear hexahedra elements in two-dimensional problem and three-dimensional problem respectively. Two simple examples of compression of saturated soil in two-dimension and three-dimension are analysed to discuss the convergence of this error estimator.

5.3.1 Definition and Evaluation of Error

Error is defined as the difference between the exact solution and value of the finite element approximation. Variables considered in the error estimate are displacement, strain, and stress. For example, an error in strain is described as

$$e_{\varepsilon} = \varepsilon^* - \varepsilon^h \tag{5.3.1}$$

and an error in stress as

$$e_{\sigma} = \sigma^* - \sigma^h \tag{5.3.2}$$

where ε^* and σ^* are the exact solutions, ε^h and σ^h the values of the finite element approximation.

To explain the approximate value of FEM and the exact solution, a one-dimensional linear approximation of strain ε^h and ε^* is shown in **Fig.5.2**.

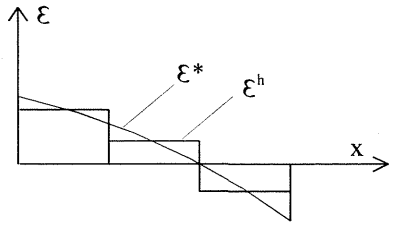

Fig.5.2 Approximate values and exact solution

The direct definitions of error described in Eqs.(5.3.1) and (5.3.2) are not convenient for use in the process of error estimation. Usually, scalar norms, such as energy norms or L_2 norms, are used to measure error. This scalar measure corresponds to the square root of the quadratic error. In this study, we used the L_2 norm to measure error, as it can be associated with errors of any quantity. For the strain (or stress) in the element *i*, the L_2 norm of the error, $\|e_\varepsilon\|_i$, is defined as

$$\|e_\varepsilon\|_i = \left(\int_{V_i} \{e_\varepsilon\}_i^T \{e_\varepsilon\}_i dv / V_i\right)^{1/2} \tag{5.3.3}$$

and the error of entire solution domain $\|e_\varepsilon\|$ is calculated by summing up the error of each element.

$$\|e_\varepsilon\| = \left(\sum_{i=1}^{nel} \|e_\varepsilon\|_i^2\right)^{1/2} \tag{5.3.4}$$

where *nel* is the total number of elements.

In the practical adaptivity process, a relative percentage error generally is used because it is more easily interpreted. The relative percentage error of solution is estimated using the error norm and the strain L_2-norm of entire solution domain. Its definition is

$$\eta = \frac{\|e_\varepsilon\|}{\sqrt{\|e_\varepsilon\|^2 + \|\varepsilon^h\|^2}} \times 100\% \tag{5.3.5}$$

where

$$\|\varepsilon^h\| = \left(\sum_{i=1}^{nel} \|\varepsilon^h\|_i^2\right)^{1/2} \tag{5.3.6}$$

The local error indicator for *i*-th element is defined in a similar way as

$$\eta_i = \left(\frac{\|e_\varepsilon\|_i^2}{\sqrt{\|e_\varepsilon\|^2 + \|\varepsilon^h\|^2}} \right)^{1/2} \times 100\% \tag{5.3.7}$$

It is clear that the energy and L_2 norms are related to the strain energy. This relationship is shown as follows:

Considering the physical relationship between the stress and strain,

$$\{\varepsilon\} = [D]^{-1}\{\sigma\} \tag{5.3.8}$$

The total potential energy, A, of a system predicted by the approximate solution of FEM is

$$A = \int_V \tfrac{1}{2}\{\sigma^h\}^T [D]^{-1}\{\sigma^h\} dv - \{R\}^T\{\bar{u}\} \tag{5.3.9}$$

where $\{R\}$ is the vector of the loads and the reaction acting on the nodes, $\{\bar{u}\}$ the vector of displacement on the nodes, and $[D]$ the stiffness matrix.

Assuming infinitesimal displacement $\{d\bar{u}\}$ on nodes, from the principle of virtual work,

$$\{R\}^T\{d\bar{u}\} = \int_V \{d\varepsilon^h\}^T\{\sigma^*\} dv \tag{5.3.10}$$

Substituting Eq. (5.3.10) in Eq. (5.3.9), the total potential energy is

$$A = \int_V \tfrac{1}{2}\{\sigma^h\}^T [D]^{-1}\{\sigma^h\} dv - \int_V \{\sigma^*\}^T\{\varepsilon^h\} dv$$

$$= \int_V \tfrac{1}{2}\{\sigma^h\}^T [D]^{-1}\{\sigma^h\} dv - \int_V \{\sigma^*\}^T [D]^{-1}\{\sigma^h\} dv \tag{5.3.11}$$

Eq. (5.3.11) can be rewritten;

$$A = \int_V \tfrac{1}{2}\{\sigma^h - \sigma^*\}^T [D]^{-1}\{\sigma^h - \sigma^*\} dv + c \tag{5.3.12}$$

where c is the constant without relation to nodal displacement.

Using another physical relationship between the stress and strain,

$$\{\sigma\} = [D]\{\varepsilon\} \tag{5.3.13}$$

By the same derivation method, the same conclusion for error of strain is

$$A = \int_V \tfrac{1}{2}\{\varepsilon^h - \varepsilon^*\}^T [D]\{\varepsilon^h - \varepsilon^*\} dv + c \tag{5.3.14}$$

From Eqs. (5.3.9) and (5.3.11), the total potential energy is interpreted as a weighted,

stress error squared quantity. When the size of an element is small enough, the un-weighted error squared quantity corresponds to the weighted error squared quantity. The relationship between the L_2 norm of error and the total potential energy is ensured. Because the L_2 norm of error is a positive definite function, the global L_2 norm of error is the sum of the local L_2 norms of error. Then the L_2 norm can be used to measure error, not only in the global mesh, but in a local element.

5.3.2 Smoothing Algorithm with Superconvergent Patch Recovery

In the error estimate process, the rather accurate values instead of the exact solution are used to calculate errors because the exact solution is not easy or impossible to obtain. Here, we use superconvergent patch recovery technique. It is a single and continuous polynomial expansion of the function describing the derivatives is used in an element patch surrounding the nodes at which recovery is desired. This expansion can be made to fit locally the superconvergent points in a least square manner or simply be an L_2 projection of the consistent finite element derivatives. In this technique, we assume that the nodal values belong to a polynomial expansion of the same complete order as the shape function and the polynomial expansion is valid over an element patch surrounding the particular assembly node considered. Such a "patch" represents a union of elements containing the vertex node. Illustration of typical patch for two-dimensional linear quadrilateral elements and three-dimensional hexahedra elements are shown in **Fig.5.3** and **Fig.5.4** respectively. This polynomial expansion will be used for nodal values of strain as:

$$\bar{\varepsilon}^* = \{P\}\{a\}^T \tag{5.3.15}$$

where {P} contains the appropriate polynomial terms and {a} is a set of unknown parameters. For four nodes quadrilateral element in two-dimension, they are given as:

$$\{P\} = \{1, x, y, z, xy\} \tag{5.3.16}$$

$$\{a\} = \{a_1, a_2, a_3, a_4\} \tag{5.3.17}$$

and for eight nodes hexahedra element in three-dimension, they are given as:

$$\{P\} = \{1, x, y, z, xy, yz, zx, xyz\} \tag{5.3.18}$$

$$\{a\} = \{a_1, a_2, a_3, \cdots, a_8\} \tag{5.3.19}$$

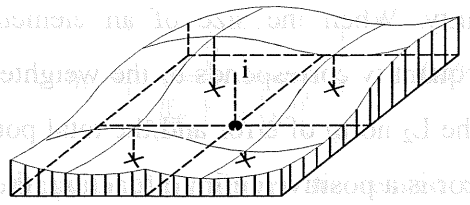

× Gauss point
• Patch assembly point,
Nodal value determined by SPR

Fig.5.3 Two-dimensional superconvergent patch recovery for quadrilateral elements

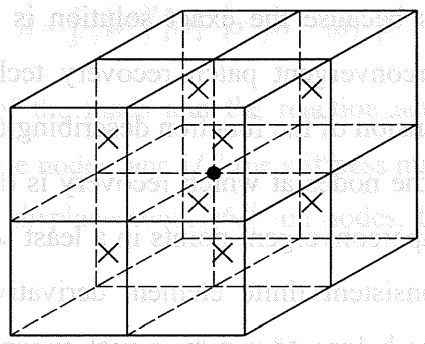

× Gauss points
• Patch assembly point
Nodal value determined by SPR

Fig.5.4 Three-dimensional superconvergent patch recovery for hexahedra elements

The unknown parameter $\{a\}$ of the expansion given in Eqs. (5.3.17) and (5.3.19) is determined by ensuring a least square fit of this expansion to the set of superconvergent or at least high accuracy sampling points existing in the patch considered if such points are available.

$$F(a)=\sum_{i=1}^{n}\left(\varepsilon^h(x_i,y_i)-\bar{\varepsilon}^*(x_i,y_i)\right)^2=\sum_{i=1}^{n}\left(\varepsilon_h(x_i,y_i)-\{P\}\{a\}^T\right)^2 \tag{5.3.20}$$

where (x_i, y_i) are the co-ordinates of a group of sampling points, n is the total number of sampling points. The minimization condition of $F(a)$ implies that $\{a\}$ satisfies

$$\sum_{i=1}^{n}\{P^T(x_i,y_i)P(x_i,y_i)\}\{a\}=\sum_{i=1}^{n}\varepsilon^h(x_i,y_i)\{P^T(x_i,y_i)\} \tag{5.3.21}$$

This can be solved in matrix form as

$$\mathbf{a} = \mathbf{A}^{-1}\mathbf{b} \tag{5.3.22}$$

where

$$\mathbf{A} = \sum_{i=1}^{n} \mathbf{P}^{\mathrm{T}}(x_i, y_i)\mathbf{P}(x_i, y_i) \qquad \text{and} \qquad \mathbf{b} = \sum_{i=1}^{n} \mathbf{P}^{\mathrm{T}}(x_i, y_i)\varepsilon^h(x_i, y_i)$$

The discrete expression form for quadrilateral elements in two-dimension is:

$$\begin{bmatrix} \sum_i P_1(\xi_i,\eta_i)P_1(\xi_i,\eta_i) & \cdots & \sum_i P_1(\xi_i,\eta_i)P_4(\xi_i,\eta_i) \\ \vdots & \ddots & \vdots \\ \sum_i P_4(\xi_i,\eta_i)P_1(\xi_i,\eta_i) & \cdots & \sum_i P_4(\xi_i,\eta_i)P_4(\xi_i,\eta_i) \end{bmatrix} \begin{Bmatrix} a_1 \\ \vdots \\ a_4 \end{Bmatrix} = \begin{Bmatrix} \sum_i P_1(\xi_i,\eta_i)\varepsilon_i^h \\ \vdots \\ \sum_i P_4(\xi_i,\eta_i)\varepsilon_i^h \end{Bmatrix} \tag{5.3.23}$$

where (ξ_i, η_i) are the normalized coordinates of a group of sampling points, as shown in **Fig.5.5**, they are calculated by

$$\xi_i = -1 + 2\frac{x_i - x_{min}}{x_{max} - x_{min}} \tag{5.3.24}$$

$$\eta_i = -1 + 2\frac{y_i - y_{min}}{y_{max} - y_{min}} \tag{5.3.24}$$

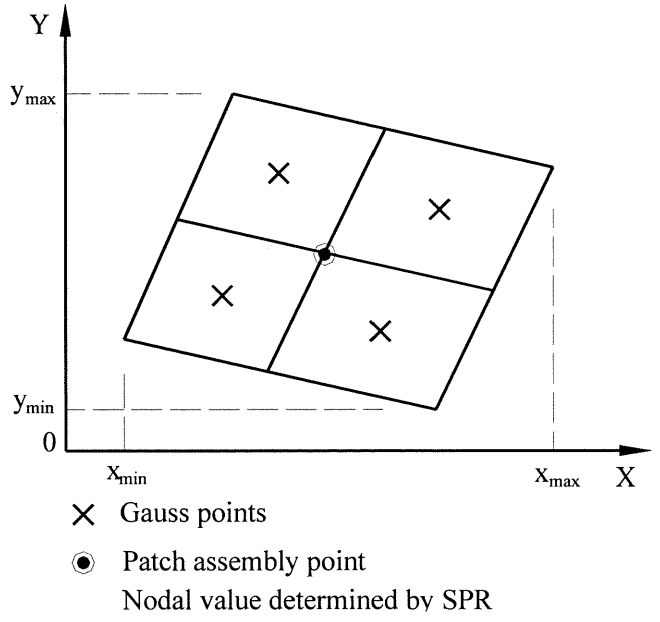

Fig.5.5 A patch of quadrilateral elements

The discrete expression form for hexahedra elements in three-dimension is:

$$\begin{bmatrix} \sum_i P_1(\xi_i,\eta_i,\zeta_i)P_1(\xi_i,\eta_i,\zeta_i) & \cdots & \sum_i P_1(\xi_i,\eta_i,\zeta_i)P_8(\xi_i,\eta_i,\zeta_i) \\ \vdots & \ddots & \vdots \\ \sum_i P_8(\xi_i,\eta_i,\zeta_i)P_1(\xi_i,\eta_i,\zeta_i) & \cdots & \sum_i P_8(\xi_i,\eta_i,\zeta_i)P_8(\xi_i,\eta_i,\zeta_i) \end{bmatrix} \begin{Bmatrix} a_1 \\ \vdots \\ a_8 \end{Bmatrix} = \begin{Bmatrix} \sum_i P_1(\xi_i,\eta_i,\zeta_i)\sigma_i^h \\ \vdots \\ \sum_i P_8(\xi_i,\eta_i,\zeta_i)\sigma_i^h \end{Bmatrix} \tag{5.3.24}$$

where (ξ_i,η_i,ζ_i) are the normalized coordinates of a group of sampling points in three-dimension and are calculated by the same way as in two-dimension.

In the case that an interior patch includes the elements with different levels of fission, no matter the number of elements in patch is 4 and 8 in two-dimension and three dimension respectively or less than the numbers, the Gauss nodes are enough to solve the Eqs.(5.3.23) and (5.3.24).

A more difficult situation arises at the domain boundary where a local patch may involve only one or two elements in two-dimension, one or four elements in three dimension. In these cases, the numbers of elements in the patches are insufficient for determination of the parameters and the nodal values on the corner or boundary. It can be solved in another way. The values of the nodes on corners or boundaries are determined from an interior patch shown in **Figs.5.6-5.7** and **Figs.5.8-5.10** for two-dimension and three-dimension respectively. Then the patches need not to be created when the patch assemble nodes are on corners or boundaries. However, all the boundary nodes values can be determined by interior patches instead of boundary patches and the results are equally accurate.

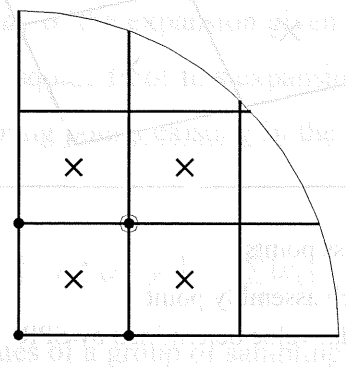

Fig.5.6 A patch of quadrilateral elements in corner

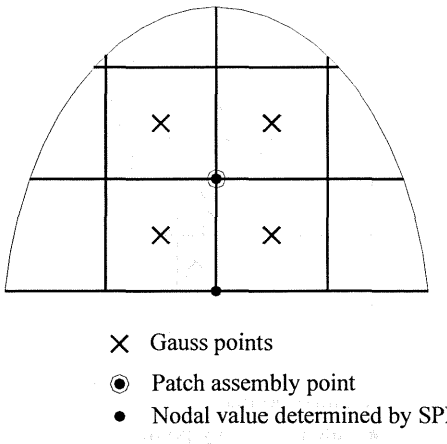

Fig.5.7 A patch of quadrilateral elements in boundary

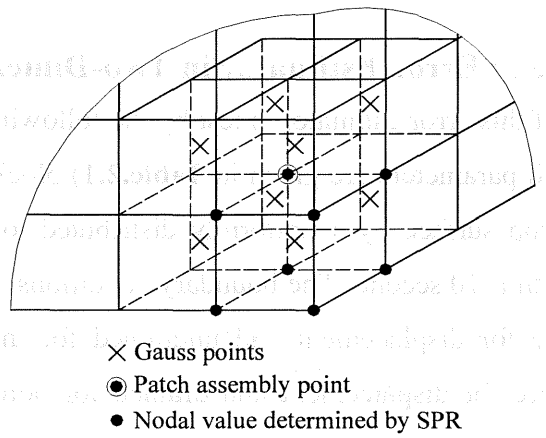

Fig.5.8 A patch of hexahedra elements on a corner

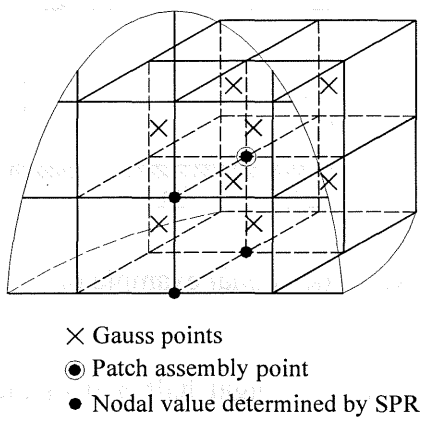

Fig.5.9 A patch of hexahedra elements on a side

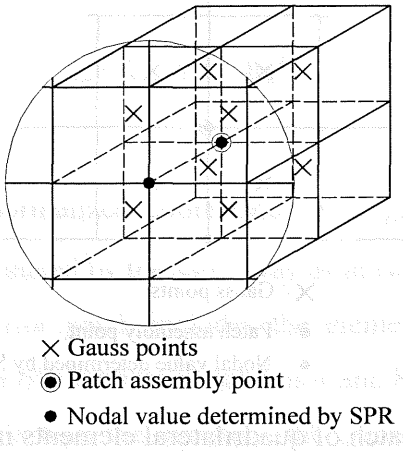

Fig.5.10 A patch of hexahedra elements on a boundary surface

5.3.3 Convergence of Error Estimator in Two-Dimension

The convergence of this error estimator is test by the following example. In **Fig.5.11**, a saturated soil (the soil parameters are given in **Table.2.1**) block 4m long and 2m high is compressed at the top surface by a uniformly distributed load. The load increases linearly to 100kn/m until t=10 second. The boundary conditions of right and left sides of the soil block are free for displacement and undrained for the pore water. The top surface boundary is free for displacement and drained for pore water. The bottom is fixed and has an undrained boundary.

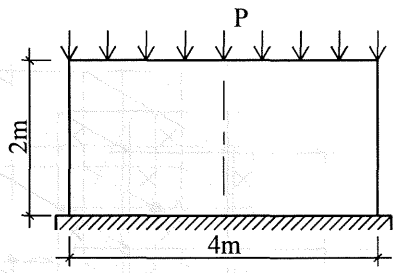

Fig.5.11 Two-dimensional example of error estimates

Because of the symmetry, only the right half part of the model is analysed using meshes with 16 elements, 100 elements and 400 elements in the error estimation. The

meshes and its boundary conditions are shown in **Figs.5.12-5.14.**

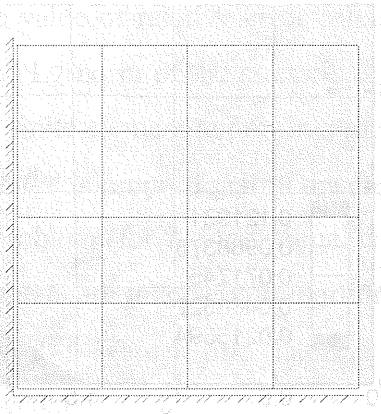

Fig.5.12 16-element mesh

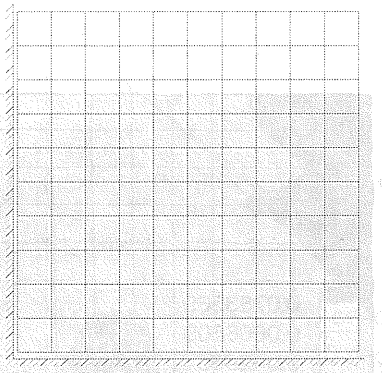

Fig.5.13 100-element mesh

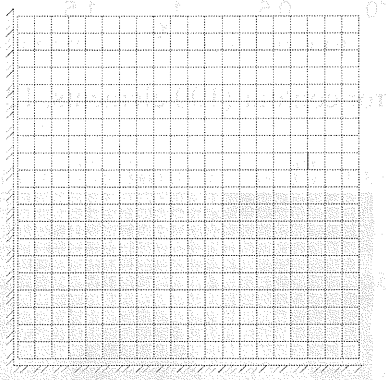

Fig.5.14 400-element mesh

Figs.5.15-5.1 7 show the relative error contours of stress in the whole mesh at time t=10 second for three cases of mesh number respectively. A comparison of the average relative errors of the 16, 100, and 400 elements shows clearly that a reduction of

element size reduces error.

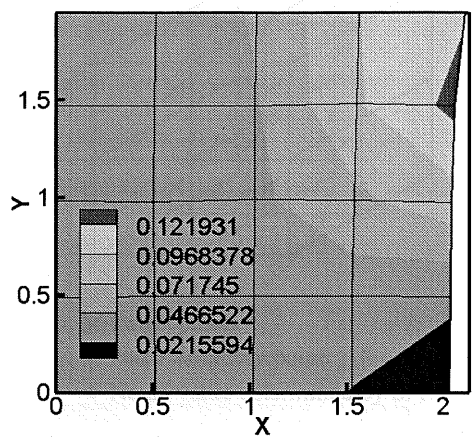

Fig.5.15 Relative error contour (16 elements, 25 nodes, t=10 second)

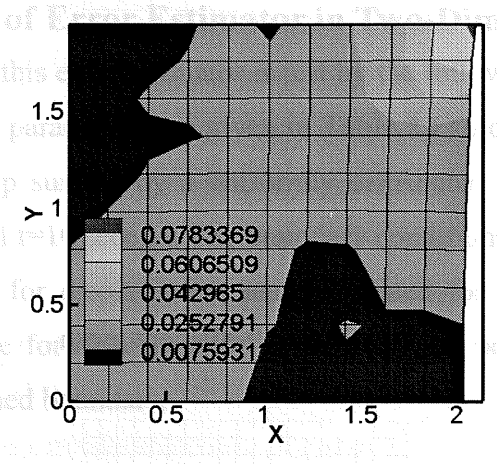

Fig.5.16 Relative error contour (100 elements, 121 nodes, t=10 second)

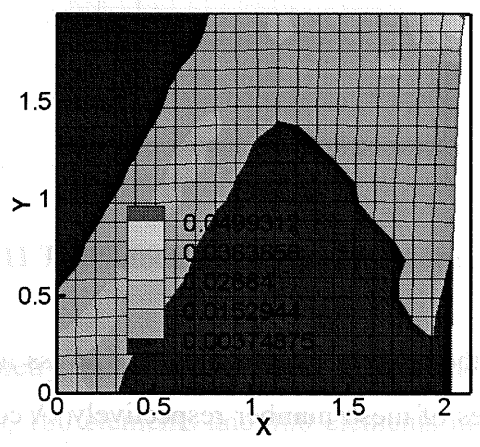

Fig.5.17 Relative error contour (400 elements, 441 nodes, t=10 second)

In **Fig.5.18,** the lines give the relation in a doubled notched specimen between the node number and the average value of relative error calculated from different meshes. The rate of convergence in the L2-norm of the stress is order O(h^p), p is the degree of the polynomial utilized in the finite element approximation, for linear element p=1; h is the size of the element, and h^{ndim} is proportional to the area, where *ndim* is the number of spatial dimensions in the problem (for 2-dimensional case, *ndim*=2). The number of nodes and the number of elements are inversely proportional to the volume. Therefore, the rate of convergence is O($h^{1/2}$). We can find that this error estimator gives a good rate of convergence as we expected.

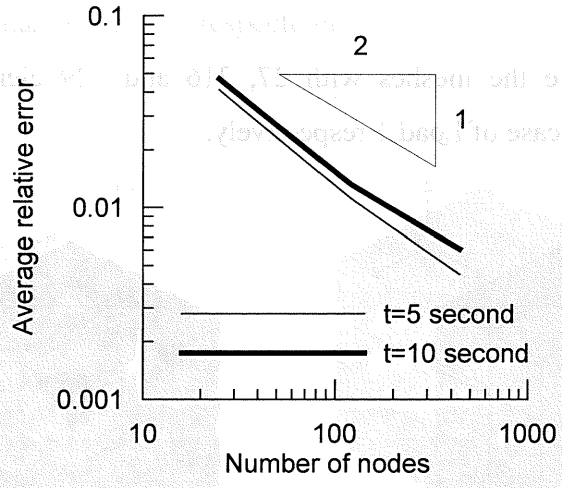

Fig.5.18 Convergence of error estimator in two-dimension

5.3.4 Convergence of Error Estimator in Three-Dimension

Another simple example is also calculated to test this error estimator in three -dimension. A saturated soil cubic block in a container which size is 3*3*3m^3, and a vertical load is applied on the top surface locally shown in **Fig.5.19**. The load is increased linearly up to 90kn/m^2 until t=0.3second. Only upper surface is drained. There are two load cases as shown in **Fig.5.19**. In case 1, the load is applied in an area with 1*1 m^2 in corner. In case 2, the load is applied in an area with 1*3 m^2 beside a side. Three meshes with 27 elements, 216 elements and 729elements are analyzed. For boundary constraint of the meshes, the bottom nodes are fixed, the nodes on side

surfaces are allowed to slide on the side surfaces.

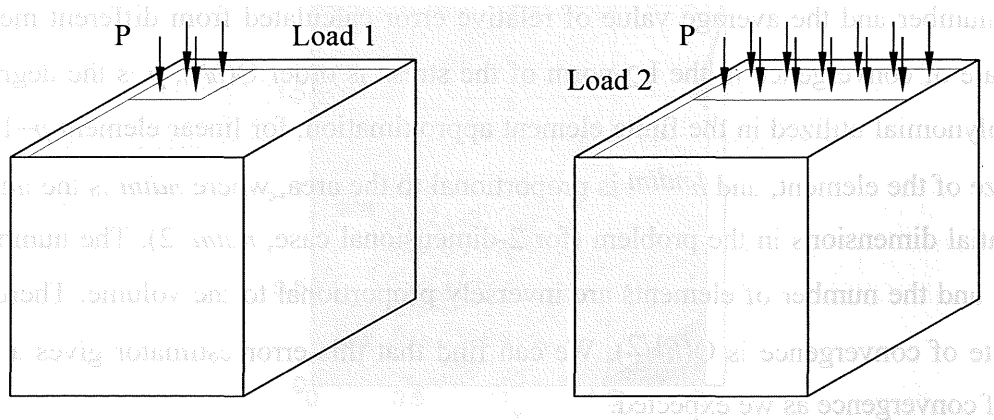

Fig.5.19 Local compression of soil with Load 1 and Load 2

Figs.5.20-5.22 give the meshes with 27, 216 and 729 elements and their error contour results for the case of Load 1 respectively.

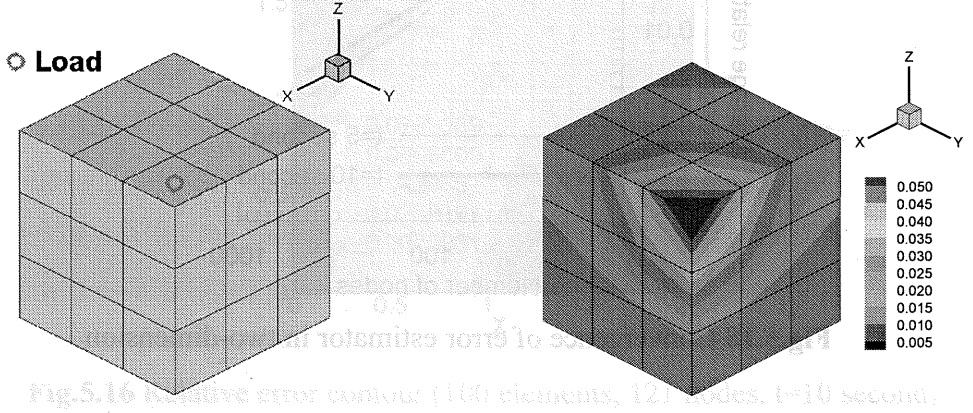

Fig.5.20. Mesh, load and error contour in Load 1 (27 elements)

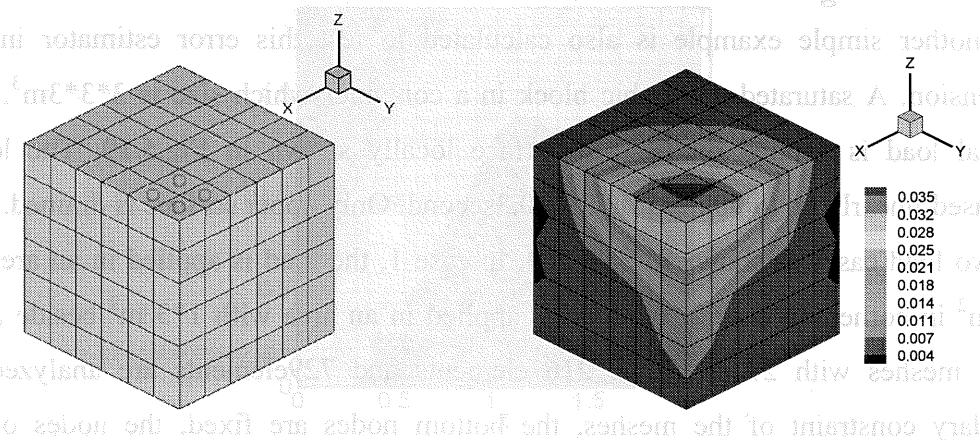

Fig.5.21. Mesh, load and error contour in Load 1 (216 elements)

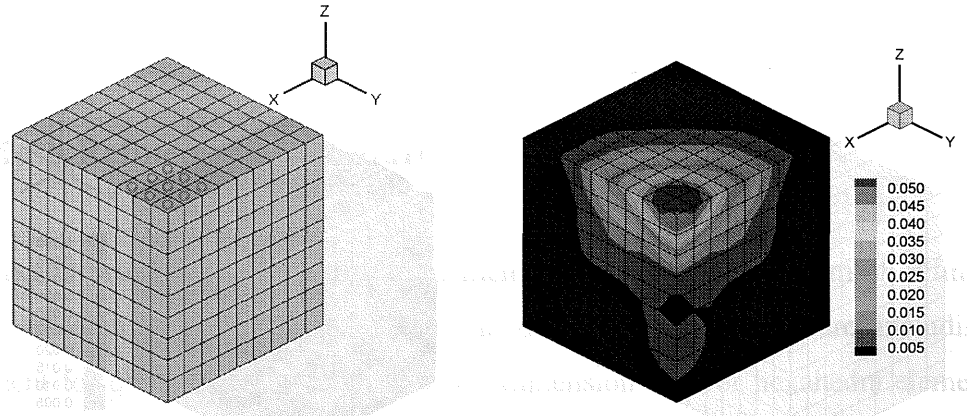

Fig.5.22. Mesh, load and error contour in Load 1 (729 elements)

Figs.5.23-5.25 give the meshes with 27, 216 and 729 elements and their error contour results for the case of Load 2 respectively.

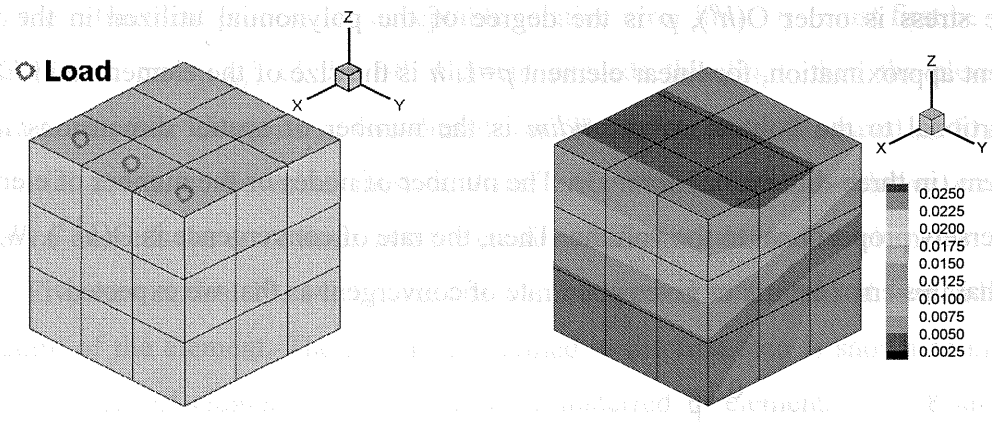

Fig.5.23. Mesh, load and error contour in Load 2 (27 elements)

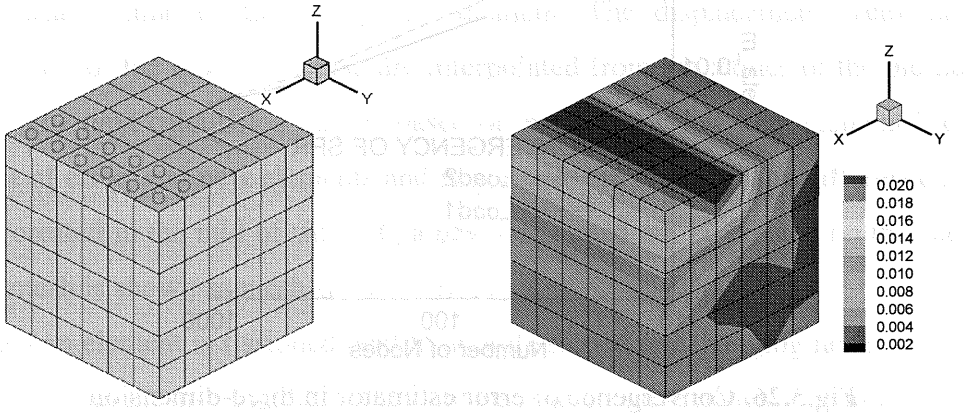

Fig.5.24. Mesh, load and error contour in Load 2 (216 elements)

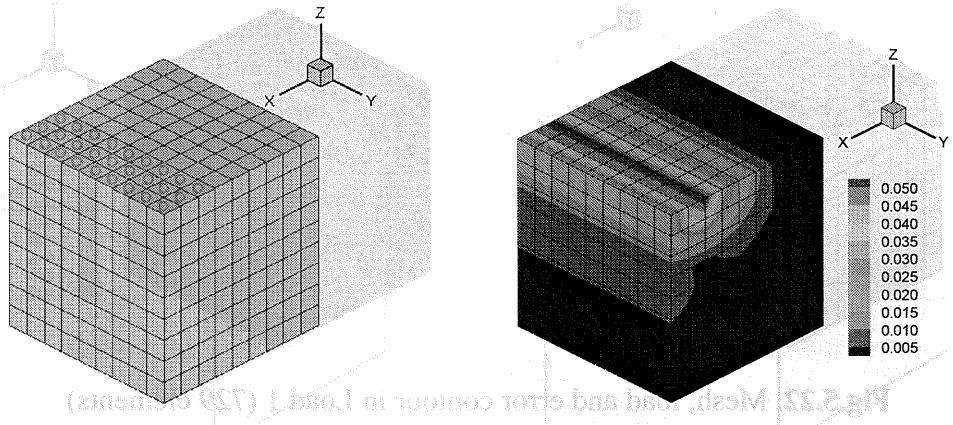

Fig.5.25. Mesh, load and error contour in Load 2 (729 elements)

In **Fig.5.26,** the lines are the relation between the nodes number and average value of relative error calculated from different mesh. The rate of convergence in the L_2-norm of the stress is order $O(h^p)$, p is the degree of the polynomial utilized in the finite element approximation, for linear element p=1. h is the size of the element, and h^{ndim} is proportional to the volume, where *ndim* is the number of spatial dimensions in the problem (in three-dimension, *ndim*=3). The number of nodes or the number of elements is inversely proportional to the volume. Then, the rate of convergence is $O(h^{1/3})$. We can find that this error estimator gives good rate of convergent as that we expected.

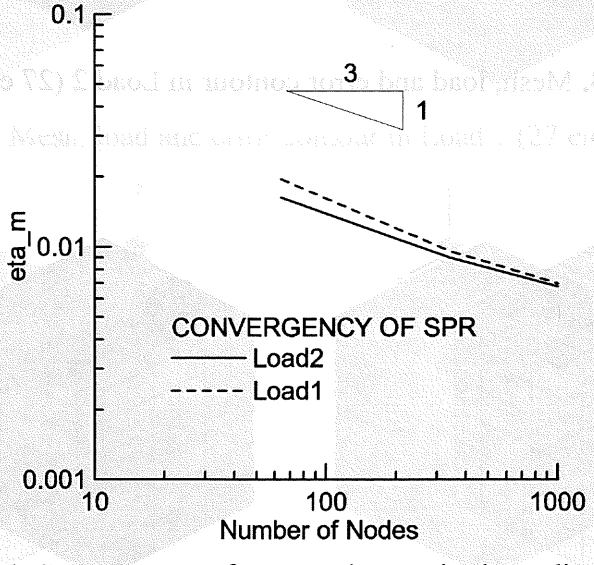

Fig.5.26. Convergence of error estimator in three-dimension

5.4 Mesh Refinement Procedure

A fission procedure belong to *h*-refinement is applied to adaptive mesh refinement in this research. This section presents the details of this procedure including its implement for quadrilateral elements in two-dimension and for hexahedra elements in three-dimension. The application of this procedure to soil-pile interaction analysis is also illustrated. Some simple examples are calculated to test the adaptive mesh refinement with the fission procedure.

5.4.1 2-D Fission Procedure for Linear Quadrilateral Elements

In the refinement process, an acceptable relative error limit $\overline{\eta}$ must first be given. If the relative error, η_i, of the *i*-th element exceeds this limit, then the element is fissioned into four elements in two-dimension. This process is illustrated in **Fig.5.27**. The initial mesh is shown as mesh-a. After error estimation, the relative error for element 5 exceeds the error limit, and the element is fissioned into four elements: 5, 7, 8, and 9. Five new nodes, 13, 14, 15, 16, and 17, are created in the mid of four sides and the centre of the element. The new mesh refined at the first step is shown as mesh-b. The parameters of element 5 in mesh-a are transferred to elements 5, 7, 8 and 9 in mesh-b, and the variables of the new elements are interpolated from the variables of element 2 in mesh-a. The pore pressure values of the new child elements are same as the pore pressure value of the old parent element. The displacement, velocities, and accelerations of the new nodes also are interpolated from the values of the old nodes in mesh-a. The next calculation step is based on mesh-b. In that step, element 2 exceeds the limit of error, and new elements and new nodes are created. The difference is that a node is created in the mid of side 7-6, a new node need not be created on this side. The refined mesh is shown as mesh-c.

When an element is fissioned next to an unfissioned one, hanging nodes are created, e. g., node 13 in mesh-b **Fig.5.27**. They are also called salve nodes. The motion of slave node 13 should be governed by the constraint of compatibility,

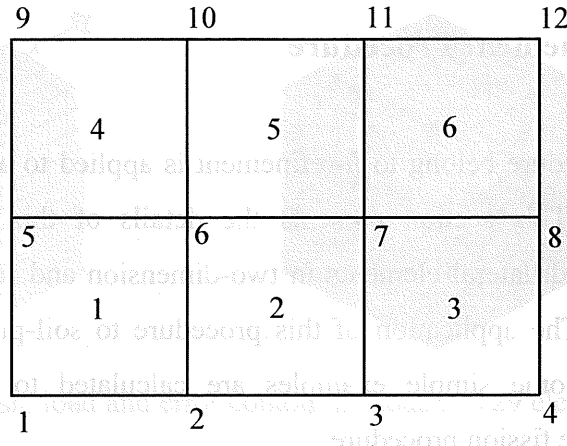

mesh-a

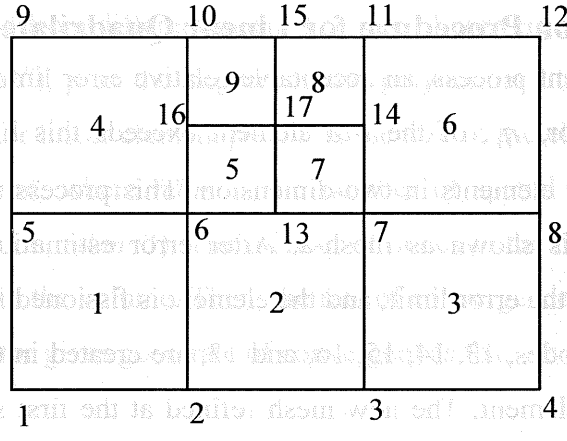

mesh-b

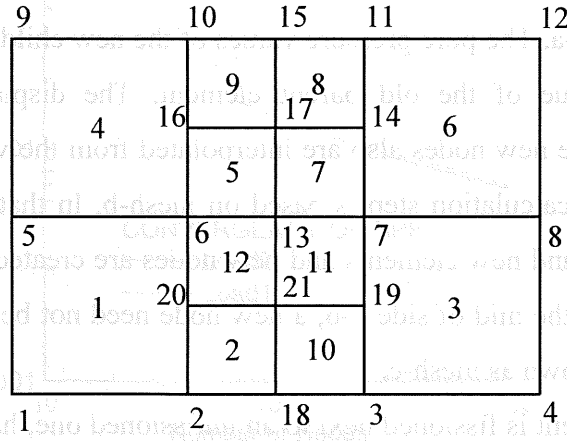

mesh-c

Fig.5.27 Fission process for quadrilateral elements in two-dimension

$$\mathbf{V}_{13} = \mathbf{T}\begin{Bmatrix}\mathbf{V}_6\\ \mathbf{V}_7\end{Bmatrix} \tag{5.4.1}$$

where **T** is a linear operator which enforces compatibility and $\mathbf{V}_6$ and $\mathbf{V}_7$ are the velocities of the master nodes. When node 13 is midway between nodes 6 and 7, **T** is defined by [**I**/2,**I**/2], in which **I** is a unit matrix. The equation of motion is not evaluated at the slave node. Instead the nodal forces at the slave nodes are added to the forces at the corresponding master nodes;

$$\begin{Bmatrix}\mathbf{F}_6\\ \mathbf{F}_7\end{Bmatrix} = \begin{Bmatrix}\mathbf{F}_6\\ \mathbf{F}_7\end{Bmatrix}^* + \mathbf{T}^T\mathbf{F}_{13} \tag{5.4.2}$$

where $\mathbf{F}_{13}$ are the nodal forces at the slave node and $\{\mathbf{F}\}^*$ those at the nodes 6 and 7 prior to the consideration of $\mathbf{F}_{13}$, This is the standard technique for treating constraints in explicit methods.

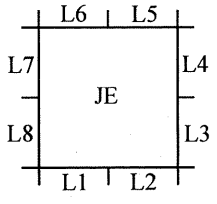

Fig.5.28 NABOR array

To clarify the interrelationship between the old and new nodes and elements, requires an elaborate data structure in the process of node and element creation.

To develop master and slave nodes during the fission process an important array NABOR(NE,8), composed of the eight neighboring element numbers of a concerned element are used (**Fig.5.28**).

NE is the number of the element. To clarify the use of the array, consider mesh-b in **Fig.5.27** with element 5 already fissioned into element 5, 7, 8, and 9. Also consider mesh-c obtained by fissioning the element 2 to element 2, 10, 11 and 12. The NABOR array for element 2 is given in **Table 5.1** for both meshes. The first thing to note is that the zero entries for L1 and L2, indicate a boundary at the bottom of element 2. Therefore, a new node needs to be created (node 18) which is a master node. Next,

L3=L4=3 indicates that element 3 extends along the entire side of element 2. Therefore a new node (node 19) must be created, which is a slave node. Now, L5=7 and L6=5, therefore a node already exists (node 13) which is a slave node in mesh-b, and, it becomes a master node when element 2 is fissioned.

Table 5.1 NABOR array for the element 2

mesh	JE	L1	L2	L3	L4	L5	L6	L7	L8
b	2	0	0	3	3	7	5	1	1
c	2	0	0	10	10	12	12	1	1

Usually, in a region consisted of a single kind of material, only one slave node is permitted to be created between two master nodes. It is reasonable and effective to guarantee the accuracy in soil elements. But for the analysis of soil-pile interaction, in the interfacing surface between soil and pile, the effect of relative deformations of pile elements to soil elements is so small that we almost can neglect it because concrete is much harder than soil. For this reason, it is reasonable to create more than one slave nodes between the master nodes in the soil-pile joint surface. In this research, adaptive mesh refinement is only applied to soil elements. Since the deformation and error of soil elements near the pile elements are larger, we refine these soil element further and, if necessary, create more than one slave node between two master nodes in the soil-pile joint surface. Some special treatment is used here as mentioned below.

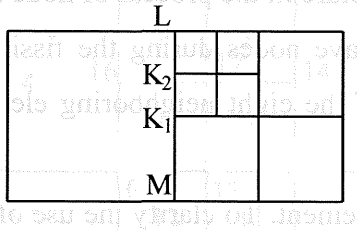

Fig.5.29 Fission Process in joint surface between soil and pile elements

If the left element is a pile element without refinement and the right fissioned elements need to be fissioned further, more than one slave node are created in the joint line *LM* as shown in **Fig.5.29**. The motion of slave node K_i should be governed by the

constraint of compatibility as

$$\mathbf{V}_{Ki} = \mathbf{T}_i \begin{Bmatrix} \mathbf{V}_L \\ \mathbf{V}_M \end{Bmatrix} \tag{5.4.3}$$

The nodal forces at the slave nodes are added to the forces at the corresponding master nodes by

$$\begin{Bmatrix} \mathbf{F}_L \\ \mathbf{F}_M \end{Bmatrix} = \begin{Bmatrix} \mathbf{F}_L \\ \mathbf{F}_M \end{Bmatrix}^* + \mathbf{T}_i^T \mathbf{F}_{Ki} \tag{5.4.4}$$

where

$$\mathbf{T}_i = \begin{bmatrix} \gamma_i^L \mathbf{I} & \gamma_i^M \mathbf{I} \end{bmatrix} \tag{5.4.5}$$

$$\gamma_i^L = \frac{\overline{K_i M}}{\overline{LM}} \quad \text{and} \quad \gamma_i^M = \frac{\overline{K_i L}}{\overline{LM}} \tag{5.4.6}$$

5.4.2 Modification of 2-D Dynamic Equations

In the governing equations, the motion of the slave nodes are not evaluated at slave node but the governing equations are modified according to Eqs.(5.4.2) and (5.4.3).

Here, The final governing equations of the FE-FD coupled method using the cyclic elasto-plastic model and updated Lagrangian formulation, Eq.(2.3.69), is represent briefly as

$$\begin{bmatrix} \tilde{\mathbf{K}} & \tilde{\mathbf{Q}} \\ \tilde{\mathbf{Q}}^T & \tilde{\mathbf{A}} \end{bmatrix} \begin{Bmatrix} {}^{t=\Delta t}\ddot{\mathbf{u}}_N \\ {}^{t=\Delta t}\mathbf{p}_N \end{Bmatrix} = \begin{Bmatrix} \mathbf{f}_u\left({}^t\dot{\mathbf{u}}, {}^t\ddot{\mathbf{u}}\right) \\ \mathbf{f}_p\left({}^t\dot{\mathbf{u}}, {}^t\ddot{\mathbf{u}}\right) \end{Bmatrix} \tag{5.4.7}$$

Modifying equations of soil mesh

As a sample, a salve node, fissioned elements and unfissioned elements are shown in **Fig.5.30**.

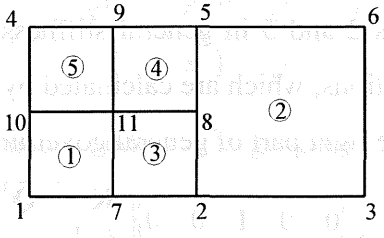

Fig.5.30 Refined mesh of soil elements in two-dimension

Eq.(5.4.1) is rewritten as the local mesh shown in **Fig.5.30**.

$$\dot{\mathbf{u}}_8 = \tfrac{1}{2}\left(\dot{\mathbf{u}}_2 + \dot{\mathbf{u}}_5\right) \tag{5.4.8a}$$

$$\ddot{\mathbf{u}}_8 = \tfrac{1}{2}\left(\ddot{\mathbf{u}}_2 + \ddot{\mathbf{u}}_5\right) \tag{5.4.8b}$$

The local governing equations for sample element 3 in refined mesh shown in **Fig.5.30** are given as

$$\begin{bmatrix} \widetilde{\mathbf{K}}^3 & \widetilde{\mathbf{Q}}^3 \\ \widetilde{\mathbf{Q}}^{3\mathrm{T}} & \widetilde{A}^3 \end{bmatrix} \begin{Bmatrix} {}^{t+\Delta t}\ddot{\mathbf{u}}_7 \\ {}^{t+\Delta t}\ddot{\mathbf{u}}_2 \\ {}^{t+\Delta t}\ddot{\mathbf{u}}_8 \\ {}^{t+\Delta t}\ddot{\mathbf{u}}_{11} \\ {}^{t+\Delta t}p^3 \end{Bmatrix} = \begin{Bmatrix} \mathbf{f}_{\mathbf{u}}^3\left({}^{t}\dot{\mathbf{u}}^3, {}^{t}\ddot{\mathbf{u}}^3\right) \\ f_p^3\left({}^{t}\dot{\mathbf{u}}^3, {}^{t}\ddot{\mathbf{u}}^3, {}^{t}p^3\right) \end{Bmatrix} \tag{5.4.9}$$

Substituting Eq. (5.4.8) into Eq. (5.4.9) and considering that the motion of slave node 8 is not included in the general equations, the modified local equations are divided into two parts. The first part is the set of modified the governing equations which should be added to the general governing equations, given as

$$\begin{bmatrix} \mathbf{I} & 0 & 0 & 0 & 0 \\ 0 & \mathbf{I} & 0 & 0 & 0 \\ 0 & 0 & 0 & \mathbf{I} & 0 \\ 0 & 0 & 0 & 0 & \mathbf{I} \end{bmatrix} \begin{bmatrix} \widetilde{\mathbf{K}}^3 & \widetilde{\mathbf{Q}}^3 \\ \widetilde{\mathbf{Q}}^{3\mathrm{T}} & \widetilde{A}^3 \end{bmatrix} \begin{Bmatrix} {}^{t+\Delta t}\ddot{\mathbf{u}}^3 \\ {}^{t+\Delta t}p^3 \end{Bmatrix} = \begin{bmatrix} \mathbf{I} & 0 & 0 & 0 & 0 \\ 0 & \mathbf{I} & 0 & 0 & 0 \\ 0 & 0 & 0 & \mathbf{I} & 0 \\ 0 & 0 & 0 & 0 & \mathbf{I} \end{bmatrix} \begin{Bmatrix} \mathbf{f}_{\mathbf{u}}^3\left({}^{t}\dot{\mathbf{u}}^3, {}^{t}\ddot{\mathbf{u}}^3\right) \\ f_p^3\left({}^{t}\dot{\mathbf{u}}^3, {}^{t}\ddot{\mathbf{u}}^3, {}^{t}p^3\right) \end{Bmatrix} \tag{5.4.10}$$

where

$${}^{t+\Delta t}\ddot{\mathbf{u}}^3 = \begin{Bmatrix} {}^{t+\Delta t}\ddot{\mathbf{u}}_7 \\ {}^{t+\Delta t}\ddot{\mathbf{u}}_2 \\ \frac{1}{2}{}^{t+\Delta t}\ddot{\mathbf{u}}_2 + \frac{1}{2}{}^{t+\Delta t}\ddot{\mathbf{u}}_5 \\ {}^{t+\Delta t}\ddot{\mathbf{u}}_{11} \end{Bmatrix}, \quad {}^{t}\dot{\mathbf{u}}^3 = \begin{Bmatrix} {}^{t}\dot{\mathbf{u}}_7 \\ {}^{t}\dot{\mathbf{u}}_2 \\ \frac{1}{2}{}^{t}\dot{\mathbf{u}}_2 + \frac{1}{2}{}^{t}\dot{\mathbf{u}}_5 \\ {}^{t}\dot{\mathbf{u}}_{11} \end{Bmatrix} \quad \text{and} \quad {}^{t}\ddot{\mathbf{u}}^3 = \begin{Bmatrix} {}^{t}\ddot{\mathbf{u}}_7 \\ {}^{t}\ddot{\mathbf{u}}_2 \\ \frac{1}{2}{}^{t}\ddot{\mathbf{u}}_2 + \frac{1}{2}{}^{t}\ddot{\mathbf{u}}_5 \\ {}^{t}\ddot{\mathbf{u}}_{11} \end{Bmatrix}$$

Another part is the additional forces on the master nodes 2 and 5 due to the slave node 8. The forces from the stiffness matrix, which are calculated by Eq. (5.4.11), are added to the places of nodes 2 and 5 in general stiffness matrix. The forces from the right parts of governing equations, which are calculated by Eq. (5.4.12), are added to the places of nodes 2 and 5 in the right part of general governing equations.

$$\Delta\mathbf{K}_2^3 = \Delta\mathbf{K}_5^3 = \frac{1}{2}\{0 \quad 0 \quad \mathbf{I} \quad 0 \quad 0\} \begin{bmatrix} \widetilde{\mathbf{K}}^3 & \widetilde{\mathbf{Q}}^3 \\ \widetilde{\mathbf{Q}}^{3\mathrm{T}} & \widetilde{A}^3 \end{bmatrix} \begin{Bmatrix} {}^{t+\Delta t}\ddot{\mathbf{u}}^3 \\ {}^{t+\Delta t}p^3 \end{Bmatrix} \tag{5.4.11}$$

$$\Delta\mathbf{f}_2^3 = \Delta\mathbf{f}_5^3 = \frac{1}{2}\{0 \quad 0 \quad \mathbf{I} \quad 0 \quad 0\} \begin{Bmatrix} \mathbf{f}_{\mathbf{u}}^3\left({}^{t}\dot{\mathbf{u}}^3, {}^{t}\ddot{\mathbf{u}}^3\right) \\ f_p^3\left({}^{t}\dot{\mathbf{u}}^3, {}^{t}\ddot{\mathbf{u}}^3, {}^{t}p^3\right) \end{Bmatrix} \tag{5.4.12}$$

These steps are also calculated for element 4. Then the governing equations of the

mesh shown in **Fig.5.30** are modified.

Modifying equations of soil-pile interaction mesh

In adaptive mesh refinement analysis of soil-pile interaction, a modified mesh is shown in **Fig.5.31**. The same modification processes are implemented for slave node 8. The difference is that the other calculation elements are elements 6 and 7 but not element 4. The modification processes of governing equations of elements 6 and 7 for slave nodes 8 and 13 are introduced as follows.

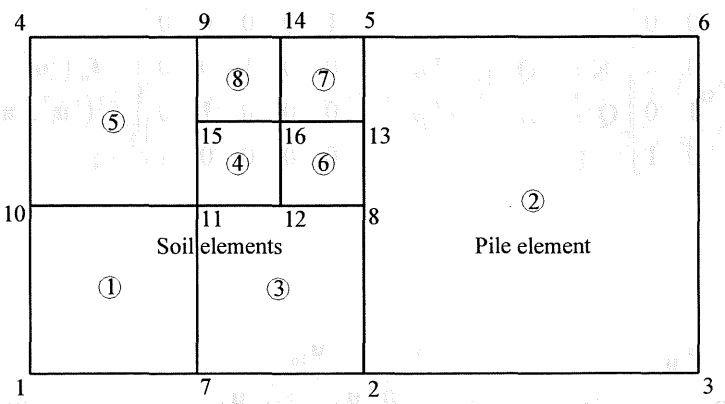

Fig.5.31 Refined mesh for soil-pile interaction in two-dimension

The effective parameters of nodes 2 and 5 to node 13 are calculated by

$$\gamma_{13}^{2}=\frac{\sqrt{(x_{13}-x_5)^2+(y_{13}-y_5)^2}}{\sqrt{(x_2-x_5)^2+(y_2-y_5)^2}} \tag{5.4.13a}$$

$$\gamma_{13}^{5}=\frac{\sqrt{(x_{13}-x_2)^2+(y_{13}-y_2)^2}}{\sqrt{(x_2-x_5)^2+(y_2-y_5)^2}} \tag{5.4.13b}$$

The motion of the slave node, node 13, is governed by the motions of its master nodes 2 and 5, and it is calculated as

$$\dot{\mathbf{u}}_{13}=\gamma_{13}^{2}\dot{\mathbf{u}}_{\mathbf{2}}+\gamma_{13}^{5}\dot{\mathbf{u}}_{\mathbf{5}} \tag{5.4.14a}$$

$$\ddot{\mathbf{u}}_{13}=\gamma_{13}^{2}\ddot{\mathbf{u}}_{\mathbf{2}}+\gamma_{13}^{5}\ddot{\mathbf{u}}_{\mathbf{5}} \tag{5.4.14b}$$

The local governing equations for sample element 7 in refined mesh shown in **Fig.5.31** are given as

$$\begin{bmatrix} \widetilde{\mathbf{K}}^7 & \widetilde{\mathbf{Q}}^7 \\ \widetilde{\mathbf{Q}}^{7\mathrm{T}} & \widetilde{A}^7 \end{bmatrix} \begin{Bmatrix} {}^{t+\Delta t}\ddot{\mathbf{u}}_{16} \\ {}^{t+\Delta t}\ddot{\mathbf{u}}_{13} \\ {}^{t+\Delta t}\ddot{\mathbf{u}}_{5} \\ {}^{t+\Delta t}\ddot{\mathbf{u}}_{14} \\ {}^{t+\Delta t}p^7 \end{Bmatrix} = \begin{Bmatrix} \mathbf{f}_{\mathrm{u}}^7\left({}^{t}\dot{\mathbf{u}}^7, {}^{t}\ddot{\mathbf{u}}^7\right) \\ f_p^7\left({}^{t}\dot{\mathbf{u}}^7, {}^{t}\ddot{\mathbf{u}}^7, {}^{t}p^7\right) \end{Bmatrix} \tag{5.4.15}$$

Substituting Eq. (5.4.14) into Eq. (5.4.15) and considering that the motion of slave node 13 is not included in the general equations, the modified local equations are divided into two parts. The first part is the set of modified the governing equations which should be added to the general governing equations, given as

$$\begin{bmatrix} \mathbf{I} & 0 & 0 & 0 & 0 \\ 0 & 0 & \mathbf{I} & 0 & 0 \\ 0 & 0 & 0 & \mathbf{I} & 0 \\ 0 & 0 & 0 & 0 & \mathbf{I} \end{bmatrix} \begin{bmatrix} \widetilde{\mathbf{K}}^7 & \widetilde{\mathbf{Q}}^7 \\ \widetilde{\mathbf{Q}}^{7\mathrm{T}} & \widetilde{A}^7 \end{bmatrix} \begin{Bmatrix} {}^{t+\Delta t}\ddot{\mathbf{u}}^7 \\ {}^{t+\Delta t}p^7 \end{Bmatrix} = \begin{bmatrix} \mathbf{I} & 0 & 0 & 0 & 0 \\ 0 & 0 & \mathbf{I} & 0 & 0 \\ 0 & 0 & 0 & \mathbf{I} & 0 \\ 0 & 0 & 0 & 0 & \mathbf{I} \end{bmatrix} \begin{Bmatrix} \mathbf{f}_{\mathrm{u}}^7\left({}^{t}\dot{\mathbf{u}}^7, {}^{t}\ddot{\mathbf{u}}^7\right) \\ f_p^7\left({}^{t}\dot{\mathbf{u}}^7, {}^{t}\ddot{\mathbf{u}}^7, {}^{t}p^7\right) \end{Bmatrix} \tag{5.4.16}$$

where

$${}^{t+\Delta t}\ddot{\mathbf{u}}^7 = \begin{Bmatrix} {}^{t+\Delta t}\ddot{\mathbf{u}}_{16} \\ \gamma_{13}^2\,{}^{t+\Delta t}\ddot{\mathbf{u}}_2 + \gamma_{13}^5\,{}^{t+\Delta t}\ddot{\mathbf{u}}_5 \\ {}^{t+\Delta t}\ddot{\mathbf{u}}_5 \\ {}^{t+\Delta t}\ddot{\mathbf{u}}_{14} \end{Bmatrix},\quad {}^{t}\dot{\mathbf{u}}^7 = \begin{Bmatrix} {}^{t}\dot{\mathbf{u}}_{16} \\ \gamma_{13}^2\,{}^{t}\dot{\mathbf{u}}_2 + \gamma_{13}^5\,{}^{t}\dot{\mathbf{u}}_5 \\ {}^{t}\dot{\mathbf{u}}_5 \\ {}^{t}\dot{\mathbf{u}}_{14} \end{Bmatrix} \text{ and } {}^{t}\ddot{\mathbf{u}}^7 = \begin{Bmatrix} {}^{t}\ddot{\mathbf{u}}_{16} \\ \gamma_{13}^2\,{}^{t}\ddot{\mathbf{u}}_2 + \gamma_{13}^5\,{}^{t}\ddot{\mathbf{u}}_5 \\ {}^{t}\ddot{\mathbf{u}}_5 \\ {}^{t}\ddot{\mathbf{u}}_{14} \end{Bmatrix}$$

Another part is the additional forces on the master nodes 2 and 5 due to the slave node 13. The forces from the stiffness matrix, which are calculated by Eq. (5.4.17), are added to the places of nodes 2 and 5 in general stiffness matrix. The forces from the right parts of governing equations, which are calculated by Eq. (5.4.18), are added to the places of nodes 2 and 5 in the right part of general governing equations.

$$\Delta\mathbf{K}_i^7 = \gamma_{13}^i \{0 \quad \mathbf{I} \quad 0 \quad 0 \quad 0\} \begin{bmatrix} \widetilde{\mathbf{K}}^7 & \widetilde{\mathbf{Q}}^7 \\ \widetilde{\mathbf{Q}}^{7\mathrm{T}} & \widetilde{A}^7 \end{bmatrix} \begin{Bmatrix} {}^{t+\Delta t}\ddot{\mathbf{u}}^7 \\ {}^{t+\Delta t}p^7 \end{Bmatrix} \tag{5.4.17}$$

where i=2, 5.

$$\Delta\mathbf{f}_i^7 = \gamma_{13}^i \{0 \quad \mathbf{I} \quad 0 \quad 0 \quad 0\} \begin{Bmatrix} \mathbf{f}_{\mathrm{u}}^7\left({}^{t}\dot{\mathbf{u}}^7, {}^{t}\ddot{\mathbf{u}}^7\right) \\ f_p^7\left({}^{t}\dot{\mathbf{u}}^7, {}^{t}\ddot{\mathbf{u}}^7, {}^{t}p^7\right) \end{Bmatrix} \tag{5.4.18}$$

The modification process for element 6 is more complex. The local governing equations for element 6 is

$$\begin{bmatrix} \widetilde{\mathbf{K}}^6 & \widetilde{\mathbf{Q}}^6 \\ \widetilde{\mathbf{Q}}^{6\mathrm{T}} & \widetilde{A}^6 \end{bmatrix} \begin{Bmatrix} {}^{t+\Delta t}\ddot{\mathbf{u}}_{12} \\ {}^{t+\Delta t}\ddot{\mathbf{u}}_{8} \\ {}^{t+\Delta t}\ddot{\mathbf{u}}_{13} \\ {}^{t+\Delta t}\ddot{\mathbf{u}}_{16} \\ {}^{t+\Delta t}p^6 \end{Bmatrix} = \begin{Bmatrix} \mathbf{f}_{\mathbf{u}}^6\left({}^{t}\dot{\mathbf{u}}^6, {}^{t}\ddot{\mathbf{u}}^6\right) \\ f_p^6\left({}^{t}\dot{\mathbf{u}}^6, {}^{t}\ddot{\mathbf{u}}^6, {}^{t}p^6\right) \end{Bmatrix} \tag{5.4.19}$$

Substituting Eqs. (5.4.8) and (5.4.14) into Eq. (5.4.19) and considering that the motions of slave nodes 8 and 13 are not included in general equations, the modified local equations are also divided into two parts. The first part is the set of modified governing equations which need to be added to the general governing equations, given as

$$\begin{bmatrix} \mathbf{I} & 0 & 0 & 0 & 0 \\ 0 & 0 & 0 & \mathbf{I} & 0 \\ 0 & 0 & 0 & 0 & \mathbf{I} \end{bmatrix} \begin{bmatrix} \widetilde{\mathbf{K}}^6 & \widetilde{\mathbf{Q}}^6 \\ \widetilde{\mathbf{Q}}^{6\mathrm{T}} & \widetilde{A}^6 \end{bmatrix} \begin{Bmatrix} {}^{t+\Delta t}\ddot{\mathbf{u}}^6 \\ {}^{t+\Delta t}p^6 \end{Bmatrix} = \begin{bmatrix} \mathbf{I} & 0 & 0 & 0 & 0 \\ 0 & 0 & 0 & \mathbf{I} & 0 \\ 0 & 0 & 0 & 0 & \mathbf{I} \end{bmatrix} \begin{Bmatrix} \mathbf{f}_{\mathbf{u}}^6\left({}^{t}\dot{\mathbf{u}}^6, {}^{t}\ddot{\mathbf{u}}^6\right) \\ f_p^6\left({}^{t}\dot{\mathbf{u}}^6, {}^{t}\ddot{\mathbf{u}}^6, {}^{t}p^6\right) \end{Bmatrix} \tag{5.4.20}$$

where

$${}^{t+\Delta t}\ddot{\mathbf{u}}^6 = \begin{Bmatrix} {}^{t+\Delta t}\ddot{\mathbf{u}}_{12} \\ \frac{1}{2}{}^{t+\Delta t}\ddot{\mathbf{u}}_2 + \frac{1}{2}{}^{t+\Delta t}\ddot{\mathbf{u}}_5 \\ \gamma_{13}^2{}^{t+\Delta t}\ddot{\mathbf{u}}_2 + \gamma_{13}^5{}^{t+\Delta t}\ddot{\mathbf{u}}_5 \\ {}^{t+\Delta t}\ddot{\mathbf{u}}_{16} \end{Bmatrix}, \quad {}^{t}\dot{\mathbf{u}}^6 = \begin{Bmatrix} {}^{t}\dot{\mathbf{u}}_{12} \\ \frac{1}{2}{}^{t}\dot{\mathbf{u}}_2 + \frac{1}{2}{}^{t}\dot{\mathbf{u}}_5 \\ \gamma_{13}^2{}^{t}\dot{\mathbf{u}}_2 + \gamma_{13}^5{}^{t}\dot{\mathbf{u}}_5 \\ {}^{t}\dot{\mathbf{u}}_{16} \end{Bmatrix} \text{ and } {}^{t}\ddot{\mathbf{u}}^6 = \begin{Bmatrix} {}^{t}\ddot{\mathbf{u}}_{12} \\ \frac{1}{2}{}^{t}\ddot{\mathbf{u}}_2 + \frac{1}{2}{}^{t}\ddot{\mathbf{u}}_5 \\ \gamma_{13}^2{}^{t}\ddot{\mathbf{u}}_2 + \gamma_{13}^5{}^{t}\ddot{\mathbf{u}}_5 \\ {}^{t}\ddot{\mathbf{u}}_{16} \end{Bmatrix}$$

Another part is the additional forces on the master nodes 2 and 5 due to the slave nodes 8 and 13. The forces from the stiffness matrix, which are calculated by Eq. (5.4.21), are added to the places of nodes 2 and 5 in general stiffness matrix. The forces from the right parts of governing equations, which are calculated by Eq. (5.4.22), are added to the places of nodes 2 and 5 in the right part of general governing equations.

$$\Delta\mathbf{K}_i^{6-8} = \frac{1}{2}\{0 \quad \mathbf{I} \quad 0 \quad 0 \quad 0\} \begin{bmatrix} \widetilde{\mathbf{K}}^6 & \widetilde{\mathbf{Q}}^6 \\ \widetilde{\mathbf{Q}}^{6\mathrm{T}} & \widetilde{A}^6 \end{bmatrix} \begin{Bmatrix} {}^{t+\Delta t}\ddot{\mathbf{u}}^6 \\ {}^{t+\Delta t}p^6 \end{Bmatrix} \tag{5.4.21a}$$

$$\Delta\mathbf{K}_i^{6-13} = \gamma_{13}^i\{0 \quad 0 \quad \mathbf{I} \quad 0 \quad 0\} \begin{bmatrix} \widetilde{\mathbf{K}}^6 & \widetilde{\mathbf{Q}}^6 \\ \widetilde{\mathbf{Q}}^{6\mathrm{T}} & \widetilde{A}^6 \end{bmatrix} \begin{Bmatrix} {}^{t+\Delta t}\ddot{\mathbf{u}}^6 \\ {}^{t+\Delta t}p^6 \end{Bmatrix} \tag{5.4.21b}$$

$$\Delta\mathbf{f}_i^{6-8} = \frac{1}{2}\{0 \quad \mathbf{I} \quad 0 \quad 0 \quad 0\} \begin{Bmatrix} \mathbf{f}_{\mathbf{u}}^6\left({}^{t}\dot{\mathbf{u}}^6, {}^{t}\ddot{\mathbf{u}}^6\right) \\ f_p^6\left({}^{t}\dot{\mathbf{u}}^6, {}^{t}\ddot{\mathbf{u}}^6, {}^{t}p^6\right) \end{Bmatrix} \tag{5.4.22a}$$

$$\Delta\mathbf{f}_i^{6-13} = \gamma_{13}^i\{0 \quad 0 \quad \mathbf{I} \quad 0 \quad 0\} \begin{Bmatrix} \mathbf{f}_{\mathbf{u}}^6\left({}^{t}\dot{\mathbf{u}}^6, {}^{t}\ddot{\mathbf{u}}^6\right) \\ f_p^6\left({}^{t}\dot{\mathbf{u}}^6, {}^{t}\ddot{\mathbf{u}}^6, {}^{t}p^6\right) \end{Bmatrix} \tag{5.4.22b}$$

where i=2, 5.

Modifying permeance of pore water between elements

If an unfissioned element besides a fissioned element, the usual permeance route crossing the intersurface should be modified as shown in **Fig.5.32**. The permeance between two unfissioned elements is taken place by the permeance between an unfissioned element and two fissioned elements. According to this reason, the terms describing the permeance of pore water in continuity equation is modified so easily. That it needn't be written out.

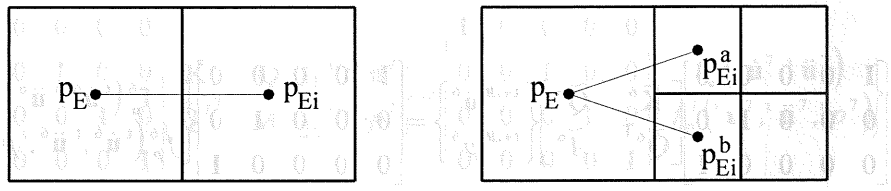

Fig.5.32 Modifying permeance of pore water in two-dimension

5.4.3 3-D Fission Procedure for Linear Hexahedra Elements

In three-dimension, linear hexahedra elements are used in adaptive finite element analysis. When the error of an element is exceeds an acceptable limit, the element is fissioned into eight children elements. This process is illustrated in **Fig.5.33**. The initial mesh is shown as mesh-a. After error estimation, the relative error for element 3 exceeds the error limit, and the element is fissioned into eight elements: 3, 8-11. Nineteen new nodes, 19-37, are created in the mid of twelve sides, the centers of six surfaces and the center of the element. The new mesh refined is shown as mesh-b. The parameters of element 3 in mesh-a are transferred to elements 3, 5-11 in mesh-b, and the variables of the new elements are interpolated from the variables of element 3 in mesh-a. The pore pressure values of the new child elements are same as the pore pressure value of the old parent element. The displacement, velocities, and accelerations of the new nodes also are interpolated from the values of the old nodes in mesh-a. The next calculation step is based on mesh-b.

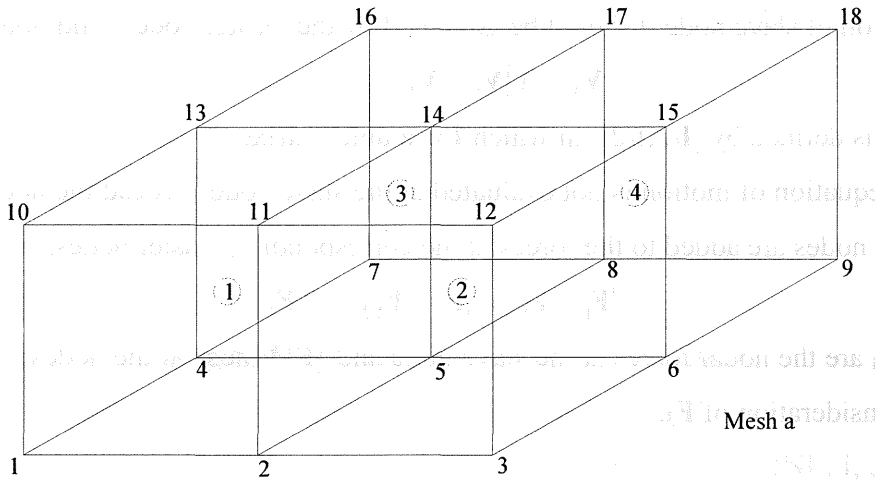

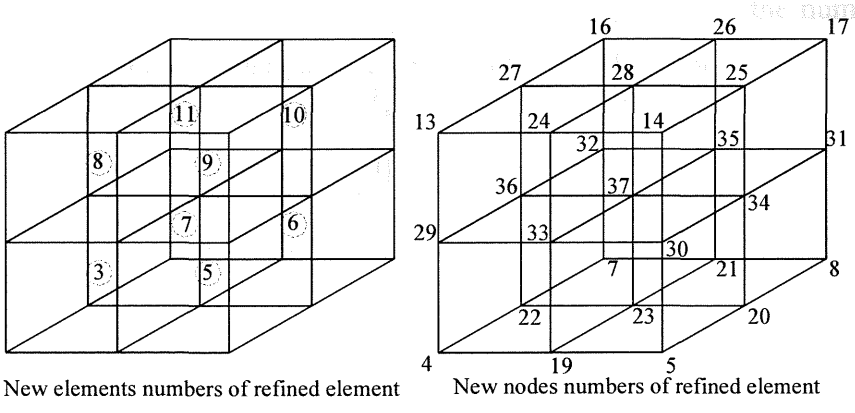

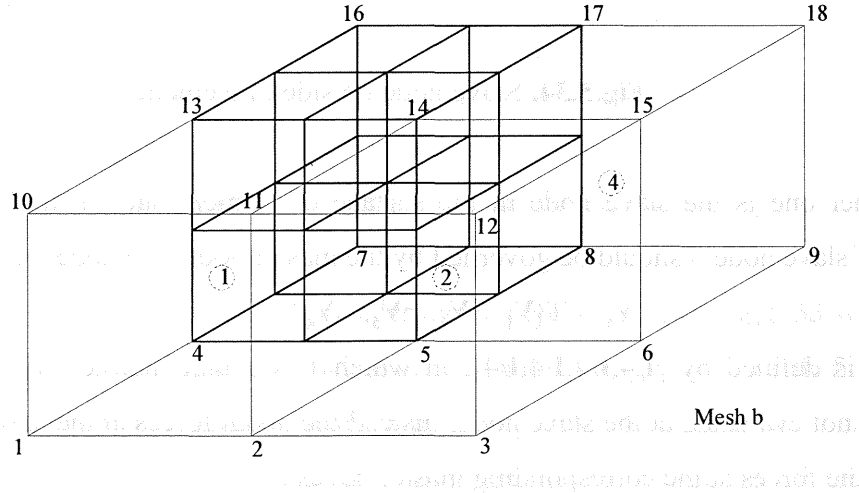

Fig.5.33. Fission procedure of hexahedra elements

When an element is fissioned next to an unfissioned one, slave nodes are created, and they are constrained by the compatibility condition of master node. There are two

kinds of slave nodes. One is the slave node on the side of element shown in **Fig.5.34**. The motion of slave node 0 should be governed by the master node 1 and node 2 as,

$$\mathbf{V}_3 = \mathbf{T}\{\mathbf{V}_1 \quad \mathbf{V}_2\}^T \tag{5.4.23}$$

where **T** is defined by [**I**/2,**I**/2], in which **I** is a unit matrix.

The equation of motion is not evaluated at the slave node. Instead the nodal forces at the slave nodes are added to the forces at the corresponding master nodes;

$$\{\mathbf{F}_1 \quad \mathbf{F}_2\} = \{\mathbf{F}_1 \quad \mathbf{F}_2\}^* + \mathbf{T}\mathbf{F}_3 \tag{5.4.24}$$

where $\mathbf{F}_3$ are the nodal forces at the slave node and **{F}*** those at the nodes 1 and 2 prior to the consideration of $\mathbf{F}_3$.

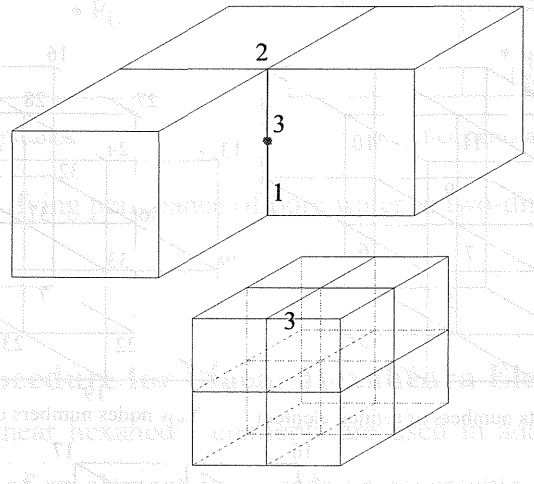

Fig.5.34. Slave node on side of element

Another one is the slave node in the surface of element shown in **Fig.5.35**. The motion of slave node 0 should be governed by the master node 1 to node 4 as,

$$\mathbf{V}_5 = \mathbf{T}\{\mathbf{V}_1 \quad \mathbf{V}_2 \quad \mathbf{V}_3 \quad \mathbf{V}_4\}^T \tag{5.4.25}$$

where **T** is defined by [**I**/4,**I**/4,**I**/4,**I**/4], in which **I** is a unit matrix. The equation of motion is not evaluated at the slave node. Instead the nodal forces at the slave nodes are added to the forces at the corresponding master nodes as

$$\{\mathbf{F}_1 \quad \mathbf{F}_2 \quad \mathbf{F}_3 \quad \mathbf{F}_4\} = \{\mathbf{F}_1 \quad \mathbf{F}_2 \quad \mathbf{F}_3 \quad \mathbf{F}_4\}^* + \mathbf{T}\mathbf{F}_5 \tag{5.4.26}$$

where $\mathbf{F}_5$ are the nodal forces at the slave node and **{F}*** those at the nodes 1 and 2 prior to the consideration of $\mathbf{F}_5$.

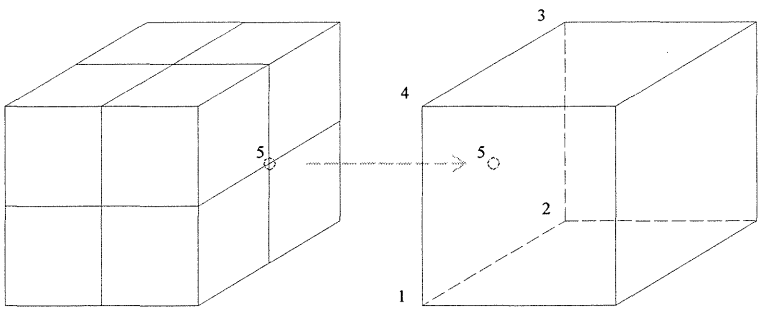

Fig.5.35. Slave node in surface of element

To define the relationship of neighbor elements, an array NABOR (NE, I, J) is used here. It is composed of the twenty-four numbers of neighbor elements on six joint surfaces with other elements. NE is the number of the element. I is the number of the surface and J is the number of neighbor element defined in **Fig.5.36**.

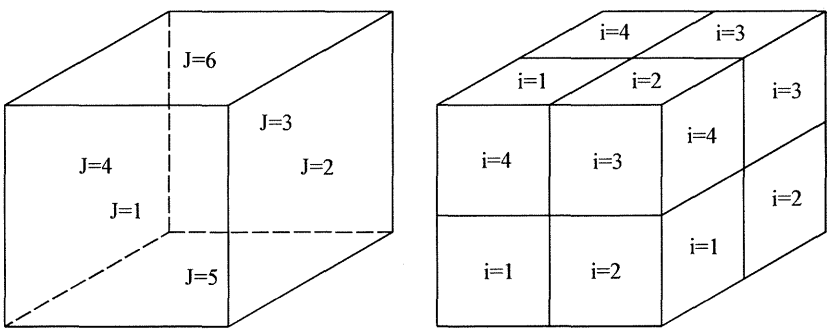

Fig.5.36 Nabor array for hexahedra element

To clarify the use of the array, consider mesh-a and mesh-b in **Fig.5.33** with fission of element 3. The NABOR arrays for elements 1 and 3 are given in **Table 5.2** for both mesh-a and mesh-b. The zero indicates a boundary at the surface of an element. The four same number in a surface indicates only one neighbor element on this surface. When an element besides fissioned elements, all numbers of the four neighbor elements on this surface are recorded in the array.

Table 5.2 Nabor(JE,I,J) for mesh-a and mesh-b

mesh	JE	J=1,I=1:4	J=2,I=1:4	J=3,I=1:4	J=4,I=1:4	J=5,I=1:4	J=6,I=1:4
a	1	0,0,0,0	2,2,2,2	3,3,3,3	0,0,0,0	0,0,0,0	0,0,0,0
b	1	0,0,0,0	2,2,2,2	3,5,8,9	0,0,0,0	0,0,0,0	0,0,0,0
a	3	1,1,1,1	4,4,4,4	0,0,0,0	0,0,0,0	0,0,0,0	0,0,0,0
b	3	1,1,1,1	5,5,5,5	7,7,7,7	0,0,0,0	0,0,0,0	8,8,8,8

As adaptive mesh refinement in two-dimension, the difference between the fission levels of neighbor elements is 1 in three-dimensional adaptive mesh refinement in order to guarantee the accuracy in soil elements. But for the analysis of soil-pile interaction adaptive analysis, in the joint surface between soil and pile, the effect of relative deformations of pile elements to soil elements is so small that we almost can neglect it because concrete is much harder than soil. For this reason, the difference of fission level between soil elements and pile element is allowed to be more than 1 in the adaptive analysis of this research, shown as **Fig.5.37**. Some special treatment is used here as follows.

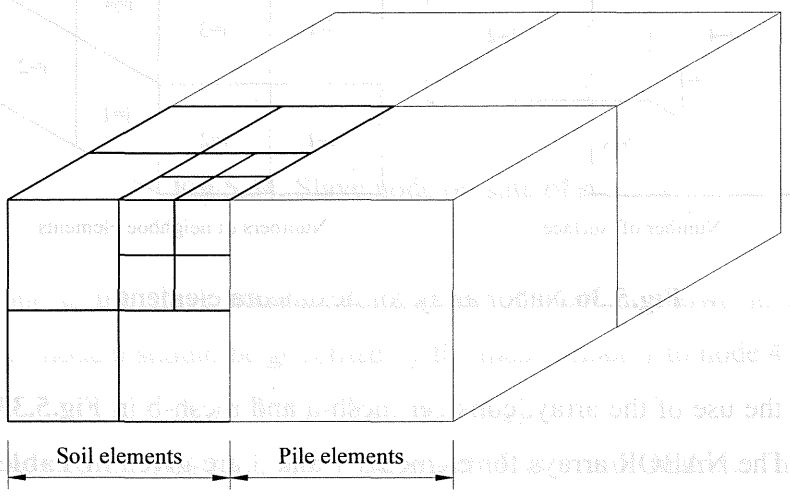

Fig.5.37 3-D Fission Process in joint surface between soil and pile elements

Considering a soil element besides two pile elements, after fissioned twice, the mesh is shown in **Fig.5.38**. In order to express the slave nodes on the joint surface clearly, soil elements and pile elements are drawn respectively. The calculation of slave nodes 5 and 6 on the surface and side respectively with fission level 1 can be implemented according

to Eqs. (5.4.23)- (5.4.26).

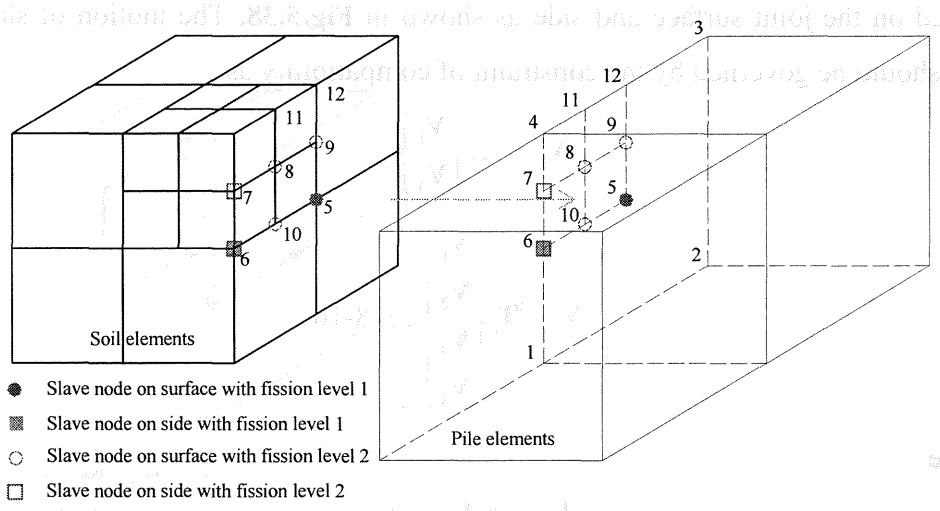

Fig.5.38. Slave nodes on joint surface between soil and pile elements

First, the effective parameters of master nodes to the slave nodes are calculated. Since the deformation of pile elements are not large, it is assumed that the vertical surfaces of pile elements are

$$\gamma_7^4 = \frac{\sqrt{(x_7 - x_1)^2 + (y_7 - y_1)^2 + (y_7 - y_1)^2}}{\sqrt{(x_4 - x_1)^2 + (y_4 - y_1)^2 + (y_4 - y_1)^2}} \tag{5.4.27a}$$

$$\gamma_7^1 = \frac{\sqrt{(x_7 - x_4)^2 + (y_7 - y_4)^2 + (y_7 - y_4)^2}}{\sqrt{(x_4 - x_1)^2 + (y_4 - y_1)^2 + (y_4 - y_1)^2}} \tag{5.4.27b}$$

$$\gamma_{11}^4 = \frac{\sqrt{(x_{11} - x_3)^2 + (y_{11} - y_3)^2 + (y_{11} - y_3)^2}}{\sqrt{(x_4 - x_3)^2 + (y_4 - y_3)^2 + (y_4 - y_3)^2}} \tag{5.4.28a}$$

$$\gamma_{11}^3 = \frac{\sqrt{(x_{11} - x_4)^2 + (y_{11} - y_4)^2 + (y_{11} - y_4)^2}}{\sqrt{(x_4 - x_3)^2 + (y_4 - y_3)^2 + (y_4 - y_3)^2}} \tag{5.4.28a}$$

$$\gamma_8^1 = \gamma_7^1\gamma_{11}^4,\ \gamma_8^2 = \gamma_7^1\gamma_{11}^3,\ \gamma_8^3 = \gamma_7^4\gamma_{11}^3,\ \gamma_8^4 = \gamma_7^4\gamma_{11}^4 \tag{5.4.29}$$

$$\gamma_9^1 = \gamma_9^2 = \tfrac{1}{2}\gamma_7^1,\ \gamma_9^3 = \gamma_9^4 = \tfrac{1}{2}\gamma_7^4 \tag{5.4.30}$$

$$\gamma_{10}^1 = \gamma_{10}^4 = \tfrac{1}{2}\gamma_{11}^4,\ \gamma_{10}^2 = \gamma_{10}^3 = \tfrac{1}{2}\gamma_{11}^3 \tag{5.4.31}$$

The right elements are a pile elements without refinement and one of the left fissioned elements is fissioned further, the slave nodes 7-10 with fission level 2 are created on the joint surface and side as shown in **Fig.5.38**. The motion of slave nodes 7-10 should be governed by the constraint of compatibility as

$$\mathbf{V}_7 = \mathbf{T}_7 \begin{Bmatrix} \mathbf{V}_1 \\ \mathbf{V}_4 \end{Bmatrix} \tag{5.4.32a}$$

$$\mathbf{V}_i = \mathbf{T}_i \begin{Bmatrix} \mathbf{V}_1 \\ \mathbf{V}_2 \\ \mathbf{V}_3 \\ \mathbf{V}_4 \end{Bmatrix}, \; i\text{=8-10} \tag{5.4.32b}$$

where

$$\mathbf{T}_7 = \begin{bmatrix} \gamma_7^1 \mathbf{I} & \gamma_7^4 \mathbf{I} \end{bmatrix} \tag{5.4.33a}$$

$$\mathbf{T}_i = \begin{bmatrix} \gamma_i^1 \mathbf{I} & \gamma_i^2 \mathbf{I} & \gamma_i^3 \mathbf{I} & \gamma_i^4 \mathbf{I} \end{bmatrix} \tag{5.4.33b}$$

The nodal forces at the slave nodes are added to the forces at the corresponding master nodes 1-4 by

$$\begin{Bmatrix} \mathbf{F}_1 \\ \mathbf{F}_2 \\ \mathbf{F}_3 \\ \mathbf{F}_4 \end{Bmatrix} = \begin{Bmatrix} \mathbf{F}_1 \\ \mathbf{F}_2 \\ \mathbf{F}_3 \\ \mathbf{F}_4 \end{Bmatrix}^* + \sum_{i=7}^{10} \mathbf{T}_i^{\mathrm{T}} \mathbf{F}_i \tag{5.4.34}$$

where where $\mathbf{F}_i$ are the nodal forces at the slave node and $\{\mathbf{F}\}^*$ those at the corresponding master nodes 1-4 prior to the consideration of $\mathbf{F}_i$.

5.4.4 Modification of 3-D Dynamic Equations

The three-dimensional governing equations of adaptive analysis of saturated soil and adaptive analysis of soil-pile interaction are modified. Eq.(5.4.7) is also used here.

Modifying three dimensional equations of soil mesh

For example, a refined are shown in **Fig.5.39**. The right elements are pile elements without refinement and the left part is refined soil elements. Nodes 5 and 6 are slave nodes and nodes 1-4 are their corresponding master node.

According to the Eqs.(5.4.23) and (5.4.25), the velocities and accelerations of slave nodes 5 and 6 are defined as

$$\dot{\mathbf{u}}_5 = \tfrac{1}{4}\left(\dot{\mathbf{u}}_1 + \dot{\mathbf{u}}_2 + \dot{\mathbf{u}}_3 + \dot{\mathbf{u}}_4\right), \quad \ddot{\mathbf{u}}_5 = \tfrac{1}{4}\left(\ddot{\mathbf{u}}_1 + \ddot{\mathbf{u}}_2 + \ddot{\mathbf{u}}_4 + \ddot{\mathbf{u}}_5\right) \tag{5.4.35}$$

$$\dot{\mathbf{u}}_6 = \tfrac{1}{2}\left(\dot{\mathbf{u}}_1 + \dot{\mathbf{u}}_2\right), \quad \ddot{\mathbf{u}}_6 = \tfrac{1}{2}\left(\ddot{\mathbf{u}}_1 + \ddot{\mathbf{u}}_2\right) \tag{5.4.36}$$

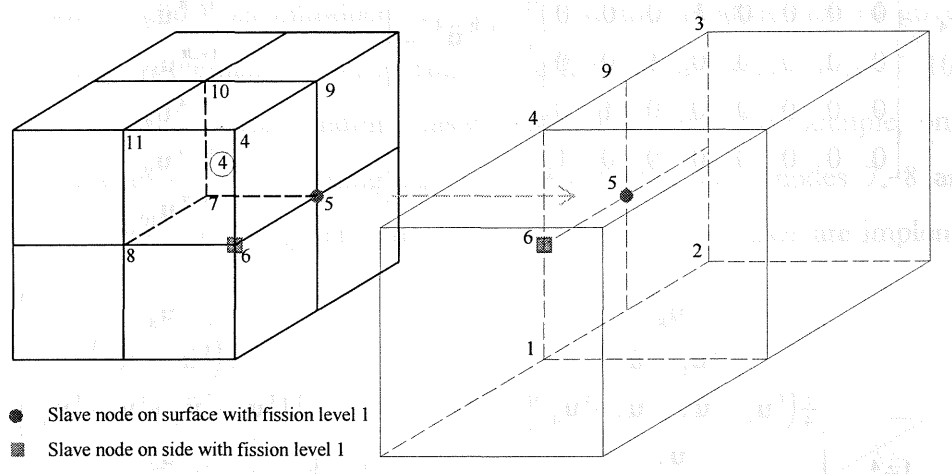

Fig.5.39 Refined mesh for soil elements in three-dimension

The local governing equations for sample element 4 in refined mesh shown in **Fig.5.39** are given as

$$\begin{bmatrix} \widetilde{\mathbf{K}}^4 & \widetilde{\mathbf{Q}}^4 \\ \widetilde{\mathbf{Q}}^{4\mathrm{T}} & \widetilde{A}^4 \end{bmatrix} \begin{Bmatrix} {}^{t+\Delta t}\ddot{\mathbf{u}}_8 \\ {}^{t+\Delta t}\ddot{\mathbf{u}}_6 \\ {}^{t+\Delta t}\ddot{\mathbf{u}}_5 \\ {}^{t+\Delta t}\ddot{\mathbf{u}}_7 \\ {}^{t+\Delta t}\ddot{\mathbf{u}}_{11} \\ {}^{t+\Delta t}\ddot{\mathbf{u}}_4 \\ {}^{t+\Delta t}\ddot{\mathbf{u}}_9 \\ {}^{t+\Delta t}\ddot{\mathbf{u}}_{10} \\ {}^{t+\Delta t}p^4 \end{Bmatrix} = \begin{Bmatrix} \mathbf{f}_{\mathbf{u}}^3\left({}^{t}\dot{\mathbf{u}}^4, {}^{t}\ddot{\mathbf{u}}^4\right) \\ f_p^4\left({}^{t}\dot{\mathbf{u}}^4, {}^{t}\ddot{\mathbf{u}}^4, {}^{t}p^4\right) \end{Bmatrix} \tag{5.4.37}$$

Substituting Eqs. (5.4.35) and (5.4.36) into Eq. (5.4.37) and considering that the motion of slave nodes 5 and 6 is not included in general equations, the modified local equations are divided into two parts. The first part is the set of modified governing equations which should be added to the general governing equations, given as

$$\widetilde{\mathbf{P}}^4 \begin{bmatrix} \widetilde{\mathbf{K}}^4 & \widetilde{\mathbf{Q}}^4 \\ \widetilde{\mathbf{Q}}^{4\mathrm{T}} & \widetilde{A}^4 \end{bmatrix} \begin{Bmatrix} {}^{t+\Delta t}\ddot{\mathbf{u}}^4 \\ {}^{t+\Delta t}p^4 \end{Bmatrix} = \widetilde{\mathbf{P}}^4 \begin{Bmatrix} \mathbf{f}_{\mathbf{u}}^4\left({}^{t}\dot{\mathbf{u}}^4, {}^{t}\ddot{\mathbf{u}}^4\right) \\ f_p^4\left({}^{t}\dot{\mathbf{u}}^4, {}^{t}\ddot{\mathbf{u}}^4, {}^{t}p^4\right) \end{Bmatrix} \tag{5.4.38}$$

where

$$\widetilde{\mathbf{P}}^4=\begin{bmatrix}\mathbf{I}&0&0&0&0&0&0&0\\0&0&0&\mathbf{I}&0&0&0&0\\0&0&0&0&\mathbf{I}&0&0&0\\0&0&0&0&0&\mathbf{I}&0&0\\0&0&0&0&0&0&\mathbf{I}&0\\0&0&0&0&0&0&0&\mathbf{I}\end{bmatrix},\quad {}^{t+\Delta t}\ddot{\mathbf{u}}^4=\begin{Bmatrix}{}^{t+\Delta t}\ddot{\mathbf{u}}_8\\\frac{1}{2}\left({}^{t+\Delta t}\ddot{\mathbf{u}}_1+{}^{t+\Delta t}\ddot{\mathbf{u}}_4\right)\\\frac{1}{4}\left({}^{t+\Delta t}\ddot{\mathbf{u}}_1+{}^{t+\Delta t}\ddot{\mathbf{u}}_2+{}^{t+\Delta t}\ddot{\mathbf{u}}_3+{}^{t+\Delta t}\ddot{\mathbf{u}}_4\right)\\{}^{t+\Delta t}\ddot{\mathbf{u}}_7\\{}^{t+\Delta t}\ddot{\mathbf{u}}_{11}\\{}^{t+\Delta t}\ddot{\mathbf{u}}_4\\{}^{t+\Delta t}\ddot{\mathbf{u}}_9\\{}^{t+\Delta t}\ddot{\mathbf{u}}_{10}\end{Bmatrix},$$

$${}^{t}\dot{\mathbf{u}}^4=\begin{Bmatrix}{}^{t}\dot{\mathbf{u}}_8\\\frac{1}{2}\left({}^{t}\dot{\mathbf{u}}_1+{}^{t}\dot{\mathbf{u}}_4\right)\\\frac{1}{4}\left({}^{t}\dot{\mathbf{u}}_1+{}^{t}\dot{\mathbf{u}}_2+{}^{t}\dot{\mathbf{u}}_3+{}^{t}\dot{\mathbf{u}}_4\right)\\{}^{t}\dot{\mathbf{u}}_7\\{}^{t}\dot{\mathbf{u}}_{11}\\{}^{t}\dot{\mathbf{u}}_4\\{}^{t}\dot{\mathbf{u}}_9\\{}^{t}\dot{\mathbf{u}}_{10}\end{Bmatrix}\quad\text{and}\quad {}^{t}\ddot{\mathbf{u}}^4=\begin{Bmatrix}{}^{t}\ddot{\mathbf{u}}_8\\\frac{1}{2}\left({}^{t}\ddot{\mathbf{u}}_1+{}^{t}\ddot{\mathbf{u}}_4\right)\\\frac{1}{4}\left({}^{t}\ddot{\mathbf{u}}_1+{}^{t}\ddot{\mathbf{u}}_2+{}^{t}\ddot{\mathbf{u}}_3+{}^{t}\ddot{\mathbf{u}}_4\right)\\{}^{t}\ddot{\mathbf{u}}_7\\{}^{t}\ddot{\mathbf{u}}_{11}\\{}^{t}\ddot{\mathbf{u}}_4\\{}^{t}\ddot{\mathbf{u}}_9\\{}^{t}\ddot{\mathbf{u}}_{10}\end{Bmatrix}$$

Another part is the additional forces on the master nodes 1-4 due to the slave nodes 5 and 6. The forces from the stiffness matrix, which are calculated by Eq. (5.4.39), are added to the places of nodes 1-4 in general stiffness matrix. The forces from the right parts of governing equations, which are calculated by Eq. (5.4.40), are added to the places of nodes 1-4 in the right part of general governing equations.

$$\Delta\mathbf{K}_1^4=\Delta\mathbf{K}_4^4=\left\{0\quad\tfrac{1}{2}\mathbf{I}\quad\tfrac{1}{4}\mathbf{I}\quad 0\quad 0\quad 0\quad 0\quad 0\right\}\begin{bmatrix}\widetilde{\mathbf{K}}^4&\widetilde{\mathbf{Q}}^4\\\widetilde{\mathbf{Q}}^{4\mathrm{T}}&\widetilde{A}^4\end{bmatrix}\begin{Bmatrix}{}^{t+\Delta t}\ddot{\mathbf{u}}^4\\{}^{t+\Delta t}p^4\end{Bmatrix}\tag{5.4.39a}$$

$$\Delta\mathbf{K}_2^4=\Delta\mathbf{K}_3^4=\left\{0\quad 0\quad\tfrac{1}{4}\mathbf{I}\quad 0\quad 0\quad 0\quad 0\quad 0\right\}\begin{bmatrix}\widetilde{\mathbf{K}}^4&\widetilde{\mathbf{Q}}^4\\\widetilde{\mathbf{Q}}^{4\mathrm{T}}&\widetilde{A}^4\end{bmatrix}\begin{Bmatrix}{}^{t+\Delta t}\ddot{\mathbf{u}}^4\\{}^{t+\Delta t}p^4\end{Bmatrix}\tag{5.4.39b}$$

$$\Delta\mathbf{f}_1^4=\Delta\mathbf{f}_4^4=\left\{0\quad\tfrac{1}{2}\mathbf{I}\quad\tfrac{1}{4}\mathbf{I}\quad 0\quad 0\quad 0\quad 0\quad 0\right\}\begin{Bmatrix}\mathbf{f}_{\mathbf{u}}^4\left({}^{t}\dot{\mathbf{u}}^4,{}^{t}\ddot{\mathbf{u}}^4\right)\\f_p^4\left({}^{t}\dot{\mathbf{u}}^4,{}^{t}\ddot{\mathbf{u}}^4,{}^{t}p^4\right)\end{Bmatrix}\tag{5.4.40a}$$

$$\Delta\mathbf{f}_2^4=\Delta\mathbf{f}_3^4=\left\{0\quad 0\quad\tfrac{1}{4}\mathbf{I}\quad 0\quad 0\quad 0\quad 0\quad 0\right\}\begin{Bmatrix}\mathbf{f}_{\mathbf{u}}^4\left({}^{t}\dot{\mathbf{u}}^4,{}^{t}\ddot{\mathbf{u}}^4\right)\\f_p^4\left({}^{t}\dot{\mathbf{u}}^4,{}^{t}\ddot{\mathbf{u}}^4,{}^{t}p^4\right)\end{Bmatrix}\tag{5.4.40b}$$

These steps are also calculated for other fissioned elements. Then the governing equations of the mesh shown in **Fig.5.39** are modified.

Modifying equations of soil-pile interaction mesh

In three-dimensional adaptive mesh refinement analysis of soil-pile interaction, a refined mesh is shown in **Fig.5.40**. The same modification processes are implemented for slave nodes 5 and 6 as introduced above. The further modification of governing equations is also implemented considering the effects of the slave nodes 7-10 with fission level 2 to their corresponding master nodes 1-4. Here, for example, only the modification processes of governing equations due to the slave nodes 7, 8 and 10 concerning with element 7 is given. The other modification processes are implemented in the same way.

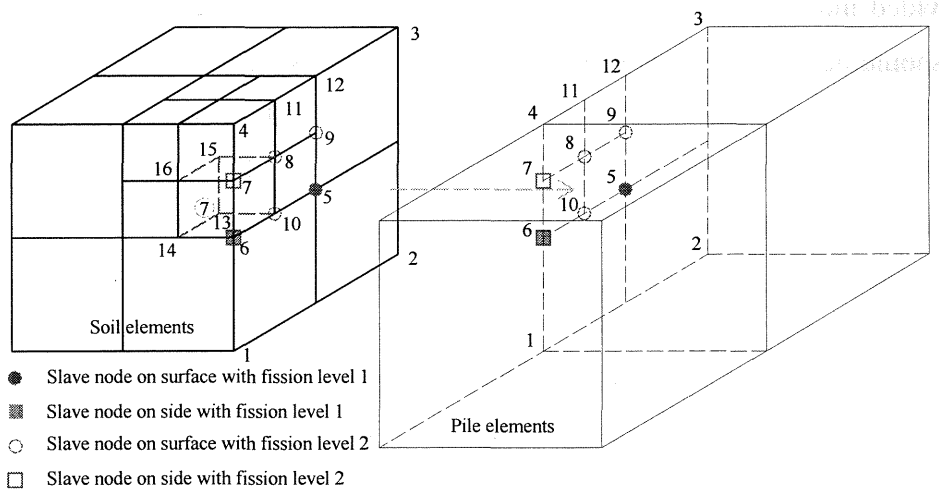

Fig.5.40 Refined mesh for soil-pile interaction in three-dimension

The motion of slave nodes 7, 8 and 10, depending on the motions of their corresponding master nodes 1-4, are calculated as

$$\dot{\mathbf{u}}_7 = \gamma_7^1\dot{\mathbf{u}}_1 + \gamma_7^4\dot{\mathbf{u}}_4,\quad \ddot{\mathbf{u}}_7 = \gamma_7^1\ddot{\mathbf{u}}_1 + \gamma_7^4\ddot{\mathbf{u}}_4 \tag{5.4.41a}$$

$$\dot{\mathbf{u}}_8 = \gamma_8^1\dot{\mathbf{u}}_1 + \gamma_8^2\dot{\mathbf{u}}_2 + \gamma_8^3\dot{\mathbf{u}}_3 + \gamma_8^4\dot{\mathbf{u}}_4,\quad \ddot{\mathbf{u}}_8 = \gamma_8^1\ddot{\mathbf{u}}_1 + \gamma_8^2\ddot{\mathbf{u}}_2 + \gamma_8^3\ddot{\mathbf{u}}_3 + \gamma_8^4\ddot{\mathbf{u}}_4 \tag{5.4.41b}$$

$$\dot{\mathbf{u}}_{10} = \gamma_{10}^1\dot{\mathbf{u}}_1 + \gamma_{10}^2\dot{\mathbf{u}}_2 + \gamma_{10}^3\dot{\mathbf{u}}_3 + \gamma_{10}^4\dot{\mathbf{u}}_4,\quad \ddot{\mathbf{u}}_{10} = \gamma_{10}^1\ddot{\mathbf{u}}_1 + \gamma_{10}^2\ddot{\mathbf{u}}_2 + \gamma_{10}^3\ddot{\mathbf{u}}_3 + \gamma_{10}^4\ddot{\mathbf{u}}_4 \tag{5.4.41c}$$

where γ_i^j is the effective parameter defined by Eqs.(5.4.27)-(5.4.31), i denotes the number of slave node and j denotes the numbers of corresponding master nodes.

The local governing equations for the sample element 7 with fission level 2 in refined mesh shown in **Fig.5.40** are given as

$$\begin{bmatrix} \widetilde{\mathbf{K}}^7 & \widetilde{\mathbf{Q}}^7 \\ \widetilde{\mathbf{Q}}^{7\mathrm{T}} & \widetilde{A}^7 \end{bmatrix} \begin{Bmatrix} {}^{t+\Delta t}\ddot{\mathbf{u}}_{14} \\ {}^{t+\Delta t}\ddot{\mathbf{u}}_{6} \\ {}^{t+\Delta t}\ddot{\mathbf{u}}_{10} \\ {}^{t+\Delta t}\ddot{\mathbf{u}}_{13} \\ {}^{t+\Delta t}\ddot{\mathbf{u}}_{16} \\ {}^{t+\Delta t}\ddot{\mathbf{u}}_{7} \\ {}^{t+\Delta t}\ddot{\mathbf{u}}_{8} \\ {}^{t+\Delta t}\ddot{\mathbf{u}}_{15} \\ {}^{t+\Delta t}p^7 \end{Bmatrix} = \begin{Bmatrix} \mathbf{f}_{\mathbf{u}}^7\left({}^{t}\dot{\mathbf{u}}^7, {}^{t}\ddot{\mathbf{u}}^7\right) \\ f_p^7\left({}^{t}\dot{\mathbf{u}}^7, {}^{t}\ddot{\mathbf{u}}^7, {}^{t}p^7\right) \end{Bmatrix} \tag{5.4.42}$$

Substituting Eq. (5.4.41) into Eq. (5.4.42) and considering that the motion of slave nodes 7, 8 and 10 are not included in general equations, the modified local equations are also divided into two parts. The first part is the set of modified governing equations which should be added to the general governing equations, given as

$$\widetilde{\mathbf{P}}^7 \begin{bmatrix} \widetilde{\mathbf{K}}^7 & \widetilde{\mathbf{Q}}^7 \\ \widetilde{\mathbf{Q}}^{7\mathrm{T}} & \widetilde{A}^7 \end{bmatrix} \begin{Bmatrix} {}^{t+\Delta t}\ddot{\mathbf{u}}^7 \\ {}^{t+\Delta t}p^7 \end{Bmatrix} = \widetilde{\mathbf{P}}^7 \begin{Bmatrix} \mathbf{f}_{\mathbf{u}}^7\left({}^{t}\dot{\mathbf{u}}^7, {}^{t}\ddot{\mathbf{u}}^7\right) \\ f_p^7\left({}^{t}\dot{\mathbf{u}}^7, {}^{t}\ddot{\mathbf{u}}^7, {}^{t}p^7\right) \end{Bmatrix} \tag{5.4.43}$$

where

$$\widetilde{\mathbf{P}}^7 = \begin{bmatrix} \mathbf{I} & 0 & 0 & 0 & 0 & 0 & 0 & 0 \\ 0 & \mathbf{I} & 0 & 0 & 0 & 0 & 0 & 0 \\ 0 & 0 & 0 & \mathbf{I} & 0 & 0 & 0 & 0 \\ 0 & 0 & 0 & 0 & \mathbf{I} & 0 & 0 & 0 \\ 0 & 0 & 0 & 0 & 0 & 0 & 0 & \mathbf{I} \end{bmatrix},$$

$${}^{t+\Delta t}\ddot{\mathbf{u}}^7 = \begin{Bmatrix} {}^{t+\Delta t}\ddot{\mathbf{u}}_{14} \\ {}^{t+\Delta t}\ddot{\mathbf{u}}_{6} \\ \sum_{i=1}^{4} \gamma_{10}^{i}\, {}^{t+\Delta t}\ddot{\mathbf{u}}_{i} \\ {}^{t+\Delta t}\ddot{\mathbf{u}}_{13} \\ {}^{t+\Delta t}\ddot{\mathbf{u}}_{16} \\ \sum_{i=1}^{2} \gamma_{7}^{i}\, {}^{t+\Delta t}\ddot{\mathbf{u}}_{i} \\ \sum_{i=1}^{4} \gamma_{8}^{i}\, {}^{t+\Delta t}\ddot{\mathbf{u}}_{i} \\ {}^{t+\Delta t}\ddot{\mathbf{u}}_{15} \end{Bmatrix}, \quad {}^{t}\dot{\mathbf{u}}^7 = \begin{Bmatrix} {}^{t}\dot{\mathbf{u}}_{14} \\ {}^{t}\dot{\mathbf{u}}_{6} \\ \sum_{i=1}^{4} \gamma_{10}^{i}\, {}^{t}\dot{\mathbf{u}}_{i} \\ {}^{t}\dot{\mathbf{u}}_{13} \\ {}^{t}\dot{\mathbf{u}}_{16} \\ \sum_{i=1}^{2} \gamma_{7}^{i}\, {}^{t}\dot{\mathbf{u}}_{i} \\ \sum_{i=1}^{4} \gamma_{8}^{i}\, {}^{t}\dot{\mathbf{u}}_{i} \\ {}^{t}\dot{\mathbf{u}}_{15} \end{Bmatrix} \quad \text{and} \quad {}^{t}\ddot{\mathbf{u}}^7 = \begin{Bmatrix} {}^{t}\ddot{\mathbf{u}}_{14} \\ {}^{t}\ddot{\mathbf{u}}_{6} \\ \sum_{i=1}^{4} \gamma_{10}^{i}\, {}^{t}\ddot{\mathbf{u}}_{i} \\ {}^{t}\ddot{\mathbf{u}}_{13} \\ {}^{t}\ddot{\mathbf{u}}_{16} \\ \sum_{i=1}^{2} \gamma_{7}^{i}\, {}^{t}\ddot{\mathbf{u}}_{i} \\ \sum_{i=1}^{4} \gamma_{8}^{i}\, {}^{t}\ddot{\mathbf{u}}_{i} \\ {}^{t}\ddot{\mathbf{u}}_{15} \end{Bmatrix}$$

Another part is the additional forces on the master nodes 1-4 due to the slave nodes 7, 8 and 10 concerning with element 7. The forces from the stiffness matrix, which are calculated by Eq.(5.4.44), are added to the places of nodes 1-4 in general stiffness

matrix. The forces from the right parts of governing equations, which are calculated by Eq.(5.4.45), are added to the places of nodes 1-4 in the right part of general governing equations.

$$\Delta\mathbf{K}_i^7 = \{0 \quad 0 \quad \gamma_{10}^i\mathbf{I} \quad 0 \quad 0 \quad \gamma_7^i\mathbf{I} \quad \gamma_8^i\mathbf{I} \quad 0\}\begin{bmatrix} \tilde{\mathbf{K}}^7 & \tilde{\mathbf{Q}}^7 \\ \tilde{\mathbf{Q}}^{7\mathrm{T}} & \tilde{A}^7 \end{bmatrix}\begin{Bmatrix} {}^{t+\Delta t}\ddot{\mathbf{u}}^7 \\ {}^{t+\Delta t}p^7 \end{Bmatrix} \tag{5.4.44}$$

$$\Delta\mathbf{f}_i^7 = \{0 \quad 0 \quad \gamma_{10}^i\mathbf{I} \quad 0 \quad 0 \quad \gamma_7^i\mathbf{I} \quad \gamma_8^i\mathbf{I} \quad 0\}\begin{Bmatrix} \mathbf{f}_u^7\left({}^t\dot{\mathbf{u}}^7, {}^t\ddot{\mathbf{u}}^7\right) \\ f_p^7\left({}^t\dot{\mathbf{u}}^7, {}^t\ddot{\mathbf{u}}^7, {}^tp^7\right) \end{Bmatrix} \tag{5.4.45}$$

where i=1-4, and $\gamma_7^2 = \gamma_7^3 = 0$.

Modifying permeance of pore water between hexahedra elements

By the same way as two-dimensional adaptive analysis introduced in section 5.2, the usual permeance route crossing the intersurface should be modified when an unfissioned element besides a fissioned element as shown in **Fig.5.41**. The permeance between two unfissioned elements is taken place by the permeance between an unfissioned element and four fissioned elements. The terms describing the permeance of pore water in three-dimensional continuity equation is modified according to this.

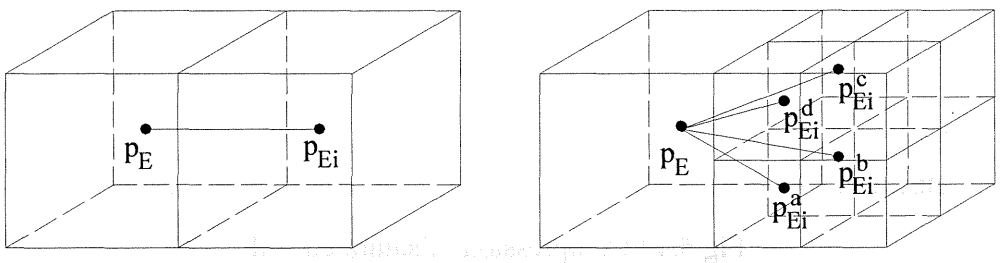

Usual permeance　　Modified permeance

Fig.5.41 Modifying permeance of pore water in three-dimension

5.5 Demonstration of Adaptive Mesh Refinement

Some simple examples are calculated here to test the adaptive mesh refinement method applied to saturated soil analysis and soil-pile interaction analysis in two-dimension and three-dimension.

5.5.1 2-D Examples

Localization of saturated soil

This is an example of a simulation of saturated soil behavior for applied surface load taking into account large deformation, in which *h*-adaptive FE analysis is implemented within the period of compression. The soil block is 2m long by 2m high, and analysis begins with a 100-element mesh, as shown in **Fig.5.42**. Displacement of nodes perpendicular to the boundary side is constrained on the left and bottom. A drained boundary condition is placed only on the upper surface. A stepwise load is applied to the right side of the top surface of the block through a rigid plate, 0.8m long, without weight. The load is increased linearly to 20kN/m during t=2 seconds.

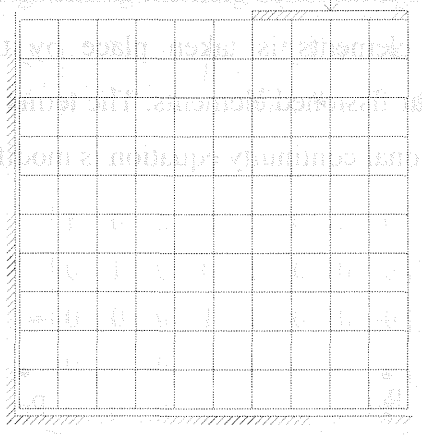

Fig.5.42 Compression of saturated soil

The saturated sand which is Ensyunada sand with relative density Dr=40% and initial void ratio e_0=0.992 is described by a cyclic elasto-plastic model. The parameters of soil are given in **Table 2.1**. Four-node quadrilateral element is used. Error of shear strain is estimated. The relative error limit $\overline{\eta}$ is assigned to 5%. The relative error distribution before mesh refinement is given as **Fig.5.43**. A large shear strain region can be seen.

The refined meshes at time t=1sec and t=2sec are given in **Fig.5.44**, (a) and (b). The elements located in the large shear strain belt zone are refined.

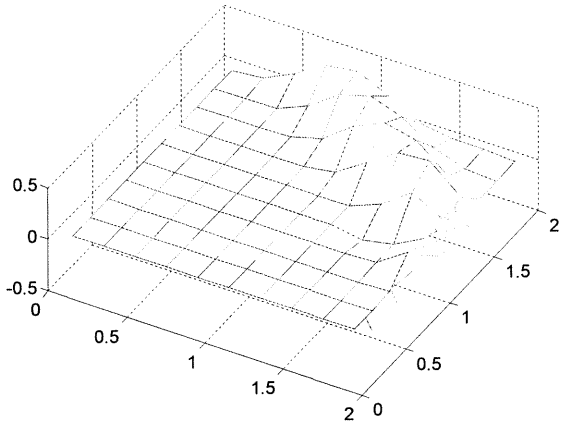

Fig.5.43 Relative error before refinement

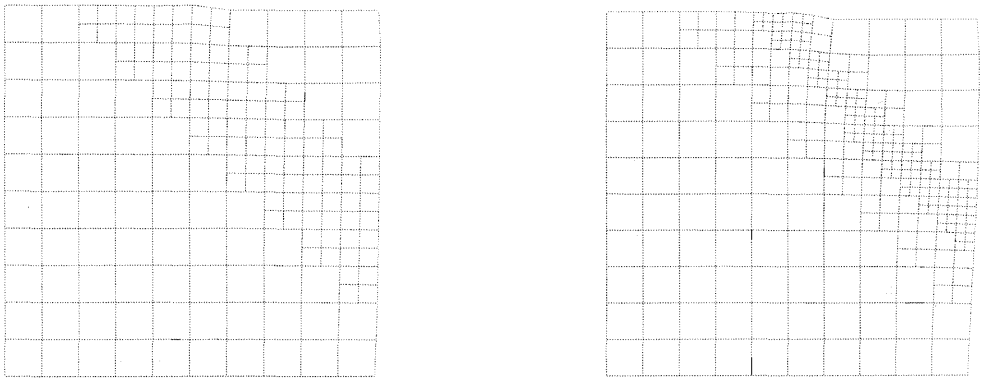

(a) t=1sec, 178 elements (b) t=2sec, 274 elements

Fig.5.44 Refined meshes

In this example, *h*-adaptive FE method is implemented in elasto-plastic analysis of saturated soil. When the large shear strain belt region is appeared, the error of shear strain is increasing evidently with increasing of shear strain. Error estimator evaluates errors successfully as shown in **Fig.5.43**. At the same time, fission scheme is used in the area with large error value indicated by error estimate. No doubt, our method is applicable to nonlinear analysis of saturated soil without liquefaction.

Simulation of shaking table experiment

The aim of this example is to check the efficiency of *h*-adaptive FE method applied to nonlinear analysis of liquefied soil. The shaking table experiment of saturated sand

(Hamada, 1994), in which flow process of liquefied soil was examined, is simulated by adaptive FE method. The detail of experiment is introduced in **Chapter 3** in detail. First, a strong vibration applied to soil container with saturated sand, which maximum value of accelerate is 100 gal, though the shaking test table until time t=7sec. This vibration causes the saturated soil liquefied. Then inclined the soil container to a certain angle (4.2%) in order to let the liquefied sand flow by gravity. The process of inclining begins from horizontal angle at time t=8.7sec and reach to the angle 4.2% at time t=10.6sec. Enshyunada sand with relative density Dr=40% and initial void ratio e_0=0.992 was used in the experiment.

The time history of acceleration shown in **Fig.5.45** is used to simulate this experimental process.

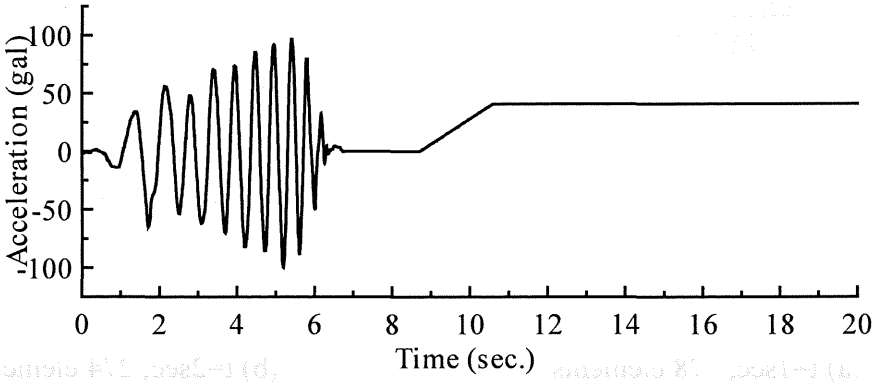

Fig.5.45 Time history of acceleration input

H-adaptive FE analysis is applied to simulate this experiment. The initial mesh with 24 elements is shown in **Fig.5.46**. The upper surface is drained boundary. Linear quadrilateral element is used. Error of strain is evaluated in error estimation. Because the aim of this example is to check adaptive FE method in liquefaction process, the fission scheme starts at time t=8.7sec.

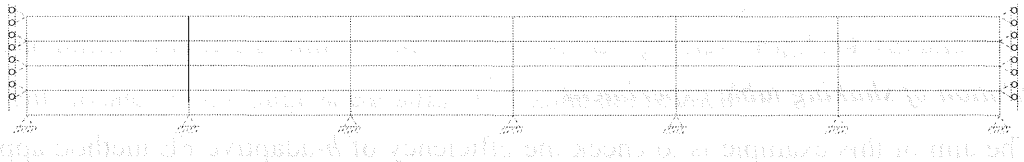

Fig.5.46 Initial mesh for liquefied sand flow

After the strong vibration from t=0sec to t=7.0sec, the saturated soil in the container is liquefied. When liquefaction happens reduction of effective stress and lose of stiffness and strength of soil. Inclining the container, liquefied soil flows driven by gravity. The flow causes large deformation and high value of discretization error. In the time of vibration, the distribution of error is irregular and the value of error is not high, but in the time of liquefaction the high values of error concentrate in the regions with large deformation. For this reason, adaptive FE method is more effective in the flow of liquefaction. In this example, the adaptive mesh refinement for liquefied soil starts from the beginning of flow. The final refined mesh is given in **Fig.5.47**. The relative error limit $\overline{\eta}$ is defined as 7%. We can find that the elements where large deformation occurs, in other words, where errors are large, are fissioned step by step and the sizes of these elements become small.

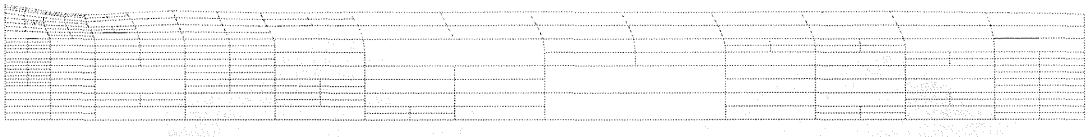

Fig.5.47 Final mesh (number of elements 366)

The final surfaces of soil calculated for 3 cases were compared in **Fig.5.48**. In case a and c, 720 elements fixed mesh and 24 elements fixed mesh were used without adaptive mesh refinement. In case b, we used adaptive mesh refinement with 24 elements as the initial mesh. We can find that although the final surface calculated with fixed 24-element mesh is fluctuate, but the final surface calculated by *h*-adaptive FE method from 24-elements mesh is almost as fine as that calculated with fixed 720-element mesh. The calculation time in case a is about 20 hours, but the calculation time in case b is about 11 hours in the same computer. We can get the conclusion that the level of accuracy of finite element method is raised while the calculation work is reduced by using adaptive mesh refinement. This result can be explained easily by the mechanism of adaptive technique. In adaptive analysis, the local elements with large error but not global mesh are refined, thus the small-sized elements with fine accuracy are used in the

region where fine mesh is needed and number of degree of freedom is used efficiently. That's the reason why the result in case b can reach almost same accuracy as the result in case a.

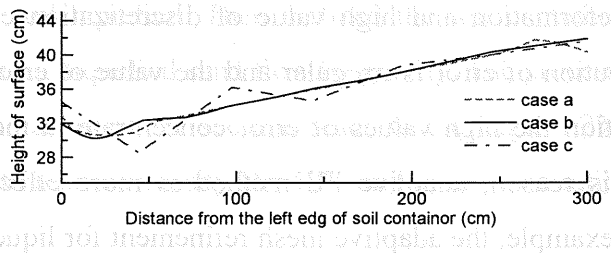

Fig.5.48 Final soil surface

From this example, we can find that h-adaptive FE method can be applied effectively to liquefaction period of elasto-plastic analysis.

5.5.2 3-D Compression of Soil Block

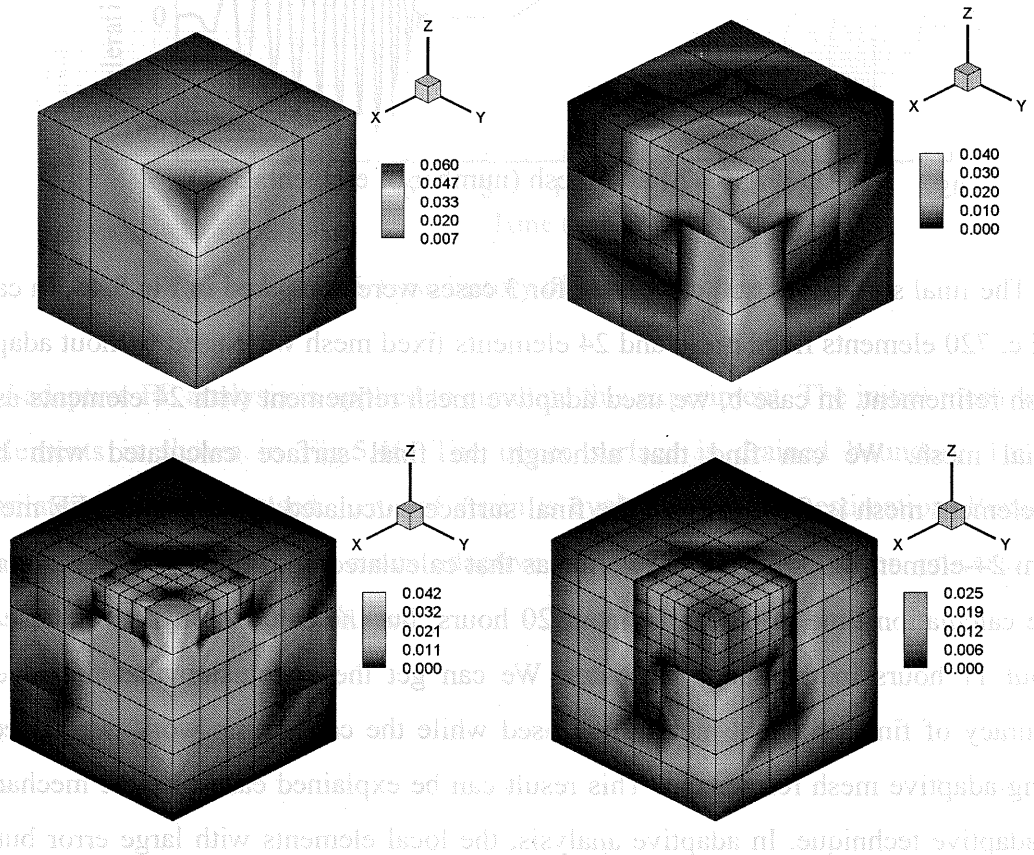

Fig.5.50. Refined meshes and relative error contours at different steps

A simple three-dimensional example is analyzed here to test the adaptive mesh refinement method. The example model is same with the example we use to check the error estimator in section 5.3.4, loading condition is Load 1. *H*-adaptive FE analysis starts from an initial mesh with 27 elements, the relative error limit is defined as 2%. The relative error contours and refined meshes at different steps are shown in **Fig.5.50**.

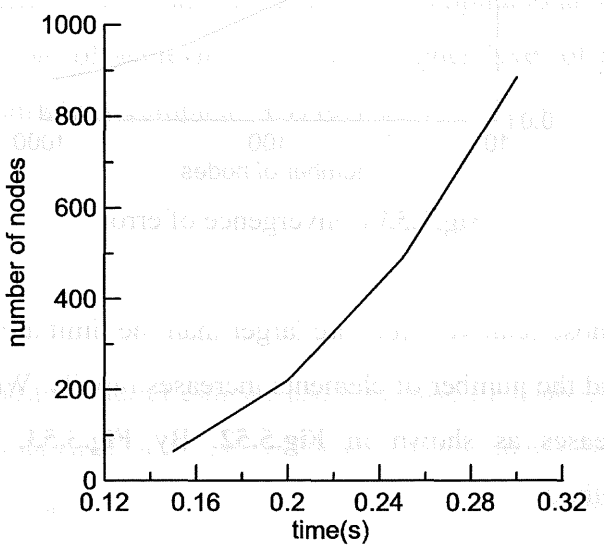

Fig.5.51 Increase of node number

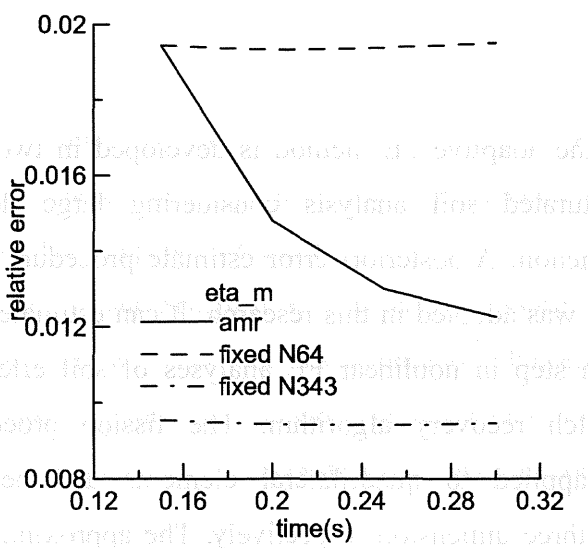

Fig.5.52 Decrease of relative error

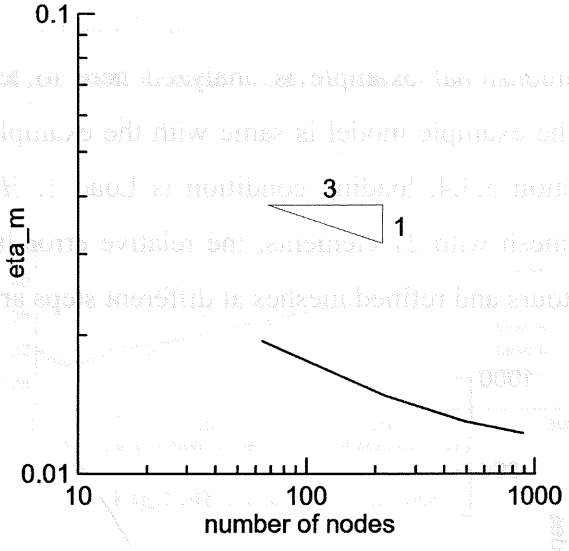

Fig.5.53 Convergence of error

The elements whose relative errors are larger than the limit are fissioned well. From **Fig.5.51**, we can find the number of elements increases rapidly. With the same time, the relative error decreases as shown in **Fig.5.52**. By **Fig.5.53**, we demonstrate the efficiency of our method.

5.6 Conclusions

In this chapter the adaptive FE method is developed in two-dimension and three -dimension for saturated soil analysis considering large deformation including liquefaction phenomenon. A posteriori error estimate procedure based on L_2 norm of strain or stress error was adopted in this research. It can estimate the error of elements after the calculation step in nonlinear FE analyses of soil effectively depending on superconvergent patch recovery algorithm. The fission procedure belong to the *h*-refinement was applied to quadrilateral elements and hexahedra elements in two-dimension and three dimension respectively. The approximation of finite element method was successively refined as to satisfy the predetermined standard of accuracy, and the efficiency of this method was confirmed in the finite element analyses. This method is easy to apply to solve practical and engineering problem.

The results of the three simple examples were given to demonstrate the efficiency of our method. These are: local compression of saturated sand caused by a stepwise loading, which are elasto-plastic analysis without liquefaction, in two-dimension; flow of liquefied sand problems considering large deformation in two-dimension; and local compression of saturated sand caused by a stepwise loading in three dimension. The results we have obtained show that this adaptive scheme is capable of achieving substantial improvements in accuracy under a limit computational effort. Generally, an adaptive mesh is capable of achieving one order higher level of accuracy as a fixed mesh with less than half of the computational resource.

References

[1] Tang X, Sato T. A posteriori error estimate and h-adaptive FE analysis of Liquefaction with large deformation, Journal of Geotechnical Engineering (accepted), 2004.

[2] Tang X, Sato T. H-adaptivity applied to liquefiable Soil in nonlinear analysis of soil-pile interaction, Soil Dynamics & Earthquake Engineering (submitted), 2004.

[3] Oka F, Yashima A, Shibata T, Kato M and Uzuoka R. FEM-FDM coupled liquefaction analysis of a porous soil using an elasto-plastic model, Applied Scientific Research, Vol. 52, pp. 209-245, 1994.

[4] Oka F, Yashima A, Tateishi A, Taguchi Y and Yamashita S. A cyclic elasto-plastic constitutive model for sand considering a plastic-strain dependence of the shear modulus, Geotechnique, Vol. 49, No. 5, pp. 661-680, 1999.

[5] Oka F, Yashima A, Kato M and Sekiguchi K. A constitutive model for sand based on the non-linear kinematic hardening rule and its application, Proceedings of 10th World Conference on earthquake Engineering, Barcelona, pp. 2529-2534, 1992.

[6] Biot MA. Mechanics of deformation and acoustic propagation in porous media, Journal of Applied Physics, Vol. 33, pp. 1482-1498, 1962

[7] Akai K and Tamura T. Study of two-dimensional consolidation accompanied by an elastic plastic constitutive equation, Proceedings of JSCE, No. 269, pp. 98-104, 1978.

[8] Di Y and Sato T. Large deformation Dynamic analysis of porous medium using FEM-FDM coupled method, Advances in Computational Engineering & Sciences (Atluri,

S.N.,Nishioka, T. and Kikuchi, M.,Eds.), Chapter 12 Multiphysics & Multibody Dynamic, Tech Science Press, 2001, (CD-ROM).

[9] Di Y and Sato T. FEM-FDM coupled method for saturated soil analysis considering large deformation, Proceedings of the 26th JSCE Earthquake Engineering Symposium, Sapporo, pp. 193-196, 2001.

[10] Kelly DW, De, JP Gago, SR and Zienkiewicz OC et.al. A Posteriori Error Analysis and Adaptive Processes in The Finite Element Method: Part I-Error Analysis, International Journal for Numerical Methods in Engineering, Vol. 19, pp. 1593-1619, 1983.

[11] Zienkiewicz OC., Huang MS and Pastor M. Localization Problems in Plasticity Using Finite Elements with Adaptive Remeshing, International Journal for Numerical. Analysis Methods of Geomechnics, Vol. 19, pp.127-148, 1995.

[12] Zienkiewicz OC and Zhu JZ. A Simple Error Estimator and Adaptive Procedure for Practical Engineering Analysis, International Journal for Numerical Methods in Engineering, Vol. 24, pp. 337-357, 1987.

[13] Zienkiewicz OC, Liu YC and Huang MS. Error Estimation and Adaptivity in Flow Formulation for Forming Problems, International Journal for Numerical Methods in Engineering, Vol. 25, pp. 23-42, 1988.

[14] Zienkiewicz OC and Zhu JZ. Error Estimates and Adaptive Refinement for Plane Bending Problems, International Journal for Numerical Methods in Engineering, Vol. 28, pp. 2839-2853, 1989.

[15] Mar A and Hicks MA. A Benchmark Computational Study of Finite Element Error Estimation, International Journal for Numerical Methods in Engineering, Vol. 39, pp. 3969-3983, 1996.

[16] Hicks MA. Coupled Computations for an Elastic-Perfectly Plastic Soil Using Adaptive Mesh Refinement, International Journal for Numerical. Analysis Methods of Geomechnics, Vol. 24, pp. 453-476, 2000.

[17] Hinton E and Campbell JS. Local and global smoothing of discontinuous finite element functions using a least squares method, International Journal for Numerical Methods in Engineering, Vol. 8, pp. 461-480, 1974.

[18] Selman A, Hinton E and Bicanic N. Adaptive Mesh Refinement for Localized Phenomena, Computer & Structures, Vol. 63, pp. 475-495, 1997.

[19] Zienkiewicz OC, Liu YC and Huang MS. Error Estimates and Convergence Rates for

Various Incompressible Element, International Journal for Numerical Methods in Engineering, Vol. 28, pp. 2191-2202, 1989.

[20] Kelly DW, De JP, Gago SR and Zienkiewicz OC et. al. A Posteriori Error Analysis and Adaptive Processes in The Finite Element Method: Part II-Adaptive Mesh Refinement", International Journal for Numerical Methods in Engineering, Vol. 19, pp. 1621-1656, 1983.

[21] Belytschko T and Tabbara M. H-Adaptive Finite Element Methods for Dynamic Problem, with Emphasis on Localization, International Journal for Numerical Methods in Engineering, Vol. 36, 4245-4265(1993).

[22] Belytschko T, Wong BL and Plaskacz EJ. Fission-fussion adaptivity in finite elements for nonlinear dynamics of shells, Computers & Structures, Vol. 33, pp. 1307-1323, 1989.

[23] Hamada M, Sato H and Kawakami T. A Consideration of the Mechanism for Liquefaction-related Large Ground Displacement, A proceedings from the fifth U.S.-Japan workshop on earthquake resistant design of lifeline facilities and countermeasures against soil liquefaction, Technical Report NCEER-94-0026, pp. 217-232, 1994.

[24] Gabaldon F and Goicolea JM. Linear and non-linear finite element error estimation based on assumed strain fields, International Journal for Numerical Methods in Engineering, Vol. 55, pp. 413-429, 2002.

[25] Zienkiewicz OC and Zhu JZ . The Supercovergent Patch Recovery and A Posteriori Error Estimates. Part II: The Recovery Technique, International Journal for Numerical Methods in Engineering, Vol. 33, pp. 1331-1364, 1992.

[26] Zienkiewicz OC and Zhu JZ. The Supercovergent Patch Recovery and A Posteriori Error Estimates. Part II: Error Estimates and Adaptivity, International Journal for Numerical Methods in Engineering, Vol. 33, pp. 1365-1382, 1992.

[27] Taylor RL, Simo JC, Zienkiewicz OC and Chan ACH. The Patch Test—A Condition for Assessing FEM Convergence, International Journal for Numerical Methods in Engineering, Vol. 22, pp. 391-462, 1986.

[28] Zienkiewicz OC and Wu J. Automatic Directional Refinement in Adaptive Analysis of Compressible Flows, International Journal for Numerical Methods in Engineering, Vol. 37, pp. 2189-2210, 1994.

[29] Zienkiewicz OC and Zhu JZ. The Superconvergent Patch Recovery (SPR) and Adaptive Finite Element Refinement, Computational Methods and Application of Mechanics Engineering, Vol. 101, pp. 207-224, 1992.

[30] Prasad MVKV and Krishnamoorthy CS. Adaptive Finite Element Analysis of Mode I Fracture in Cement-Based Materials, International Journal for Numerical. Analysis Methods of Geomechnics, Vol. 25, pp. 1131-1147, 2001.

[31] Tang X, Sato T. Adaptive mesh refinement and error estimate for 3-D seismic analysis of liquefiable soil considering large deformation, Journal of Natural Disaster Science (submitted), 2004.

Chapter 6

Adaptive Analysis of Ground Flow and Pile-Soil Interaction Considering Large Deformation of Liquefaction

6.1 Introduction

In this chapter, the posteriori error estimates based on superconvergent patch recovery smoothing technique and the *h*-adaptive mesh refinement are applied to four practical examples of seismic analysis using finite deformation theory. These examples include two-dimensional and three-dimensional soil flow due to liquefaction as well as soil-pile interaction problems. The efficiency of the *h*-adaptive FE method is demonstrated by these practical examples.

Section 6.2 presents a two-dimensional example of embankment constructed on the liquefiable soil; section 6.3 presents a two-dimensional example of soil-pile interaction analysis; section 6.4 presents three-dimensional example of embankment seismic analysis; section 6.5 presents a three-dimensional example of soil-pile interaction

analysis.

Adaptive analysis results of mesh deformation, error distribution, average error history, displacement responses are calculated and compare with FEM results. For the examples of soil-pile interaction analysis, the displacement and the curvature of pile are also check in detail. Updated Lagrangian formulations are used in the governing equations to deal with the large deformation of liquefaction flow. In section 6.2, the results calculated with finite deformation theory are compared with those with infinitesimal assumption.

The approximation is successively refined to satisfy the predetermined standard of accuracy and the efficiency of this method is confirmed in the finite element analysis. This method is easy to apply for solving practical engineering problems.

6.2 2-D Adaptive Analysis of Embankment in Earthquake

The first numerical example is the seismic analysis of two-dimensional embankment. In this example, *h*-adaptive FE method using updated Lagrangian formulation is applied to an earthquake response analysis of embankment sitting on liquefiable soil. An overall elasto-plastic process including liquefaction is analyzed. The efficiency of *h*-adaptive FE method applied to two-dimensional liquefiable soil problem of practical engineering is checked.

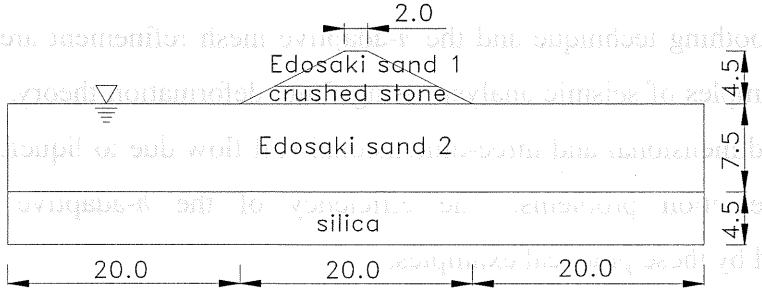

Fig.6.1 Two-dimensional example embankment

The model of embankment and soil layer is shown in **Fig.6.1**. The embankment is

2m wide on the top and 20m wide in the bottom. There are two kinds of soil without pore water in the embankment, Edosaki sand 1 and crushed stone. The soil region we considered is 60m wide and 12m deep. There are two kinds of saturated soil, Edosaki sand 2 and silica in the soil layers. The dynamic parameters of these soils are given in **Table 6.1**. The initial stresses of elements are calculated with gravity.

Table 6.1 Parameters of soil (t, m, s)

Material parameter	Edosaki sand 1	Crushed stone	Edosaki sand 2	silica
Density $\rho(t/m^3)$	1.75	1.54	1.857	1.990
Coefficient of permeability **k**(m/s)	-	-	1.7E-5	2.5E-5
Initial void ratio e_0	0.856	0.856	0.856	0.676
Compression index λ	0.0264	0.0264	0.0264	0.0250
Swelling index κ	0.0055	0.0055	0.0055	0.0025
Initial shear modulus ratio G_0/σ_{m0}	829	829	829	1280
Over consolidation ratio **OCR**	1.0	1.0	1.0	1.0
Phase transformation stress ratio M_m	0.91	0.91	0.91	0.91
Failure stress ratio M_f	1.12	1.12	1.12	1.51
Hardening parameter B_0	3000	3000	3000	5000
Hardening parameter B_1	0.0	0.0	0.0	0.0
Hardening parameter C_f	-	-	60	100
Plastic reference strain γ^P	-	-	0.01	0.004
Elastic reference strain γ^E	-	-	0.03	0.09
Dilatancy parameter D_0	0.0	0.0	5	1.2
Dilatancy parameter **n**	0.0	0.0	1.2	4.0

The linear quadrilateral element with four nodes is selected in the initial mesh with 216 elements shown as **Fig.6.2**. The elements in liquefiable soil layers are 2.5 m long and 1.5 m high. The displacement of bottom boundary are fixed, side boundary is fixed in horizontal direction. Drainage is allowed only on the top boundary surface of the mesh.

We use a time history of horizontal acceleration shown in **Fig.6.3** as input load. It was recorded during Hyogoken-Nanbu earthquake, the maximum value is 722 gal. Only 9 seconds is used in our analysis.

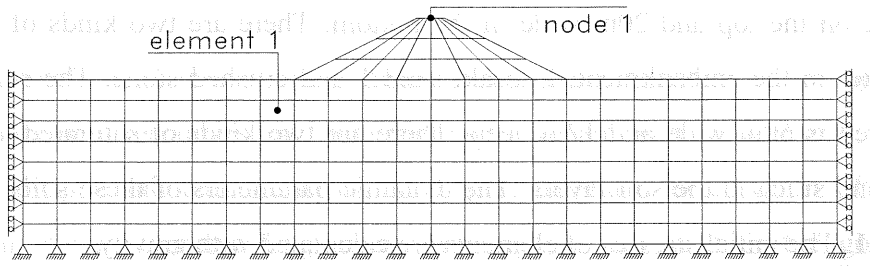

Fig.6.2 Initial mesh of embankment with 216 elements

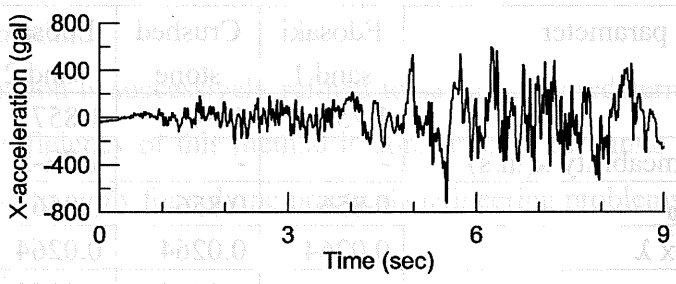

Fig.6.3 Input acceleration

The curve of extra pore water pressure ratio (EPWPR) of element 1 is given in **Fig.6.4** for two cases, infinitesimal deformation assumption (small deformation) and finite deformation assumption (large deformation). When the value of EPWPR turns to 1.0, the effective stress in the element turns to 0 and the stiffness of the element loses completely. At this time the soil is liquefied and we can find that the soil begin to turn into a stable liquefaction state at time t=6.0 second. We give the analysis results from t=0.0 second to t=9.0 second. In this period, the saturated soil shows all states of a liquefaction process, from elastic state to plastic state.

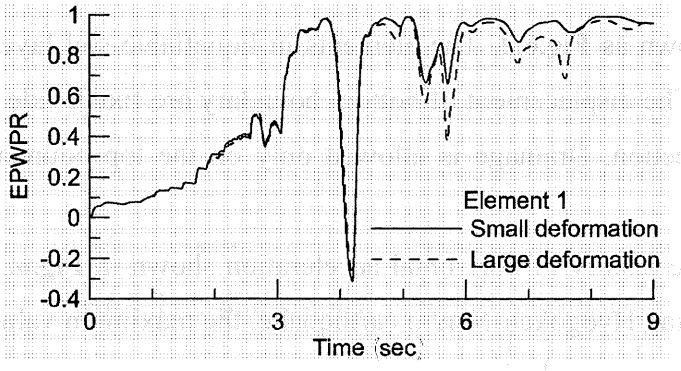

Fig.6.4 EPWPR of element 1

In this analysis, a posteriori error estimates algorithm depending on superconvergent patch recovery technique is used. The L_2-norm of strain is selected to evaluate the error. It indicates the zone, where the gradient of strain or the deformation is larger, with higher error value. Of course, fine mesh is needed in this zone. The mesh refinement is carried out according to the distribution of relative error. As a reference variable of error estimates, strain is better than stress because strain gives much smoother distribution of relative error.

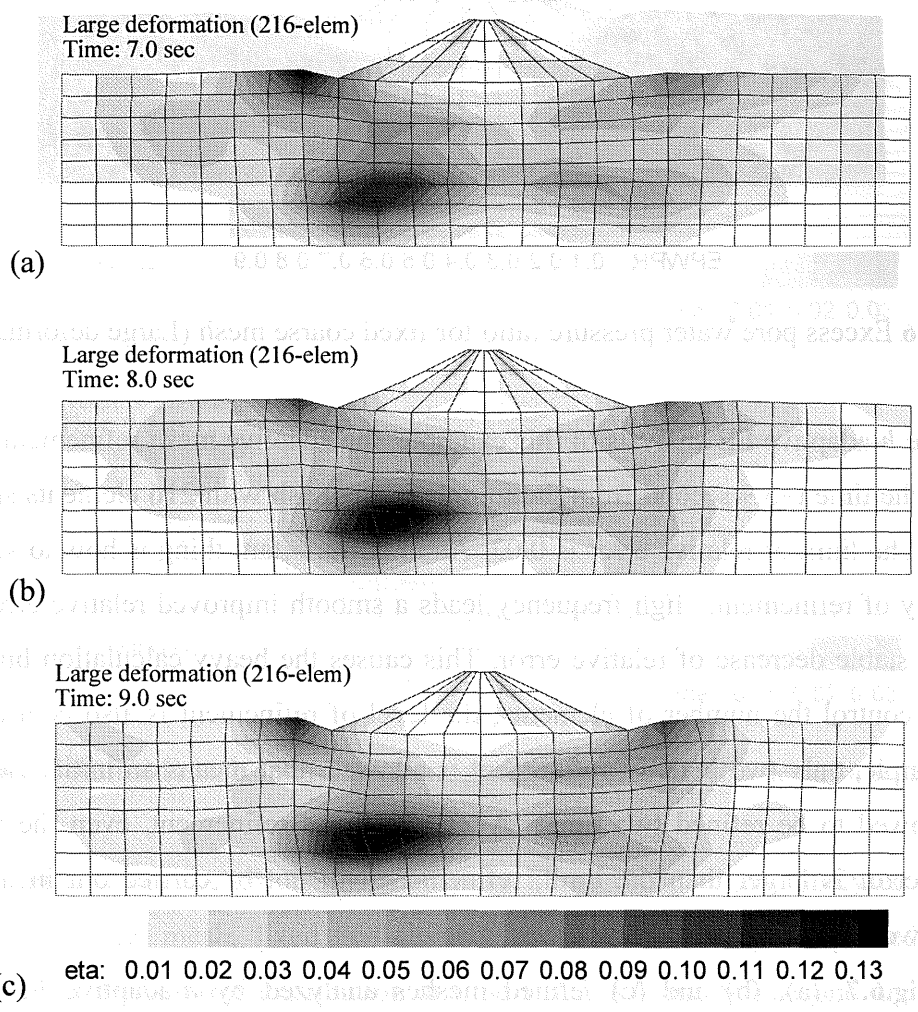

Fig.6.5 Results of fixed coarse mesh and relative error (Large deformation)

In **Fig.6.5**, (a), (b) and (c), the deformed meshes and their distributions of relative errors at t=7.0, 8.0 and 9.0 second analyzed with fixed 216-element mesh are given respectively. The deformation and strain in the regions besides the foot of embankment

and under the embankment are larger than other regions. The values of relative error in these regions are increased. The elements in this region are also with large deformation and strain. They are the main part of the whole mesh that effects the displacement of the embankment.

The excess pore water pressure ratio (EPWPR) at time t=7 second for fixed 216-element is also given in **Fig.6.6**. From this, we can find large part of saturated soil is liquefied.

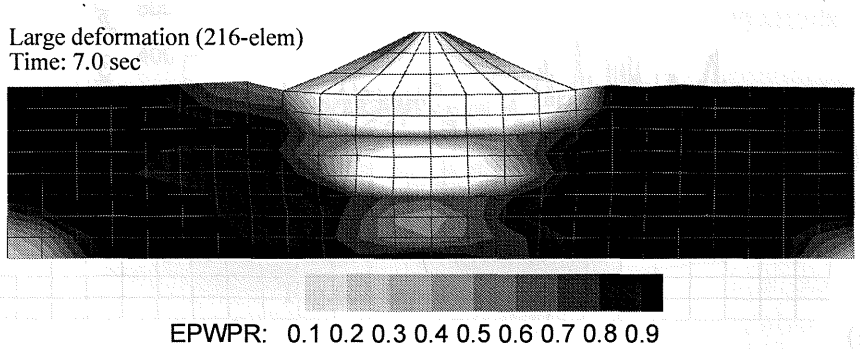

Fig.6.6 Excess pore water pressure ratio for fixed coarse mesh (Large deformation)

In the *h*-adaptive FE analysis of this example, the adaptive mesh refinement process starts at the time t=5.9 second from the initial coarse mesh with 216 elements shown as **Fig.6.2**. The limit of relative error is 0.03. Another important thing is how to select the frequency of refinement. High frequency leads a smooth improved relative error curve showing stable decrease of relative error. This causes the heavy calculation burden. In order to control the number of elements, the level of refinement is also controlled. In this example, only two level of refinement is allowed, that means an initial element is only allowed to be refined two times. After two times refinement, even the value of relative error is larger than the limit, refinement will not be carried out in this zone refined two times.

In **Fig.6.7**, (a), (b) and (c) refined meshes analyzed by *h*-adaptive FEM using updated Lagrangian method are given. The elements in the region with large error, as same as where we mentioned before, are refined step by step. The relative error values of refined mesh decrease in a large degree. The mesh becomes fine while the number of elements is increasing. In this example, after two level refinements, the value of relative error in the whole mesh is less than the limit of 0.03.

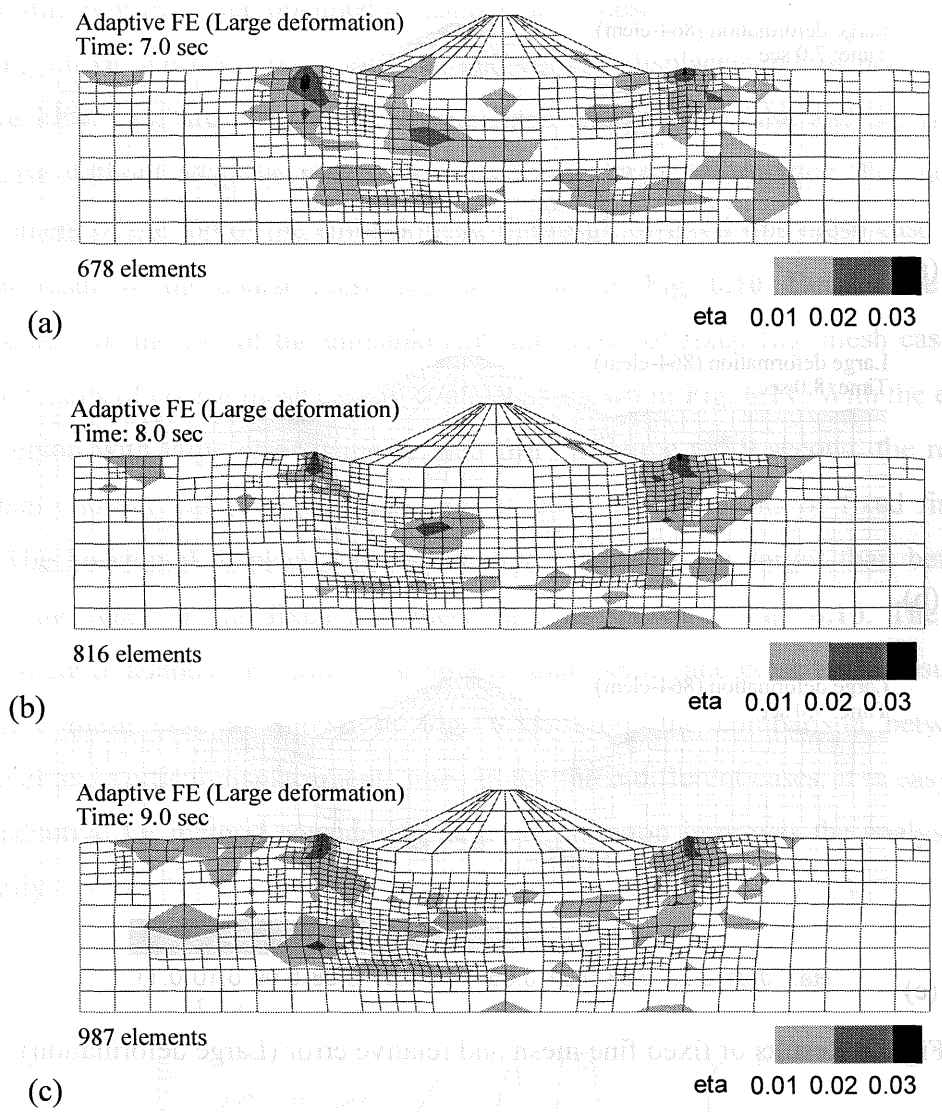

Fig.6.7 Refined mesh and relative error with adaptive FE (Large deformation)

In order to check the efficiency of adaptive FE method, we also analysed the same example with fine mesh, fixed 864-element mesh without adaptive procedure. The meshes with relative error distribution at time t=7.0, 8.0 and 9.0 second are given as **Fig.6.8.**(a), (b) and (c) respectively. It is evident that the value of relative error of the fine mesh is much less. The distribution of the relative error is also depending on the deformation of the elements. The regions near the foot of embankment or under it are in higher value of relative error than other regions. It is evident that refinement of these elements improves the accuracy of the embankment displacement response.

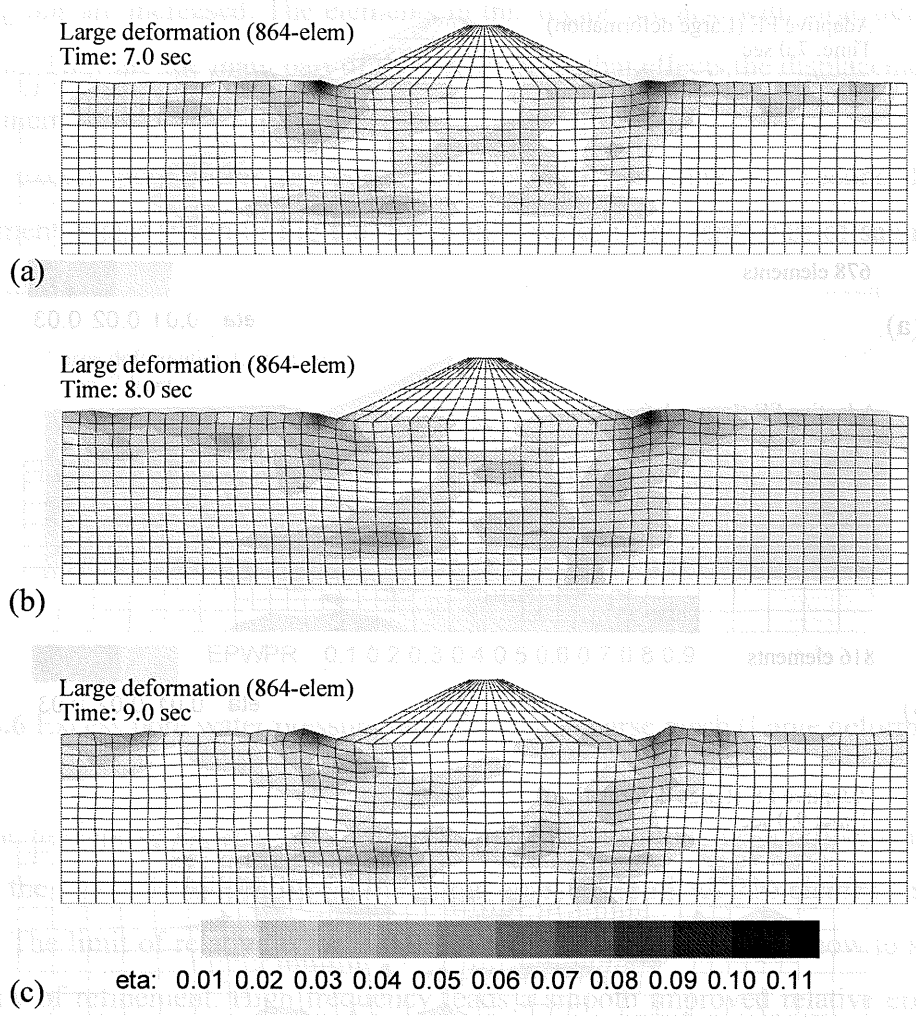

Fig.6.8 Results of fixed fine mesh and relative error (Large deformation)

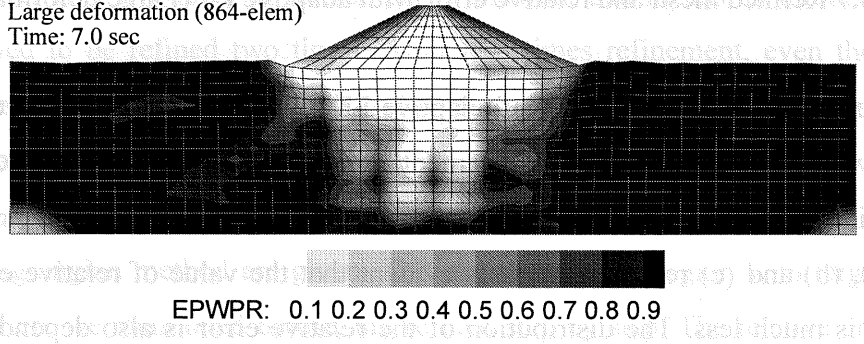

Fig.6.9 Excess pore water pressure ratio for fixed fine mesh (Large deformation)

The excess pore water pressure of this mesh at time t=7.0 second is shown in

Fig.6.9. The distribution of excess pore water pressure obtained by using fine mesh is a little bit different from that obtained by using coarse mesh.

In **Figs.6.10** and **6.11**, the horizontal and vertical displacements of node 1 for the adaptive FEM case are compared with the fixed coarse mesh case and the fixed fine mesh case without adaptive procedure considering large deformation. For horizontal displacement of the top of the embankment, the result of fixed fine mesh case is larger than the result of the coarse mesh case as shown in **Fig. 6.10**. But for the vertical displacement of the top of the embankment, the result of fixed fine mesh case is less than the results of coarse mesh case in contrast as shown in **Fig. 6.11**. With the elements in the region with large error being refined from the time t=5.9 second, the results of horizontal and vertical displacements turns to close to the results of fixed fine mesh cases. The horizontal displacement in adaptive FE case turns larger than before and close to the result in the fixed fine mesh case as shown in **Fig. 6.10**. The vertical displacement in adaptive FE case turns smaller than before and close to the result in the fixed fine mesh case as shown in **Fig. 6.11**. From the comparison between the horizontal and vertical displacements lines in the three different cases, it is easy to find that *h*-adaptive FE method considering large deformation improves the analysis result efficiently.

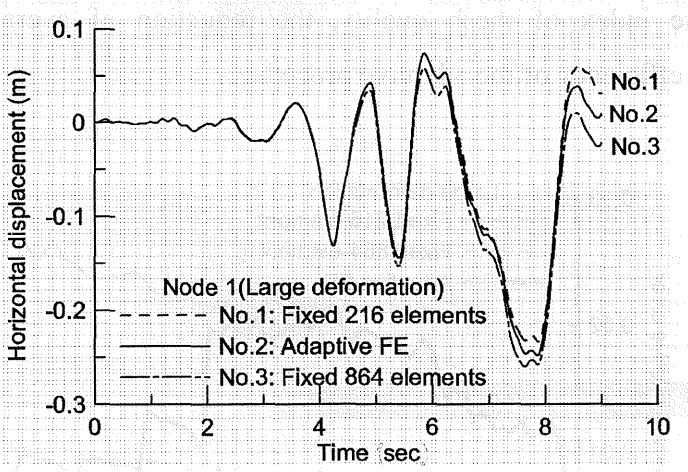

Fig.6.10 Horizontal displacement of node 1 for large deformation

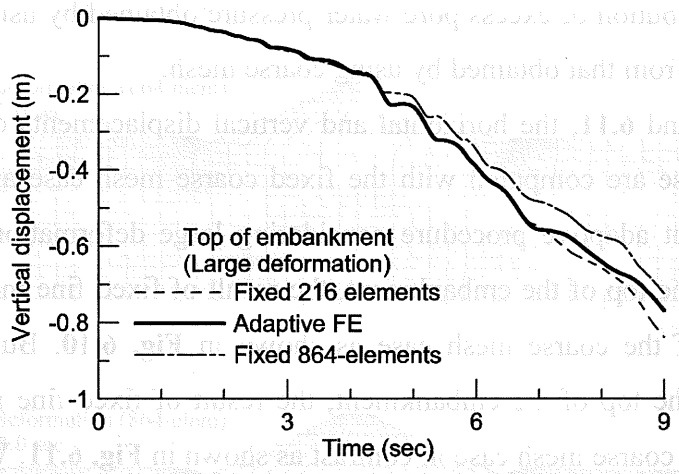

Fig.6.11 Vertical displacement of node 1 for large deformation

The average relative errors of whole mesh in large deformation case are given as **Fig.6.12**. It is indicates that the average relative error of fixed coarse mesh with 216 elements is larger than the value of fixed fine mesh with 864 elements. In the analysis of adaptive FE considering large deformation, the value of average relative error decreases after adaptive procedure starts at time t=5.9 second. With the adaptive process going on, the value of average relative error closes to the value of fixed fine mesh with 864 elements and exceeds it to reach a new lower level. The aim of adaptive procedure is to improve the accuracy of finite element analysis via reducing the size of elements. As an effective evaluate index of mesh quality, the reduction of average relative error demonstrates the efficiency of the adaptive procedure.

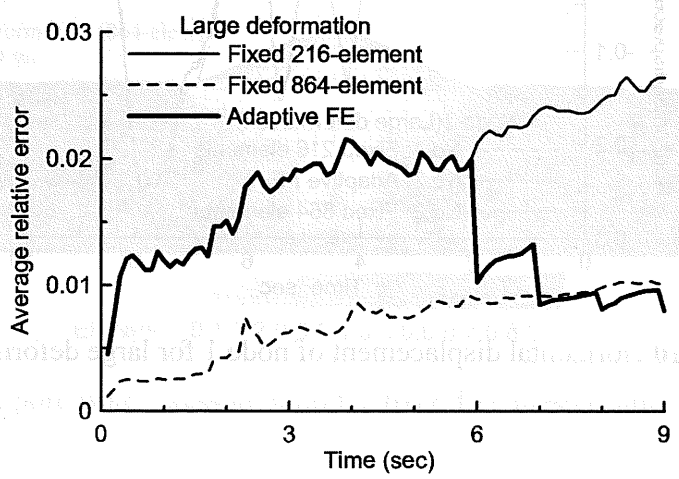

Fig.6.12 Average relative error (large deformation)

As a comparison with the results considering large deformation, we also give the results of adaptive FE analysis basing on the assumption of infinitesimal deformation.

At first, deformed mesh of the fixed coarse mesh at time t=7.0, 8.0 and 9.0 second are given in **Fig. 6.13**. The contours of relative error are also included in the figures Although the general deformation due to liquefaction are not so large, but there are some region with large deformation, especially in the areas near or under the embankment.

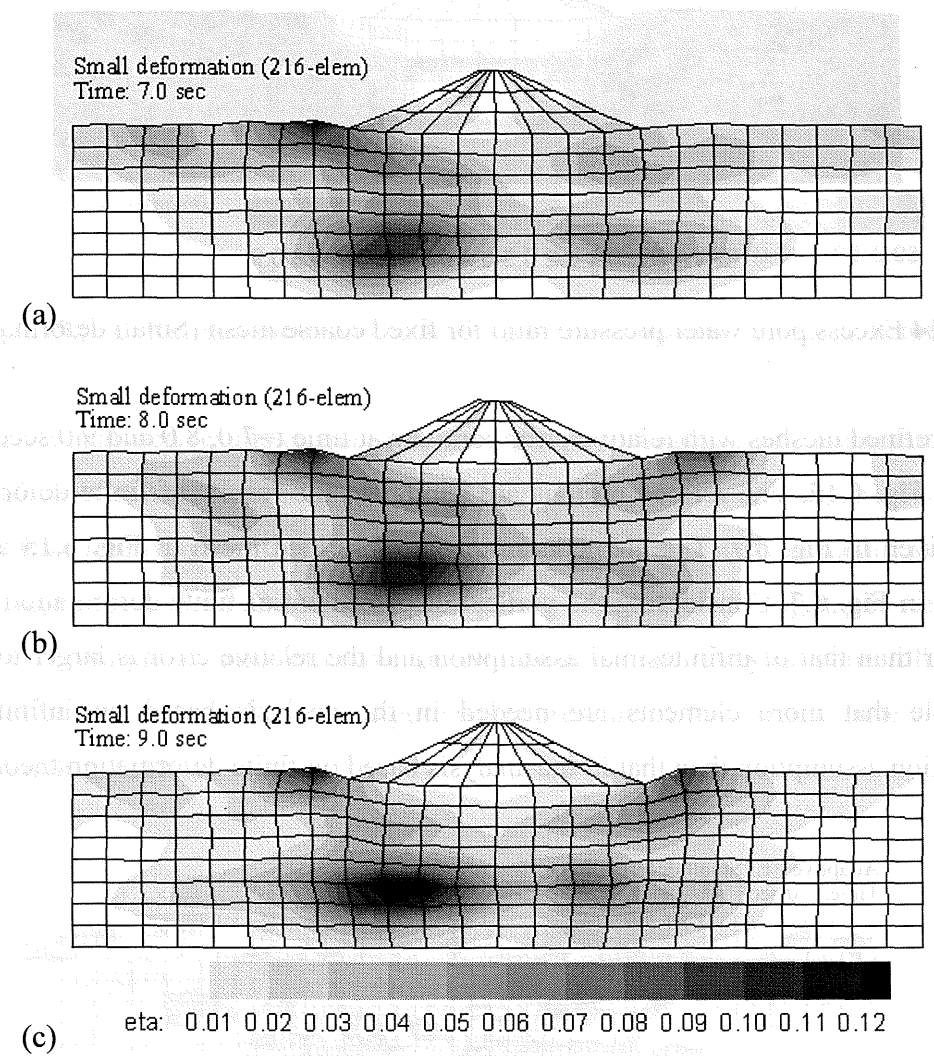

Fig.6.13 Results of fixed coarse mesh and relative error (Small deformation)

We can find the difference between the two results of the infinitesimal assumption and finite deformation assumption by comparing **Fig. 6.5** with **Fig. 6.13**. The vertical

deformation of the last case shown in **Fig.6.13** are larger than the deformation of the other case shown in **Fig.6.5**, and the relative errors of the last case are larger.

The excess pore water pressure ratio (EPWPR) at time t=7.0 second for fixed 216-element with infinitesimal deformation assumption is given in **Fig.6.14**. We can find liquefied level of saturated soil is almost same with the result obtained by finite deformation theory given in **Fig. 6.6**.

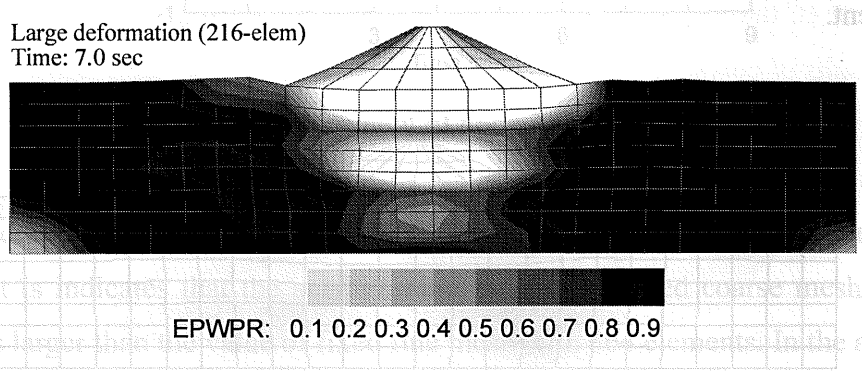

Fig.6.14 Excess pore water pressure ratio for fixed coarse mesh (Small deformation)

The refined meshes with relative error contours at time t=7.0, 8.0 and 9.0 second are given in **Fig. 6.15**. The refined regions are similar to the results of finite deformation theory given in **Fig. 6.7**. The elements numbers of refined mesh in **Fig. 6.15** are less than that in **Fig. 6.7**. Considering the vertical displacement of finite deformation theory are larger than that of infinitesimal assumption and the relative error is larger too, it is reasonable that more elements are needed in the analysis based on infinitesimal deformation assumption than that in the analysis based on finite deformation theory.

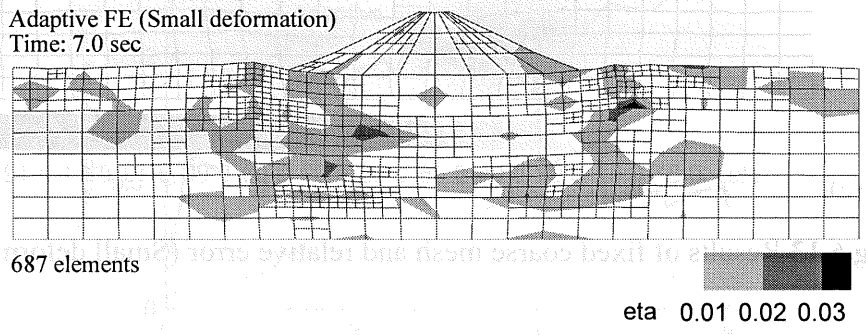

(a)

Fig.6.15.(a) Refined mesh and relative error with adaptive FE(Large deformation)

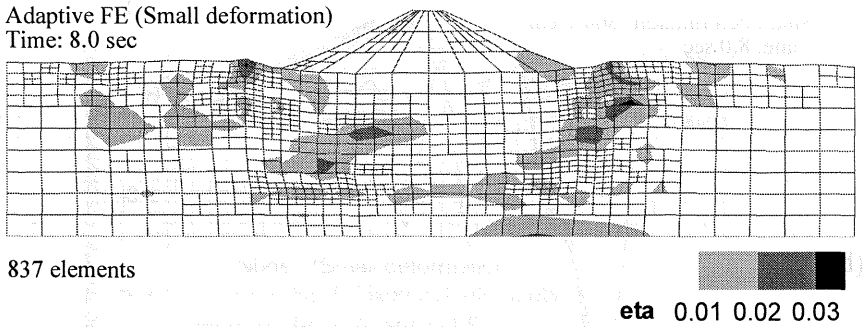

(b)

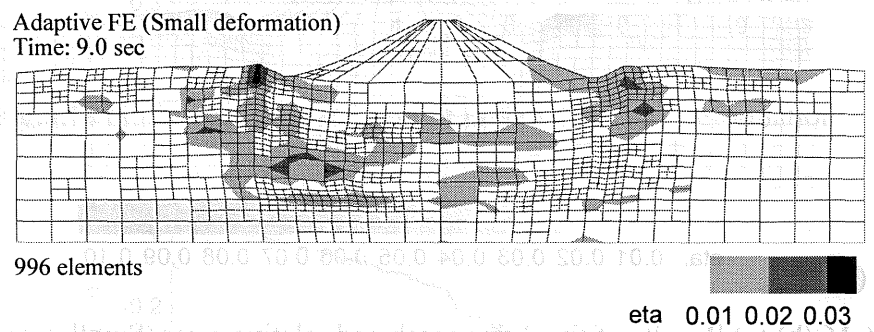

(c)

Fig.6.15.(b,c) Refined mesh and relative error with adaptive FE(Large deformation)

The FE analysed results of the same example with the fine mesh in the condition of infinitesimal deformation assumption are compared with adaptive FE results. The meshes with relative error distribution at time t=7.0, 8.0 and 9.0 second are given as in **Fig. 6.16**.(a), (b) and (c) respectively. Comparing **Fig. 6.15** with **Fig. 6.16**, we can find adaptive technique is also effective in two-dimensional analysis with infinitesimal deformation assumption. The excess pore water pressure of this mesh at time t=7 second is given in **Fig. 6.17**.

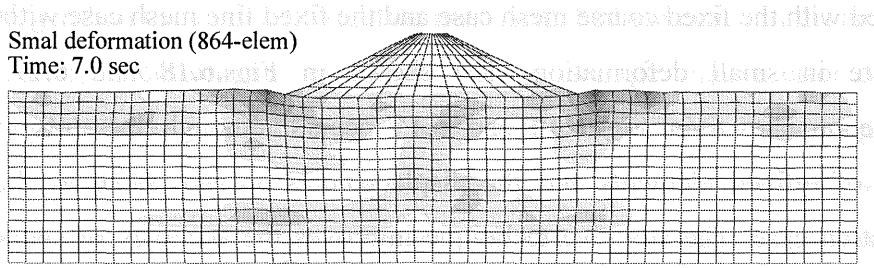

(a)

Fig.6.16.(b),(c) Results of fixed fine mesh and relative error (Small deformation)

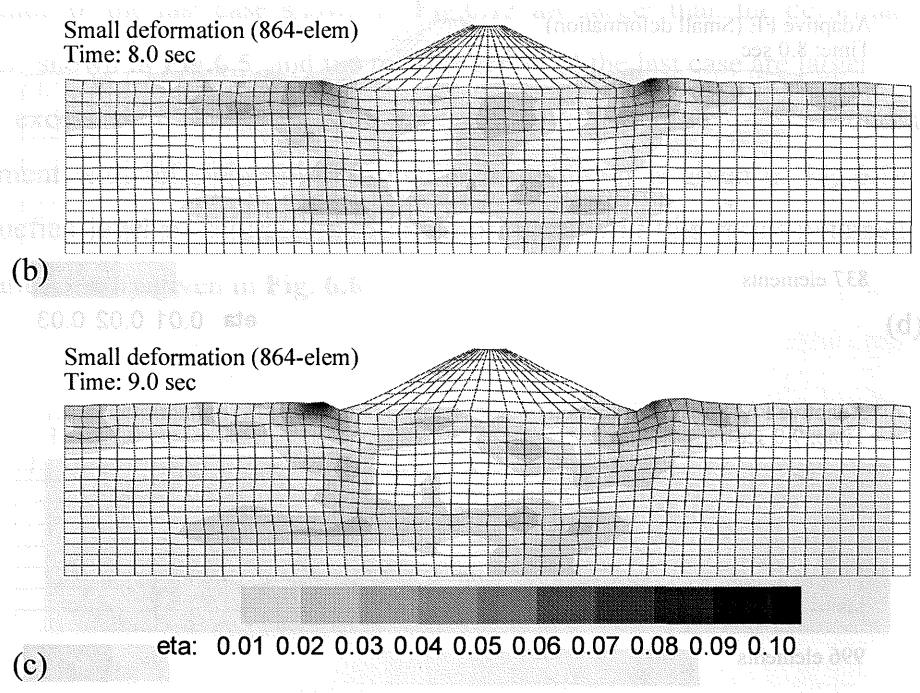

Fig.6.16.(b),(c) Results of fixed fine mesh and relative error (Small deformation)

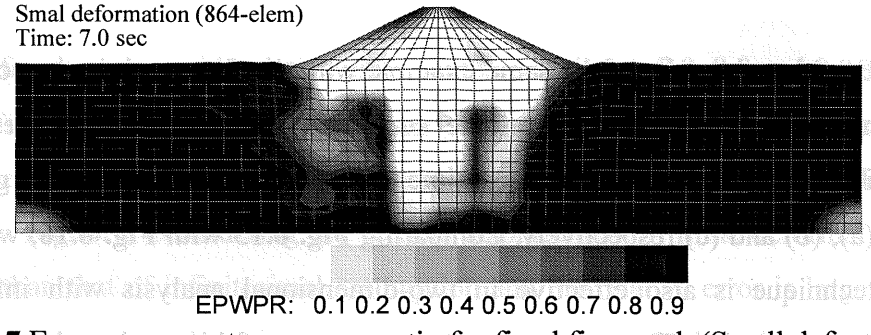

Fig.6.17 Excess pore water pressure ratio for fixed fine mesh (Small deformation)

The horizontal and vertical displacements of node 1 in the adaptive FEM case are compared with the fixed coarse mesh case and the fixed fine mesh case without adaptive procedure in small deformation case shown in **Figs.6.18** and **6.19**. The same phenomenon shown in **Figs.6.10** and **6.11** occurs although the deformed meshes, number of refined elements and the displacements are not same as those in large deformation case. The adaptive technique improves the accuracy of coarse mesh and makes the displacement curves close to the curves of fixed fine mesh in two-dimensional analysis with infinitesimal assumption.

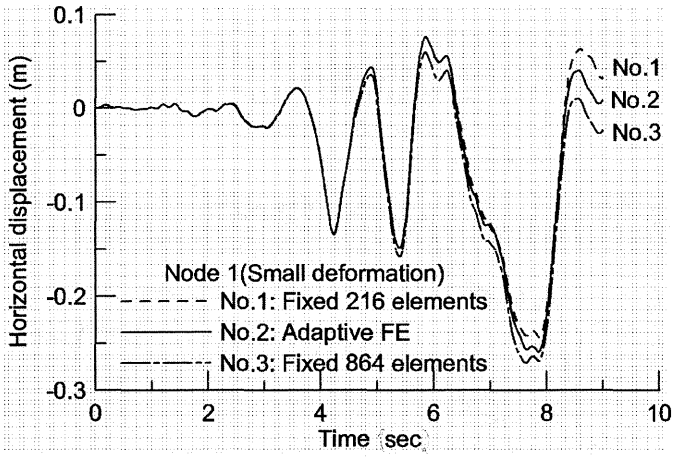

Fig.6.18 Horizontal displacement of node 1 for small deformation

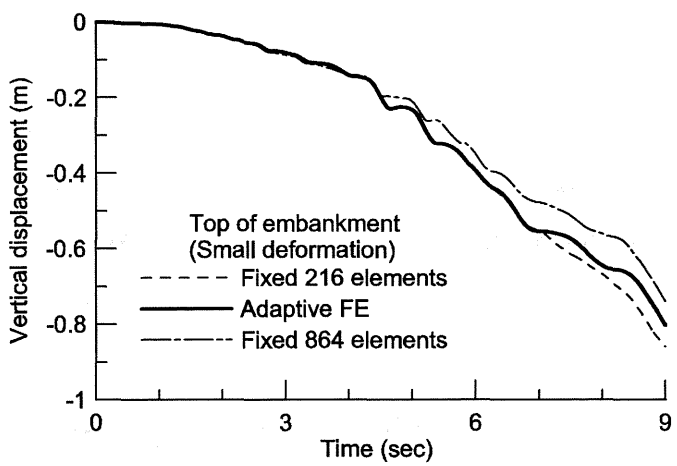

Fig.6.19 Vertical displacement of node 1 for small deformation

The average relative errors of whole mesh in small deformation case are also given as **Fig.6.20**. It is indicates that the average relative error of fixed coarse mesh with 216 elements is larger than the value of fixed fine mesh with 864 elements. In the analysis of adaptive FE in small deformation case, the value of average relative error decreases after adaptive procedure starts at time t=5.9 second. With the adaptive process going on, the value of average relative error closes to the value of fixed fine mesh with 864 elements and exceeds it to reach a new lower level. The aim of adaptive procedure is to improve the accuracy of finite element analysis via reducing the size of elements. As an effective evaluate index of mesh quality, reducing of average relative value demonstrates the efficiency of the adaptive procedure.

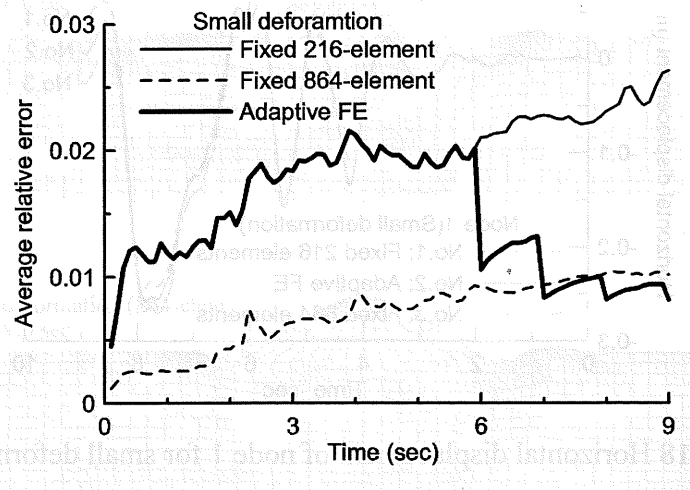

Fig.6.20 Average relative error (Small deformation)

By this example, *h*-adaptive FE method is demonstrated to be effective in application to two-dimensional elasto-plastic analysis of saturated soil including an overall liquefaction process. No matter with finite deformation theory or with infinitesimal deformation assumption are used, this method works well.

6.3 2-D Adaptive Analysis of Pile-Soil Interaction System

In this section, a two-dimensional numerical example, seismic response analysis of a soil-pile interaction system using adaptive FE method is introduced. The efficiency of h-adaptive FE method applied to two-dimensional soil pile interaction analysis is checked.

6.3.1 Introduction of 2-D soil-pile interaction example

As shown in **Fig. 6.21**, a concrete pile shown as the shadow elements, which is driven in 18m-deep saturated Ensyunada sand (Dr=40%). The Yang's modulus of the pile is E=2.45e7 kN/m^2. The parameters of this saturated soil are given in **Table 6.2**.

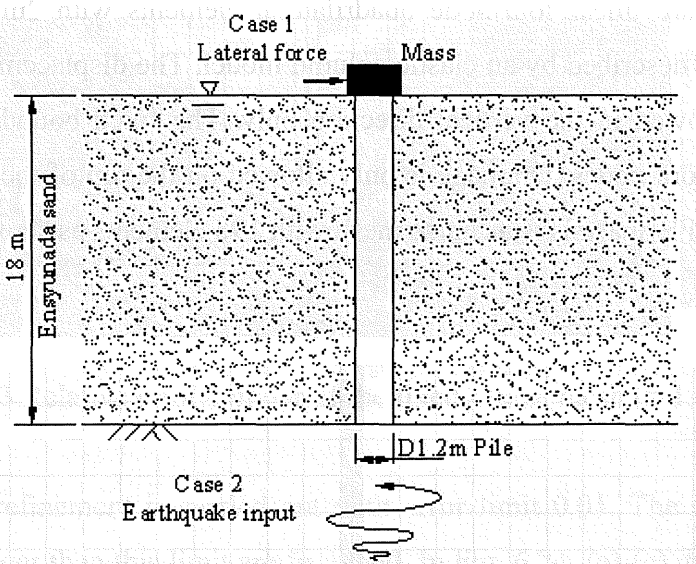

Fig. 6.21 Two-dimensional soil-pile interaction system

Table 6.2 Material parameters of saturated soil

	Soil parameter
Density, ρ (t/m^3)	1.83
Coefficient of permeability, k (m/s)	6.9×10^{-6}
Initial void ratio, $\mathbf{e_0}$	0.992
Compression index, λ	0.025
Swelling index, κ	0.0025
Initial shear modulus ratio, $\mathbf{G_0/\sigma'_{m0}}$	1000
Failure stress ratio, $\mathbf{M_f}$	0.71
Phase transformation stress ratio, $\mathbf{M_m}$	0.96
Hardening parameter, $\mathbf{B_0}$	5500
Hardening parameter, $\mathbf{B_1}$	30
Control parameter of anisotropy, $\mathbf{C_d}$	2000
Dilatancy parameter, $\mathbf{D_0}$	1.0
Dilatancy parameter, η	3.0

A 400kN mass is added on top of pile as the load from super structure. The selected area of the soil is 42m long, and the diameter of the pile is 1.2m. The pile is resting in the center. The constitutive model of soil is an effective cyclic elasto-plastic model. The

elements of soil are linear four-node quadrilateral elements with 2m length and 2m width. The pile is described by an elastic column model. The displacement of two sides boundaries is allowed in the vertical direction only. The fixed boundary condition is given for the bottom nodes. Drainage is only allowed on the top of the soil. The initial mesh of adaptive FE analysis is a coarse mesh with 198 elements as shown in **Fig.6.22**.

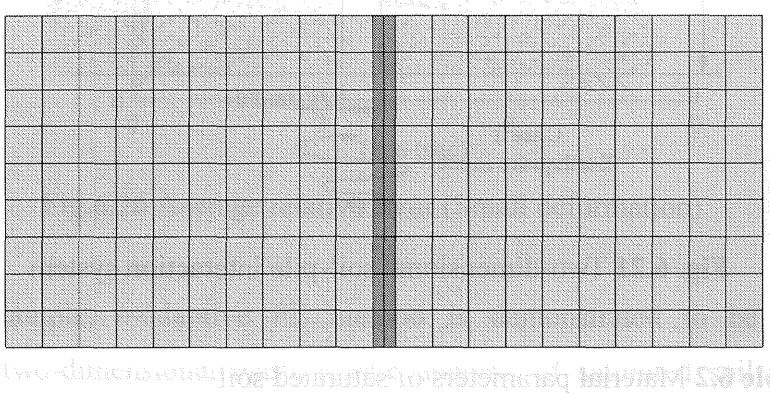

Fig. 6.22 Initial mesh of soil-pile interaction system

Two load cases are used in the adaptive FE analysis as shown in **Fig. 6.21**. The first one is a horizontal force acting on the top of pile. The value of the force increases gradually to 100 kN during 2 seconds. It is used to demonstrate the error estimates and adaptive FE method. Another load is an acceleration time history recorded during Hyogoken-Nanbu earthquake. It is used to check the efficiency of adaptive FE method applied to seismic response analysis of soil-pile interaction.

In adaptive analysis of soil-pile interaction, only soil elements are refined because that large deformation of soil elements makes relative error larger. The refinement of these elements improves the accuracy of soil-pile interaction analysis effectively.

6.3.2 Result of analysis with horizontal force for 2-D soil-pile interaction

The refinement starts from time t=1.0 second. The relative error contour at this time is given in **Fig. 6.23**. The relative error near the head of the pile is large because the large deformation of pile causes the large deformation of surrounding soil elements as shown in the figure.

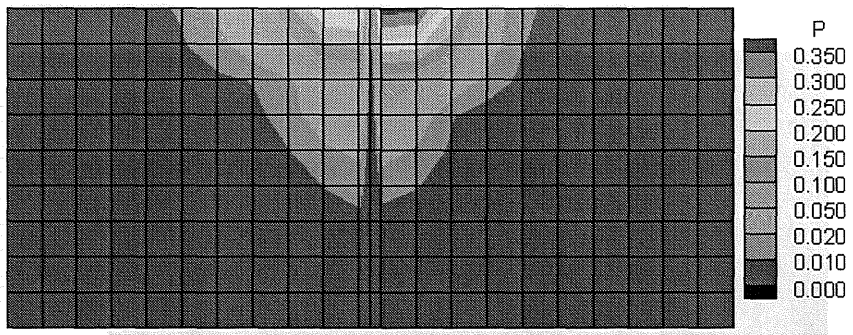

Fig. 6.23 Relative error contour of the fixed coarse mesh (t=1.0 second)

H-adaptive refinement is carried out with error limit 0.01. The elements with the relative error larger than this limit are fissioned. In Fig. 6.24. (a)-(c), the refined meshes at time t=1.0, 1.5 and 2.0 second are given. The mesh is refined one time per 0.1 second. The refinement level is three, that means an initial soil element is allowed to be fissioned three times if necessary. The elements in the region with large relative error value are refined well step by step.

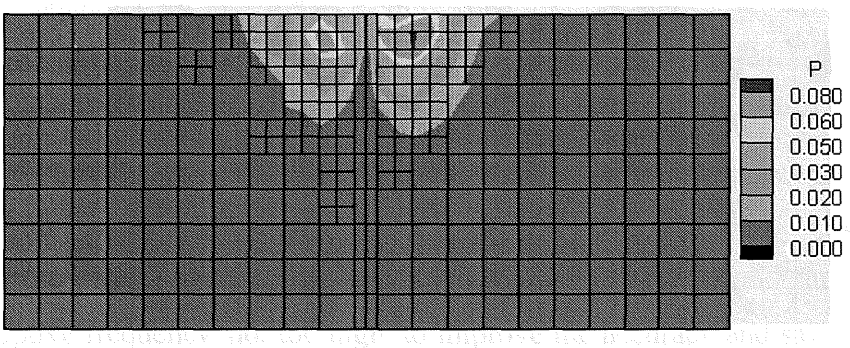

(a). t=1.0 second, dt=0.1 second, 282 elements

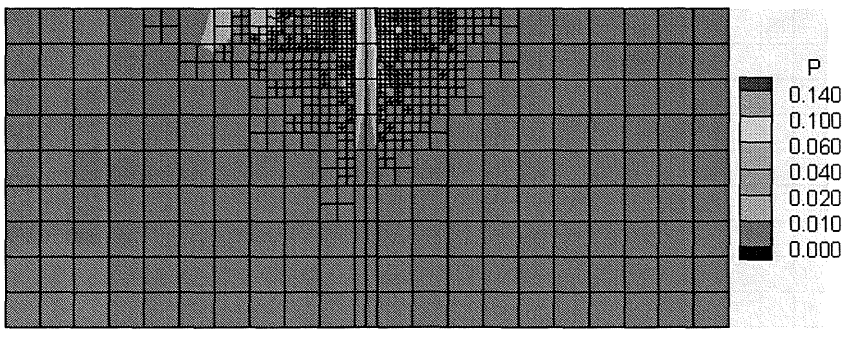

(b). t=1.5 second, dt=0.1 second, 861 elements

Fig. 6.24.(a),(b) Refined mesh and relative error contour with dt=0.1 second

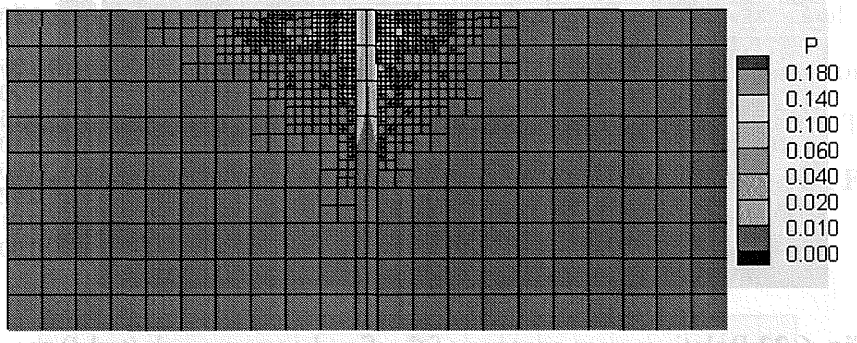

(c). t=2.0 second, dt=0.1 second, 945 elements

Fig. 6.24.(c) Refined mesh and relative error contour with dt=0.1 second

Fig. 6.25 gives another refinement result with a different frequency of refinement, one time per 0.5 second. Comparing the refined meshes with different frequency, it is easy to find that higher refinement frequency cases results in finer quality of mesh.

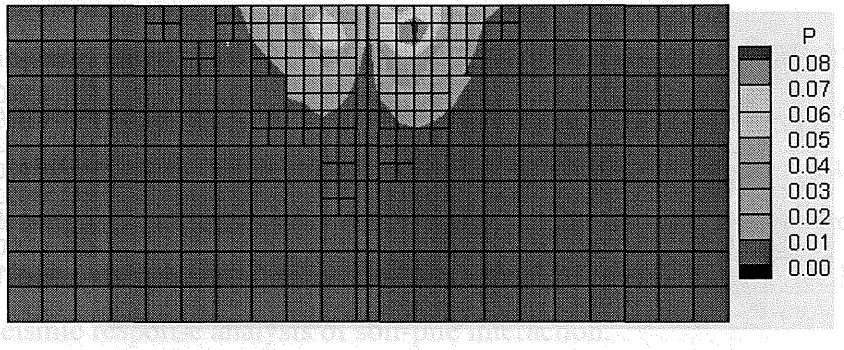

(a). t=1.0 second, dt=0.5 second, 282 elements

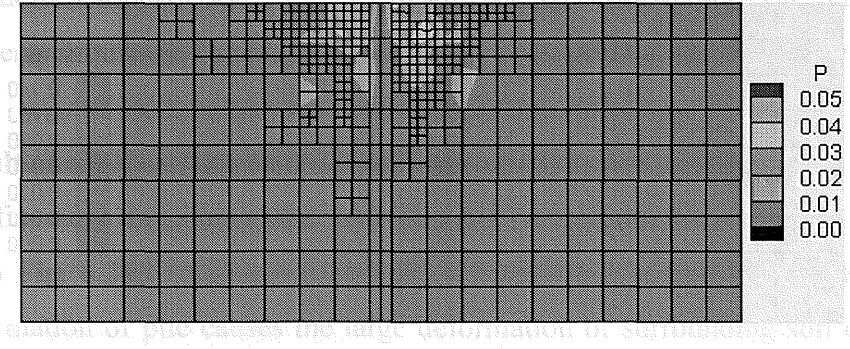

(b). t=1.5 second, dt=0.5 second, 441 elements

Fig. 6.25.(a),(b) Refined mesh and relative error contour with dt=0.5 second

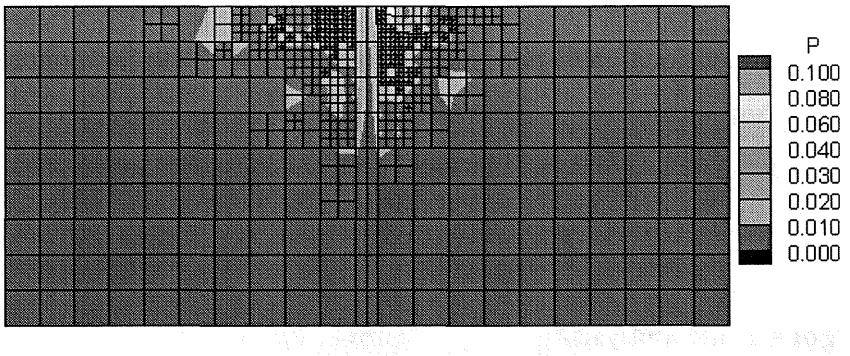

(c). t=2.0 second, dt=0.5 second, 690 elements

Fig. 6.25.(c) Refined mesh and relative error contour with dt=0.5 second

The quality of a mesh is evaluated by the average relative error calculated in the whole mesh. Here we compare the values of average relative error calculated with the fixed coarse mesh and that of adaptive analysis for two different adaptive frequency cases shown in **Fig. 6.26**. The two error values of adaptive analysis are lower than the value of fixed coarse mesh after adaptive process starts at time t=1.0 second. The efficiency of adaptive FE method is demonstrated. Comparing the two error curves calculated with different adaptive frequency, we can find that a stable reduction of mesh error is obtained when we use a high adaptive frequency. The reduction of mesh error with a low frequency is not as stable as that with high frequency. Anyway, adaptive analysises with these two frequencies improve the accuracy of the mesh effectively. Considering the burden of calculation, the author recommends to use an appropriate value of adaptive frequency, not too high, to improve the accuracy and save calculation time.

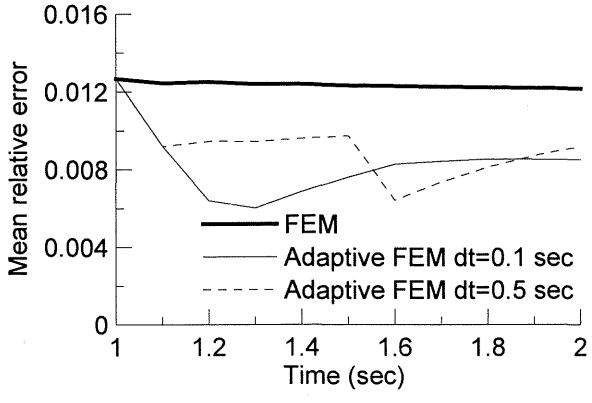

Fig. 6.26 Average relative errors of soil elements

In the two-dimensional soil-pile interaction analysis with a monotonous load, adaptive FE method improves the accuracy of the mesh effectively. The motion of the pile cases the surrounding soil near the head of pile deforming evidently. It is easy to find high relative values in these elements.

6.3.3 Result of seismic analysis

The second case is a seismic analysis of soil-pile interaction. The input acceleration time history is shown in **Fig. 6.27** with a maximum value of 722 cm/sec^2. The excess pore water pressure ratio response of the soil (depth=3m, 11m) is shown in **Fig.6.28**. We can find that liquefaction starts at time t=5.0-6.0 seconds.

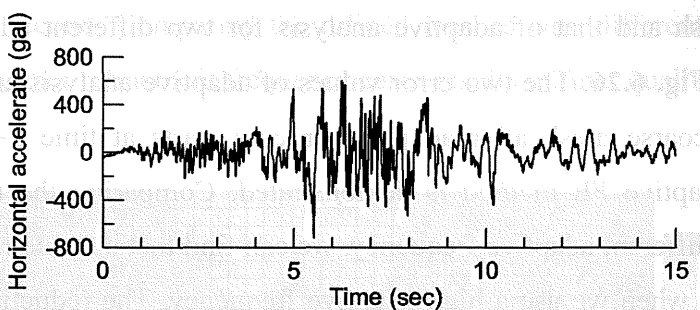

Fig. 6.27 Input acceleration

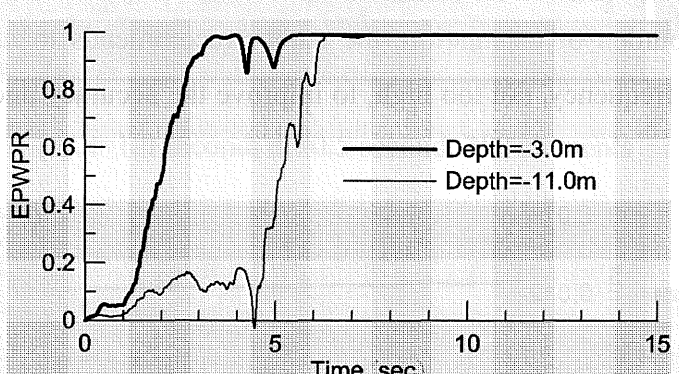

Fig. 6.28 Excess pore water pressure ratio response of soil for 2-D soil-pile interaction

The contour of EPWPR at time t=6.0 second is shown in **Fig. 6.29**. The upper part of soil is almost in liquefied condirion. For comparison, responses without adaptive process are also calculated with the fixed coarse mesh with 198 elements and the fine

mesh with 756 elements.

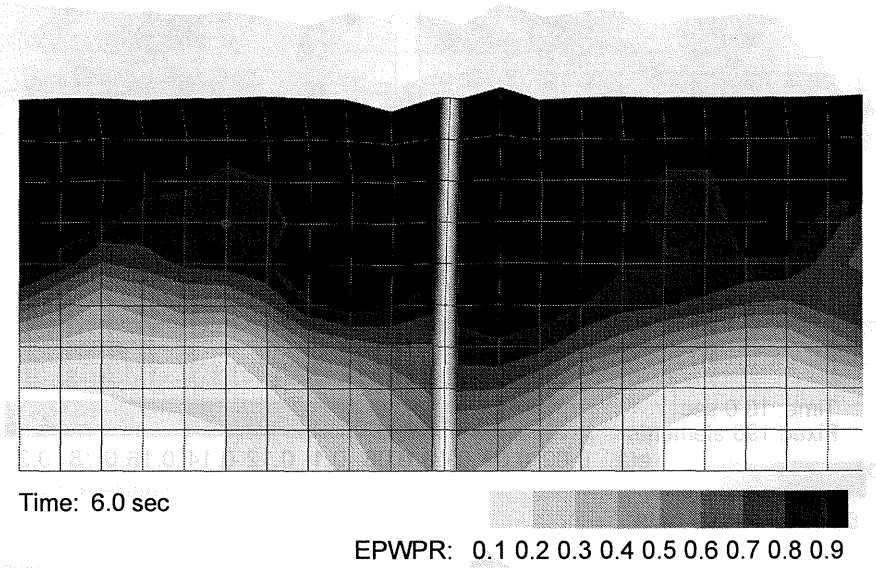

Fig. 6.29 EPWPR of the fixed coarse mesh for 2-D soil-pile interaction

The analysis result of the fixed coarse mesh without adaptive process and their relative error contours are shown in **Fig. 6.30**. As a dynamic process of a soil-pile interaction system, the region with high error value does not only concentrate near the head of the pile, but distributes in the upper part of soil with large deformation. That is the difference between the results of dynamic analysis and analysis with monotonous load. But the region near the head of pile has higher error value than other regions.

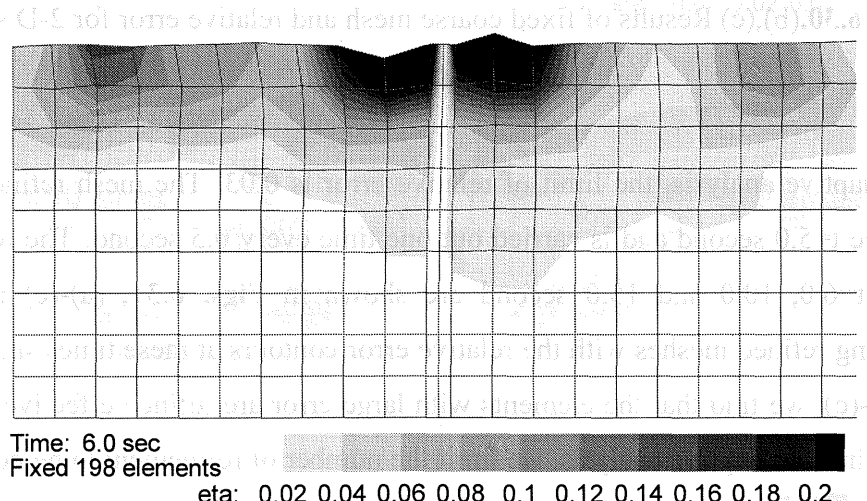

(a)

Fig. 6.30.(a) Results of fixed coarse mesh and relative error for 2-D soil-pile interaction

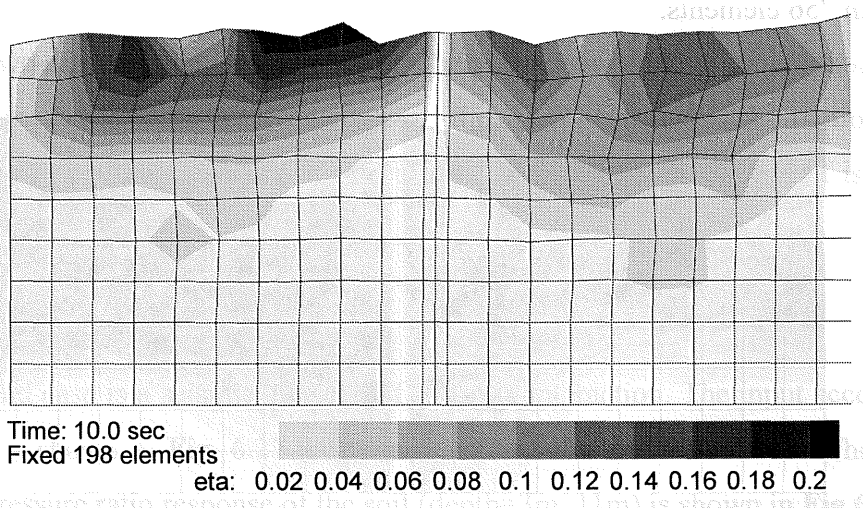

(b)

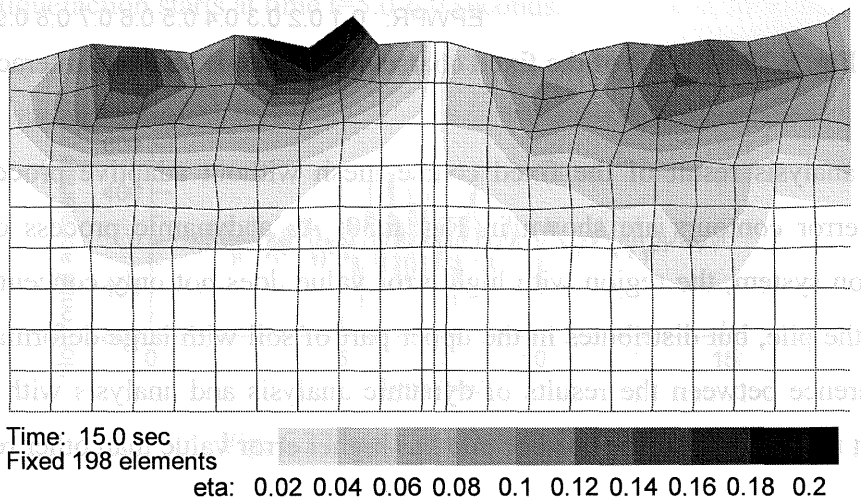

(c)

Fig. 6.30.(b),(c) Results of fixed coarse mesh and relative error for 2-D soil-pile interaction

In adaptive analysis, the limit of relative error is 0.03. The mesh refinement starts from time t=5.0 second and is carried out one time every 0.5 second. The refined mesh at time t=6.0, 10.0 and 15.0 second are shown in **Figs. 6.31.** (a)-(c) respectively. Comparing refined meshes with the relative error contours at these times shown in **Figs. 6.30.** (a)-(c), we find that the elements with large error are refined effectively using our method. In this adaptive analysis, we limit the number of refinement to be not more than 2 times in order to reduce the number of elements. That means the elements those are refined twice will not be refined even if the error in them exceeds the limit of relative error.

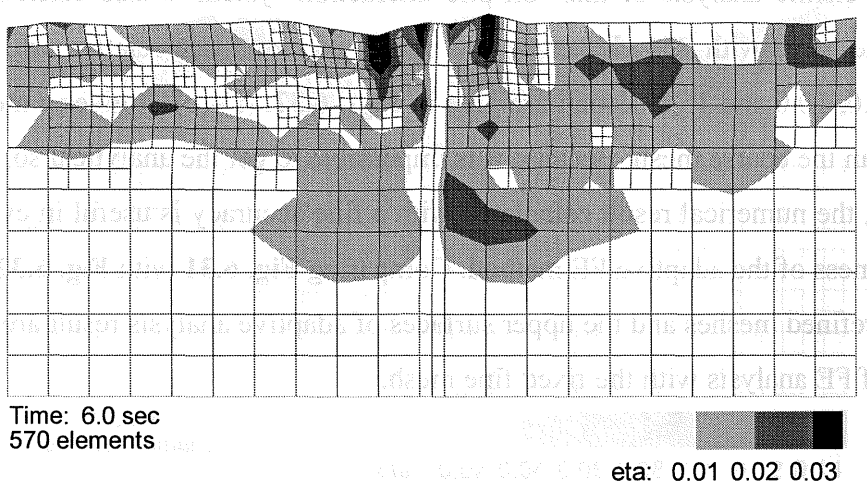

(a)

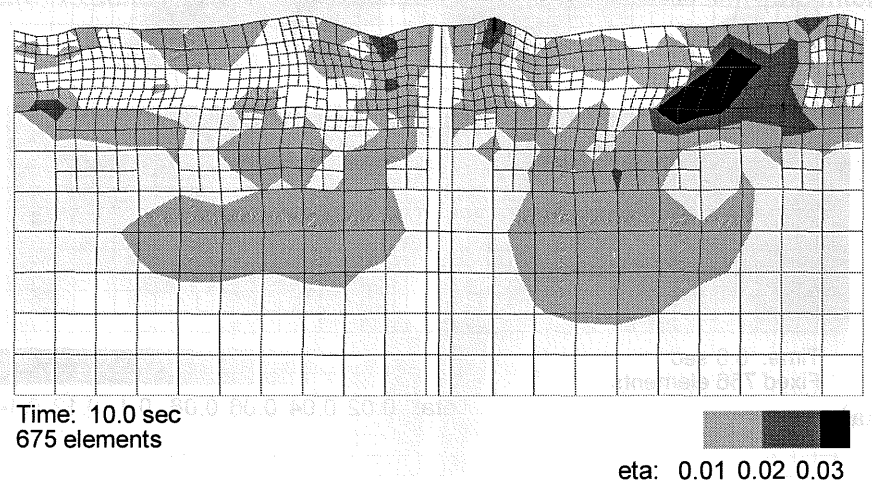

(b)

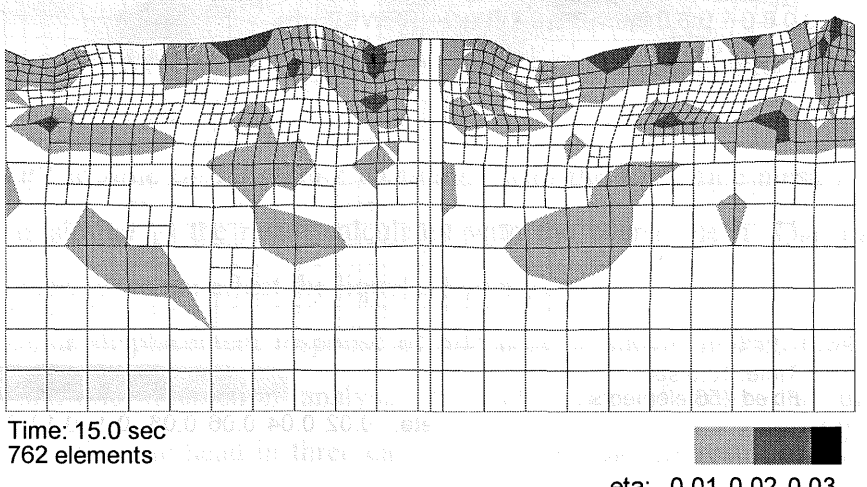

(c)

Fig. 6.31 Refined meshes and relative error contours of 2-D soil-pile interaction

The seismic analysis of this soil-pile interaction system is also carried out with a fixed fine mesh with 756 elements. The results including the relative error contour at time t=6.0, 10.0 and 15.0 second are give in **Figs. 6.32.** (a)-(c). It gives a more accurate result than the coarse mesh. Because it is impossible to get the analytical solution of this problem, the numerical result calculated with a fine accuracy is useful in evaluating the effectiveness of the adaptive FE method. Comparing **Fig. 6.31** with **Fig. 6.32**, it is found that the refined meshes and the upper surfaces of adaptive analysis result are close to the results of FE analysis with the fixed fine mesh.

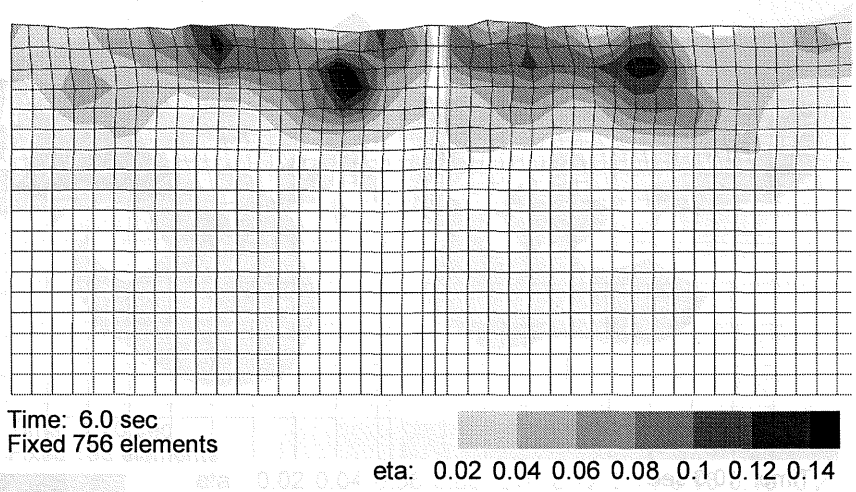

(a)

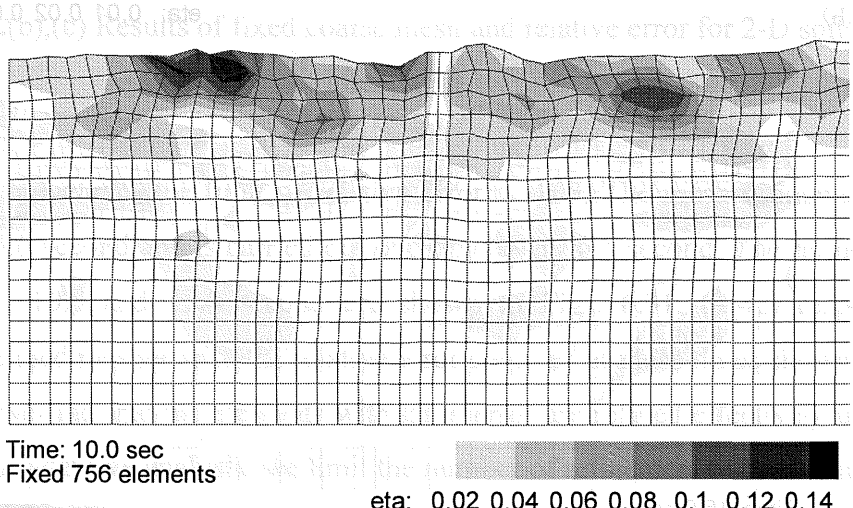

(b)

Fig. 6.32.(a),(b) Results of fixed fine mesh and relative error for 2-D soil-pile interaction

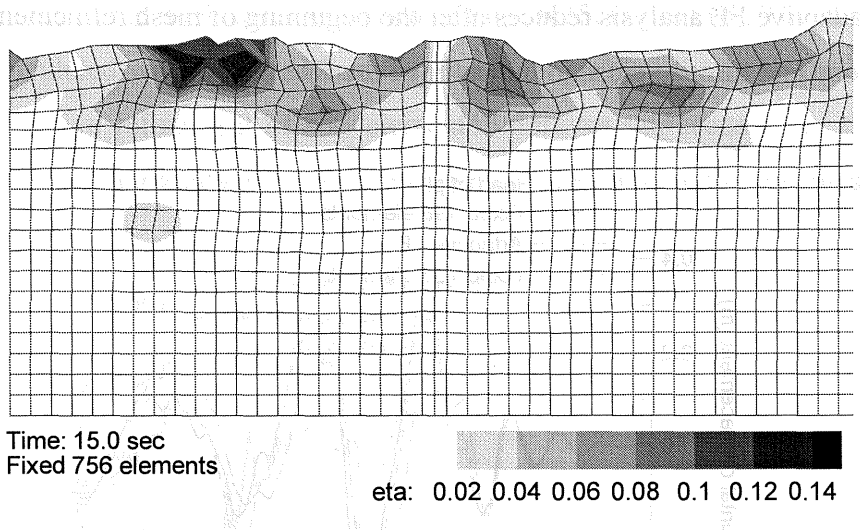

(c)

Fig. 6.32.(c) Results of the fine mesh and relative error for 2-D soil-pile interaction

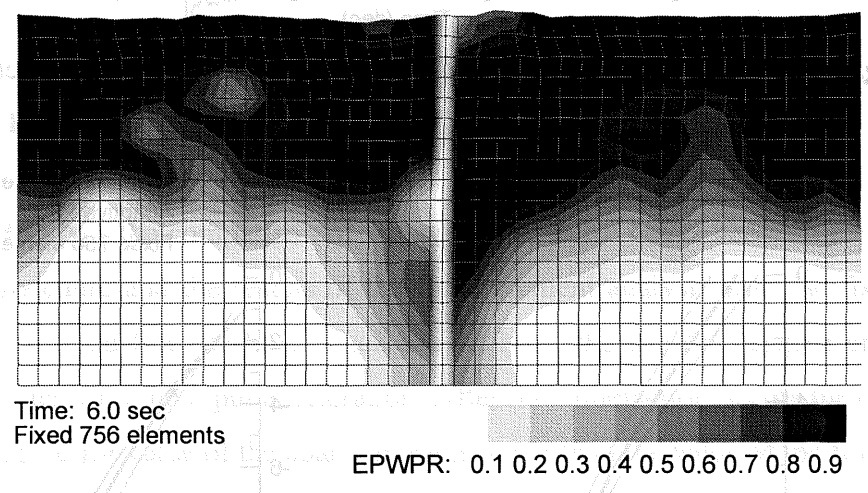

Fig. 6.33 EPWPR of the fixed coarse mesh for 2-D soil-pile interaction

The EPWPR at time t-=6.0 second calculated with the fixed fine mesh is given in **Fig. 6.33**. It is similar to the result calculated with the coarse mesh. That means the quality of the mesh does not affect the liquefaction history.

The horizontal displacement response of pile head is shown in **Fig. 6.34**. In two-dimensional soil-pile interaction analysis, the difference of horizontal directional displacements on the pile head in three cases is evident, and the result of the adaptive calculations gives a different displacement value on the pile head comparing with the result of finite element analysis without adaptive process. In general, the horizontal

displacement of the fixed fine mesh is less than the value of the fixed coarse mesh. The value of adaptive FE analysis reduces after the beginning of mesh refinement at the time t=5.0 second and turns to close to the value of the fine mesh.

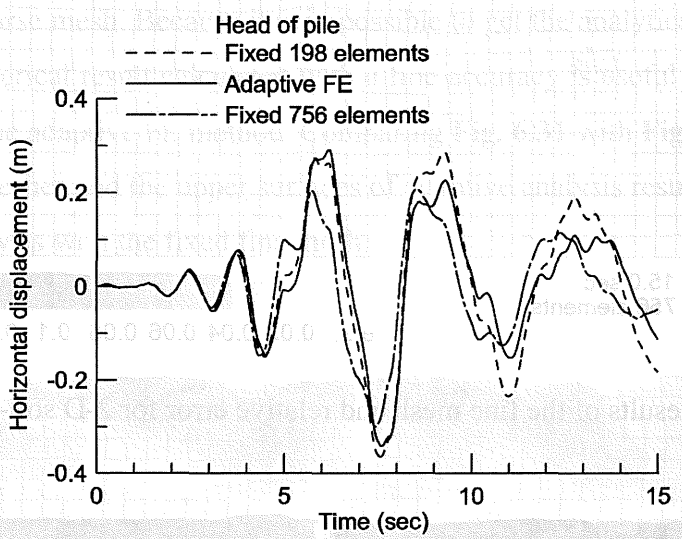

Fig. 6.34 Horizontal displacement of pile head for 2-D soil-pile interaction

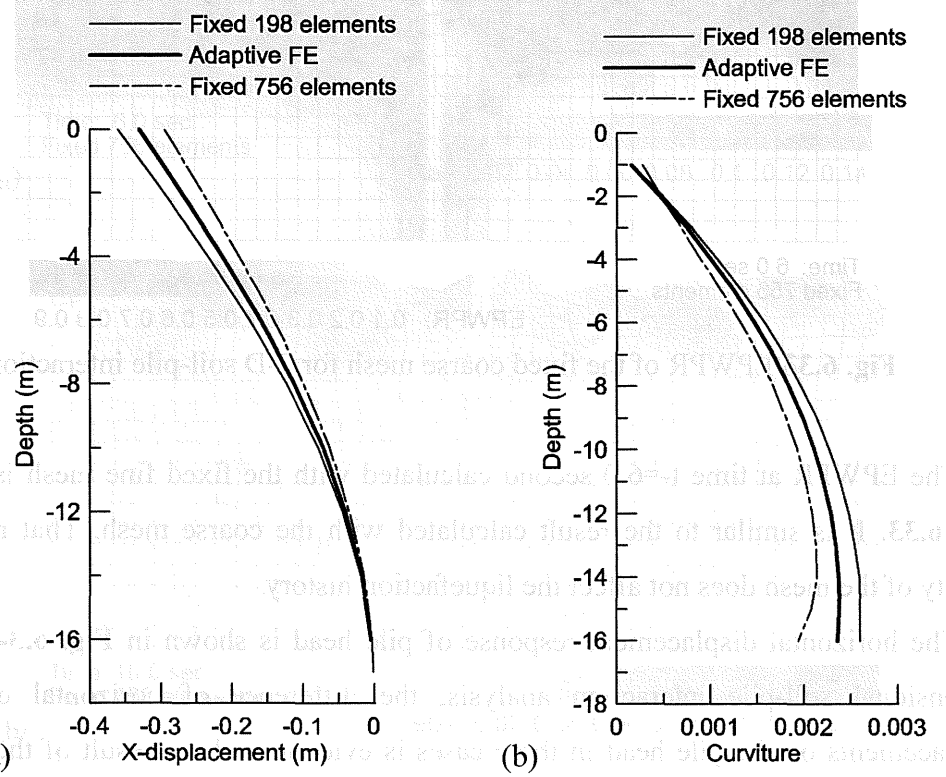

Fig. 6.35 Displacements and curvatures of pile for 2-D soil-pile interaction (t=7.5 sec)

We compare the horizontal displacements and curvatures of the pile at the time t=7.5 second calculated in the three cases as shown in **Figs. 6.35.** (a) and (b). The deformation of the pile calculated with the fixed coarse mesh is larger than that with the fixed fine mesh. The adaptive refinement of soil elements improves the accuracy of the coarse mesh and makes the horizontal displacement approach the value of the fine mesh.

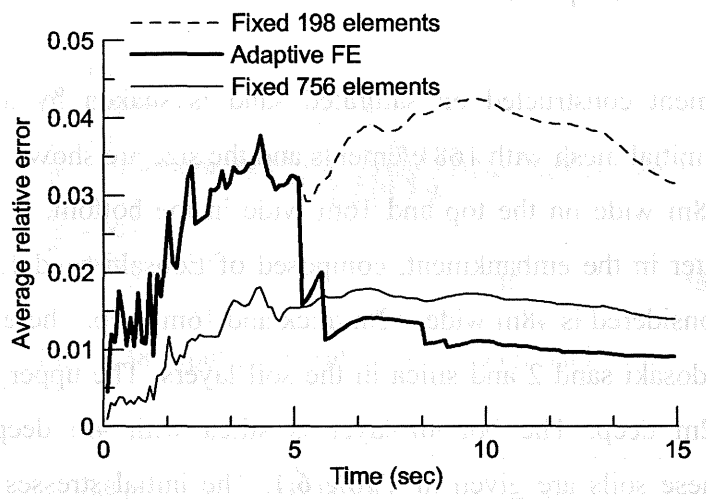

Fig. 6.36 Average relative error of soil for 2-D soil-pile interaction

Fig. 6.36 gives the comparison of the average relative errors between the results of adaptive procedure and the results of the finite element analysis with the fixed coarse mesh and the fixed fine mesh. In a seismic analysis, the average relative error of the mesh fluctuates with the input acceleration. After the liquefaction occurs the error value increases. The error value of the coarse mesh is larger than the value of the fine mesh. In adaptive FE analysis, before the adaptive process starts, the error value is same as the value of the initial coarse mesh. After the adaptive mesh refinement starts, the error value decreases with the mesh refinement going on. It even reaches a new lower value than the value of the fixed fine mesh.

The results of these two examples demonstrate the efficiency of *h*-adaptive FE method applied to two-dimensional soil-pile interaction analysis. With this method, the soil elements with large error are refined well and the accuracy of analysis is improved effectively.

6.4 3-D Adaptive Analysis of Embankment During Earthquake

In this section three-dimensional seismic analysis of embankment with *h*-adaptive FE method is introduced. Updated Lagrangian formulation is adopted in the governing equations of finite element method to deal with the large deformation of liquefied soil. An effective cyclic elasto-plastic model is used to describe the material nonlinearity of saturated soil.

An embankment constructed on saturated sand is shaken by an earthquake in x-direction. The initial mesh with 168 elements and the size are shown in **Fig. 6.37**. The embankment is 8m wide on the top and 16m wide in the bottom. It is a kind of soil without pore water in the embankment, composed of Edosaki sand 1. The foundation soil region we considered is 48m wide, 12m thick and 16m deep. There are two kinds of saturated soil, Edosaki sand 2 and silica in the soil layers. The upper layer is Edosaki sand 2 with 12m deep. The bottom layer is silica with 4m deep. The dynamic parameters of these soils are given in **Table 6.1**. The initial stresses of elements are calculated with gravity.

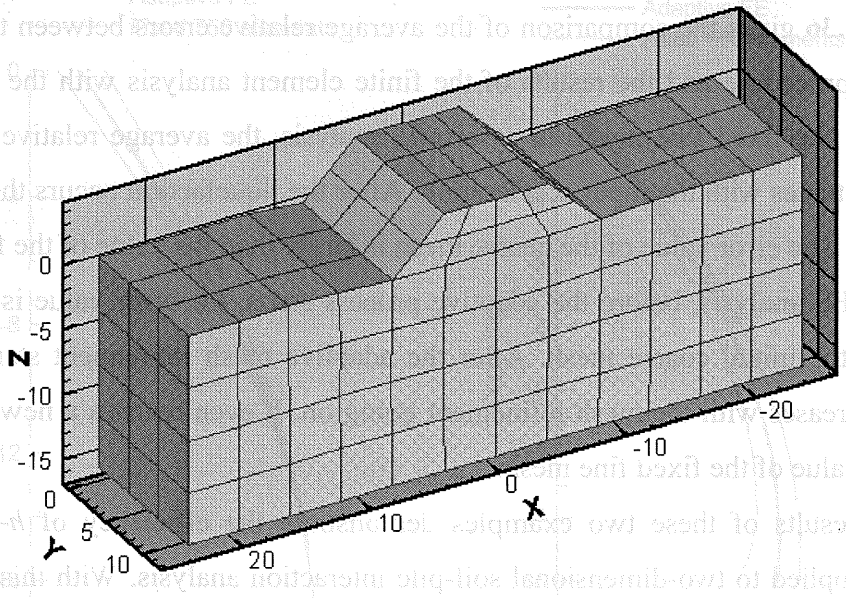

Fig. 6.37 Initial mesh of 3-D embankment model

The linear hexahedra element with eight nodes is used. The elements in liquefiable

soil layers are cubic elements with 4.0 m sides. The displacement of bottom boundary are fixed, side boundary is fixed in horizontal direction and allowed to slide on the surface. Drainage is allowed only on the top boundary surface of the mesh.

Input earthquake acceleration is a modified earthquake acceleration history with 60% of maximum acceleration of original record as shown in **Fig. 6.38**. The maximum value is 433 gal.

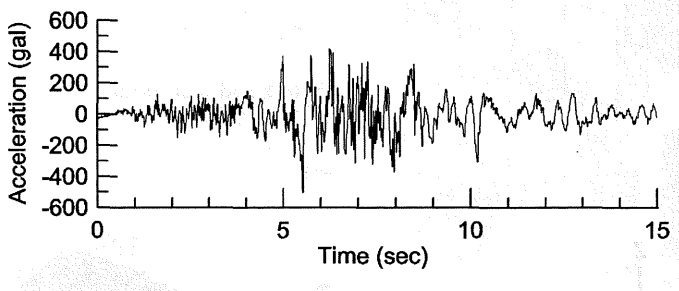

Fig. 6.38 Input acceleration for 3-D embankment

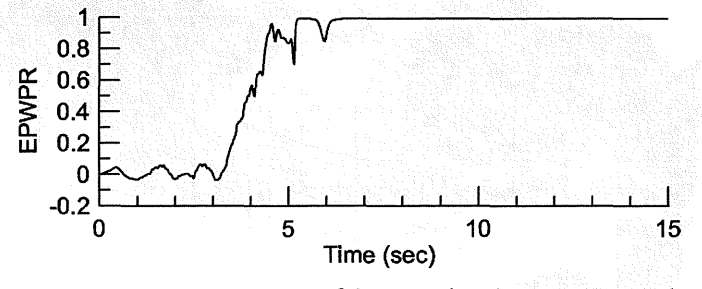

Fig. 6.39 EPWPR response of 3-D embankment example

Fig. 6.39 gives the time history of EPWPR of soil with 6m depth. We can find liquefaction occurs at about 6 second.

First, the deformed meshes and their distributions of relative errors at t=7.0, 11.0 and 15.0 second analyzed with fixed coarse mesh are given in **Fig.6.40.** (a), (b) and (c) respectively. The L_2-norm of strain is used to evaluate the error. The deformation and strain in the regions besides the foot of embankment and under the embankment are larger than other regions. The values of relative error in these regions are increased.

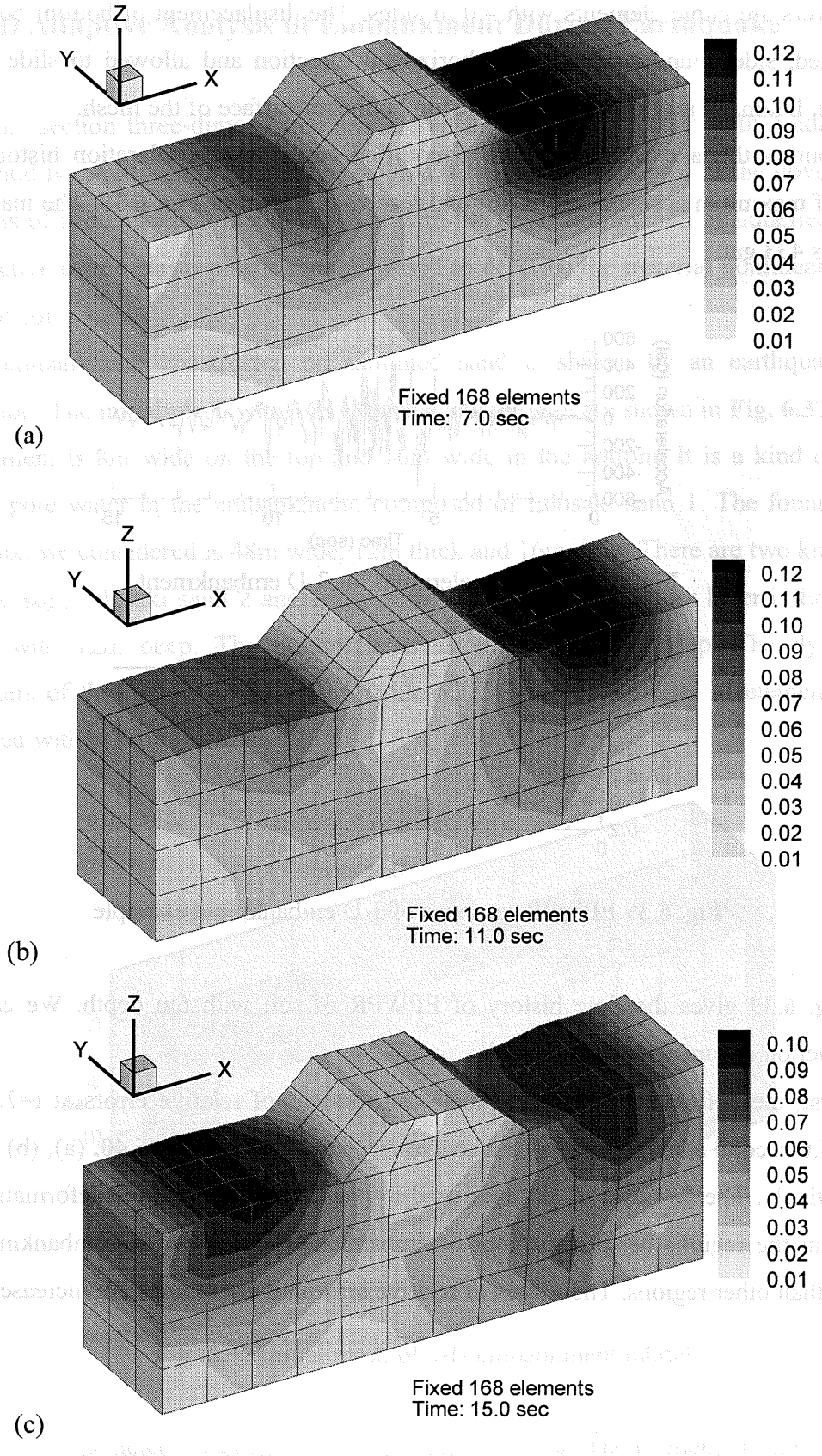

Fig. 6.40 Results of the coarse mesh and relative error for 3-D embankment

The adaptive mesh refinement process starts at the time t=6.5 second from the initial coarse mesh with 168 elements. The limit of relative error is 0.07. The adaptive mesh refinement is carried out one time per second. Only two level of refinement is allowed. The refined meshes analyzed by *h*-adaptive FEM using updated Lagrangian method at time t=7.0, 11.0 and 15.0 second are given in **Fig.6.41.** (a), (b) and (c) respectively.

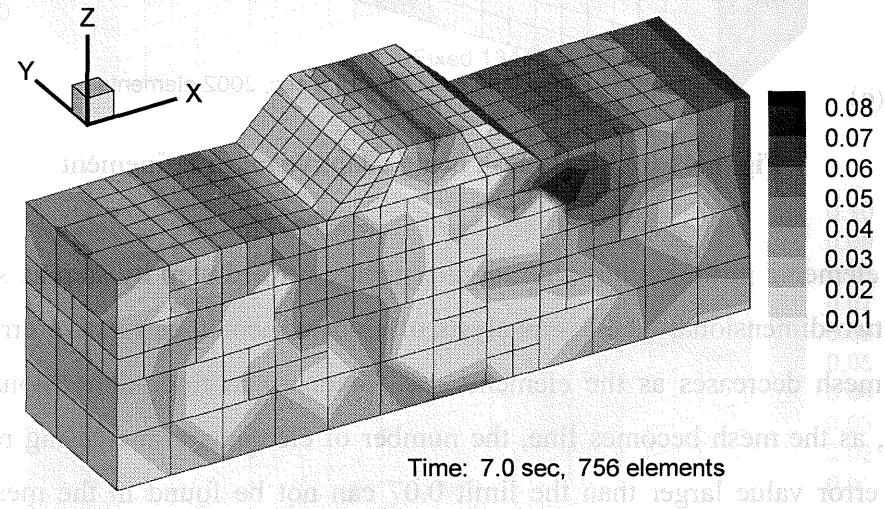

(a)

Fig. 6.41.(a) Final mesh using adaptive mesh refinement

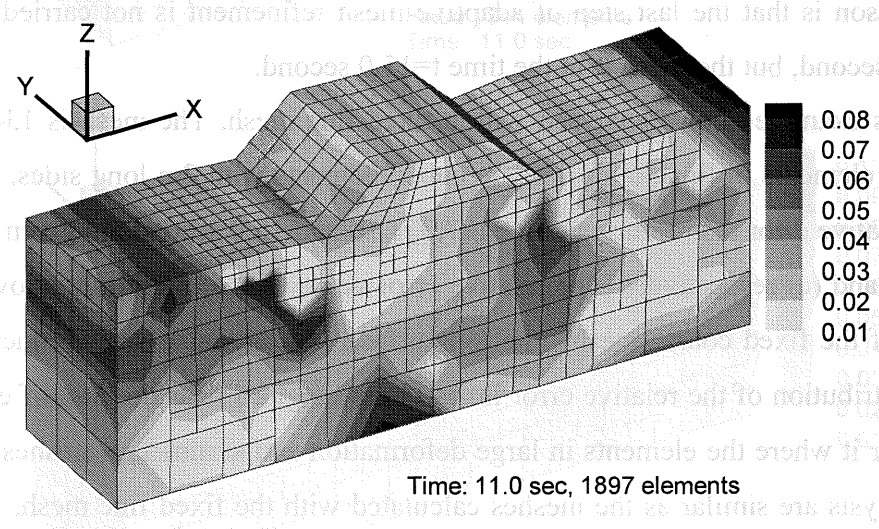

(b)

Fig. 6.41.(a),(b) Final mesh using adaptive mesh refinement

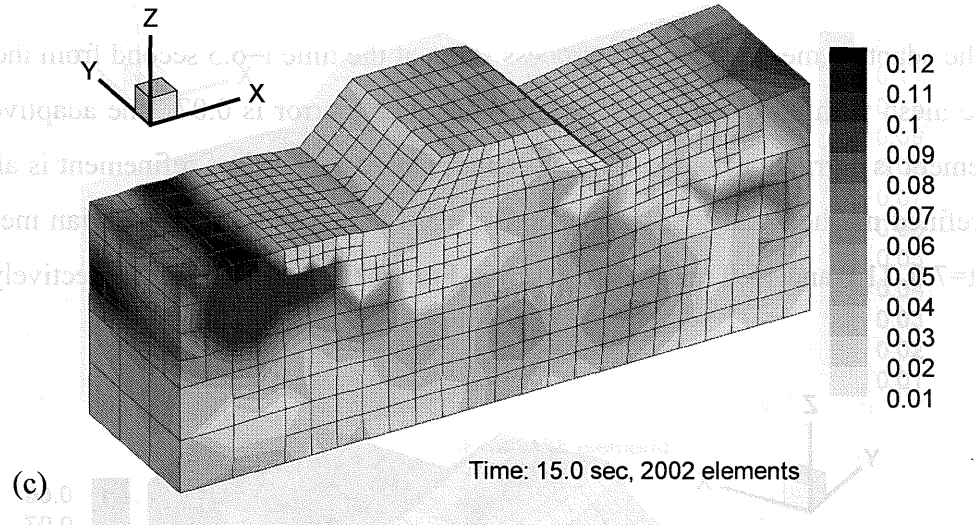

(c)

Fig. 6.41.(c) Final mesh using adaptive mesh refinement

The elements in the region with large error are refined step by step as same as the case of two-dimensional adaptive analysis of embankment. The relative error value of refined mesh decreases as the elements are fissioned. In three-dimensional adaptive analysis, as the mesh becomes fine, the number of elements is increasing rapidly. The relative error value larger than the limit 0.07 can not be found in the mesh with the adaptive level lower than 2 in **Fig. 6.41.** (a) and (b). But we can find in **Fig. 6.41.** (c). The reason is that the last step of adaptive mesh refinement is not carried out at time t=14.5 second, but the mesh is at the time t=15.0 second.

This example is also analysed with a fixed fine mesh. The mesh is 1344 elements and the elements of liquefiable soil are cubic elements with 2m long sides. The meshes with relative error distribution at time t=7.0, 11.0 and 15.0 second are given in **Fig.6.42.** (a), (b) and (c) respectively. The relative error value of the fine mesh is lower than the value of the fixed coarse mesh. The top surface of liquefiable soil is much smoother. The distribution of the relative error is also in the regions near the foot of embankment or under it where the elements in large deformation and strain. The meshes of adaptive FE analysis are similar as the meshes calculated with the fixed fine mesh. It is evident that refinement of these elements improves the accuracy of the embankment displacement result.

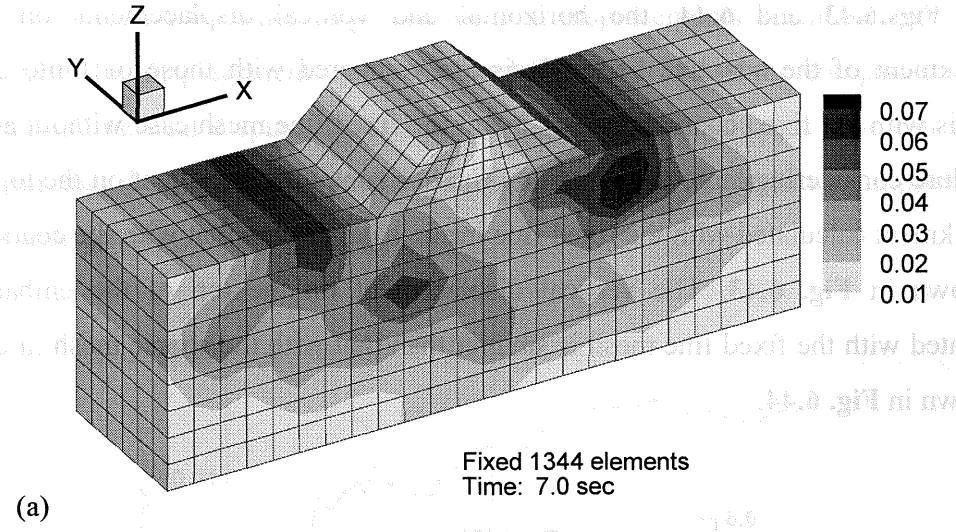

(a)

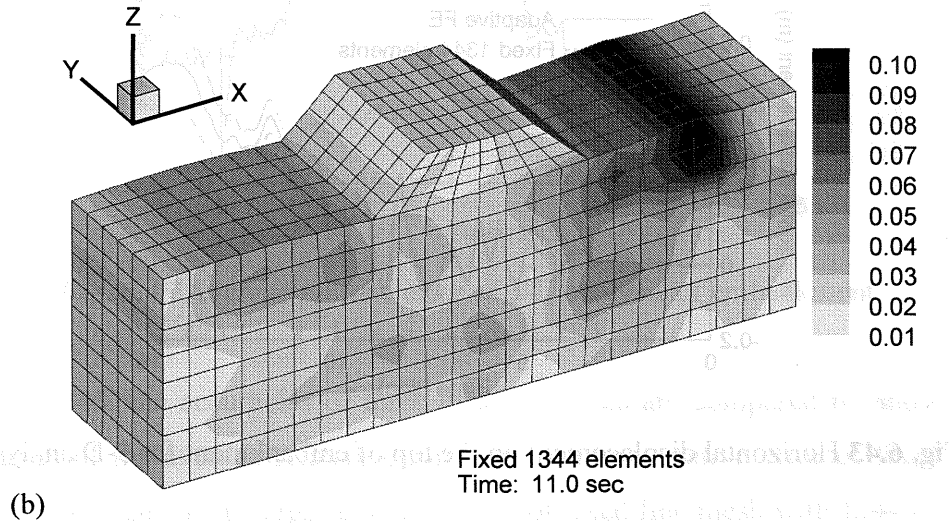

(b)

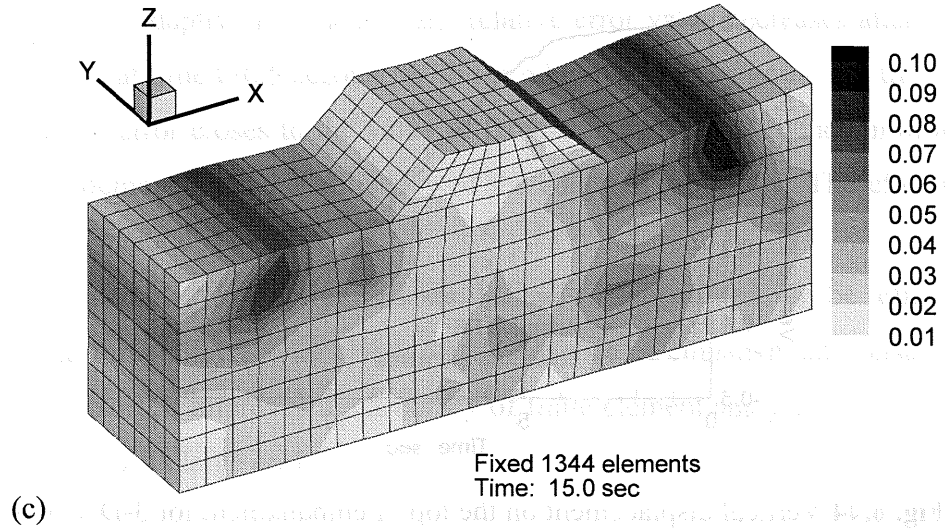

(c)

Fig. 6.42 Results of fixed fine mesh and relative error

In **Figs.6.43** and **6.44**, the horizontal and vertical displacements on top of embankment of the adaptive FE analysis are compared with those of finite element analysis with the fixed coarse mesh case and the fixed fine mesh case without adaptive procedure considering large deformation. The horizontal displacement on the top of the embankment calculated with the fixed fine mesh is larger than that with the coarse mesh as shown in **Fig. 6.43**. The vertical displacement on the top of the embankment calculated with the fixed fine mesh is smaller than that with the coarse mesh in contrast as shown in **Fig. 6.44**.

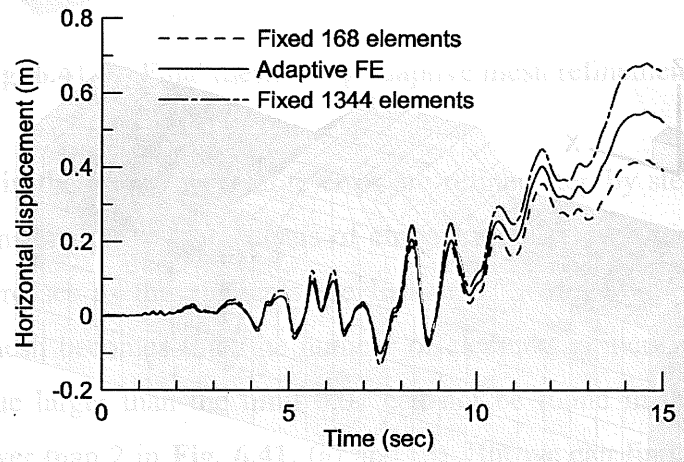

Fig. 6.43 Horizontal displacement on the top of embankment for 3-D analysis

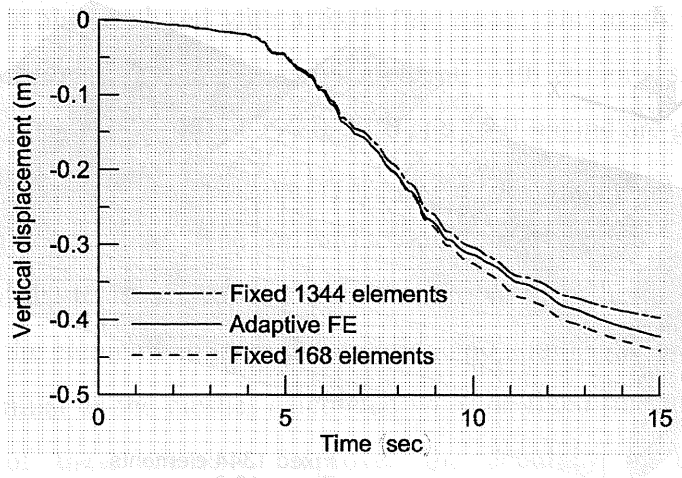

Fig. 6.44 Vertical displacement on the top of embankment for 3-D analysis

With the mesh refinement going on, the horizontal displacement calculated with

adaptive FE method becomes large and vertical displacements becomes small. They more close to the displacement values of fixed fine mesh. From the comparison of the horizontal and vertical displacements lines of the three different cases, we can get the conclusion that *h*-adaptive FE method considering large deformation improves the accuracy efficiently.

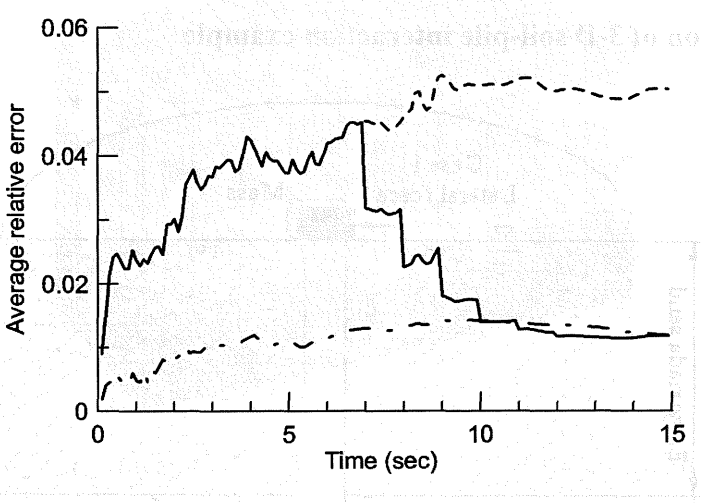

Fig. 6.45 Average relative error of 3-D analysis of embankment

In **Fig. 6.45**, the accuracies of three different cases are compared by showing the three curves of the average relative errors. The average relative error of fixed coarse mesh with 168 elements is larger than the value of fixed fine mesh with 1344 elements. In the analysis of adaptive FE, the average relative error value decreases after adaptive procedure starts at time t=6.5 second. With the adaptive process going on, the value of average relative error closes to the value of fixed fine mesh. The reduction of average relative error demonstrates the efficiency of the adaptive procedure. The effectiveness of adaptive FE method is evident.

By this example, *h*-adaptive FE method is demonstrated to be effective in application to three-dimensional elasto-plastic analysis of embankment constructed on the liquefiable soil. It improves the accuracy of finite element analysis via reducing the size of elements with large error.

6.5 3-D Adaptive Analysis of Pile-Soil Interaction System

The last numerical example is a three-dimensional seismic response analysis of a soil-pile interaction system with adaptive FE method. The efficiency of *h*-adaptive FE method applied to three-dimensional soil-pile interaction analysis is demonstrated.

6.5.1 Introduction of 3-D soil-pile interaction example

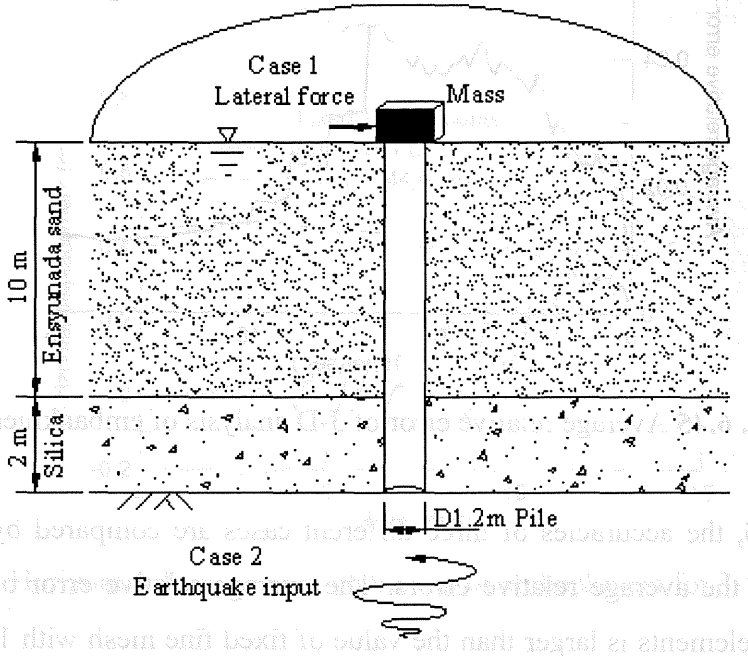

Fig. 6.46 3-D soil-pile interaction example

We use the same soil-pile interaction model as the one introduced in section 4.3. The general condition of the model is introduced in that section. Two load cases are analyzed with the adaptive FE method. As shown in **Fig. 6.46**, the first one is a horizontal force acting on the top of pile. The value of the force increases gradually to 100 kN during 2 seconds. It is used to demonstrate the error estimates and adaptive FE method. Another load is an acceleration time history as same as that introduced in section 4.3. It is used to check the efficiency of adaptive FE method applied to three-dimensional seismic analysis of soil-pile interaction.

As same as the adaptive analysis of two-dimensional soil-pile interaction, only soil elements are refined because that large deformation of soil elements makes relative

error larger. The refinement of these elements is effective to improve the accuracy of soil-pile interaction analysis. The initial mesh of adaptive FE analysis is a coarse mesh with 198 elements as shown in **Fig.6.47**.

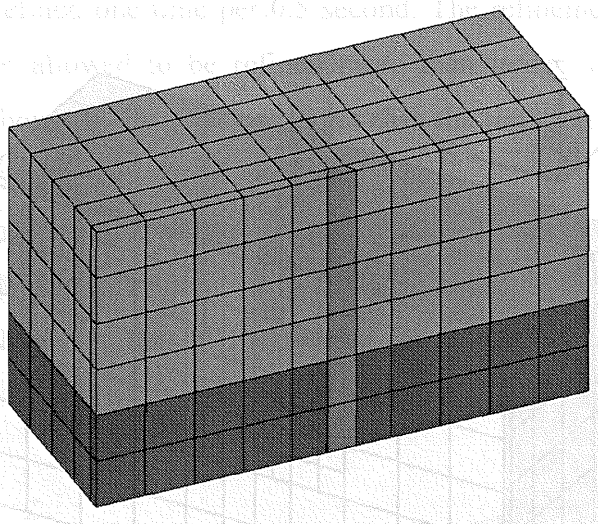

Fig. 6.47 Initial coarse mesh of 3-D soil-pile interaction system with 198 elements

6.5.2 Result of analysis with horizontal force for 3-D soil-pile interaction

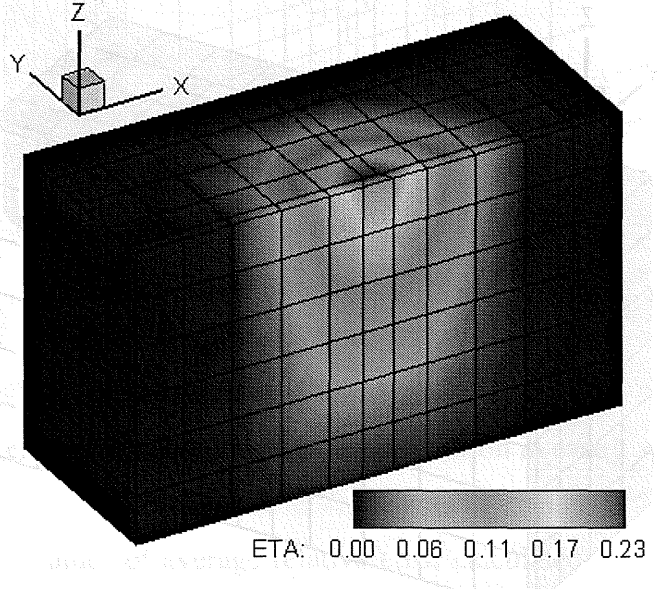

Fig. 6.48 Relative error contour of the coarse mesh with 330 elements (t=1.0 sec)

The relative error contour at the time t=1.0 second is given in **Fig. 6.48**. The

refinement starts from time t=1.0 second according to this distribution of the error. The relative error of the elements surrounding the head of the pile is large because the large displacement of pile causes the large deformation of surrounding soil elements as shown in the figure.

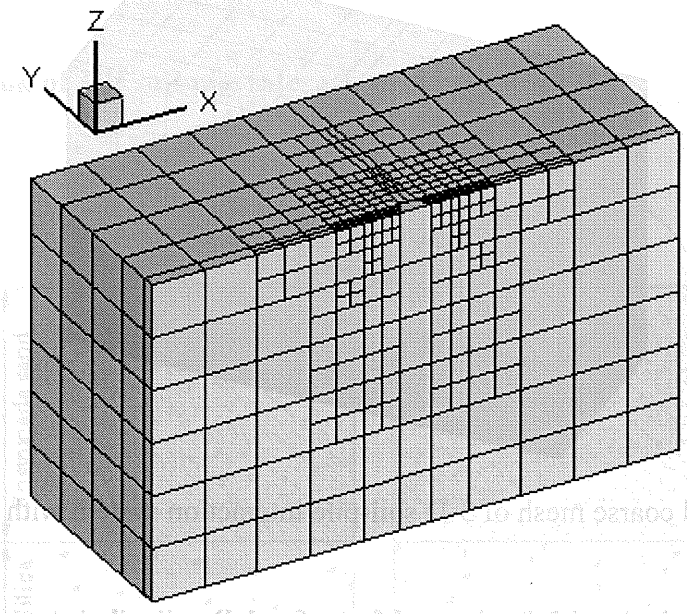

(a) t=1.5 sec, 1331 elements

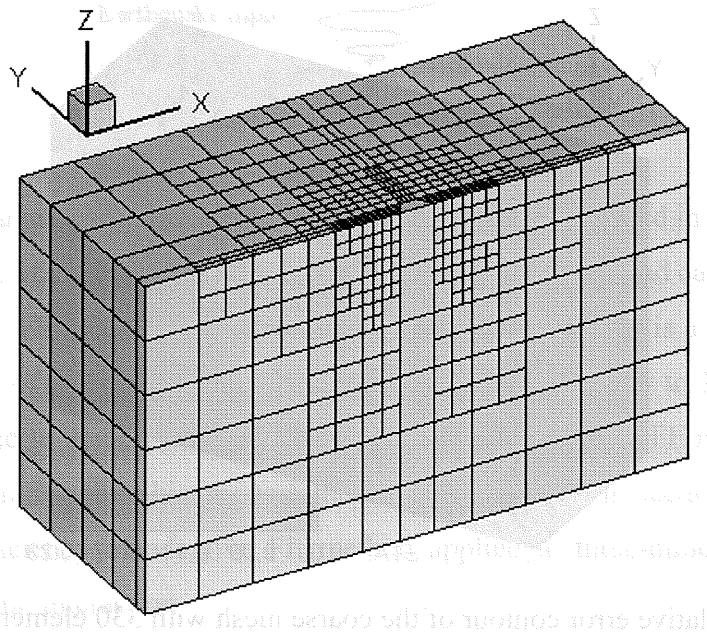

(b) t=2.0 sec, 1940 elements

Fig. 6.49.(a),(b) Refined meshes of 3-D soil-pile interaction in case 1 with dt=0.5 sec

The error limit of *h*-adaptive refinement is 0.05. The elements with the relative error larger than the limit are fissioned. Two adaptive frequencies are used in this adaptive analysis. In **Figs. 6.49.** (a) and (b), the refined meshes at time t=1.5 and 2.0 second are given. The mesh is refined one time per 0.5 second. The refinement level is two. Any initial element is not allowed to be refined more than twice. The elements, whose relative error value shown in **Fig. 6.48** are larger than the limit, are refined well step by step.

The refined meshes with another frequency of refinement, one time per 0.2 second are given in **Fig. 6.50**. The element numbers of refined mesh in **Fig. 6.50** are more than those in **Fig. 6.49**. It shows that higher refinement frequency cases finer quality of mesh.

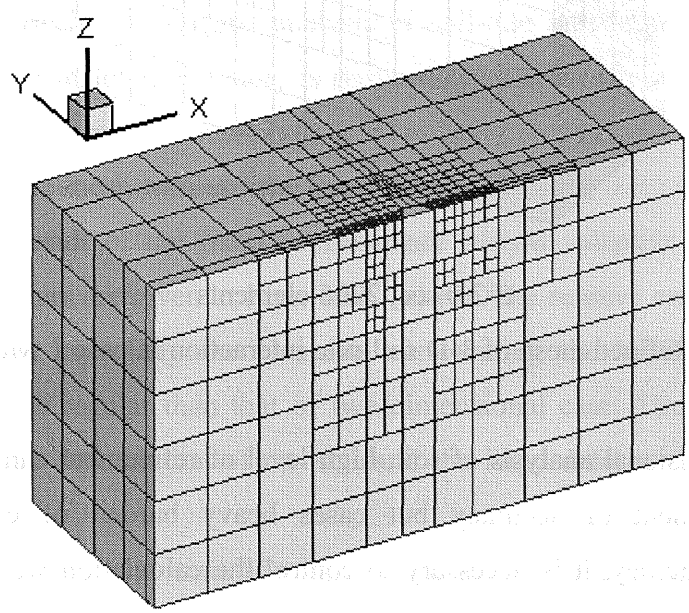

t=1.5 sec, 1849 elements

Fig. 6.50.(a) Refined mesh of 3-D soil-pile interaction in case 1 with dt=0.2 sec

In **Fig. 6.51**, the values of average relative error calculated in three different cases are compared. The two error values of adaptive analysis becomes lower than the value of fixed coarse mesh after adaptive process starts at time t=1.0 second. The efficiency of adaptive FE method applied to three-dimensional soil-pile interaction analysis is

demonstrated. The adaptive analysis with high refinement frequency gives a quick and stable improvement of accuracy as shown in the figure. At the same time, more elements are created. In the refinement of three-dimensional mesh, one element fission to eight elements. The increase speed of element number is very fast than the speed of two-dimensional adaptive analysis.

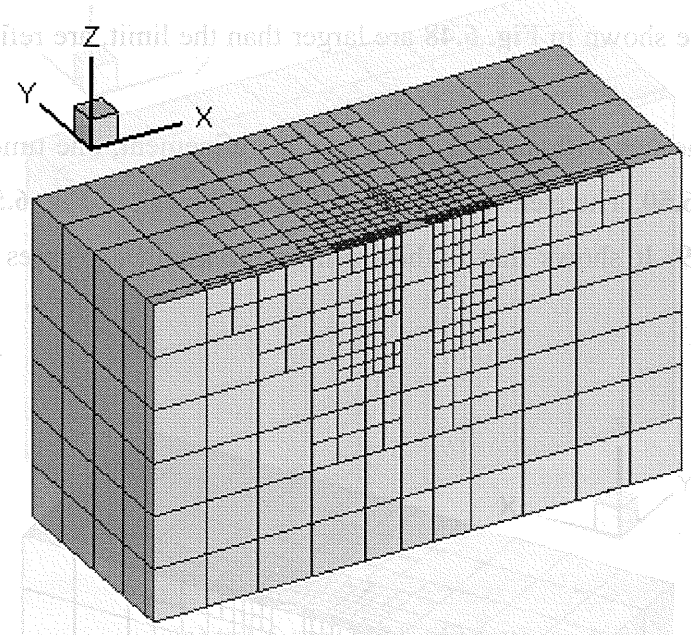

t=2.0 sec, 2206 elements

Fig. 6.50.(b) Refined mesh of 3-D soil-pile interaction in case 1 with dt=0.2 sec

In three-dimensional analysis of soil, high level of refinement can not give further evident improvement of accuracy but cases heavy burden of calculation. With improving the accuracy, it is necessary to control the calculation work via giving the limit of mesh refinement level and reducing the frequency of mesh refinement.

The example of three-dimensional soil-pile interaction analysis with a monotonous load demonstrates the efficiency of adaptive FE method. The method improves the accuracy of the mesh effectively by refining the soil elements with large error surrounding the head of pile. The error estimator can find these element effectively.

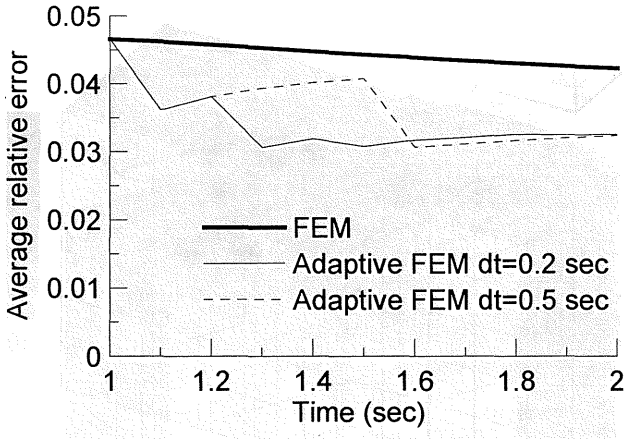

Fig. 6.51 Average relative error of 3-D soil-pile interaction in case 1

6.5.3 Result of seismic analysis of 3-D soil-pile interaction

The second case is 3-D seismic analysis of soil-pile interaction with adaptive FE method. The input acceleration history is shown in **Fig. 6.27** with a maximum value of 722 cm/sec^2. For comparison, responses without adaptive process are also calculated with the fixed coarse mesh with and the fixed fine mesh.

The analysis result of the fixed coarse mesh without adaptive process and their relative error contours are given in **Figs. 6.52.** (a)-(c). The relative error values of upper elements are large especially the elements surrounding the head of the pile. This distribution is more regular than that of two-dimensional case. The movement of the pile cases the large deformation of the soil and the large deformation cases the large relative error.

In adaptive analysis, the limit of relative error is 0.07. The mesh refinement starts from time t=5.5 second and is carried out one time every 0.5 second. The limit the refinement is 2. The refined mesh at time t=6.0, 10.0 and 15.0 second are shown as **Figs. 6.53.** (a)-(c) respectively. It is easy to find that the elements in the region with large error shown in **Figs. 6.52.** (a)-(c) are refined well. The element number increases quickly with the mesh refinement.

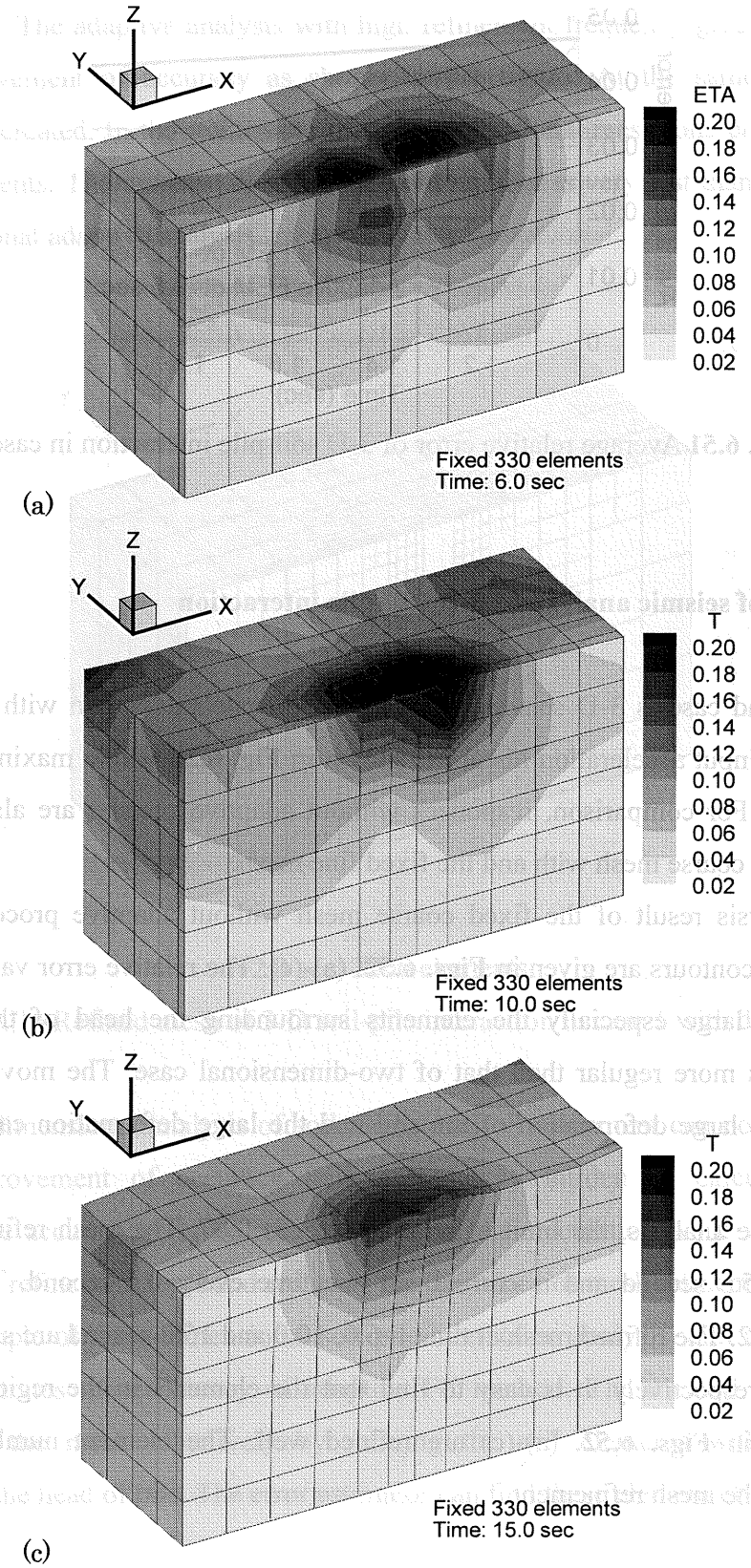

Fig. 6.52 Results of fixed coarse mesh and relative error for 3-D soil-pile interaction

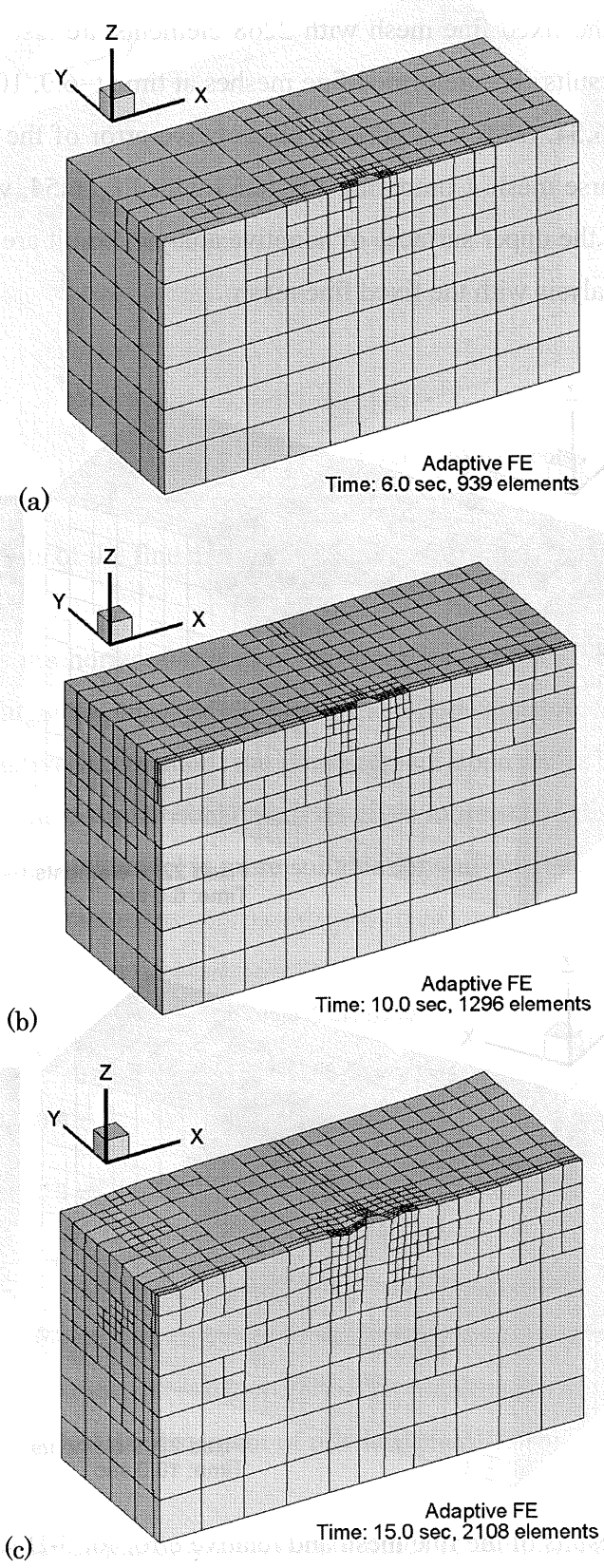

Fig. 6.53 Refined meshes and relative error contours of 3-D soil-pile interaction

The results of the fixed fine mesh with 2268 elements are also given to check the adaptive analysis results. The deformed fine meshes at time t=6.0, 10.0 and 15.0 second are given in **Figs. 6.54.** (a)-(c). In general, the relative error of the fine mesh is small than that of the coarse mesh. Comparing **Fig. 6.53** with **Fig. 6.54**, we can find that the refined meshes and the upper surfaces of adaptive analysis result are close to the results of finite element analysis with the fixed fine mesh.

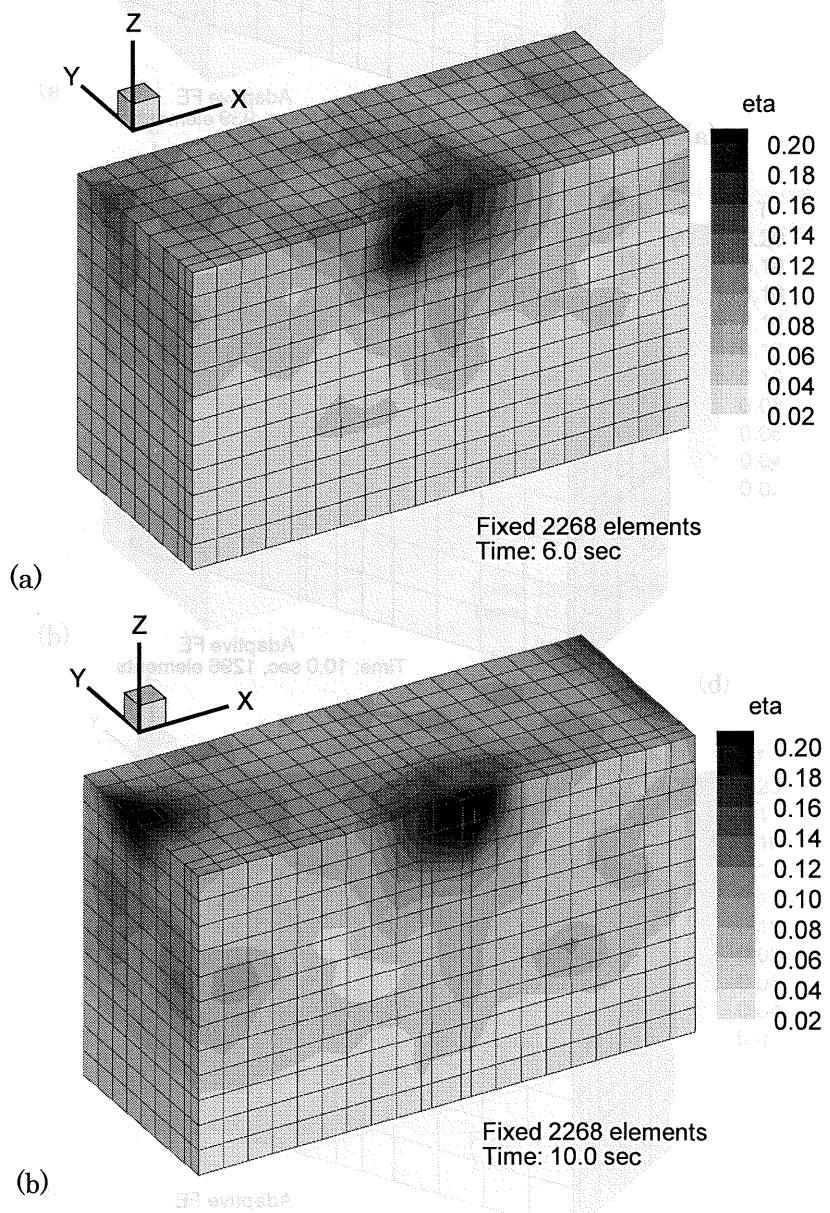

Fig. 6.54.(a),(b) Results of the fine mesh and relative error for 3-D soil-pile interaction

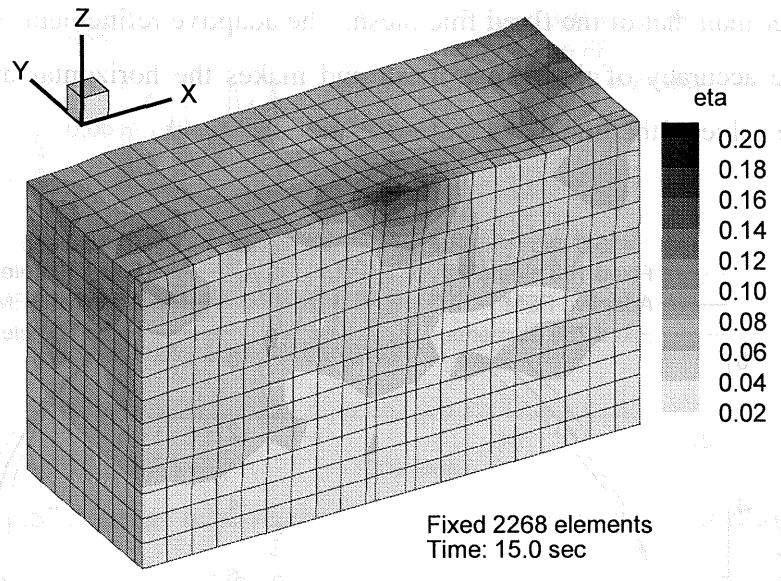

(c)

Fig. 6.54.(c) Results of the fine mesh and relative error for 3-D soil-pile interaction

Fig. 6.55 shows the horizontal displacement curves of pile head. The displacement of coarse mesh is larger than that of the fine mesh. With improvement the accuracy of the mesh using adaptive FE method, the displacement approaches to the result of fine mesh evidently. The three-dimensional analysis gives more stable displacement curve of pile. The three-dimensional model is more suitable for soil-pile interaction analysis.

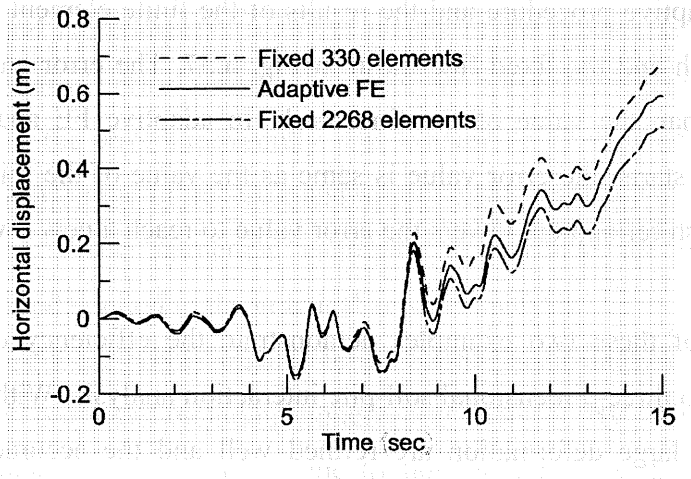

Fig. 6.55 Horizontal displacement of pile head for 3-D soil-pile interaction

The final horizontal displacements and curvatures of the pile calculated in the three cases are compared in **Figs. 6.35.** (a) and (b). The pile deformation of the fixed coarse

mesh is larger than that of the fixed fine mesh. The adaptive refinement of soil elements improves the accuracy of the coarse mesh and makes the horizontal displacement to approach the value of the fine mesh.

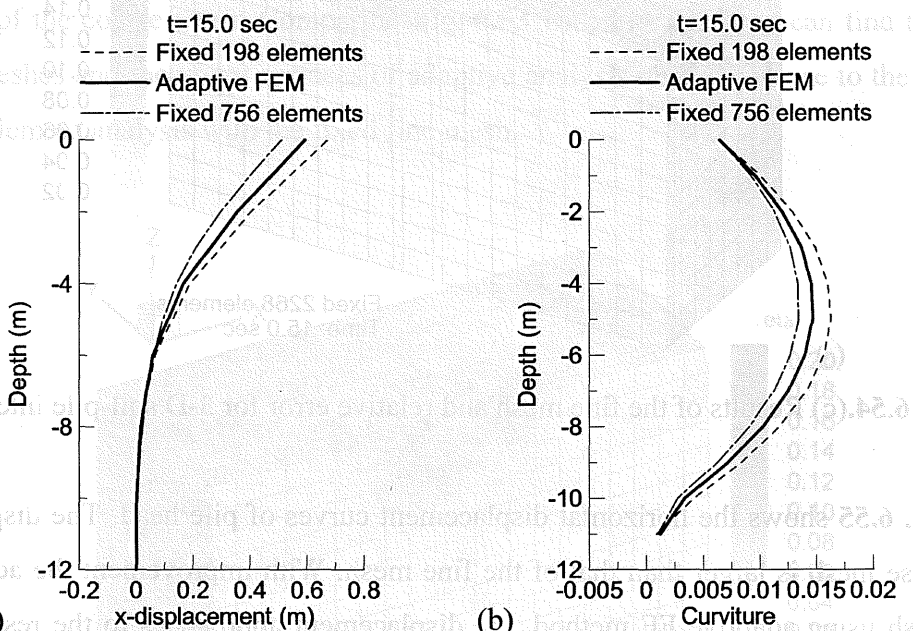

Figs. 6.56 Displacements and curvatures of pile for 3-D soil-pile interaction (t=15 sec)

In a usual way, the average relative errors of the three cases are compared between the results of adaptive procedure and the results of the finite element analysis with the fixed coarse mesh and the fixed fine mesh in **Fig. 6.57**. The error value of the coarse mesh is larger than the value of the fine mesh. In adaptive FE analysis, before the adaptive process starts, the error value is same as the value of the initial coarse mesh. The adaptive mesh refinement lowers the error value to reach a new lower the value to a satisfied value.

The results of these two examples demonstrate the efficiency of *h*-adaptive FE method applied to three-dimensional soil-pile interaction analysis. With this method, the soil elements in large deformation are refined well and the accuracy of analysis is improved effectively.

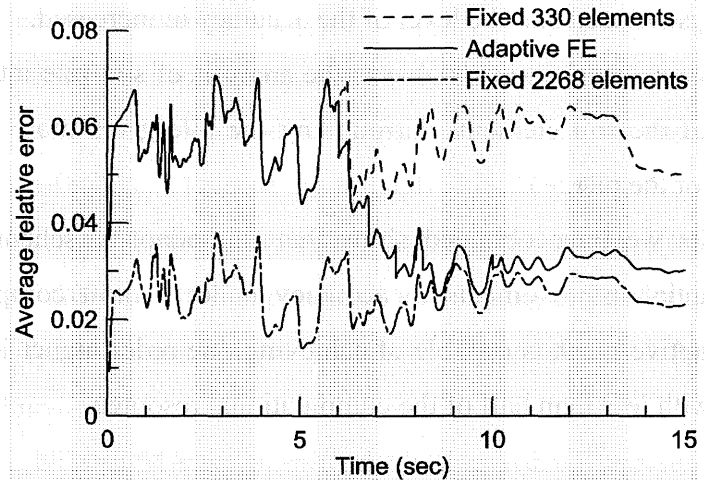

Fig. 6.57 Average relative error of soil for 3-D soil-pile interaction

6.6 Conclusion and remarks

This chapter presents four numerical examples including two-dimensional seismic analysis of embankment, two-dimensional analysis of soil-pile interaction system, three -dimensional seismic analysis of embankment and three-dimensional analysis of soil-pile interaction system. The displacement, deformation and relative error results of adaptive FE method are compared with the results of the coarse meshes and the fine meshes. The posteriori error estimator based on superconvergent patch recovery technique evaluates the error successfully. The *h*-adaptive FE method refines the mesh according to the distribution of the error and improves the accuracy of the finite element method effectively. These numerical examples demonstrate the efficiency of the *h*-adaptive FE method applied to the practical seismic analysis.

The *h*-adaptive FE method is suitable to the elasto-plastic analysis of saturated soil, especially to those problems including liquefaction analysis. By refining the elements with large deformation or large error due to liquefaction flow, the accuracy of the nonlinear numerical analysis is improved effectively.

The *h*-adaptive FE method is suitable to three-dimensional dynamic analysis. By giving the limit of adaptive level and selecting a suitable adaptive frequency, the

calculation work is reduced and the level of the accuracy in increased.

The *h*-adaptive FE method is suitable to the analysis of soil-pile interaction system. The refinement of the soil elements surrounding the pile gives more accurate motion and deformation of the pile.

All the results we have obtained show that this adaptive scheme is capable of achieving substantial improvements in accuracy under a limit computational effort. Generally, an adaptive mesh is capable of achieving one order higher level of accuracy as a fixed mesh with less than half of the computational resource.

References

[1] Tang X, Sato T. A posteriori error estimate and h-adaptive FE analysis of Liquefaction with large deformation, Journal of Geotechnical Engineering (accepted), 2004.

[2] Tang X, Sato T. H-adaptivity applied to liquefiable Soil in nonlinear analysis of soil-pile interaction, Soil Dynamics & Earthquake Engineering (submitted), 2004.

[3] Tang X, Sato T. Adaptive mesh refinement and error estimate for 3-D seismic analysis of liquefiable soil considering large deformation, Journal of Natural Disaster Science (submitted), 2004.

[4] Finn WDL, Fujida N. Piles in liquefiable soil: seismic analysis and design issues. Soil Dynamics and Earthquake Engineering 2002; 22: 731-42.

[5] Yang Z, Jeremic B. Numerical analysis of pile behavior under lateral loads in layered elastic-plastic soils. International Journal for Numerical and Analytical Methods in Geomechanics 2002; 26: 1385-1406.

[6] Oka F, Yashima A, Shibata T, Kato M, Uzuoka R. FEM-FDM coupled liquefaction analysis of a porous soil using an elasto-plastic model. Applied Scientific Research 1994; 52: 209-45.

[7] Oka F, Yashima A, Tateishi A, Taguchi Y, Yamashita S. A cyclic elato-plastic constitutive model for sand considering plastic-strain dependence of the shear modulus. Geotechnique 1999; 49(5): 661-80.

[8] Oka F, Yashima A, Kato M, Sekiguchi K. A constitutive model for sand based on the

non-linear kinematic hardening rule and its application. Proceedings of 10th World Conference on earthquake Engineering, Barcelona 1992. p. 2529-34.

[9] Akai, K, Tamura T. Study of two-dimensional consolidation accompanied by an elastic plastic constitutive equation. Proceedings of JSCE 1978; 269: 98-104.

[10] Di Y, Sato T. Large deformation dynamic analysis of porous medium using FEM-FDM coupled method. Advances in Computational Engineering & Sciences (CD-ROM, Atluri, S.N.,Nishioka, T. and Kikuchi, M.,Eds.), Chapter 12 Multiphysics & Multibody Dynamic. Tech Science Press; 2001.

[11] Di Y, Sato T. FEM-FDM coupled method for saturated soil analysis considering large deformation. Proceedings of the 26th JSCE Earthquake Engineering Symposium (Sapporo) 2001: 193-96.

[12] Di Y, Sato T. Liquefaction analysis of saturated soils taking into account variation in porosity and permeability with large deformation. Computers and Geotechnics 2003; 30: 623-35.

[13] Di Y, Sato T. A practical numerical method for large strain liquefaction analysis od saturated soils. Soil Dynamics and Earthquake Engineering 2004; 24: 251-60.

[14] Kelly DW, De JP, Gago SR, Zienkiewicz OC, et al. A posteriori error analysis and adaptive processes in the finite element method: Part I-Error Analysis. International Journal for Numerical Methods in Engineering 1983; 19: 1593-619.

[15] Zienkiewicz OC, Huang MS, Pastor M. Localization problems in plasticity using finite elements with adaptive remeshing. International Journal for Numerical and Analytical Methods in Geomechanics 1995; 19: 127-48.

[16] Zienkiewicz OC, Zhu JZ. A simple error estimator and adaptive procedure for practical engineering analysis. International Journal for Numerical Methods in Engineering 1987; 24: 337-57.

[17] Zienkiewicz OC, Liu YC, Huang MS. Error estimation and adaptivity in flow formulation for forming problems. International Journal for Numerical Methods in Engineering 1988; 25: 23-42.

[18] Zienkiewicz OC, Zhu JZ. Error estimates and adaptive refinement for plane bending problems. International Journal for Numerical Methods in Engineering 1989. 28: 2839-53.

[19] Mar A, Hicks MA. A benchmark computational study of finite element error estimation. International Journal for Numerical Methods in Engineering 1996; 39: 3969-83.

[20] Hicks MA. Coupled computations for an elastic-perfectly plastic soil using adaptive mesh refinement. International Journal for Numerical and Analytical Methods in Geomechanics 2000; 24: 453-76.

[21] Hinton E, Campbell JS. Local and global smoothing of discontinuous finite element functions using a least squares method. International Journal for Numerical Methods in Engineering 1974; 8: 461-80.

[22] Selman A, Hinton E, Bicanic N. Adaptive mesh refinement for localized phenomena. Computer & Structures 1997; 63: 475-95.

[23] Zienkiewicz OC, Liu YC, Huang MS. Error estimates and convergence rates for various incompressible element. International Journal for Numerical Methods in Engineering 1989; 28: 2191-202.

[24] Kelly WD, De JP, Gago SR, Zienkiewicz OC, et al. A posteriori error analysis and adaptive processes in the finite element method: Part II-Adaptive mesh refinement. International Journal for Numerical Methods in Engineering 1983; 19: 1621-56.

[25] Belytschko T, Tabbara M. H-adaptive finite element methods for dynamic problem, with emphasis on localization. International Journal for Numerical Methods in Engineering 1993; 36: 4245-65.

[26] Belytschko T, Wong BL, Plaskacz EJ. Fission-fusion adaptivity in finite elements for nonlinear dynamics of shells. Computers & Structures 1989; 33: 1307-23.

[27] Hamada M, Sato H, Kawakami T. A consideration of the mechanism for liquefaction-related large ground displacement. A proceedings from the fifth U.S.-Japan workshop on earthquake resistant design of lifeline facilities and countermeasures against soil liquefaction, Technical Report NCEER-94-0026; 1994. p. 217-32.

Chapter 7

Concluding Remarks

The effort of this research is focused on the numerical analysis methods of liquefiable soil. The aim is to improve the approximate quality of nonlinear numerical simulation of liquefaction process with large deformation. Two main parts are included in the thesis: three-dimensional FE-FD analysis of liquefiable soil considering large deformation using the cyclic elasto-plastic constitutive model and the fluidal elasto-plastic constitutive model; *h*-adaptive FE analysis of liquefiable soil. The new methods proposed here are suitable to solve the problems of the seismic analysis of soil structures and soil-pile interaction in liquefiable soil with large deformation. The major works and conclusions obtained in this thesis are summarized as follows.

(1) 3-D Analysis of Liquefiable Soil Considering Large Deformation

In the first part, the author introduced the development of three-dimensional FE-FD coupled method using updated Lagrangian formulation. The cyclic elasto-plastic model and the fluidal elasto-plastic model were adopted as the constitutive model of

liquefiable soil to deal with material nonlinearity. The governing equations of three-dimensional FE-FD method for the cyclic elasto-plastic constitutive model and the fluidal elasto-plastic constitutive model are developed using updated Lagrangian formulation. Updated Lagrangian formulation is used in the governing equations of three-dimensional FE-FD coupled method to deal with geometrical nonlinearity caused by large deformation. Although this research has been achieved in two-dimensional problems, the development of this method in three-dimensional analysis was the first time and showed special worth to practical engineering.

Some simple examples were analyzed to demonstrate the efficiency of this method. The adaptation of this method to elasto-plastic analysis of saturated soil was tested by single element simulation example. It was shown that this method could simulate the elasto-plastic behavior of saturated soil. One dimensional finite strain consolidation example was analyzed to test the updated Lagrangian formulation applied to three-dimensional FE-FD coupled method considering large deformation. The good agreement was found between numerical and analytical solutions of this example. The example of liquefied soil flow was also simulated to test the updated Lagrangian formulation applied to Newton viscous fluid. The result of this analysis was shown to be able to obtain numerical results close to that obtained by Enlerian method.

The results of two practical three-dimensional examples were given. Two examples demonstrated that this three-dimensional FE method using updated Lagrangian formulation could effectively simulate the earthquake induced ground flow in the seismic analysis of soil structures and dynamic analysis of soil-pile interaction.

(2) Adaptive Mesh Refinement for Dynamic Analysis of Liquefaction

The second part of the thesis was application of adaptive technique to non-linear FE analyses of saturated soil considering large deformation including liquefaction phenomenon. In previous researches, adaptive techniques were used to solve the static or transient problems with monotonous loads. In this research, adaptive FE method was applied to a seismic analysis in which the loads was an earthquake acceleration history including few thousands steps of time increments and cyclic vibration. The author used fission procedure belonging to the *h*-refinement indicated by the error estimates of

elements in adaptive FE method. The application was developed ont only in two-dimension but in three-dimension. It was also applied to the soil-pile interaction analysis. The special treatment of slave nodes in the joint sides or side surfaces was proposed in the fission procedure of soil-pile interaction analysis. In a standard fission procedure, the difference of adaptive levels between neighbor elements was limited no more than 1. That means only one slave node was allowed to create in a joint side or side surface considering the compatibility of the neighbor elements with same material. In the adaptive analysis soil-pile interaction, pile is much harder than the soil and the compatibility constrain is satisfied in the joint sides or side surfaces between the pile and soil. For this reason, more than one slave nodes were allowed to create in one joint side or joint side surface. The approximation was successively refined as to satisfy the predetermined standard of accuracy, and the efficiency of this method was confirmed in the finite element analyses. This method is easy to be applied to solve practical and engineering problem. In transient analysis, the limits of error are from 1%-5%. Although there have been a few researches to introduce adaptive mesh refinement to dynamics analysis, the limits of error in dynamics analysis are 2%-7%. The selection of an appropriate adaptive frequency is recommended.

This method was tested with some simple examples. First the examples of vertical compression in two- and three-dimension were calculated. The efficiency of this method to saturated soil within un-liquefied state is demonstrated. Then, adaptive analysis of shaking table test is conducted to demonstrate the efficiency of this method to the soil in liquefaction state. In these examples, the meshes were refined well according to the distribution of the error and the average error of the whole mesh was reduced.

A posteriori error estimate based on L_2 norm of strain error was adopted in the adaptive FE method. It could estimate the error of elements after every step of calculation in nonlinear FE analyses of soil effectively. Superconvergent patch recovery technique was used in the error estimates. The convergence of this error estimates method was tested with two- and three-dimensional examples with different quality meshes in two- and three-dimension. The convergence ratios were some as the values predicted. This method is easy to implement into any code and the calculation based on this method is very simple as well as the advantage in saving computation time is evident. This is a reliable indicator for mesh refinement.

Four practical examples of seismic analysis with finite deformation theory were calculated with adaptive FE method at last . These examples include two-dimensional and three-dimensional, soil flow due to liquefaction and soil-pile interaction problems. Adaptive analysis results of mesh deformation, error distribution, average error history, displacement responses were calculated and compare with FEM results. For the examples of soil-pile interaction analysis, the displacement and the curvature of pile were also checked in detail. The efficiency of the *h*-adaptive FE method was demonstrated further by these practical examples.

The *h*-adaptive FE method is suitable to the elasto-plastic analysis of saturated soil, especially to those problems including liquefaction analysis. By refining the elements with large deformation or large error due to liquefaction flow, the accuracy of the nonlinear numerical analysis is improved effectively. The *h*-adaptive FE method is suitable to three-dimensional dynamic analysis. The application of adaptivity to three-dimensional nonlinear analysis of saturated soil is also a valuable attempt in the developments of adaptive techniques. By giving the limit of adaptive level and selecting a suitable adaptive frequency, the calculation work is reduced and the level of the accuracy is increased. It is also suitable to the analysis of soil-pile interaction system. The refinement of the soil elements surrounding the pile gives more accurate motion and deformation of the pile. All the results we have obtained showed that this adaptive scheme was capable of achieving substantial improvements in accuracy under a limit computational effort. Generally, an adaptive mesh is capable of achieving one order higher level of accuracy than a fixed mesh with a half of the computational resource.

Author's Related Research Activities

(1) Xiaowei Tang and Tadanobu Sato. A Posteriori Error Estimate and *H*-adaptive FE Analysis of Liquefaction with Large Deformation, Journal of Geotechnical Engineering (Accepted), 2004.

(2) Xiaowei Tang and Tadanobu Sato. *H*-adaptivity Applied to Liquefiable Soil in Nonlinear Analysis of Soil-Pile Interaction, Soil Dynamics & Earthquake Engineering (Accepted), 2004.

(3) Xiaowei Tang and Tadanobu Sato. Adaptive mesh refinement and error estimate for 3-D seismic analysis of liquefiable soil considering large deformation, Journal of Natural Disaster Science (submitted), 2004.

(4) Xiaowei Tang and Tadanobu Sato. *H*-adaptivity Applied to Liquefiable Soil in Nonlinear Analysis of Soil-Pile Interaction, Proceedings of the 11th International Conference on Soil Dynamics & Earthquake Engineering & The 3rd International Conference on Earthquake Geotechnical Engineering, pp.760-767, 2004.

(5) Xiaowei Tang and Tadanobu Sato. 3-D Adaptive FEM and Error Estimate Based on Superconvergent Path Recovery for Liquefaction, The 59th National Conference of JSCE, 2004.

(6) Xiaowei Tang and Tadanobu Sato. *H*-adaptivity for 3-D Seismic Analysis of Embankment Constructed on Liquefiable Soil, Proceedings of the Third KU-KAIST-NTU Seminar on Civil Engineering Research, pp.146-153, 2004.

(7) Xiaowei Tang and Tadanobu Sato. Updated Lagrangian Analysis of Liquefaction Using Adaptive Mesh Refinement, The 58th National Conference of JSCE, 2003.

(8) Xiaowei Tang and Tadanobu Sato. Application of Adaptive Mesh Refinement for Large Deformation Analysis of Liquefiable Ground, The 38th National Conference of JGS, 2003.

(9) Xiaowei Tang and Tadanobu Sato. Error Estimation and Adaptive Mesh Refinement in Updated Lagrangian FEM for Liquefiable Soil, Proceedings of NTU/NCREE-KU Joint Seminar on Civil Engineering Research, pp.175-184, 2003.

(10) Xiaowei Tang, Feng Zhang and Tadanobu Sato. 3-D Numerical Analysis on Soil -Pile Interaction of Liquefied Ground Considering Large Deformation, The 57th National Conference of JSCE, 2002.

(11) Xiaowei Tang and Tadanobu Sato. Effects of Multi-directional Input Motion to Responses of Pile in liquefiable Soils, The 37th National Conference of JGS, 2002.

(12) Xiaowei Tang and Tadanobu Sato. Dynamic Analysis of Saturated Porous Medium by 3D FEM-FDM Coupled Method Considering Large Deformation, Proceedings of KAIST-KU Joint Seminar on Earthquake Engineering, pp.83-88, 2002.

Acknowledgements

The author began to carry out the research described in this dissertation in the division of Dynamics of Foundation Structure at the Disaster Prevention Research Institute of Kyoto University in April 2001. In the three years and few months study here, the author has absorbed plenty of the knowledge of science and technology, felt the long history, the age-old cultural tradition, the fine academia and the outstanding contributions to the world of Kyoto University. The doctoral course at Kyoto University is a proud career in the author's life. At the time to finish the dissertation, the author would like to express deep gratitude and the best wishes to all the persons and the organs who have given him helps and supports.

First of all, the author wishes to express his sincerest thanks to the author's supervisor, Professor Tadanobu Sato, the head of the division of dynamics of foundation structures, for his continuous guidance, warm encourage, strict discipline and generous support during the author's doctoral course. The author has benefited a great deal from Professor Sato's expertise.

The author is very grateful to Professor Hirokazu Iemura and Professor Susumu Iai from Kyoto University, members of his dissertation committee, for reviewing the draft of this dissertation, valuable comments and encouragement.

The author greatly appreciates Dr. Sumio Sawada, associate professor of Kyoto University and Dr. Riki Honda for their incentive suggestions and valuable discussions on many respects of the author's research activities. The appreciation is extended to Miss Ayako Nakamura, Miss Matsunoki and Miss K. Kotani, the secretaries at the division of Dynamics of Foundation Structures due to their helps in the author's doctoral course.

The author is indebted to Professor Kenzo Toki of Kyoto University for the introducing and help when the author entered Kyoto University.

Special thanks extended to Dr. Y. Di and Dr. Y. Moon for providing the relevant materials of this research. The thanks also go to all of the author's classmates at the division of Dynamics of Foundation Structures due to their kindly helps during the

author's doctoral course.

The author is grateful to the Ministry of Education, Science and Culture of Japan for the scholarship and to the Disaster Prevention Research Institute of Kyoto University for providing the Research Assistant position during the study.

During the four years of study in Japan, the author's wife has been living in his Chinese hometown to bring up their son and take care of his father and mother. The author also has benefited from the continuous encourages and supports of his father and mother's. The author's brother has provided moral and financial supports to him. Here, the author is greatly indebted to them.